DISS. ETH NO. 26204

HYBRID CIRCUIT QED WITH SPIN QUBITS

A thesis submitted to attain the degree of

DOCTOR OF SCIENCES of ETH Zurich

(Dr. sc. ETH Zurich)

presented by

Andreas Johannes Landig

MSc ETH Physics, ETH Zurich

born on 27.10.1989

citizen of Germany

accepted on the recommendation of

Prof. Dr. Klaus Ensslin, examiner
Prof. Dr. Guido Burkard, co-examiner
Prof. Dr. Thomas Ihn, co-examiner
Prof. Dr. Andreas Wallraff, co-examiner

2019

Abstract

Single photons and single electrons can be confined spatially in a solid-state device by using a millimeter-sized superconducting microwave resonator for the photons and nanoscale electrodes to form quantum dots for the electrons. The confined electrons realize a quantum mechanical two-level system (qubit), whose dipole interaction with single photons in the resonator is studied in the field of hybrid circuit quantum electrodynamics (hybrid circuit QED). These studies aim at investigating fundamental physics of quantum dots and light-matter interaction. They also work towards the realization of a scalable quantum dot based device for quantum information processing, where circuit QED is the main platform for state-of-the-art quantum information devices with superconducting qubits.

So far, hybrid circuit QED studies were mainly focused on charge states in double quantum dots. In this thesis we explore hybrid circuit QED with a focus on spin states in gallium arsenide quantum dots, motivated by the potentially longer coherence time of qubits based on quantum dot spin states instead of charge states. These experiments are performed at millikelvin temperatures using an experimental setup that was in large parts designed in this work. We also advance the hybrid circuit QED device technology by developing a resonator that is magnetic field resilient and has a high characteristic impedance of the order of one kiloohm. This increases the qubit-photon coupling strength and allows for experiments in a magnetic field.

In our first experiment we investigate spin states in a two-electron double quantum dot. There, the resonator acts as a spin-selective probe since it only couples with the spin-singlet states, which form a charge qubit, but is insensitive to the spin-triplet states. By probing the magnetic-field-dependent resonator transmission, we extract information about the singlet-triplet energy spectrum. In the presence of a double quantum dot voltage bias, we investigate a phenomenon called spin-blockade, which is based on a fundamental symmetry requirement for quantum states of electrons.

While the qubit decoherence rate exceeds the qubit-photon coupling strength in the first experiment, the situation is reversed in our second study. There, we report strong coupling between single microwave photons and a three-electron spin-qubit, called resonant exchange (RX) qubit. We resolve the vacuum Rabi mode splitting, which is the experimental signature of strong coupling, with a coupling strength of 31 MHz and a qubit decoherence rate of 20 MHz. We tune both quantities electrostatically and obtain a minimal decoherence rate of 10 MHz for 23 MHz of coupling strength.

The demonstration of strong spin-photon interaction is an important step towards long-range qubit-qubit interaction that involves spin qubits, which is realized in our third experiment. There, we implement a coherent link that controllably couples a RX qubit and a superconducting transmon qubit on the same device over a distance that is several orders of magnitude longer than the physical size of the spin qubit. We realize the link with a frequency-tunable high impedance resonator that is built of an array of superconducting quantum interference devices. The resonator couples strongly to both qubits, since the coupling rates of 52 MHz and 180 MHz extracted from the vacuum Rabi mode splitting exceed the corresponding decoherence rates of 11 MHz and 1 MHz for the RX qubit and the transmon, respectively. We spectroscopically observe coherent qubit-qubit interaction in the resonant and dispersive regime, where the interaction is mediated by real or virtual resonator photons, respectively. For the latter coupling scheme, we resolve an exchange splitting of 32 MHz.

Zusammenfassung

Einzelne Elektronen und einzelne Photonen lassen sich in einem festkörperbasierten Mikrochip räumlich begrenzen, indem ein millimetergrosser supraleitender Mikrowellenresonator für die Photonen verwendet wird und nanometergrosse Elektroden einen Quantenpunkt für die Elektronen bilden. Die räumlich begrenzten Elektronen bilden ein quantenmechanisches Zwei-Zustands-System (Qubit) aus, dessen Dipolwechselwirkung mit einzelnen Photonen im Resonator auf dem Gebiet der hybriden Schaltkreis-Quantenelektrodynamik (hybride Schaltkreis-QED) erforscht wird. Diese wissenschaftlichen Untersuchungen verfolgen das Ziel, grundlegende physikalische Zusammenhänge von Quantenpunkten und der Wechselwirkung von Licht mit Materie zu erforschen. Auch arbeiten sie an der Realisierung eines aus Quantenpunkten bestehenden skalierbaren Systems für die Quanteninformationsverarbeitung, wobei Schaltkreis-QED die Plattform der Wahl für hochmoderne, aus supraleitenden Quantenbits bestehende Quanteninformationssysteme darstellt.

Der Fokus bisheriger Forschung auf dem Gebiet der hybriden Schaltkreis-QED lag auf Ladungszuständen in Doppelquantenpunkten. Motiviert durch die potenziell längeren Kohärenzzeiten von Qubits, die auf Spinzuständen in Quantenpunkten basieren, im Vergleich zu solchen die Ladungszustände verwenden, widmen wir uns in der vorliegenden Doktorarbeit der hybriden Schaltkreis-QED und richten den Fokus auf Spinzustände in galliumarsenid basierten Quantenpunkten. Unsere Experimente werden im Millikelvin-Temperaturbereich in einem Messaufbau durchgeführt, der zu grossen Teilen während dieser Doktorarbeit entwickelt wurde. Durch die Entwicklung eines im Magnetfeld kompatiblen Hochimpedanz-Resonators, der eine charakteristische Impedanz in der Grössenordnung von einem Kiloohm aufweist, bringen wir zudem die Chip-Technologie von hybriden Schaltkreis-QED Systemen weiter voran.

In unserem ersten Experiment untersuchen wir Spinzustände von zwei Elektronen in einem Doppelquantenpunkt. Der Resonator agiert dabei als ein auf Spin sensitiver Detektor, da er ausschliesslich an Spin-Singulett-Zustände, welche ein Ladungsqubit

bilden, jedoch nicht an Spin-Triplett-Zustände koppelt. Durch Messung der magnetfeldabhängigen Transmission durch den Resonator können wir Rückschlüsse auf das Energiespektrum der Singulett-Triplett Zustände ziehen. Bei angelegter Spannung an den Doppelquantenpunkt beobachten wir ein als Spin-Blockade bekanntes Phänomen, welches auf grundlegenden quantenphysikalischen Symmetrieeigenschaften von Elektronen beruht.

Während in unserem ersten Experiment die Dekohärenzrate des Qubits die Kopplungsstärke an das Photon übersteigt, ist die Situation in unserem zweiten Experiment umgekehrt. Dort zeigen wir starke Kopplung zwischen einzelnen Mikrowellenphotonen und einem aus drei Elektronen bestehenden Spinqubit, welches als resonantes Austauschwechselwirkungsqubit (RAW Qubit) bezeichnet wird. Wir lösen die Rabi Vakuummodenaufspaltung, die experimentelle Signatur der starken Kopplung, mit einer Kopplungsstärke von 31 MHz und einer Dekohärenzrate des Qubits von 20 MHz auf. Wir regeln beide Grössen elektrostatisch und erhalten eine minimale Dekohärenzrate von 10 MHz bei einer Kopplungsstärke von 23 MHz.

Die starke Kopplung zwischen Spinqubit und Photon ist ein wichtiger Schritt in Richtung einer langreichweitigen Kopplung zweier Qubits, die Spinqubits beinhaltet, welche wir in unserem dritten Experiment realisieren. Dort verwenden wir ein steuerbares kohärentes Verbindungselement, um ein RAW Qubit und ein supraleitendes Transmon Qubit auf einem Mikrochip über eine Distanz, welche die physikalische Ausdehnung des RAW Qubits um mehrere Grössenordnungen übersteigt, zu koppeln. Das Verbindungselement besteht aus einem frequenzabstimmbaren Hochimpedanz-Resonator, der aus einer linearen Kette von supraleitenden Quanteninterferenzeinheiten aufgebaut ist. Der Resonator koppelt stark an beide Qubits, da die aus der Rabi Modenaufspaltung extrahierten Kopplungsstärken von 52 MHz und 180 MHz für das RAW Qubit und das Transmon die dazugehörigen Dekohärenzraten von 11 MHz und 1 MHz übersteigen. Wir beobachten spektroskopisch die kohärente Wechselwirkung beider Qubits, welche entweder durch reelle oder virtuelle Photonen im Resonator vermittelt wird. Für das virtuelle Kopplungsschema lösen wir eine Austauschaufspaltung von 32 MHz auf.

Contents

List of symbols

Symbols

Symbol	Explanation
$\vert 0/1\rangle$	qubit ground/excited state, resonator state with 0/1 photons
B	magnetic field
C	capacitance
E	energy
g_{i}	resonator-qubit(i) coupling strength
g	g-factor
G	amplifier gain
$\hat{\mathrm{H}}$	Hamiltonian
I	current
$\tilde{\mathrm{I}}$	in-phase component
J	exchange splitting
l	length
L	inductance
$\bar{n}$	average photon number
Q	resonator quality factor
$\tilde{\mathrm{Q}}$	quadrature component
$\hat{\mathbf{S}}$	spin operator
S_{xy}	scattering parameter
t	interdot tunnel coupling
T	temperature
T_2^*	dephasing time
U	Coulomb energy
V	voltage
w	center conductor width
Z	characteristic impedance
γ_1	relaxation rate
γ_2	decoherence rate
γ_φ	pure dephasing rate
Γ	reservoir tunneling rate
$\Delta\phi$	phase difference
δ	charge qubit detuning
Δ	RX qubit detuning parameter
Δ_{ij}	RF tones i and j detuning
Δ_{sc}	superconducting gap
ε	RX qubit asymmetry parameter
κ	resonator decay rate
μ	electrochemical potential
ν	frequency
$\hat{\sigma}_i, \hat{\tau}_i$	Pauli operator
Φ	magnetic flux
χ	dispersive frequency shift
Ψ	wave function
ω	angular frequency

(Sub/super)scripts

The following (sub/super)scripts are used with one or more symbols (e.g. ν_{RX}, E_{RX}).

(Sub/super)script	Explanation
C	charging
CQ	charge qubit
cr	coupling resonator
d	drive tone
dRX	RX drive tone
e	electron
exc	excitation
ext	external
g	gate
gen	generator
HF	hyperfine
int	internal
J	Josephson
JC	Jaynes-Cummings
kin	kinetic
l	length
ld	loaded
rL	left reservoir
L	left quantum dot
M	middle quantum dot
mag	magnetic
MID	measurement-induced
p	probe tone
P	Purcell
q	arbitrary qubit
QPC	quantum point contact
qr	qubit-resonator
r	resonator
R	right quantum dot
res	resonant
rp	resonator-probe
rr	read-out resonator
rR	right reservoir
RX	resonant exchange qubit
s	source
sd	source-drain
sf	spin-flip
SQ	SQUID
T	transmon qubit
TC	Tavis-Cummings
Z	Zeeman
ZPF	zero-point fluctuation

Physical constants

Constant	Explanation	Value
e	Elementary charge	$1.602 \times 10^{-19}\,\mathrm{C}$
ε_0	Vacuum permittivity	$8.854 \times 10^{-12}\,\mathrm{F/m}$
$h = 2\pi\hbar$	Planck's constant	$6.626 \times 10^{-34}\mathrm{Js}$ $4.136\,\mu\mathrm{eV/GHz}$
k_{B}	Boltzmann constant	$1.381 \times 10^{-23}\mathrm{J/K}$ $86.17\,\mu\mathrm{eV/K}$
m_{e}	Electron mass	$9.109 \times 10^{-31}\,\mathrm{kg}$
μ_0	Vacuum permeability	$4\pi \times 10^{-7}\mathrm{H/m}$
μ_{B}	Bohr magneton	$9.274 \times 10^{-24}\mathrm{J/T}$ $57.88\,\mu\mathrm{eV/T}$

Chapter 1

Introduction

Electrons are one of the main constituents of matter. As such, they reveal phenomena that require a quantum mechanical description. For instance the spin of the electron, which would in a classical picture correspond to its intrinsic angular momentum, is found to be quantized. If subject to a magnetic field, only two values with the same magnitude are measured that correspond to two states with either parallel or anti-parallel spin alignment with respect to the field. The magnetic field splits both states energetically thus forming a quantum mechanical two-level system (qubit). Against classical intuition, the spin can be in a superposition of both states before a measurement. Another example that lacks a classical counterpart is that electrons with the same spin are always found at different locations (orbitals) since the Pauli exclusion principle (Pauli, 1940) requires them to be distinct in at least one quantum number. This principle is the basis of the atomic shell structure and contributes to a difference in the Coulomb energy between states of electrons with different or the same spin orientation since the latter requires the electrons to be at distinct positions (orbitals) (Hanson et al., 2007). The energy difference, called exchange energy, leads to macroscopic phenomena such as magnetic ordering (Feynman et al., 1989) and allows to entangle spins of electrons with overlapping wave functions (Burkard et al., 1999) on a microscopic level.

These and other examples of quantum mechanical phenomena have motivated researchers to engineer controllable quantum states from single or multiple electrons with the prospect of studying fundamental physics (Kouwenhoven et al., 1997) and utilizing the quantum systems for quantum information processing (Loss et al., 1998, DiVincenzo et al., 2000). For the latter, the electron spin is especially appealing since it is not directly affected by electric field fluctuations in its environment thus preserving the quantum coherence for relatively long times of the order of microseconds (Kawakami et al., 2014). Millisecond coherence times can be achieved in materials that allow for isotopic purification like silicon (Veldhorst et al., 2014), where magnetic noise produced by the spins of the nuclei, which couple via hyperfine interaction to the spin of the electron, is drastically reduced. In this context also graphene is promising since it naturally consists of $\approx 99\%$ nuclear spin-free isotopes.

Investigating quantum effects of single electrons in solid state systems requires to engineer structures that confine the electrons within a region of space that is comparable to their de Broglie wavelength. Typical structure sizes are of the order of ten to hundreds of nanometers and can nowadays be readily fabricated to large extent thanks to the industrial goal to continuously reduce the transistor size (Moore, 1965). Such nanostructures that confine electrons in all three spatial directions are referred to as quantum dots. One way to realize them experimentally is to utilize a semiconductor heterostructure that hosts a two-dimensional layer of conducting electrons tens of nanometers below the surface and to deplete these electrons locally by electrostatic gating with nanoscale metallic electrodes that are patterned on top of the structure. This and other implementations of single quantum dots as well as tunnel coupled arrays of quantum dots (Kouwenhoven et al., 1997, Hanson et al., 2007) have widely been used in electronic transport measurements to investigate classical and quantum mechanical effects such as Coulomb blockade (Scott-Thomas et al., 1989), electron tunneling (Wees et al., 1989) or spin blockade (Ono et al., 2002).

A crucial step for quantum information processing with single-electron spin qubits was to demonstrate coherent control and read-out of single electron spins with oscillating magnetic (Koppens et al., 2006) and electric fields, where the electrical control relies on spin-charge coupling due to intrinsic (Nowack et al., 2007) or engineered (Pioro-Ladrière et al., 2008) spin-orbit coupling. The latter coupling mechanism was used to address two spins in a double quantum dot (DQD) individually and to realize two-qubit entangling gates that are based on exchange interaction (Veldhorst et al., 2015, Zajac et al., 2018, Watson et al., 2018). Coherent single-qubit (Petta et al., 2005, Wu et al., 2014) and two-qubit (Shulman et al., 2012) control was also demonstrated for a two-electron DQD spin qubit, with a spin-singlet and a spin-triplet state as the computational basis states. Since the single- and two-electron spin qubits carry a different spin for the ground state compared to the excited state, spin-orbit coupling is required for qubit control by electrical fields. This is different for a three-electron spin qubit that was proposed in Ref. DiVincenzo et al., 2000, where both qubit states are within the same spin subspace and have the same charge distribution but different spin arrangements. There, spin-charge coupling is intrinsic due to exchange and enables control by electric fields only as demonstrated for coherent single-qubit operations in Refs. Laird et al., 2010, Gaudreau et al., 2012, Medford et al., 2013a,b.

The two-qubit interactions mentioned above were mediated by exchange interaction or electrostatic coupling, both of which are limited to a short range that is of the order of the size of a quantum dot. While short-range coupling might be sufficient for nearest-neighbor coupling in small one-dimensional (Mills et al., 2019) or two-dimensional (Mortemousque et al., 2018) arrays of quantum dots, it becomes technologically more challenging with growing system size and imposes a major obstacle for implementing the estimated number of physical qubits of $10^6 - 10^8$ that are potentially required to perform relevant quantum algorithms (Vandersypen et al., 2017). Possible solutions are intermediate coupling schemes that employ, for instance, superexchange (Baart et al., 2017) or electronic cavities (Nicolí et al., 2018) to reach coupling lengths of up to a few micrometers. This length can be boosted by three to four orders of magnitude using circuit quantum electrodynamics (circuit QED), where microwave photons confined in superconducting resonators mediate the qubit-qubit interaction (Majer et al., 2007). Since its invention 15 years ago (Blais et al., 2004, Wallraff et al., 2004), circuit QED has both been a stimulant for quantum information experiments with superconducting qubits, where it provides the framework for high fidelity two-qubit gate operations (DiCarlo et al., 2009, Barends et al., 2014) and quantum non-demolition read-out (Wallraff et al., 2005, Walter et al., 2017), and enabled fundamental studies for instance of non-classical states of light (Houck et al., 2007), quantum many-body physics (Roushan et al., 2017) or quantum nonlocality (The BIG Bell Test Collaboration, 2018). These studies are based on coherent coupling of qubit and microwave photons by electric-dipole interaction, which is realized in the so-called strong coupling regime. There, the rate at which excitations are exchanged between the qubit and the resonator exceeds the photon loss rate in the resonator and the qubit decoherence rate.

In the weak coupling regime, where the strong coupling condition is not met, experiments with charge (Frey et al., 2012, Toida et al., 2013, Basset et al., 2013, Viennot et al., 2014, Stockklauser et al., 2015, Deng et al., 2015), spin (Petersson et al., 2012) and valley (Mi et al., 2017b) states in resonator-coupled quantum dots demonstrated an approach to study quantum dot physics alternative to transport-related studies. Coherent effects in such hybrid circuit QED experiments were however fully washed out due to the large decoherence rates of the quantum dot states that exceeded their coupling strength to the photons by at least one order of magnitude (Burkard et al., 2019). By increasing the coupling strength to hundreds of MHz with high impedance resonators (Stockklauser et al., 2017) or by lowering the decoherence rate to a few MHz via a noise reduction in the qubit environment (Mi et al., 2017c, Bruhat et al., 2018), the strong coupling limit was recently reached for DQD charge qubits, where quantum information is encoded in the electron charge distribution. Further hybrid circuit QED experiments demonstrated charge qubit control and read-out (Scarlino et al., 2019a) via the resonator as well as microwave photon-mediated coupling of two charge qubits (Woerkom et al., 2018).

While the difference in the charge distribution of the charge qubit states naturally results in an electric dipole coupling rate to the microwave photons that is of the order of MHz, direct spin-photon coupling is only possible by magnetic dipole interaction, which is at maximum only hundreds of Hz (Burkard et al., 2019). This coupling strength can be enhanced significantly by employing the idea of spin-charge coupling introduced above. With intrinsic or engineered spin-orbit coupling or exchange interaction, spin-photon coupling strengths of the order of MHz were estimated for a single-electron spin qubit in a single (Trif et al., 2008) or a double quantum dot (Cottet et al., 2010, Hu et al., 2012, Beaudoin et al., 2016, Benito et al., 2017), for a two-electron DQD spin qubit (Burkard et al., 2006, Jin et al., 2012) as well as for a three-electron spin qubit in a triple quantum dot (TQD) (Taylor et al., 2013, Russ et al., 2015b, Srinivasa et al., 2016). Once strong spin-photon coupling can be achieved, qubit-qubit coupling via the resonator that involves a spin qubit is a next important step for spin qubits in the context of quantum information processing.

In this thesis we perform three different hybrid circuit QED experiments, which all have in common that they involve few-electron spin states in laterally defined quantum dots in a semiconductor heterostructure made from gallium arsenide/aluminum gallium arsenide (GaAs/AlGaAs). These experiments are realized in an experimental setup presented in chapter 2 that was built up and in large parts newly designed in this thesis. In chapters 3 and 4 we introduce the physical concepts and the experimental realization of the three different qubits and superconducting microwave resonators that we employ for the experiments in this thesis. The realized qubits are a two-electron DQD charge qubit and a three-electron TQD spin qubit as well as a superconducting transmon qubit. The implemented resonators are a high impedance resonator that is built of superconducting quantum interference devices (SQUIDs) (Stockklauser et al., 2017) as well as a 50 Ω Al resonator (Frey et al., 2012) and a high impedance magnetic field resilient niobium titanium nitride (NbTiN) resonator. The design and fabrication for the latter resonator was developed in this thesis based on similar work in Ref. Samkharadze et al., 2016. Its fabrication and characterization are discussed in detail in chapter 4. In chapter 5 we introduce theoretical descriptions of hybrid circuit QED as a closed and an open quantum system and discuss the two cases of either a single qubit or two qubits coupled to the resonator. Since open quantum systems involve dissipative dynamics, we introduce decoherence models for the qubits with a focus on the three-electron spin qubit.

In the first experiment in chapter 6, we couple a NbTiN resonator and a DQD two-electron charge qubit in the weak coupling regime. We characterize this interaction and investigate singlet-triplet physics in the absence and presence of a DQD bias voltage by probing the resonator transmission in a variable external magnetic field. Since the resonator is only sensitive to the singlet state, we can deduce information about the singlet-triplet energy spectrum for the zero bias measurements and observe spin blockade previously known from transport studies as well as an unconventional spin blockade that is triggered by the presence of resonator photons in the finite bias data.

The second experiment in chapter 7 realizes the strong coupling regime between single microwave photons in the NbTiN resonator and a three-electron spin qubit. We explain the implementation of this so-called resonant exchange (RX) qubit in a TQD and present the spectroscopic signature of its interaction with the resonator. We observe the vacuum Rabi mode splitting, the signature of strong coupling, and demonstrate the tunability of the qubit-photon coupling strength and decoherence rate.

In chapter 8 we present the results of our third experiment, where the RX qubit is coupled over a distance of a few hundred micrometers via a SQUID array resonator to a transmon qubit. We introduce the sample design and characterize both qubits individually via the resonator, to which both are strongly coupled. We report RX qubit operation at different working points that are characterized by the ratio of the qubit-photon coupling strength over the qubit decoherence rate. We also demonstrate coherent coupling of the RX qubit and the transmon via the resonator in the resonant as well as in the dispersive regime.

Chapter 2

Experimental setup

In this thesis we study quantum systems that have a separation between their lowest discrete energy levels of about 6 GHz, which corresponds to a temperature of approximately 300 mK. To initialize them in their ground state, the experiments need to be performed at millikelvin temperatures well below 300 mK, which minimizes undesired thermal excitations. To control and probe the quantum systems, they are connected by direct current (DC) and microwave (RF) lines to room temperature electronics. The desired power of the RF signals at the quantum systems is at the level of single RF photons, which is of the order of 10^{-17} W. The desired electron temperature is around 30 mK. This is challenging at first glance, since the lines and electronics inevitably introduce thermal noise as well as heat load. In addition, thermalization can be problematic at mK temperatures where the thermal conductivity rapidly decreases and the thermal resistance at material interfaces becomes relevant (Pobell, 2007). The engineering challenge has been resolved in many previous works such as for example recently in Ref. Krinner et al., 2019 and meanwhile also in commercial solutions by obeying the following design rules: minimize the noise level via well thermalized filters or attenuators and shield the system from radiative sources while keeping the heat load sufficiently low in order to not heat up the system. We follow the same rules in this chapter and present an experimental setup that was built up in the course of this thesis.

We first provide an overview of the experimental setup in section 2.1 and subsequently discuss its main components in more detail in sections 2.2-2.5. A list of the commercially available components that are built into the setup can be found in Appendix D.

2.1 Overview

We identify four main components of the experimental setup that is illustrated schematically in Fig. 2.1. The first component is a dilution refrigerator, where a pulse-tube cooler and a phase transition in a ^{3}He-^{4}He mixture provide sufficient cooling power to decrease the temperature from room temperature at the refrigerator top plate sequentially to about 10 mK at its base plate. The radiation shields shown in Fig. 2.1 are thermalized at different temperature stages. They protect lower temperature regions from thermal radiation at higher temperatures. For the experiments presented in chapters 6 and 7, the refrigerator is equipped with a superconducting magnet (not shown in Fig. 2.1). The magnet produces a field[1] of a few tesla that is approximately homogeneous within a small volume of $\approx 1\,\mathrm{cm}^3$ below the base plate. Further details about the refrigerator are not discussed in this thesis since it is commercially available and its working principles can for example be found in Ref. Pobell, 2007.

The second component of the experimental setup is the sample, which is the heart of our experiments as it contains the quantum systems. The elements for mounting

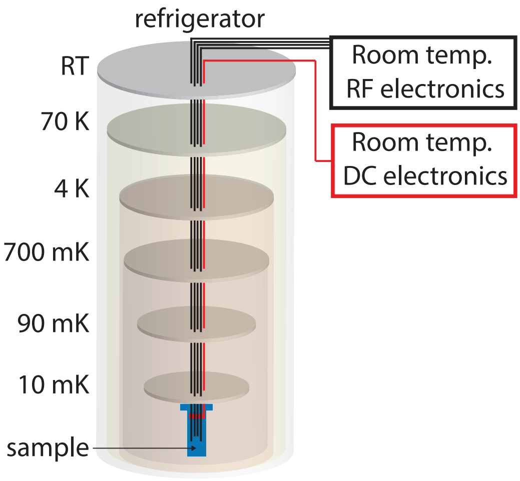

Figure 2.1 Setup overview. Simplified illustration of the main components of the experimental setup. RF (black) and DC (red) control lines connect the electronics at room temperature to a sample inside a dilution refrigerator. The holder for the sample is shown in blue. The temperatures at the different refrigerator plates are indicated. Note that radiation shields are illustrated as semi-transparent cylindrical shapes in different colors for better visibility.

---

[1] For the experiments in chapters 6 and 7 we use a 5 T single-axis and a $6-1-1$ T three-axis magnet, respectively.

and shielding the sample were developed in the course of this thesis and are discussed in detail in section 2.5. The third and fourth components in Fig. 2.1 are the DC and RF setups that consist of electronics at room temperature as well as of parts at cryogenic temperatures that connect to the sample. In section 2.4 we provide an overview of the DC setup and discuss the RF setup in more depth in sections 2.2 and 2.3, since it was in parts engineered in this thesis. Read-out and control of the measurement equipment is realized with the commercial software tool *Labber*.

2.2 Cryogenic RF setup

The coaxial microwave lines inside the refrigerator are shown in Fig. 2.2(a). The refrigerator cooling power at the different temperature plates decreases with temperature. To ensure that the presence of the heat-conducting coaxial cables does not introduce an excessive heat load into the refrigerator, their outer conductor is thermalized at every temperature stage. Note that the metallic inner and outer conductors of the coaxial cables are separated by a dielectric material, which has a different thermal contraction compared to the metal. Thermalizing the outer conductor therefore likely does not completely thermalize the inner conductor at cryogenic temperatures (Bianchetti, 2010). Better thermalization of the inner conductor is possible at temperature stages where attenuators are installed. These elements attenuate the signal together with thermal noise from higher temperature stages and provide an electrical connection between the inner and the outer conductor.

In practice, the attenuator and the outer conductor are thermalized with the refrigerator by using the copper (Cu) clamps shown in Figs. 2.2(b) and (c), respectively. These clamps consist of five flexible meander shaped “fingers” [see insets in Figs. 2.2(b)-(c)]. To clamp the attenuator or the outer conductor of the RF lines, a metallic rod is inserted in the center of the clamp and tightened at both ends [see insets in Figs. 2.2(b)-(c)]. This bents the “fingers” and results in a high contact force that persists at cryogenic temperatures since the amount of the bent likely exceeds differences in thermal contractions between the interfaced materials. The high contact force is a key ingredient for good thermalization as it reduces the thermal resistance at the contact interface by increasing the effective contact area (Pobell, 2007). The thermal resistance is further reduced by plating the clamps with gold (Au), which prevents oxidization of the Cu surface. We use brass screws with inserted beryllium copper (BeCu) springs [see green rectangle in Fig. 2.2(b)] to tighten the clamps to the refrigerator plates. The springs are compressed by $\approx 1\,\mathrm{mm}$ at room temperature to ensure a high contact force also at low temperatures. Note that because brass has a larger thermal contraction compared to the Cu plates of the refrigerator (Pobell, 2007), a brass screw without the spring should in principle also allow to achieve large contact forces at low temperatures. Note also that we use vacuum grease (Apiezon N) at the interface of every thermal connection of a setup component with the refrigerator plates. This was found to increase thermal conductivity in Ref. Bräm, 2018.

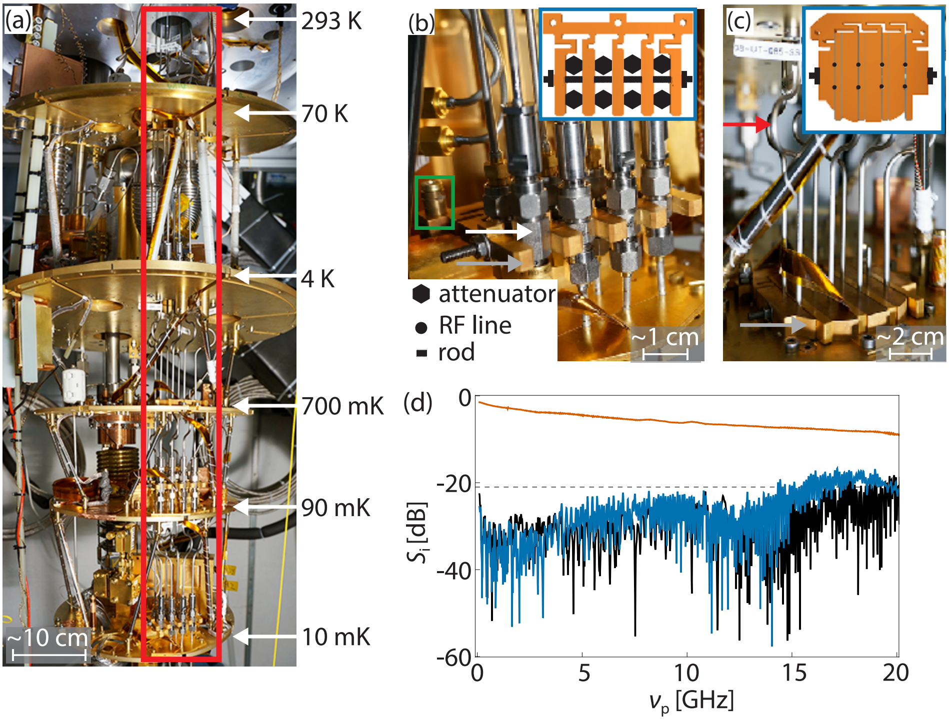

Figure 2.2 Cryogenic RF setup. (a) Optical micrograph of the opened dilution refrigerator with the plates at room temperature. The temperatures at different plates in the operational state are indicated. Microwave lines are installed within the region highlighted with a red rectangle. (b)-(c) Optical micrograph and schematic of the clamps that thermalize the attenuators (b) or the outer conductor (c) of the RF lines with the refrigerator plates. The gray arrows mark the clamps, which are also schematically illustrated in the insets. A white arrow indicates an exemplary attenuator, the green rectangle highlights a brass screw with an inserted BeCu spring. The bend in an exemplary RF line is marked with a red arrow. (d) S_{21} (orange), S_{11} (blue) and S_{22} (black) as a function of frequency ν_p for an exemplary RF line measured at room temperature. The dashed line is drawn at −21 dB.

We solder connectors to the RF lines to connect them to the attenuators. To determine the quality of this connection we measure the reflection and transmission spectrum of the cables as shown in Fig. 2.2(d). We ensure that the return loss is below the typical return loss of commercially available cables of $\approx 21\,\mathrm{dB}$ for frequencies of up to $15\,\mathrm{GHz}$. To reduce the force on the solder joint between the RF lines and their respective connectors due to thermal contraction, we introduce a bend into the lines [see red arrow in Fig. 2.2(c)].

Three different types of RF lines with different configurations of attenuators and amplifiers are installed in the refrigerator as depicted in Fig. 2.3. The experiment was designed for one line each of type A and B and six lines of type C. The RF line A is attenuated with three $20\,\mathrm{dB}$ attenuators in addition to about $10\,\mathrm{dB}$ of distributed attenuation due to the microwave cables. The high attenuation reduces the noise level to an average thermal occupation at $5\,\mathrm{GHz}$ of $\bar{n} \approx 10^{-3}$ (Krinner et al., 2019) and allows to reach signals at the level of single microwave photons at the sample. The attenuation is distributed over three temperature plates ($20\,\mathrm{dB}$ each) to ensure that the dissipated power does not exceed the cooling power at the plates.

Similar to the sample input-signal on line A, the signal coming from the sample is of the order of $10^{-17}\,\mathrm{W}$. It is directed with line B through a high electron mobility transistor (HEMT) amplifier that provides an amplification of $\mathrm{G}_{\mathrm{HEMT}} \approx 33\,\mathrm{dB}$ and a noise temperature of $\mathrm{T}_{\mathrm{HEMT}} \approx 2.7\,\mathrm{K}$[2]. We use a superconducting NbTi microwave line to minimize loss for a signal propagating from the sample to the amplifier. Two circulators at base temperature and one isolator at $90\,\mathrm{mK}$ protect the sample with a total attenuation of $\approx 60\,\mathrm{dB}$ from thermal noise while only weakly attenuating the signal from the sample by $\approx 0.5\,\mathrm{dB}$. The usable frequency range of line B is limited by the $4-8\,\mathrm{GHz}$ bandwidth of the circulators since the insertion loss of the circulators increases significantly outside this frequency band. The working principle of these circulators relies on the magnetization of a ferrite component, which requires to shield them from stray fields produced by the superconducting magnet inside the refrigerator. We therefore use commercial circulators with a magnetic field compatibility of up to $150\,\mathrm{mT}$.

The third type of cryogenic RF lines is line C in Fig. 2.3(a). The purpose of this line is to achieve a maximum signal level of the order of $100\,\mathrm{nW}$ at the sample without exceeding the cooling power of the refrigerator. We therefore use a sequence of $20\,\mathrm{dB}$, $10\,\mathrm{dB}$ and $3\,\mathrm{dB}$ attenuators in addition to the intrinsic distributed attenuation of the

---

[2] Amplifier specifications for the experiments in chapters 6 and 7. In chapter 8 we use a HEMT with $\mathrm{G}_{\mathrm{HEMT}} \approx 39\,\mathrm{dB}$ and $\mathrm{T}_{\mathrm{HEMT}} \approx 2.3\,\mathrm{K}$ within the frequency range from $4-8\,\mathrm{GHz}$ (see Appendix D).

microwave line of ≈ 10 dB. The signal at line C is routed via a bias tee, which is installed at the 10 mK stage and allows to apply a DC signal on top of the RF tone (see section 2.5), to the sample.

For the experiments presented in this thesis use the two different configurations shown in Fig. 2.3(b) to connect RF lines A and B to the sample. The details of the

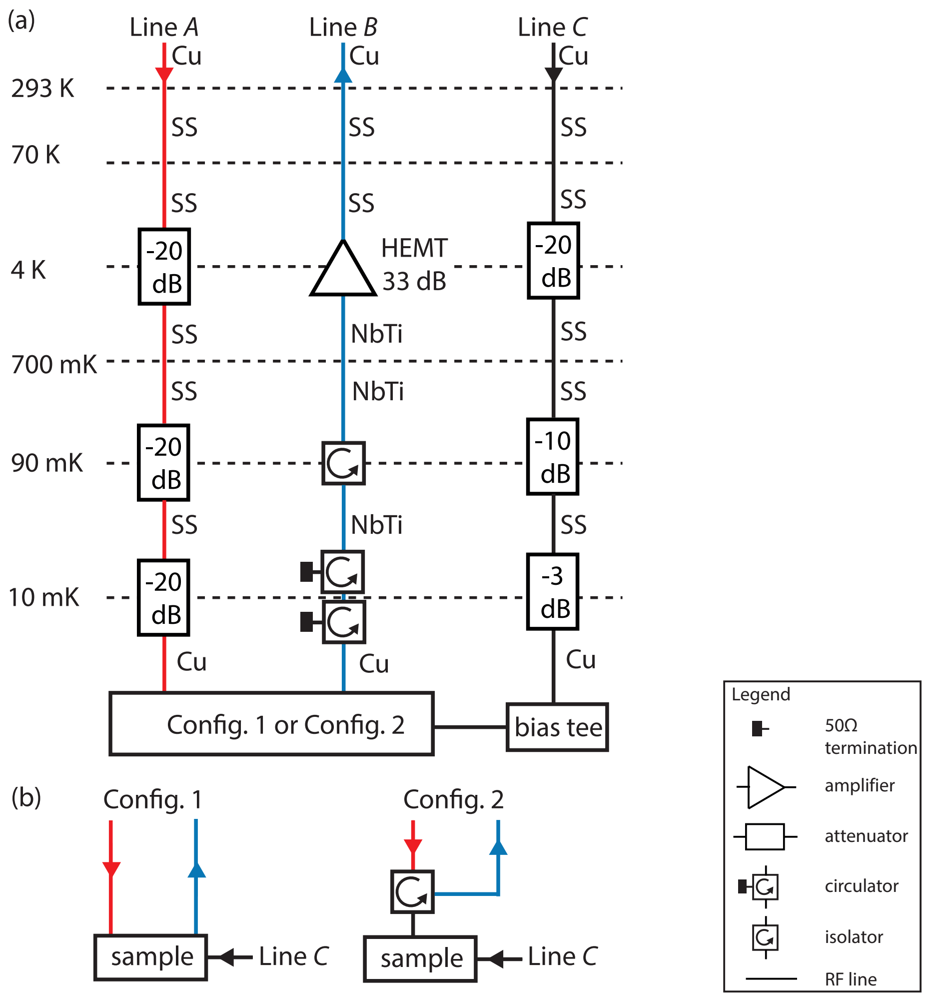

Figure 2.3 Cryogenic RF lines. (a) Schematic illustration of the three different types of RF lines that are installed inside the refrigerator. The damping of attenuators and the gain of amplifiers is specified. The material of the lines is either Cu, stainless steel (SS) or NbTi. (b) Transmission (left) or reflection (right) measurement configuration.

connection from the base plate to the sample are explained in section 2.5. Configuration 1 realizes a transmission measurement, where the signal from line A is directly transmitted through the sample to line B, while configuration 2 is used for a reflection measurement, where the signal from line A is reflected by the sample and directed with a circulator to line B.

Finally, we comment on the material of the cryogenic RF lines in Fig. 2.3(a). We use copper (Cu) lines to connect microwave components that are at the same temperature since these lines provide a low attenuation. Due to their large thermal conductivity, they are however not suited to connect different temperature stages inside the refrigerator. We use stainless steel (SS) lines for this purpose. They introduce a substantially smaller heat load compared to the Cu lines due to their lower thermal conductivity. The NbTi microwave cable used for line C is superconducting and therefore provides a low dissipation together with a high thermal isolation.

2.3 Room temperature RF setup

The cryogenic RF setup presented in section 2.2 is connected at room temperature to the RF setup shown in Fig. 2.4. This room temperature setup was designed in the group of Prof. Wallraff at ETH Zurich. It was adapted and assembled to be used for the experiments presented in this thesis. We provide an overview of this setup below and refer for more details to Ref. Businger, 2015.

Microwave signals are generated at the signal-generation stage outlined in red in Fig. 2.4. RF tones at two different frequencies ν_p and ν_d1 are combined and sent to line A, while a single tone is applied at frequency ν_d2 to line C. For both lines, DC blocks prevent frequency components below 10 MHz from reaching the sample. In addition we use a bandpass filter for line C, since noise on this line is significantly less attenuated compared to line A [see Fig. 2.3(a)].

The signal coming from the HEMT amplifier via line B [see Fig. 2.3(a)] is amplified in a room temperature amplification stage that is highlighted in blue in Fig. 2.4. In principle there are two signals at frequencies ν_p and ν_d1 on line B since both tones are applied to the sample via line A. In the following we are only interested in the tone at ν_p. The first amplifier of the amplification stage is an ultra-low noise (ULN) amplifier with a gain of $\mathrm{G}_\mathrm{ULN} \approx 34\,\mathrm{dB}$ and a noise temperature of $\mathrm{T}_\mathrm{ULN} \approx 76\,\mathrm{K}$. The noise temperature $\mathrm{T}_\mathrm{noise}$ of this linear array of the HEMT and ULN amplifier is given as (Pozar, 2005)

$$T_{\text{noise}} = T_{\text{HEMT}} + \frac{T_{\text{ULN}}}{G_{\text{ULN}}}. \tag{2.1}$$

The second term in Eq. (2.1) is negligible since $T_{\text{HEMT}} \gg T_{\text{ULN}}/G_{\text{ULN}}$. The noise due to the HEMT therefore limits the signal to noise in our experiments. The room temperature amplification stage in Fig. 2.4 also contains a low-noise (LN) amplifier with a gain of $G_{\text{LN}} \approx 30\,\text{dB}$ and a noise temperature of $T_{\text{LN}} \approx 473\,\text{K}$[3] that is connected to the first amplifier via a 10 dB attenuator in order to suppress standing waves between the amplifiers. Note that this second amplifier adds the term $T_{\text{LN}}/(G_{\text{ULN}}G_{\text{LN}})$ to Eq. (2.1), which is again negligible compared to T_{HEMT}.

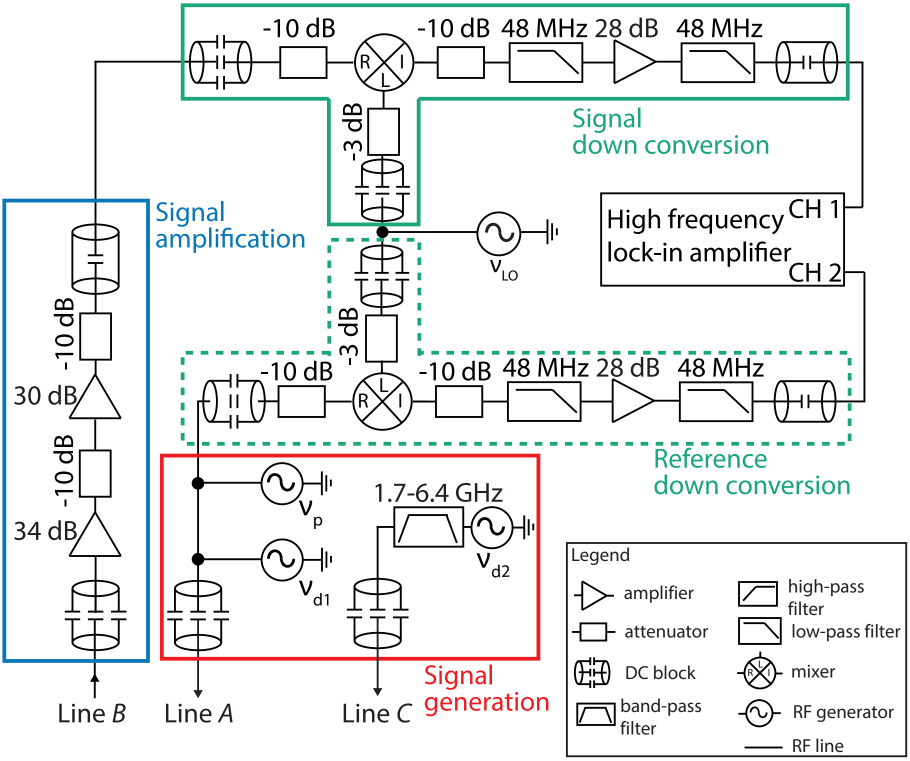

Figure 2.4 Room temperature RF setup. Schematic illustration of the signal-generation (red), amplification (blue) and down-conversion (green) stages that connect at room temperature to the microwave lines A-C [cf. Fig. 2.3(a)].

---

[3] This amplifier is used in chapters 6 and 7. In chapter 8 we use an amplfier with $G_{\text{LN}} \approx 28\,\text{dB}$ and $T_{\text{LN}} \approx 149\,\text{K}$ (see Appendix D).

The microwave signal at frequency ν_p can be described by $\mathrm{S}(t)e^{2\pi i \nu_\mathrm{p} t}$, where $e^{2\pi i \nu_\mathrm{p} t}$ is the carrier signal and $\mathrm{S}(t)$ is the complex-valued signal amplitude (Pozar, 2005). Since we are interested in measuring the amplitude and phase of $\mathrm{S}(t)$, the signal is further processed after the amplification stage with the down-conversion stage outlined with a solid green line in Fig. 2.4. There, the signal is down converted in a heterodyne detection scheme to an intermediate frequency (IF) ν_IF by mixing it with a local oscillator signal that is generated with a signal generator at frequency $\nu_\mathrm{LO} = \nu_\mathrm{p} - \nu_\mathrm{IF}$. We use IF frequencies between 25 MHz and 30 MHz. The IF signal is further amplified by 28 dB and filtered from high-frequency components above 48 MHz. In a last step, we send the signal to one of the two input channels of a high frequency lock-in amplifier that is discussed below. We use a second down-conversion stage outlined with a dashed green line in Fig. 2.4 to process a reference tone at ν_p that was split off during signal generation and therefore not sent through the refrigerator (see red region in Fig. 2.4). The down-converted reference signal is connected to the second input channel of the high frequency lock-in amplifier. Note that both down-conversion stages are connected to the same local oscillator for a common phase reference and contain the same microwave components[4].

We use the *UHFLI* from *Zurich Instruments* as the high frequency lock-in amplifier. It is a FPGA based device that first digitizes the IF (voltage) signal at both channels with an analog-to-digital converter (ADC) at a sampling rate of 1.8 GSa/s and a vertical resolution of 12 bit. The signals are subsequently demodulated inside the UHFLI to DC and typically averaged for $10-100$ ms in our experiments. As a result of the down conversion from ν_p to DC we obtain a time averaged amplitude that is proportional[5] to $|\mathrm{S}(t)|$ and the phase $\arg[\mathrm{S}(t)]$ for both signals. For a reflection or transmission measurement configuration [cf. Fig. 2.3(b)] we identify in the following the time averaged amplitude of the signal from the sample with $|\mathrm{S}_{11}|$ or $|\mathrm{S}_{21}|$, respectively. In contrast to the value of the phase of the individual down-converted signals, their difference $\Delta\phi$ is insensitive to phase drifts of the signal generator phase over time for fixed ν_p as well as to phase jumps that occur when sweeping ν_p. The *UHFLI* is also equipped with a rubidium atomic clock that provides a 10 MHz reference signal, which we use to synchronize the *UHFLI* with all RF signal generators.

The amplification and down-conversion stages are each assembled on a single board as shown in Fig. 2.5(a). This modular design allows to compactly mount the

---

[4] For the experiment in chapter 8 we use a 20 dB attenuator instead of 10 dB attenuation (used in chapters 6 and 7) at the signal input of the reference down-conversion stage in order to further attenuate the LO signal that leaks via the mixer (typical isolation ≈ 30 dB) to line A.

[5] It is not equivalent to $|\mathrm{S}(t)|$ due to the gain and attenuation of the signal in the down-conversion board.

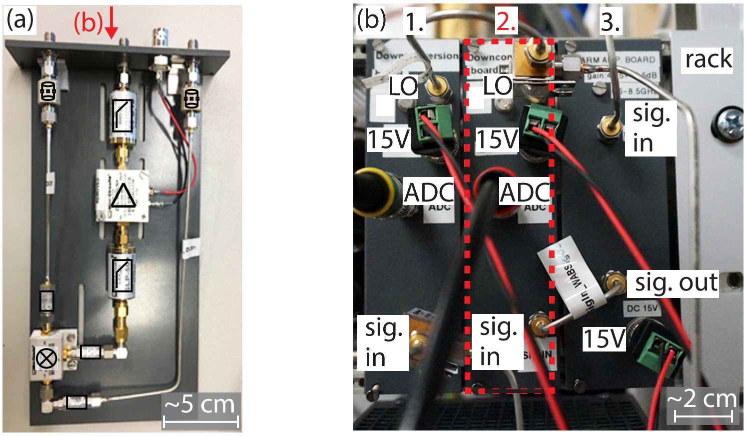

Figure 2.5 Microwave boards. (a) Image of a down-conversion board. The microwave components are labelled with the corresponding symbols (cf. symbol legend in Fig. 2.4). The red arrow indicates the direction of sight for (b). (b) Picture of two down-conversion boards (labelled as 1. and 2.) and one amplification board (marked as 3.) that are mounted in a rack. The board from (a) is highlighted with a dashed red rectangle. The labels next to the connectors refer to the following: "15 V" (connection of amplifiers to a 15 V power supply), "LO" (connection to the local oscillator), "sig. in/out" (connection to RF signal input/output), "ADC" (connection to the *UHFLI*).

boards in a rack as depicted in Fig. 2.5(b).

2.4 DC setup

In this section we present the room temperature electronics and the cryogenic wiring that is used to route DC signals to the refrigerator base plate and to supply the necessary voltages and currents to the HEMT amplifier. This setup was assembled from components that were developed by the electrical engineer Peter Märki in our research group. The components that connect the wiring from the base plate to the sample are discussed in section 2.5.

While the temperature of the refrigerator base plate is at about 10 mK, the electron temperature of the sample can easily be one order of magnitude higher. This is mainly because cooling of electrons via their host lattice is strongly reduced at mK temperatures, where the heat flow $\dot{Q}$ due to electron-phonon coupling scales as $\dot{Q} \propto T_e^5 - T_{ph}^5$ (Wennberg et al., 1986), with the electron (phonon) temperature T_e (T_{ph}). Sample electrons are dominantly cooled by electrically connecting them to cold electrons in the sample wiring, where more efficient cooling is possible via heat sinks to the refrigerator plates (Samkharadze et al., 2011). The setup presented in this section is therefore designed to reach a low electron temperature in the DC wiring at the base plate and consequently at the sample by following two approaches. First, heat sinks are designed to provide good thermal contact between the electrons in the wires and the refrigerator plates. Second, low-pass filters are installed at room temperature and at the base plate that allow the DC signal to pass but attenuate the high frequency components of the thermal noise that would otherwise heat up the electrons.

The DC voltage signals that are applied to the sample are of the order of 1 V. They are generated at room temperature with low-noise voltage sources[6]. Subsequently the signals pass a 1 : 5 voltage divider and a low-pass filter from surface mounted devices (SMD) with a cutoff frequency of 13 Hz. Note that this filter stage is limited by thermal noise produced by the filter resistors at room temperature. Another filter stage at base temperature is presented in section 2.5. Environmental noise that is present due to electrical equipment or other radiative sources outside the refrigerator is shielded by integrating the voltage sources and the filter stage into a single device with a RF tight metallic casing that is shown in Figs. 2.6(a)-(b). External measurement equipment can be connected to the device via BNC ports. The electrical connection of the voltage sources to the DC cable inside the refrigerator is also realized within the casing since it is mounted directly on top of the refrigerator room feedthrough of the DC cable.

The DC cable routes the signals to the base plate of the refrigerator. It is a flat band cable that consists of 24 signal carrying manganin wires that are capacitively decoupled from each other by placing a grounded wire between each pairs of wires. The flat band cable embeds the wires between a top and bottom polyimide layer. More details about the cable can be found in Ref. Bräm, 2018. We thermalize the flat band cable with the refrigerator plates by using the BeCu clamp shown in Fig. 2.6(b). The clamp deforms at room temperature and therefore exerts a high force also at cryogenic temperatures (Bräm, 2018). The resulting large contact area between the cable and the plates realizes a good heat sink to efficiently cool the electrons in the cable.

While for most of the DC lines the current is negligibly small due to a large sample resistance to ground, it is of the order of 1 μA for some of the lines. This current is measured with I/V converters that are also integrated into the device shown in Figs. 2.6(a)-(b).

We use a separate flat band cable to operate the HEMT amplifier that is installed at

---

[6] The root mean square (rms) voltage noise for the bare voltage sources without filters is $V_{\mathrm{rms}} \approx 165\,\mathrm{nV}$ in the range from $0.1 - 10\,\mathrm{Hz}$ for operation at 8.3 V.

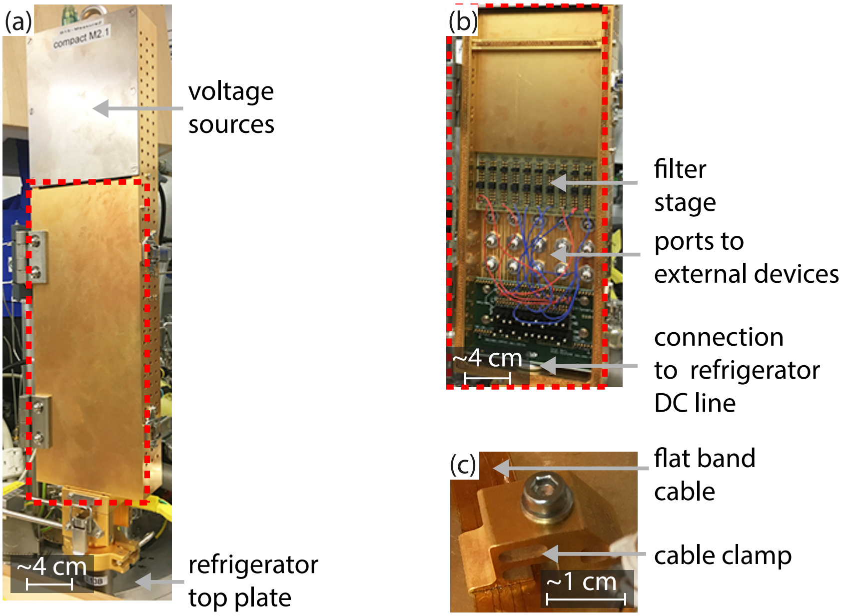

Figure 2.6 DC setup components. (a)-(b) Optical micrographs of the device that is mounted on top of the refrigerator and comprises DC voltage sources, a filter stage, ports for external devices and a connection to the DC cable inside the refrigerator. The part of the device outlined in red in (a) is opened in (b). (c) Image of an exemplary flat band cable section that is pressed to a refrigerator plate with a clamp.

the 4 K stage (cf. section 2.2). The cable connects at room temperature via a low-pass filter (470 μH, 100 nF) inside a breakout box to the power supply of the amplifier that was designed in Ref. Bianchetti, 2010.

2.5 Sample holder and shielding

In this section we describe the components of the experimental setup that are installed at the base plate of the refrigerator in order to mount the sample and to connect it to the RF and DC wiring that was presented in sections 2.2 and 2.4. These components were designed such that they can be well thermally anchored with the base plate. This ensures that they do not heat up the RF and DC lines and provide a low phonon temperature for cooling the sample lattice. The second guideline for the design was to protect the sample from radiative sources in its environment such as for example radiation from higher temperature plates that is likely not perfectly shielded from the shields mounted to the refrigerator plates as well as environmental electrical noise that couples via ports from outside to inside of the refrigerator. For the experiment in chapter 8 the sample is also shielded against external magnetic fields.

The RF and DC lines are directed from the base plate to the sample holder shown in Fig. 2.7(a) that is mounted with a high contact force to the base plate by using screws with inserted BeCu springs [cf. Fig. 2.2(b)]. The circulators, which connect one RF line from the base plate to the sample holder, are also visible in Fig. 2.7(a). The sample holder is a single workpiece of oxygen-free high thermal conductivity (OFHC) Cu[7]. The size of the sample holder is constraint by the dimension of the core of a superconducting magnet that needs to fit the holder for the experiments that require an external magnetic field. Another design constraint for the holder is that the sample needs to be mounted parallel and in the homogeneous region of this magnetic field,

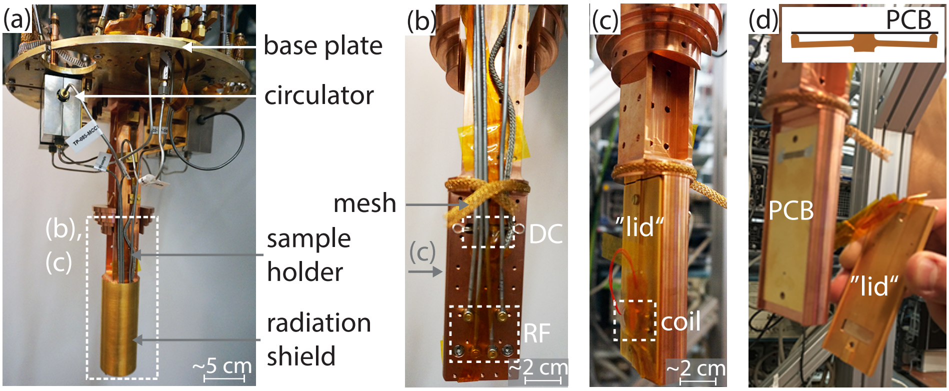

Figure 2.7 Sample holder. (a) Optical micrograph of the components mounted at the bottom of the refrigerator base plate. Some components are labelled and described in the text. (b)-(c) Image of the front (b) and the back (c) of the area outlined with a white rectangle in (a) after removing the radiation shield. The arrow in (b) indicates the direction of sight for (c). The rectangles highlight regions that are discussed in the text. (d) Similar image section as in (c) with the "lid" removed. A schematic illustration of the "lid" and the PCB cross section once they are tightened together with a screw (not shown) is depicted in the inset.

---

[7] This sample holder material was used for the experiments in chapter 8. For the experiments in chapters 6 and 7 we used an electrolytic-tough-pitch (ETP) Cu sample holder with the identical design. The OFHC Cu holder has the potential advantage of reduced magnetic noise from molecular oxygen (Müller et al., 2017b) that is present in ETP Cu. We do not have experimental evidence of this advantage, which could be due to the insensitivity of our experiments to the sample holder material.

which is directed along the axis of the holder.

In the following we explain layer by layer the components that shield and thermalize the sample. If magnetic field shielding is required, two cylindrical cryoperm[8] shields are installed around the sample (not shown in Fig. 2.7). The radiation shield shown in Fig. 2.7(a) is installed for every experiment. It has a cylindrical shape and is closed at one end. To efficiently screen radiation from outside the shield at its open end, a good electrical connection between the sample holder and the shield is necessary that persists at cryogenic temperatures. We realize this connection with a flexible metallic mesh [see Fig. 2.7(b)] that is compressed in order to slide the radiation shield on top of the sample holder. RF and DC lines connect to the sample holder in the region inside the shield outlined with dashed rectangles in Fig. 2.7(b). In the rear view of this region in Fig. 2.7(c), a BeCu "lid" is visible, which thermalizes a printed circuit board (PCB) with the sample holder [see Fig. 2.7(d)]. Note that the sample is mounted on the PCB as discussed below. The "lid" is designed to yield a large contact force at two edges of the PCB since it is bent by tightening it with screws to the sample holder [see Fig. 2.7(d) inset].

In Fig. 2.7(c) a coil[9] is visible that is fixed to the "lid". This coil is used in chapter 8 to apply magnetic fields of the order of 1 mT to the sample. The coil material as well as its connection from the base plate to the 4 K plate is superconducting NbTi to prevent excessive heat load. To reduce magnetic field fluctuations, the coil line is filtered with a 7.8 kHz lumped element low-pass filter at 4 K, where it connects via a manganin flat band cable (see section 2.4) to another low-pass filter with a cutoff frequency of 50 mHz inside a breakout box at room temperature.

The final connection of the DC and RF lines to the sample is realized on the PCB shown in Fig. 2.8(a). The front and backside of the PCB has an Au-plated[10] Cu metallization. The DC lines are connected to a socket in the upper part of the PCB and filtered with SMD low-pass filters (15 nF, 10 kΩ) with a cutoff frequency of 7.6 kHz. The space between the socket and the filter stage could be used in future PCB designs for additional SMD or on-chip filtering. The RF lines connect via SMP microwave sockets to 50 Ω planar RF lines on the PCB. These planar lines are coplanar waveguide transmission lines that will be introduced in chapter 4. The dielectric constant and the thickness of the PCB is similar to the sample such that their transmission line geometries are comparable. We keep the front and backside of the PCB on the same potential

---

[8] Material with a high magnetic permeability at cryogenic temperatures.

[9] It is 12 mm in diameter and has 4000 turns.

[10] Nickel-free plating (immersion silver/immersion gold) to prevent magnetic stray fields.

(refrigerator ground) by connecting them with multiple metallized holes (vias). The large number of vias suppresses parasitic standing waves on the PCB. DC and RF signals can be superimposed with SMD bias tees that contain a 10 kΩ resistor and a 10 nF capacitor. The DC and RF lines on the PBC are wire bonded with Al wires to the corresponding contacts on the sample as shown in Fig. 2.8(c). The PCB lines and the sample contacts are in the same plane to reduce the reflection of microwave signals. This is realized by inserting the sample into a region where the front metallization and the dielectric of the PCB are removed. We use polymethyl methacrylate (PMMA) to glue the sample to the PCB. Before wire bonding, all DC lines on the PCB are shorted to the PCB ground using a conducting wire. This reduces the risk of electrostatic discharge that can occur due to small metallic structures that are present on the sample. The wire is fixed at the back of the DC socket as shown in Fig. 2.8(b). It is removed after installing the PCB in the refrigerator and connecting it to the (at that time grounded) refrigerator DC lines.

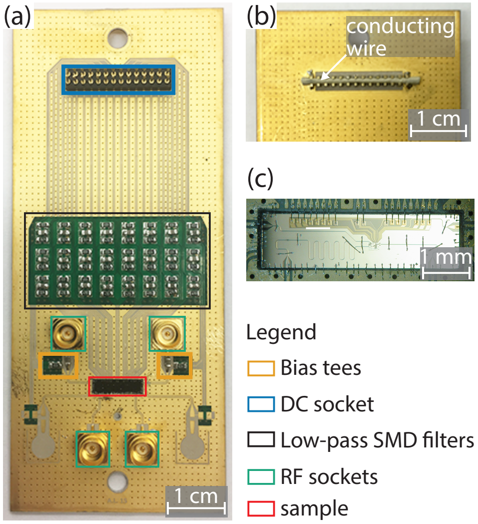

Figure 2.8 PCB and sample. (a) Optical micrograph of the PCB. Different components are highlighted and discussed in the text. Note that two out of four bias tees are assembled. (b) Image of a section of the back of the PCB. The pins of the DC socket are shorted to the PCB ground with a conducting wire. (c) Picture of a bonded sample.

2.6 Conclusion and outlook

In this chapter we presented an experimental setup that allows to probe quantum systems at the level of single electrons and single microwave photons. While some setup components were newly designed in this thesis, such as the thermalization components for the RF lines as well as the shielding, holder and circuit board for the sample, others were adapted from prior work. The experiments in chapters 6-8 demonstrate the setup functionality.

In the following we list some modifications of the experimental setup that could be implemented, if required, for the usage in future experiments. Noise on the DC line can possibly be further reduced by integrating Thermocoax cables into the DC wiring at the base temperature. These cables provide large attenuation at MHz to THz frequencies (Zorin, 1995, Baer et al., 2015). An improvement of the signal to noise ratio of the microwave read-out would be possible by employing for example a Josephson parametric dimer (Eichler et al., 2014) or a Josephson traveling-wave parametric amplifier (Macklin et al., 2015). Such an amplifier would be installed as a first amplification stage close to the sample and provide near-quantum-limited amplification before a second amplification at 4K by a HEMT amplifier.

Chapter 3

Solid-state qubits

A variety of physical implementations of a qubit in a condensed matter system are proposed, under basic investigation or already integrated into a few-qubit quantum architecture (Acín et al., 2018). They are required to provide a scalable system that allows precise control on time scales that are fast compared to the loss of quantum information due to incoherent interaction with the environment (DiVincenzo, 2000). The qubit implementations can be sorted into two categories. Those in the first category use the microscopic building blocks of the condensed matter system, i.e. single electrons, holes and nuclei. There, a two-level system is either intrinsic due to the atomic excitation spectrum of impurity atoms (Awschalom et al., 2013) or it is artificially induced by spatial confinement of electrons or holes (Kouwenhoven et al., 1997, Hanson et al., 2008). In the second category, qubits are encoded into macroscopic quantum states that condense into the same phases such as superconducting or topological phases (Devoret et al., 2005, Sarma et al., 2015).

In this chapter we introduce the three different solid-state qubits that are implemented in this thesis in chapters 6-8. In the first two sections 3.1 and 3.2 we focus on two microscopic qubit systems, where the logical qubit states are either encoded in the charge distribution (charge qubit) (Hayashi et al., 2003) or the spin degree of freedom (spin qubit) (Loss et al., 1998, DiVincenzo et al., 2000) of single or few electrons in quantum dots. In section 3.3 we give a brief overview of the superconducting transmon qubit (Koch et al., 2007) - a macroscopic solid-state qubit.

3.1 Double quantum dot charge qubit

We introduce electrostatically-defined quantum dots as well as basic properties of DQDs in subsections 3.1.1 and 3.1.2, respectively. In subsection 3.1.3 we restrict our consideration to two electrons in a DQD and discuss the charge states, which form a charge qubit, as well as the spin states. We also introduce the spin-blockade phenomenon that is known from transport experiments (Ono et al., 2002, Johnson et al., 2005a).

3.1.1 Electrostatically defined GaAs/AlGaAs quantum dots

To implement qubits that are formed by single electrons within a solid-state system, precise control over the system at the level of engineering the electron wave function is required. A suitable material for such a purpose is a GaAs/AlGaAs heterostructure since it can be grown as a highly pure crystalline structure with atomic scale precision using molecular beam epitaxy (Manfra, 2014). As schematically depicted in Fig. 3.1(a), it consists of a sequence of GaAs and $Al_xGa_{1-x}As$[1] layers that are grown on top of a GaAs wafer that has a thickness of about 500 μm.

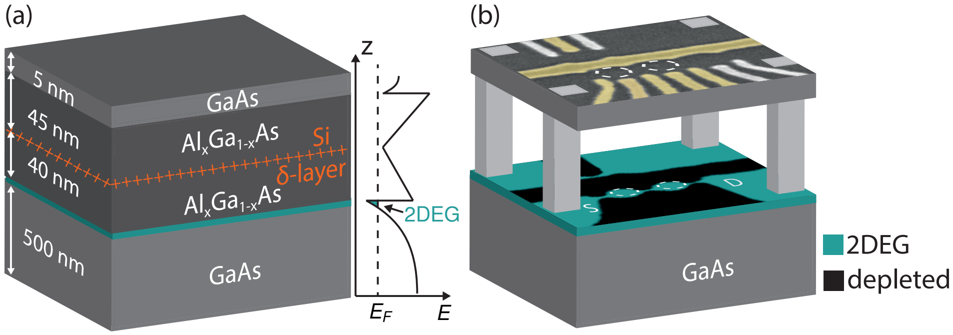

Figure 3.1 Heterostructure and electrostatic depletion. (a) GaAs/AlGaAs heterostructure (left) grown on top of a GaAs wafer (not shown). Spatial dependence of the conduction band edge, which is below the Fermi energy (E_F) in the region of the 2DEG. (b) Schematic from (a) without the $Al_xGa_{1-x}As$ layers such that regions with (green) and without (black) 2DEG are visible. Ohmic contacts (gray columns) to the source (S) and drain (D) electron reservoirs are indicated. A SEM image of a gate structure used to form two quantum dots (white circles) is shown on top of the heterostructure. The gate structure is explained in detail in Fig. 3.2.

---

[1] For the heterostructures used in this thesis, x is in the range from $30-31\%$.

In a region close to the interface of GaAs and $\mathrm{Al}_x\mathrm{Ga}_{1-x}\mathrm{As}$, the conduction band is below the Fermi energy since both materials have different band gaps. Consequently, electrons are confined in a potential well in growth direction, where they occupy the lowest subband. This layer of electrons is however free to move in plane and referred to as two-dimensional electron gas (2DEG). The electrons stem from a δ—doping layer of silicon (Si) that is introduced during growth. Within this work we use heterostructures[2] with a 2DEG electron density $n_\mathrm{e} \approx 2 \times 10^{11}\,\mathrm{cm}^{-2}$ and a mobility $\mu \approx 3 \times 10^{6}\,\mathrm{cm}^2/\mathrm{Vs}$.

The Fermi wavelength of the 2DEG electrons, $\lambda_\mathrm{F} = \sqrt{2\pi/n_\mathrm{e}} \approx 56\,\mathrm{nm}$, characterizes the length scale for observing quantum effects in the heterostructure. We achieve lateral confinement of electrons within the 2DEG on this length scale by applying negative voltages to metallic gate electrodes that are patterned on top of the heterostructure with electron beam lithography. The gates couple capacitively to the 2DEG and deplete it locally. Using the gate design illustrated in Fig. 3.1(b) we thereby form two conducting islands that are tunnel coupled to two electron reservoirs, marked as source "S" and drain "D". The electrons in the reservoirs are directly contacted from the surface with ohmic contacts (Taylor et al., 1994).

The system is controlled by manipulating the gate voltages V_i indicated in Fig. 3.2(a) such that the electric fields produced by the gates form a potential landscape that is similar to the idealized double-well potential in Fig. 3.2(b). There, electrons are trapped in two potential minima (islands) that have a depth that can be controlled

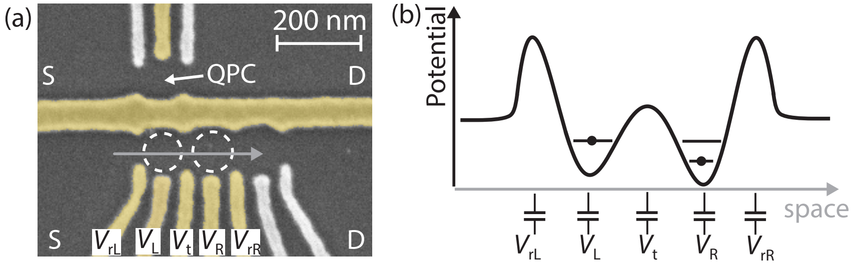

Figure 3.2 Formation of a DQD. (a) False-colored SEM image of an exemplary metallic gate structure that is used to form a DQD (white circles) and a QPC by electrostatic depletion with gate voltages V_i. Ohmic contacts to source (S) and drain (D) electron reservoirs are labelled. (b) Schematic of the idealized spatial dependence of the electrostatic potential along the line indicated by a gray arrow in (a).

---

[2] These structures were grown by Dr. Reichl in the group of Prof. Wegscheider at ETH Zurich (Reichl, 2014).

with the voltages V_L and V_R on the so-called plunger gates. The local potential maxima between the two islands as well as between the individual islands and the reservoirs form tunnel barriers for the electrons that can be adjusted with the voltages V_t and $V_{rL/R}$, respectively. The two islands confine electrons in all three dimensions in a small region of space, which introduces a discrete energy spectrum as shown in Fig. 3.2(b) that is similar to the energy spectrum of an atom. These islands can therefore be regarded as zero-dimensional objects and are referred to as quantum dots. Two energy scales are relevant for the quantum dot spectrum, for which we calculate order of magnitude estimates following Ref. Ihn, 2010.

As quantum dots host electrons in a small region of space, electron-electron interaction plays an important role. The energy cost to add an electron to a quantum dot is quantified by the Coulomb charging energy $E_{CD} = e^2/C_\Sigma$, where e is the electron charge and C_Σ the total capacitance of the quantum dot. It characterizes the difference between the electrostatic energies for adding the N-th and the $(N+1)$-th electron to the quantum dot that already contains $(N-1)$ and N electrons, respectively. We estimate $E_{CD} \approx 3.5\,\text{meV}$ by modeling the quantum dot as a metallic disc with a total capacitance $C_\Sigma = 8\varepsilon_0\varepsilon_r r$, where ε_0 is the vacuum permittivity, $\varepsilon_r = 12.9$ the dielectric constant of GaAs and $r = 50\,\text{nm}$ the disk radius. Here we estimate the disk radius from the gate geometry [see circles in Fig. 3.2(a)] as an upper boundary estimate for the dot size due to the electrostatic confinement. In order to form a quantum dot with a well defined number of electrons on it, the tunneling resistance R_t to the reservoirs has to exceed the resistance quantum h/e^2 ($\approx 26\,\text{k}\Omega$). This result is derived using Heisenberg's uncertainty relation $E_{CD}\Delta t > h$, with the single electron charging time $\Delta t = R_t C_\Sigma$. Another condition is that the charging energy is well above the thermal energy of the electrons. This condition is fulfilled in our experiments that are performed at electronic temperatures of $T_e \approx 50\,\text{mK}$ because $k_B T_e \approx 4\,\mu\text{eV} \ll E_{CD}$.

The second relevant energy scale for the quantum dot spectrum is the single-particle level spacing, which is the energy separation between the electron orbital eigenstates within the quantum dot. Assuming a parabolic confinement potential we obtain $\Delta E_{spl} = \hbar^2/(4m^* r^2) \approx 110\,\mu\text{eV}$, where $m^* = 0.067 m_e$ and m_e are the effective and free electron masses, respectively. Hence, the charging energy dominates the quantum dot spectrum. However, as $\Delta E_{spl} \gg k_B T_e$, excited states of the quantum mechanical energy levels are not relevant in this work.

In Fig. 3.2(a) we also indicate a quantum point contact (QPC), which is a single narrow constriction between two electron reservoirs that is formed by electrostatic gating. Its conductance is sensitive to small changes in the electrostatic potential in its vicinity. Consequently, we use it as a detector for changes in the charge occupation of the quantum dots (Field et al., 1993). For more details on QPCs we refer to Ref. Ihn, 2010.

3.1.2 Properties of a double quantum dot

By placing two quantum dots in close proximity as shown in Fig. 3.2(a), a DQD is formed. A schematic illustration of a typical DQD energy diagram is depicted in Fig. 3.3. There, we limit the consideration to a total number of two electrons in the DQD, which will be relevant below. We describe tunneling between two quantum dots due to an overlap of their wave functions with the tunneling matrix element t. While interdot tunneling is a coherent process further discussed in subsection 3.1.3, tunneling between the DQD and the left (right) electron reservoirs is treated perturbatively as an incoherent process at rate Γ_{rL} (Γ_{rR}).

The DQD electrochemical potentials $\mu(\mathrm{N_L},\mathrm{N_R})_{(\mathrm{N'_L},\mathrm{N'_R})}$ shown in Fig. 3.3 quantify the energy cost $\mathrm{E}(\mathrm{N_L},\mathrm{N_R})-\mathrm{E}(\mathrm{N'_L},\mathrm{N'_R})$ for the transition $(\mathrm{N'_L},\mathrm{N'_R}) \rightarrow (\mathrm{N_L},\mathrm{N_R})$ that adds or removes an electron from either of the two quantum dots. Thereby, $\mathrm{E}(\mathrm{N_L},\mathrm{N_R})$ is the energy of the DQD state with $\mathrm{N_L}$ ($\mathrm{N_R}$) electrons on the left (right) quantum dot. The electrochemical potentials in the source and drain reservoirs are μ_{s} and μ_{dr}, respectively. Their difference is determined by a voltage bias $\mathrm{V_{sd}}$ across the DQD as $\mu_{\mathrm{dr}}-\mu_{\mathrm{s}} = -|e|\mathrm{V_{sd}}$.

Note that the diagram in Fig. 3.3 is simplified in the following manner. First, we indicate the electrochemical potentials of the occupation states of the individual quantum dots and omit their hybridization due to interdot tunneling. Second, whether an electrochemical potential is indicated in the left or right quantum dot depends on from

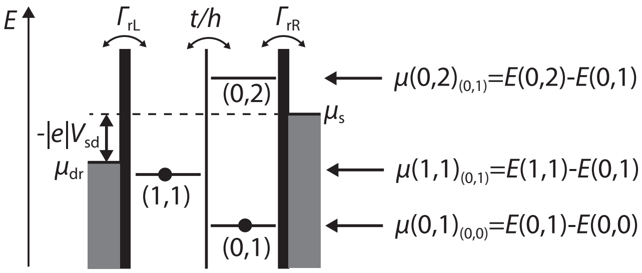

Figure 3.3 DQD energy diagram. Schematic of electrochemical potentials μ_i (horizontal lines) for two-electron charge states with energies $\mathrm{E}(\mathrm{N_L},\mathrm{N_R})$ in a DQD that is coupled to source and drain reservoirs at finite source-drain bias $\mathrm{V_{sd}}$.

which reservoir an electron can tunnel into the corresponding DQD state. For example, $\mu(1,1) = \mathrm{E}(1,1) - \mathrm{E}(0,1)$ is depicted in the left dot as it is defined with respect to $\mathrm{E}(0,1)$. Hence, for instance the transition $(0,1) \rightarrow (1,1)$ involves tunneling from the left reservoir into the left dot. Third, the subscript for $\mu(\mathrm{N_L}, \mathrm{N_R})$ is typically omitted in literature and also in this thesis if the reference state $(\mathrm{N'_L}, \mathrm{N'_R})$ is apparent from the energy diagram.

We configure a DQD using the gate structure in Fig. 3.2(a) and measure the differential conductance through the QPC as a function of the plunger gate voltages in Fig. 3.4(a). As mentioned in the context of Fig. 3.2, the plunger gates tune mainly the depth of the DQD potential minima and hence the DQD electrochemical potentials. We observe pronounced changes in the QPC signal in Fig. 3.4(a) as an experimental signature for a changing number of electrons in the DQD (Field et al., 1993). These changes are along hexagon-shaped regions, which indicates that within these regions the DQD charge occupation is stable while electrons are added or removed from the DQD at their boundaries. The data in Fig. 3.4(a) is therefore referred to as a charge stability diagram. Along the boundaries that are parallel to the black dashed line in Fig. 3.4(a), the left dot electrochemical potential is aligned with the left reservoir elec-

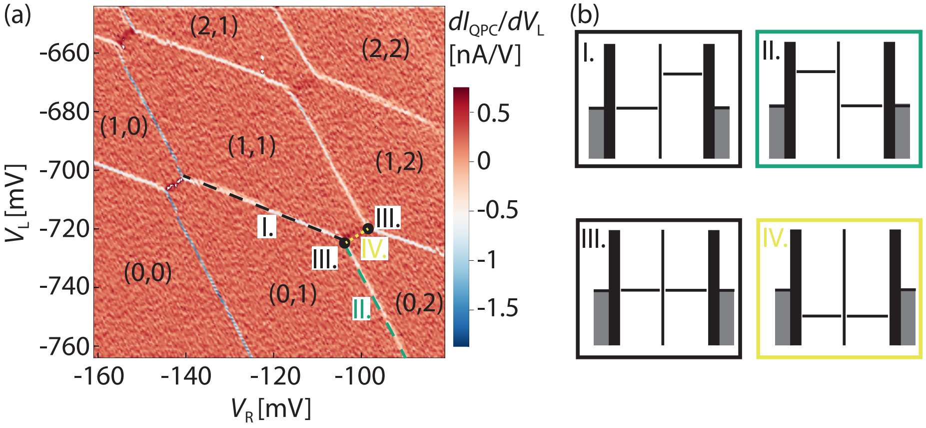

Figure 3.4 Few-electron DQD charge stability diagram and level alignment. (a) Differential QPC current $d\mathrm{I_{QPC}}/d\mathrm{V_L}$ as a function of right and left plunger gate voltages $\mathrm{V_R}$ and $\mathrm{V_L}$. Regions with a stable charge configuration $(\mathrm{N_L}, \mathrm{N_R})$ are indicated. Their boundaries are apparent as changes in the differential current. The dashed lines as well as the triple points (filled black circles) are discussed in the text. (b) DQD level alignment at the positions indicated with numbers in (a).

trochemical potential [see I. in Fig. 3.4(b)]. Consequently, elastic tunneling between the reservoir and the left dot is possible. Conversely, the electrochemical potentials of the right quantum dot and the right reservoir are aligned at the boundaries that are parallel to the green dashed line in Fig. 3.4(a) [see II. in Fig. 3.4(b)]. The boundaries are tilted as a results of a cross-capacitance between the plunger gates and their respective neighboring quantum dot as well as due to an interdot capacitive coupling. If the DQD electrochemical potentials are not aligned with the reservoirs and higher order tunneling processes are not relevant[3], tunneling between the reservoirs and the DQD is suppressed such that the DQD charge occupation is stable. By tuning the plunger gate voltages more negative, the electrochemical potentials in the DQD shift to higher energy and are emptied if they exceed the electrochemical potential in the leads. This sequentially empties the DQD. Once no more boundaries are observed by tuning the plunger gate voltages more negative, the $(0,0)$ charge configuration is reached. Consecutively, a well defined number of electrons can be loaded into the DQD by tuning the plunger gate voltages more positive and crossing the corresponding number of boundary lines.

At the corners of the hexagon-shaped regions in the charge stability diagram, both DQD electrochemical potentials are degenerate and aligned with the electrochemical potential in the leads [see III. in Fig. 3.4(b)]. These positions are referred to as triple points, as there three charge states coexist. As a result, elastic electron transport from the source to the drain is possible. For instance, at the two triple points indicated in Fig. 3.4(a), the corresponding transport cycles are $(0,1) \longleftrightarrow (1,1) \longleftrightarrow (0,2) \longleftrightarrow (0,1)$ and $(1,1) \longleftrightarrow (0,2) \longleftrightarrow (1,2) \longleftrightarrow (1,1)$ such that electrons can tunnel from source to drain and vice versa. If a finite source-drain bias is applied, the transport cycle becomes directional as discussed in subsection 3.1.4.

Along the line indicated in yellow in Fig. 3.4(a), the DQD charge states $(1,1)$ and $(0,2)$ are decoupled from the reservoirs such that the number of electrons in the DQD is constant but interdot tunneling is possible [see IV. in Fig. 3.4(b)]. This line exists between every pair of triple points and is referred to as interdot charge transfer line since there the states $(\mathrm{N}+1,\mathrm{M})$ and $(\mathrm{N},\mathrm{M}+1)$ with an excess electron in the left or right quantum dot are degenerate. The charge rearrangement between the dots is visible in the QPC response in Fig. 3.4(a).

---

[3] This is a good approximation in the regime $\mathrm{R}_t \gg h/e^2 \approx 26\,\mathrm{k}\Omega$, where the tunneling resistance R_t between the quantum dots and their respective reservoir exceeds the resistance quantum h/e^2 (Kouwenhoven et al., 1997).

3.1.3 Two-electron double quantum dot charge qubit

We now focus on the interdot charge transfer line for two electrons in a DQD that is visible in the charge stability diagram in Fig. 3.5(a). Note that we restrict the discussion to charge states in the DQD and discuss the relevance of the electron spin in subsection 3.1.4. Since the DQD is decoupled from the reservoirs, it can be considered as a quantum dot molecule (Ihn, 2010) with two relevant levels at energies $\mathrm{E}(1,1)$ and $\mathrm{E}(0,2)$. We parametrize the energy detuning of these levels with $\delta \equiv \mathrm{E}(1,1) - \mathrm{E}(0,2)$. The dashed lines in Fig. 3.5(b) illustrate that in the absence of interdot tunnel coupling t, depending on the sign of δ either $(1,1)$ or $(0,2)$ is the ground state, while the states are degenerate at $\delta = 0$. For a finite t, i.e. electron tunneling between the dots is allowed, this degeneracy is lifted as the charge states hybridize. As a result, a symmetric ground state $|0_{\mathrm{CQ}}\rangle$ and an anti-symmetric excited state $|1_{\mathrm{CQ}}\rangle$ is formed. These two states, highlighted in color in Fig. 3.5(b), are the basis states of the so-called charge qubit (Hayashi et al., 2003). The qubit is described by the Hamiltonian

$$\hat{\mathrm{H}}_{\mathrm{CQ}} = -\frac{1}{2}(\delta\hat{\tau}_z + 2t\hat{\tau}_x), \tag{3.1}$$

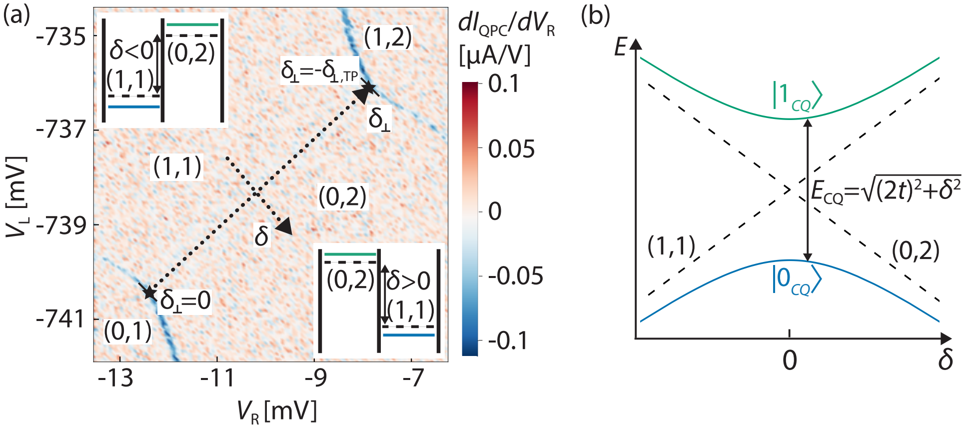

Figure 3.5 Two-electron charge qubit. (a) Charge stability diagram indicating the axes for the parameters $\delta_\perp$ and δ. The triple points are separated in $\delta_\perp$ by $\delta_{\perp,\mathrm{TP}}$. Solid (dashed) lines indicate the quantum dot energy levels in the presence (absence) of interdot tunnel coupling. (b) Energy of the (hybridized) $(1,1)$ and $(0,2)$ charge states in the absence (presence) of interdot tunnel coupling t. The charge qubit ground (blue) and excited (green) states are separated by the qubit energy E_{CQ}.

where $\hat{\tau}_z = |(0,2)\rangle\langle(0,2)| - |(1,1)\rangle\langle(1,1)|$ and $\hat{\tau}_x = |(0,2)\rangle\langle(1,1)| + |(1,1)\rangle\langle(0,2)|$ are the Pauli operators in the occupation basis $\{|(0,2)\rangle, |(1,1)\rangle\}$. The Hamiltonian can be transformed into its representation in the ground and excited state eigenbasis giving

$$\hat{\mathrm{H}}_{\mathrm{CQ}} = \hat{\mathrm{U}}_0 \hat{\hat{\mathrm{H}}}_{\mathrm{CQ}} \hat{\mathrm{U}}_0^\dagger = \frac{\mathrm{E}_{\mathrm{CQ}}}{2}\hat{\sigma}_z \tag{3.2}$$

with $\hat{\sigma}_z = |1_{\mathrm{CQ}}\rangle\langle 1_{\mathrm{CQ}}| - |0_{\mathrm{CQ}}\rangle\langle 0_{\mathrm{CQ}}|$, the qubit energy

$$\mathrm{E}_{\mathrm{CQ}} = \sqrt{\delta^2 + (2t)^2} \tag{3.3}$$

and the unitary operator

$$\hat{\mathrm{U}}_0 = \sin(\theta/2)\hat{\sigma}_x - \cos(\theta/2)\hat{\sigma}_z, \tag{3.4}$$

where the mixing angle θ is defined as $\cos(\theta) \equiv -\delta/\mathrm{E}_{\mathrm{CQ}}$. Using this definition of the mixing angle, the qubit states can be written as

$$|0_{\mathrm{CQ}}\rangle = \cos(\theta/2)\,|(1,1)\mathrm{S}\rangle + \sin(\theta/2)\,|(0,2)\mathrm{S}\rangle \text{ and} \tag{3.5}$$

$$|1_{\mathrm{CQ}}\rangle = \sin(\theta/2)\,|(1,1)\mathrm{S}\rangle - \cos(\theta/2)\,|(0,2)\mathrm{S}\rangle\,. \tag{3.6}$$

We deduce from Eq. (3.3) that for a fixed t, the charge qubit energy is minimal at $\delta = 0$. This detuning point is also referred to as a sweet spot, since $\partial \mathrm{E}_{\mathrm{CQ}}/\partial\delta|_{\delta=0} = 0$, such that the qubit energy is insensitive to fluctuations in δ to first order. This is further discussed in subsection 5.4.2 in the context of the qubit decoherence.

We parametrize a second energy axis in Fig. 3.5(a) normal to the δ axis with $\delta_\perp \equiv 1/2[\mathrm{E}(1,1) + \mathrm{E}(0,2)] - \mathrm{E}(0,1)$. Hence, the two triple points in Fig. 3.5(a) are at $\delta_\perp = \delta = 0$ and at $\delta_\perp = -\delta_{\perp,\mathrm{TP}}$, $\delta = 0$. The parameter $\delta_{\perp,\mathrm{TP}}$ quantifies a combination of interdot capacitive coupling and tunnel coupling (Ihn, 2010).

The special case of a two-electron charge qubit treated here can be generalized to any finite number of electrons in the DQD by replacing $|(1,1)\rangle$ and $|(0,2)\rangle$ with two charge states that have an excess electron either in the left or right quantum dot (Stockklauser et al., 2017). This generalization is valid as long as other DQD charge or orbital excited states are well separated in energy from the qubit states and therefore not relevant.

3.1.4 Transport spin-blockade

So far, the spin quantum number of the DQD electrons was omitted. Once the orbital wave functions Ψ_L in the left and Ψ_R in the right quantum dot overlap due to finite tunnel coupling, the states are typically written in terms of two-particle wave functions with an orbital component and a spin component. We introduce this notation below by following Ref. Ihn, 2018.

There is $2^2 = 4$ possible spin states for two electrons. For the $(1,1)$ charge state, we obtain one spin-singlet state (total spin $\mathrm{S} = 0$) and three spin-triplet states ($\mathrm{S} = 1$) as listed in Table 3.1. The wave-function representations in Table 3.1 are constructed to be anti-symmetric under electron exchange, since electrons are fermions (Pauli, 1940). Thereby, the symbol $|\Psi_\mathrm{L}\Psi_\mathrm{R}\rangle$ indicates, that electron one (two) is in orbital state Ψ_L (Ψ_R), while $|\uparrow\downarrow\rangle$ signifies the that electron one (two) is in the spin-up (spin-down) state. Typically, the wave functions are written in the occupation number representation where, for example, $|\uparrow,\downarrow\rangle = \frac{1}{\sqrt{2}}(|\Psi_\mathrm{L}\Psi_\mathrm{R}\rangle\,|\uparrow\downarrow\rangle - |\Psi_\mathrm{R}\Psi_\mathrm{L}\rangle\,|\downarrow\uparrow\rangle)$ indicates an electron (electron one or two) with spin-up in the left dot and an electron (electron one or two) with spin-down in the right dot.

For the $(0,2)$ charge state, a spin-triplet state requires the two electrons to occupy different orbitals as the Pauli exclusion principle states that two fermionic states cannot have the same quantum numbers. In addition, the orbital wave function of the spin-triplet state, which is a symmetric spin state, needs to be anti-symmetric, while it has to be symmetric for the spin-singlet state, which is an anti-symmetric spin state. As a result, the total wave function is anti-symmetric. The Coulomb interaction leads to an energy difference between the symmetric and the anti-symmetric orbital wave functions, which is denoted as exchange energy as it origins from the requirement that the total wave function has to be anti-symmetric under particle exchange. Due to the combination of Pauli exclusion and exchange, the spin-triplet state is estimated to be

	S	S_z	wave function representation	occ. number repr.
$(1,1)\mathrm{S}$	0	0	$\frac{1}{2}(|\Psi_\mathrm{L}\Psi_\mathrm{R}\rangle + |\Psi_\mathrm{R}\Psi_\mathrm{L}\rangle) \otimes (|\uparrow\downarrow\rangle - |\downarrow\uparrow\rangle)$	$\frac{1}{\sqrt{2}}(|\uparrow,\downarrow\rangle - |\downarrow,\uparrow\rangle)$
$(1,1)\mathrm{T}_+$	1	+1	$\frac{1}{\sqrt{2}}(|\Psi_\mathrm{L}\Psi_\mathrm{R}\rangle - |\Psi_\mathrm{R}\Psi_\mathrm{L}\rangle) \otimes (|\uparrow\uparrow\rangle$	$|\uparrow,\uparrow\rangle$
$(1,1)\mathrm{T}_0$	1	0	$\frac{1}{2}(|\Psi_\mathrm{L}\Psi_\mathrm{R}\rangle - |\Psi_\mathrm{R}\Psi_\mathrm{L}\rangle) \otimes (|\uparrow\downarrow\rangle + |\downarrow\uparrow\rangle)$	$\frac{1}{\sqrt{2}}(|\uparrow,\downarrow\rangle + |\downarrow,\uparrow\rangle)$
$(1,1)\mathrm{T}_-$	1	-1	$\frac{1}{\sqrt{2}}(|\Psi_\mathrm{L}\Psi_\mathrm{R}\rangle - |\Psi_\mathrm{R}\Psi_\mathrm{L}\rangle) \otimes |\downarrow\downarrow\rangle$	$|\downarrow,\downarrow\rangle$

Table 3.1 Two-electron wave functions. Two-electron spin-singlet and spin-triplet states with $(1,1)$ charge configuration according to Ref. Ihn, 2018.

about 1 meV $\gg k_\mathrm{B}\mathrm{T}_\mathrm{e}$ higher in energy than the spin-singlet state (Hanson et al., 2007) and omitted in the following.

In total, there are four relevant spin states for $(1,1)$ and one for $(0,2)$. The system Hamiltonian can be written as

$$\hat{\mathrm{H}}_{\mathrm{ST}} = \begin{array}{cl} \begin{array}{ccccc} \langle(0,2)\mathrm{S}| & \langle(1,1)\mathrm{S}| & \langle(1,1)\mathrm{T}_-| & \langle(1,1)\mathrm{T}_0| & \langle(1,1)\mathrm{T}_+| \end{array} & \\ \left(\begin{array}{ccccc} -\delta/2 & -t & 0 & 0 & 0 \\ -t & \delta/2 & 0 & 0 & 0 \\ 0 & 0 & \delta/2+\mathrm{E}_\mathrm{Z} & 0 & 0 \\ 0 & 0 & 0 & \delta/2 & 0 \\ 0 & 0 & 0 & 0 & \delta/2-\mathrm{E}_\mathrm{Z} \end{array}\right) & \begin{array}{l} |(0,2)\mathrm{S}\rangle \\ |(1,1)\mathrm{S}\rangle \\ |(1,1)\mathrm{T}_-\rangle \\ |(1,1)\mathrm{T}_0\rangle \\ |(1,1)\mathrm{T}_+\rangle\,. \end{array} \end{array} \tag{3.7}$$

The Zeeman energy $\mathrm{E}_\mathrm{Z} = g\mu_\mathrm{B}\mathrm{B}$ leads to an energy splitting of the triplet states that can be controlled by an external magnetic field B, where g [≈ -0.4 in GaAs (Nowack et al., 2007)] is the g-factor and μ_B the Bohr magneton. Spin-singlet and spin-triplet states are not coupled via tunneling, as tunneling is a spin-conserving process. Figure 3.6 shows the energy dispersion of the eigenstates of the Hamiltonian in Eq. (3.7). The spin-singlet states, which are the charge qubit states from Fig. 3.5(b), do not anti-cross with the triplet states. Coupling mechanisms for spin-singlet and spin-triplet states are spin-orbit and hyperfine interaction. They are neglected in Eq. (3.7) as they are typically weak in GaAs compared to other energy scales (Stepanenko et al., 2012). A potential influence of singlet-triplet mixing on experiments presented in this thesis is

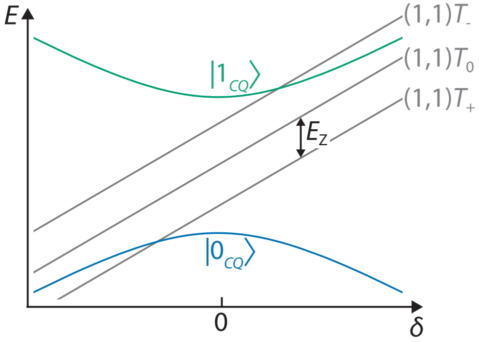

Figure 3.6 Two-electron singlet-triplet spectrum. Energies of the two-electron spin-singlet (blue, green) and spin-triplet states (gray) as a function of δ at a finite magnetic field. The triplet states are split by the Zeeman energy E_Z.

discussed in subsection 6.3.3.

The spin-conservation in electron tunneling can be observed as a current rectification in a DQD at finite source-drain bias (Ono et al., 2002). This is illustrated for a two-electron DQD in Fig. 3.7. For a positive source-drain bias in Fig. 3.7(a), an electron can only tunnel into the DQD via the right lead and the only accessible state is $(0,2)$S. Hence, the transport cycle is $(0,1) \rightarrow (0,2)$S $\rightarrow (1,1)$S $\rightarrow (0,1)$, which is permitted as the tunneling processes conserve spin. For negative bias illustrated in Fig. 3.7(b), an electron enters the DQD from the left lead forming either $(1,1)$S or $(1,1)$T. Note that we assume a small magnetic field $E_Z \ll k_B T_e$, such that $(1,1)$T is either $(1,1)T_0$, $(1,1)T_+$ or $(1,1)T_-$. If the electron tunnels into the $(1,1)$S state, the transport sequence $(1,1)$S $\rightarrow (0,2)$S $\rightarrow (0,1)$ is permitted as it conserves the spin. However, transport is blocked if the electron tunnels into a $(1,1)$T state, as it can only transition to $(0,2)$S by a spin flip. As the spin-flip tunneling rates are typically orders of magnitude slower than spin-conserving tunneling rates, this leads to a significant reduction of the DQD current for negative bias compared to positive bias and is referred to as spin blockade (Ono et al., 2002, Johnson et al., 2005a). The alternative transport cycle $(0,1) \longrightarrow (1,1)$T $\longrightarrow (0,2)$T $\longrightarrow (0,1)$ is energetically inaccessible as the energy of the $(0,2)$T state is significantly higher than that of the $(0,2)$S state. This energy difference is related to the Pauli exclusion principle (see discussion above). Consequently, the spin-blockade phenomenon is often referred to as Pauli spin-blockade.

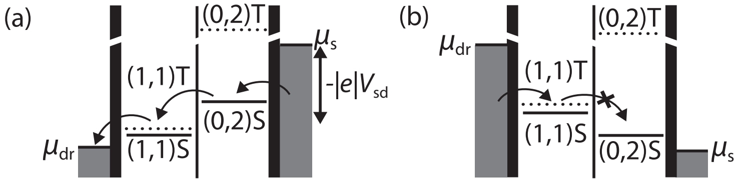

Figure 3.7 Transport spin-blockade. DQD electron transport cycle for positive (a) and negative (b) source-drain bias in the presence of a small magnetic field. Solid and dotted lines indicate the electrochemical potentials for spin-singlet and spin-triplet states, respectively. Transitions that involve a spin-flip are marked with a cross. The figure is adapted from Ref. Ihn, 2010.

3.2 Triple quantum dot spin-qubit (RX qubit)

For the charge qubit discussed in section 3.1, the qubit state is encoded in the charge distribution and therefore sensitive to charge noise. This is considered to be the main decoherence mechanism of the qubit (Basset et al., 2013) as further discussed in subsection 5.4.2.

The coherence time of a solid-state qubit can be increased by encoding the qubit state into the spin degree of freedom of a single electron, which is insensitive to electric field fluctuations (Loss et al., 1998). By applying an external magnetic field, the Zeeman energy lifts the spin degeneracy, which forms a two-level system with the electron spin parallel or anti-parallel to the external magnetic field for the qubit ground or excited state, respectively. Full control of this spin qubit is possible either by oscillating magnetic fields (Koppens et al., 2006) or by oscillating electric fields that couple to the spin by modulation of the g-factor of the material, by spin-orbit (Nowack et al., 2007) or by hyperfine interaction (Laird et al., 2007). Thereby, oscillating electric fields are generally preferred as among others they can be engineered to act more locally compared to magnetic fields such that individual spin qubits can be addressed separately (Pioro-Ladrière et al., 2008). The spin-orbit interaction is either intrinsic of the material or artificially induced by a micromagnet, which is a small magnetic structure that causes a magnetic field gradient in the vicinity of the qubit (Tokura et al., 2006).

One potential disadvantage of the single-electron spin qubit is that its energy is determined by the Zeeman splitting, which causes dephasing due to magnetic field fluctuations. By adding a second electron and a second quantum dot, this sensitivity can be reduced. The logical qubit states of the so-called singlet-triplet qubit are encoded into the lowest energy singlet state ($|0_{\mathrm{CQ}}\rangle$ in Fig. 3.6) and the $(1,1)\mathrm{T}_0$ state in a two-electron double quantum dot, both within the $\mathrm{S}_z = 0$ subspace however with different total spin. While the qubit energy can be controlled electrically via the DQD detuning δ (Petta et al., 2005), a gradient in the magnetic field across the DQD is necessary to form a coupling between the qubit states. This can be achieved by dynamically polarizing the nuclear spins in the qubit host material (Foletti et al., 2009) or with a micromagnet (Wu et al., 2014). A potential drawback of the singlet-triplet qubit is that it cannot be controlled by electric fields only.

This is resolved by using a three-electron spin qubit. The concept of this spin qubit is to span the qubit subspace by states with equal charge distributions and spin quantum numbers but different spin distributions. This is analogous to charge qubits, where the charge distribution (excess electron in the left or the right quantum dot) defines the qubit states. The three-electron spin qubit states are split energetically due to exchange interaction. This is in contrast to the single-electron spin qubit, where the qubit energy is set by an external magnetic field. Different implementations of three electron spin qubits exist, both in double and triple quantum dots, where for example the exchange interaction is either always turned on or only on demand by pulsing the qubit control parameters. A detailed discussion of these different implementations as well as a discussion about the advantages and disadvantages of the single-electron and two-electron spin qubits can be found in Ref. Russ et al., 2017. The spin qubit we implement in this thesis is a three-electron qubit named resonant exchange (RX) qubit.

In subsections 3.2.1-3.2.3 we introduce the RX qubit Hamiltonian and the energy spectrum as well as the contribution of different spin and charge states to the qubit states. In subsection 3.2.4 we explain the electrostatic tuning of a TQD into the few-electron regime.

3.2.1 RX qubit Hamiltonian

We implement the resonant exchange qubit with three electrons in a linear TQD. The Hubbard model describes the interaction of electrons located on different sites (here quantum dots) due to Coulomb repulsion. It also considers the kinetic energy of the electrons as tunneling between different sites as well as spin selection rules, i.e. Pauli exclusion. The TQD with a single available orbital state per left (L), middle (M) and right (R) quantum dot is described by the extended Hubbard Hamiltonian (Taylor et al., 2013, Russ et al., 2015a)

$$\begin{aligned}\hat{\mathrm{H}}_{\mathrm{Hub}} = &\sum_{i\in\{\mathrm{L,M,R}\}} \left[\tilde{\varepsilon}_i \hat{n}_i + \mathrm{U}_i(\hat{n}_i - n_{gi})^2\right] + \sum_{i\neq j} \mathrm{U}_{ij}(\hat{n}_i - n_{gi})(\hat{n}_j - n_{gj}) + \\ &\sum_{i\neq j}\sum_{\sigma=\uparrow,\downarrow} t_{ij}(\hat{d}^{\dagger}_{i,\sigma}\hat{d}_{j,\sigma} + \mathrm{h.c}).\end{aligned} \tag{3.8}$$

The first and second term quantifies the two energy scales for a single quantum dot that were already introduced in subsection 3.1.1. This is the single-particle level energy $\tilde{\varepsilon}_i$ and the Coulomb energy U_i due to electron-electron interaction of electrons on dot i. Thereby, $\hat{n}_i = \sum_\sigma \hat{d}^{\dagger}_{i,\sigma}\hat{d}_{i,\sigma}$ is the number operator of dot i, $\hat{d}_{i,\sigma}$ ($\hat{d}^{\dagger}_{i,\sigma}$) annihilates (creates) an electron with spin $\sigma = \uparrow, \downarrow$ in quantum dot i, and n_{gi} is the gate number that relates to the effective charge $en_{gi} = \sum_k \mathrm{C}_{i,k}(\mathrm{V}_k - \mathrm{V}_{k,0})$ induced on dot i by gate potentials V_k that couple with capacitances $\mathrm{C}_{i,k}$ to dot i, which is occupied with zero electrons at $V_{k,0}$. The second sum describes the mutual charging energy U_{ij} between electrons in dots i and j. The last term describes tunneling between dots i and j with tunneling amplitude t_{ij}. We consider tunneling between nearest neighbor dots that also conserves spin, such that we obtain $t_{\mathrm{LM}} = t_{\mathrm{ML}} \equiv t_{\mathrm{L}}/\sqrt{2}$, $t_{\mathrm{MR}} = t_{\mathrm{RM}} \equiv t_{\mathrm{R}}/\sqrt{2}$ and $t_{\mathrm{LR}} = t_{\mathrm{RL}} = 0$.

In the following we derive the relevant Hilbert space for the RX qubit by first introducing the relevant charge configurations and then discussing the relevant spin states. We implement the qubit in a regime where the relevant charge configurations are $(1,1,1)$, $(2,0,1)$ and $(1,0,2)$ as illustrated in Fig. 3.8, where $(\mathrm{N_L},\mathrm{N_M},\mathrm{N_R})$ indicates $\mathrm{N_L}$ electrons in the left, $\mathrm{N_M}$ electrons in the middle and $\mathrm{N_R}$ electrons in the right quantum dot. We define the asymmetry parameter ε and the detuning parameter Δ as

$$\begin{aligned} \varepsilon &\equiv \frac{1}{2}[\mathrm{E}(1,0,2) - \mathrm{E}(2,0,1)] \\ \Delta &\equiv \mathrm{E}(1,1,1) - \frac{1}{2}[\mathrm{E}(2,0,1) + \mathrm{E}(1,0,2)], \end{aligned} \tag{3.9}$$

where $\mathrm{E}(\mathrm{N_L},\mathrm{N_M},\mathrm{N_R})$ denotes the energy of the charge state $(\mathrm{N_L},\mathrm{N_M},\mathrm{N_R})$. These parameters are defined in the absence of interdot tunnel coupling. Hence they can directly be expressed in terms of charging energies using the first two sums in Eq. (3.8):

$$\varepsilon = \frac{3}{2}(\mathrm{U_L} - \mathrm{U_R}) + n_{\mathrm{gL}}(\frac{1}{2}\mathrm{U_{LR}} - \mathrm{U_L}) + \frac{1}{2}n_{\mathrm{gM}}(\mathrm{U_{MR}} - \mathrm{U_{LM}}) + n_{\mathrm{gR}}(\mathrm{U_R} - \frac{1}{2}\mathrm{U_{LR}}) \tag{3.10}$$

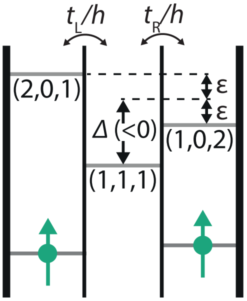

Figure 3.8 RX qubit detuning parameters. Schematic of the TQD, defining the asymmetry and detuning parameters ε and Δ, respectively. The three gray lines indicate the possible energy levels for the addition of the third electron.

$$\begin{aligned}\Delta = &-\frac{3}{2}(\mathrm{U_L}+\mathrm{U_R})+\mathrm{U_M}+\mathrm{U_{LM}}-\mathrm{U_{LR}}+\mathrm{U_{MR}}+n_{\mathrm{gL}}(\mathrm{U_L}-\mathrm{U_{LM}}+\frac{1}{2}\mathrm{U_{LR}})+\\ &n_{\mathrm{gM}}(-2\mathrm{U_M}+\frac{1}{2}\mathrm{U_{LM}}+\frac{1}{2}\mathrm{U_{MR}})+n_{\mathrm{gR}}(\mathrm{U_R}+\frac{1}{2}\mathrm{U_{MR}}-\mathrm{U_{MR}}).\end{aligned} \tag{3.11}$$

Experimentally, we control ε and Δ via the plunger gate potentials, which tune the gate charges n_{gi}. At $\Delta = \varepsilon = 0$, the relevant charge configurations are degenerate. Note that we operate the qubit in a regime were both Δ and ε are much smaller than the interdot and the single-dot charging energies to ensure that other charge states are not relevant.

Now considering also spin, there are $2^3 = 8$ possible spin configurations for three spins. For the asymmetric charge configurations $(2,0,1)$ and $(1,0,2)$, the three triplet states within the doubly occupied dots do not play a role because they are energetically not accessible due to the singlet-triplet splitting (see subsection 3.1.4). This leaves us with two relevant spin configurations for each of the two asymmetric charge configurations. Two of them, with $S_z = 1/2$ of total spin, are depicted in the top row of Fig. 3.9. The other two (not shown) are obtained by flipping the spin in the singly occupied dot giving $S_z = -1/2$. These spin configurations of the asymmetric charge configurations couple by tunneling to spin configurations of the $(1,1,1)$ charge configurations as depicted in the bottom row of Fig. 3.9. Only the displayed spin configurations are rel-

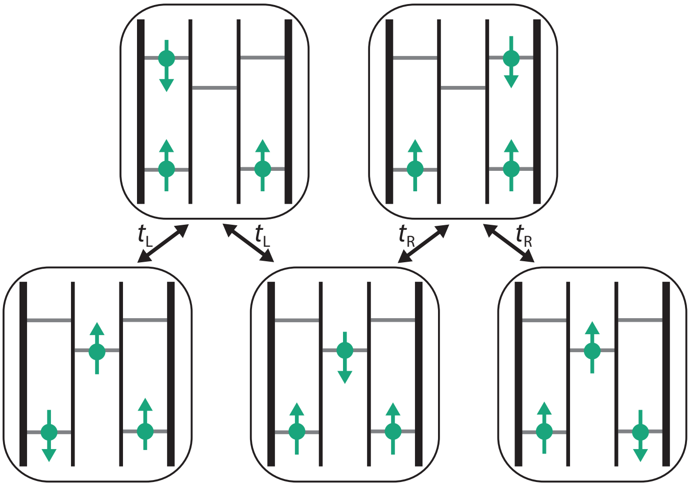

Figure 3.9 RX basis states. Illustration of the three-electron states in the TQD that form the spin qubit. The states mix via tunnel couplings t_L and t_R between the left and middle and the right and middle quantum dots, respectively.

evant, because tunneling conserves both the total spin and the spin z-component. The $(1,1,1)$ configurations in Fig. 3.9 couple by exchange interaction between electrons in neighboring dots: an electron in the middle dot can be exchanged with an electron with opposite spin in the left (right) dot via tunneling to the asymmetric charge state.

The RX qubit states are formed as a coherent superposition of the five basis states with $S_z = 1/2$ depicted in Fig. 3.9. An equivalent set of basis states with $S_z = -1/2$ exists, but is not depicted. These different S_z-states can mix by magnetic field fluctuations in the quantum dots that are produced by the nuclei in the host material. A typical magnitude of these fluctuations is of the order of a few mT in GaAs (Hanson et al., 2007). By splitting the different S_z subsets energetically with an external magnetic field, the mixing can be suppressed. We study this effect theoretically in subsection 5.4.1.1 as well as experimentally in chapters 7 and 8.

The spin and charge configurations depicted in Fig. 3.9 were illustrated in the absence of interdot tunnel coupling. In order to calculate the RX qubit states, it is useful to derive their state representations in an angular momentum basis, since electron tunneling conserves spin. We start with the $(1,1,1)$ charge configurations, where the occupation number representations for all possible states are shown in Table 3.2.
As the three-spin Hilbert space is $\mathscr{H}_{3\text{spin}} = \mathscr{H}_{3/2} \otimes \mathscr{H}_{1/2} \otimes \mathscr{H}_{1/2}$, we obtain one quadruplet of states with $S = 3/2$ and two doublets of states each with $S = 1/2$. Note that the wave-function representation of the states in Table 3.2 can be constructed from the Slater determinant of three single-particle wave functions (see Appendix A). The occupation number representation of the states of the $(1,0,2)$ and $(2,0,1)$ charge configurations

	S	S_z	occ. number repr.
$Q_{+3/2}$	3/2	+3/2	$\|\uparrow,\uparrow,\uparrow\rangle$
$Q_{1/2}$	3/2	+1/2	$\frac{1}{\sqrt{3}}(\|\downarrow,\uparrow,\uparrow\rangle + \|\uparrow,\downarrow,\uparrow\rangle + \|\uparrow,\uparrow,\downarrow\rangle)$
$Q_{-1/2}$	3/2	−1/2	$\frac{1}{\sqrt{3}}(\|\downarrow,\downarrow,\uparrow\rangle + \|\downarrow,\uparrow,\downarrow\rangle + \|\uparrow,\downarrow,\downarrow\rangle)$
$Q_{-3/2}$	3/2	−3/2	$\|\downarrow,\downarrow,\downarrow\rangle$
$D_{1/2}$	1/2	+1/2	$\frac{1}{\sqrt{2}}(\|\uparrow,\uparrow,\downarrow\rangle - \|\downarrow,\uparrow,\uparrow\rangle)$
$D_{-1/2}$	1/2	−1/2	$\frac{1}{\sqrt{2}}(\|\downarrow,\downarrow,\uparrow\rangle - \|\uparrow,\downarrow,\downarrow\rangle)$
$D'_{1/2}$	1/2	+1/2	$\frac{1}{\sqrt{6}}(2\|\uparrow,\downarrow,\uparrow\rangle - \|\uparrow,\uparrow,\downarrow\rangle - \|\downarrow,\uparrow,\uparrow\rangle)$
$D'_{-1/2}$	1/2	−1/2	$\frac{1}{\sqrt{6}}(2\|\downarrow,\uparrow,\downarrow\rangle - \|\downarrow,\downarrow,\uparrow\rangle - \|\uparrow,\downarrow,\downarrow\rangle)$

Table 3.2 $(1,1,1)$ wave functions. Occupation number representation of $(1,1,1)$ charge states with total spin S and spin z-component S_z (Russ et al., 2017).

	S	S_z	occ. number repr.
$D_{L,1/2}$	1/2	+1/2	$\lvert\uparrow\downarrow,0,\uparrow\rangle$
$D_{L,-1/2}$	1/2	−1/2	$\lvert\uparrow\downarrow,0,\downarrow\rangle$
$D_{R,1/2}$	1/2	+1/2	$\lvert\uparrow,0,\uparrow\downarrow\rangle$
$D_{R,-1/2}$	1/2	−1/2	$\lvert\downarrow,0,\uparrow\downarrow\rangle$

Table 3.3 $(2,0,1)$ and $(1,0,2)$ wave functions. Occupation number representation of $(2,0,1)$ and $(1,0,2)$ charge states for given S and S_z.

in the angular momentum basis with a spin-singlet in the doubly occupied dot are indicated in Table 3.3. We obtain two doublets with either two electrons in the left or the right quantum dot.

We now identify the five states $\{D_{1/2}, D'_{1/2}, Q_{1/2}, D_{L,1/2}, D_{R,1/2}\}$ with $S_z = 1/2$ from Tables 3.2 and 3.3 as the angular momentum basis of the RX qubit Hilbert space. We use the following definitions and write the basis states in terms of the creation and annihilation operators from Eq. (3.8):

$$\begin{aligned}
|\tilde{0}_{RX}\rangle &\equiv D'_{1/2} = \frac{1}{\sqrt{6}}(2d^\dagger_{L,\uparrow}d^\dagger_{M,\downarrow}d^\dagger_{R,\uparrow} - d^\dagger_{L,\uparrow}d^\dagger_{M,\uparrow}d^\dagger_{R,\downarrow} - d^\dagger_{L,\downarrow}d^\dagger_{M,\uparrow}d^\dagger_{R,\uparrow})|\mathrm{vac}\rangle \\
|\tilde{1}_{RX}\rangle &\equiv D_{1/2} = \frac{1}{\sqrt{2}}(d^\dagger_{L,\uparrow}d^\dagger_{M,\uparrow}d^\dagger_{R,\downarrow} - d^\dagger_{L,\downarrow}d^\dagger_{M,\uparrow}d^\dagger_{R,\uparrow})|\mathrm{vac}\rangle \\
|\tilde{2}_{RX}\rangle &\equiv D_{L,1/2} = d^\dagger_{L,\uparrow}d^\dagger_{L,\downarrow}d^\dagger_{R,\uparrow}|\mathrm{vac}\rangle \\
|\tilde{3}_{RX}\rangle &\equiv D_{R,1/2} = d^\dagger_{L,\uparrow}d^\dagger_{R,\uparrow}d^\dagger_{R,\downarrow}|\mathrm{vac}\rangle \\
|\tilde{4}_{RX}\rangle &\equiv Q_{1/2} = 1/\sqrt{3}(d^\dagger_{L,\downarrow}d^\dagger_{M,\uparrow}d^\dagger_{R,\uparrow} + d^\dagger_{L,\uparrow}d^\dagger_{M,\downarrow}d^\dagger_{R,\uparrow} + d^\dagger_{L,\uparrow}d^\dagger_{M,\uparrow}d^\dagger_{R,\downarrow})|\mathrm{vac}\rangle,
\end{aligned} \tag{3.12}$$

where $|\mathrm{vac}\rangle$ denotes the fermionic vacuum state. Coupling between these states by tunneling is described by the last term in the Hubbard Hamiltonian in Eq. (3.8). By evaluating these tunneling Matrix elements and using the definitions of Δ and ε from Eqns. (3.10)-(3.11), we can rewrite the Hubbard Hamiltonian from Eq. (3.8) as

$$\hat{H}_{\mathrm{Hub}} = \begin{array}{c} \\ \left(\begin{array}{ccccc} \langle\tilde{0}_{RX}| & \langle\tilde{1}_{RX}| & \langle\tilde{2}_{RX}| & \langle\tilde{3}_{RX}| & \langle\tilde{4}_{RX}| \\ 0 & 0 & -\frac{\sqrt{3}}{2}t_R & \frac{\sqrt{3}}{2}t_L & 0 \\ 0 & 0 & \frac{1}{2}t_R & \frac{1}{2}t_L & 0 \\ -\frac{\sqrt{3}}{2}t_R & \frac{1}{2}t_R & -\varepsilon-\Delta & 0 & 0 \\ \frac{\sqrt{3}}{2}t_L & \frac{1}{2}t_L & 0 & \varepsilon-\Delta & 0 \\ 0 & 0 & 0 & 0 & 0 \end{array}\right) \end{array} \begin{array}{l} \\ |\tilde{0}_{RX}\rangle \\ |\tilde{1}_{RX}\rangle \\ |\tilde{2}_{RX}\rangle \\ |\tilde{3}_{RX}\rangle \\ |\tilde{4}_{RX}\rangle, \end{array} \tag{3.13}$$

where the energies of the states are defined with respect to $\mathrm{E}(1,1,1)$, i.e. $\mathrm{E}(2,0,1)-\mathrm{E}(1,1,1)=-\varepsilon-\Delta$ and $\mathrm{E}(1,0,2)-\mathrm{E}(1,1,1)=-\Delta+\varepsilon$. As expected, the state $|\tilde{4}_{\mathrm{RX}}\rangle$ with $\mathrm{S}=3/2$ does not couple via tunneling with the other four states, each with $\mathrm{S}=1/2$. We refer to $|\tilde{4}_{\mathrm{RX}}\rangle$ as the leakage state. By numerically diagonalizing Eq. (3.13) and omitting all but the lowest two energy states, we obtain the RX qubit Hamiltonian

$$\hat{\mathrm{H}}_{\mathrm{RX}}=\frac{1}{2}\mathrm{E}_{\mathrm{RX}}\hat{\sigma}_z, \tag{3.14}$$

where E_{RX} is the RX qubit energy and $\hat{\sigma}_z=|1_{\mathrm{RX}}\rangle\langle 1_{\mathrm{RX}}|-|0_{\mathrm{RX}}\rangle\langle 0_{\mathrm{RX}}|$ is a Pauli operator in the basis of the RX qubit ground and excited states $|0_{\mathrm{RX}}\rangle$ and $|1_{\mathrm{RX}}\rangle$, respectively. The qubit states, written as a linear combination of the basis states $|\tilde{k}_{\mathrm{RX}}\rangle$ defined in Eq. (3.12), are

$$|0_{\mathrm{RX}}\rangle=\sum_{k=0}^{3}c_k^{(0_{\mathrm{RX}})}|\tilde{k}_{\mathrm{RX}}\rangle \quad \text{and} \quad |1_{\mathrm{RX}}\rangle=\sum_{k=0}^{3}c_k^{(1_{\mathrm{RX}})}|\tilde{k}_{\mathrm{RX}}\rangle \tag{3.15}$$

with $\sum_{k=0}^{3}c_k^{(0_{\mathrm{RX}}/1_{\mathrm{RX}})}=1$.

3.2.2 RX qubit energy spectrum

We plot the eigenenergies of the Hamiltonian in Eq. (3.13) as a function of ε at $\Delta=0$ and as a function of Δ at $\varepsilon=0$ in Fig. 3.10(a) and Fig. 3.10(b), respectively. The eigenenergy of $|\tilde{4}_{\mathrm{RX}}\rangle$ is a constant as the state does not couple to any of the other states as is was discussed above. It therefore corresponds to the energy of the $(1,1,1)$ states for $t_{\mathrm{L}}=t_{\mathrm{R}}=0$. The RX qubit states are the two lowest energy states in Figs. 3.10(a)-(b). Their energy difference, i.e. the RX qubit energy E_{RX}, is shown in Figs. 3.10(c)-(d). It increases with increasing charge asymmetry parameter $|\varepsilon|$ in analogy to the charge qubit energy in Eq. (3.3), where δ quantified the charge asymmetry. By increasing $|\Delta|$, E_{RX} in Fig. 3.9(d) decreases. For positive Δ at $\varepsilon=0$, $\mathrm{E}(1,1,1)>\mathrm{E}(1,0,2),\mathrm{E}(2,0,1)$ such that the middle quantum dot effectively acts as a tunnel barrier for an excess electron either in the left or the right quantum dot. By increasing Δ, the barrier height increases, which decreases the left-right tunnel coupling and hence the qubit energy analogous to a charge qubit, where E_{CQ} decreases with decreasing t. The decrease of E_{RX} with increasing negative Δ is due to the decreasing exchange interaction between the $(1,1,1)$ states proportional to t^2/Δ, which is discussed below.

For symmetric tunnel couplings, the RX qubit exhibits a first order sweet spot in ε and Δ at $\varepsilon=\Delta=0$. This is a double sweet spot (DSS), as both $\partial\mathrm{E}_{\mathrm{RX}}/\partial\Delta|_{\varepsilon=0}=0$ and

$\partial E_{RX}/\partial \varepsilon|_{\Delta=0} = 0$. Furthermore, as $\partial^2 E_{RX}/\partial \Delta^2|_{\varepsilon=0} < 0$ and $\partial^2 E_{RX}/\partial \epsilon^2|_{\Delta=0} > 0$, the DSS is a saddle point in energy. Its position is shifted for asymmetric tunnel couplings as indicated by the dashed lines in Figs. 3.10(c)-(d) and discussed in detail in Ref. Russ et al., 2015a.

Note that for the derivation of the RX qubit states we did not consider the $(1,1,1)$ states with $S = 3/2$ ($Q_{x/y}$ in Table 3.2) since for the choice of external magnetic field and interdot tunnel coupling used for most of the experiments in this thesis, they are all energetically well above the qubit excited state energy[4]. For large magnetic fields $B \geq 1\,T$ the state with $S = S_z = 3/2$ is energetically close to the qubit states and

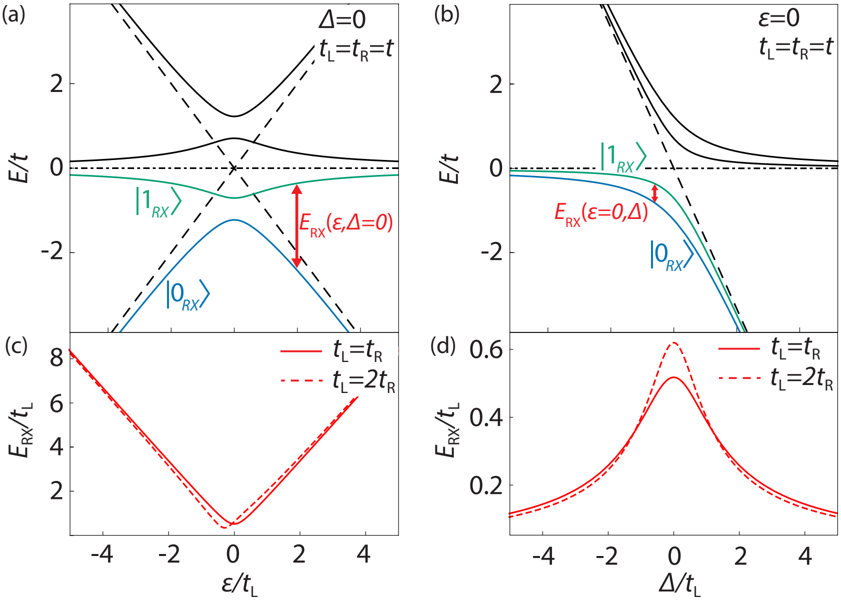

Figure 3.10 RX qubit spectrum. (a)-(b) Eigenenergies E/t of the Hamiltonian in Eq. (3.13) for $t_L = t_R = t$ as a function of ε/t at $\Delta = 0$ in (a) and as a function of Δ/t for $\varepsilon = 0$ in (b). Dashed lines in (a)-(b) indicate the energy of the charge states $(2,0,1)$ and $(1,0,2)$ for $t_L = t_R = 0$. The dash-dotted line shows the energy of the $(1,1,1)$ charge state for $t_L = t_R = 0$, which coincides with the energy of the $|\tilde{4}_{RX}\rangle$ state. The RX qubit states $|0_{RX}\rangle$ (blue) and $|1_{RX}\rangle$ (green) are highlighted. (c)-(d) RX qubit energy E_{RX} as a function of ε/t_L in (c) and Δ/t_L in (d) for symmetric (solid line) and asymmetric (dashed line) tunnel couplings.

---

[4] For $t_L = t_R = t$ and $B = 0$, the $S = 3/2$ states are $\approx E_{RX}$ above the qubit excited state energy at $\varepsilon = \Delta = 0$ [see dash-dotted and green line in Figs. 3.10(a)-(b)].

eventually becomes the ground state of the system by further increasing B as discussed in section 7.7.

3.2.3 RX qubit state composition

The RX qubit states are a superposition of the states $\{|\tilde{0}_{\mathrm{RX}}\rangle, |\tilde{1}_{\mathrm{RX}}\rangle\}$ and $\{|\tilde{2}_{\mathrm{RX}}\rangle, |\tilde{3}_{\mathrm{RX}}\rangle\}$ defined in Eq. (3.12) with symmetric $(1,1,1)$ and asymmetric $(2,0,1)$, $(1,0,2)$ charge configurations, respectively. To quantify this state composition, we use Eq. (3.15) to define for each of the qubit states $|0_{\mathrm{RX}}\rangle$ and $|1_{\mathrm{RX}}\rangle$ the parameter $\mathrm{P}_{(1,1,1)}(k_{\mathrm{RX}})$ with $k \in \{0,1\}$ to be the sum of the occupation probabilities of the $(1,1,1)$ basis states:

$$\mathrm{P}_{(1,1,1)}(k_{\mathrm{RX}}) = \left(c_0^{k_{\mathrm{RX}}}\right)^2 + \left(c_1^{k_{\mathrm{RX}}}\right)^2 \tag{3.16}$$

In analogy, we define the occupation probabilities of the asymmetric charge states:

$$\mathrm{P}_{(2,0,1)}(k_{\mathrm{RX}}) = \left(c_2^{k_{\mathrm{RX}}}\right)^2, \tag{3.17}$$

$$\mathrm{P}_{(1,0,2)}(k_{\mathrm{RX}}) = \left(c_3^{k_{\mathrm{RX}}}\right)^2 \tag{3.18}$$

These quantities depend on Δ as depicted in Fig. 3.11 for symmetric tunnel couplings at $\varepsilon = 0$. We choose $\varepsilon = 0$ since the qubit is implemented in this thesis at the sweet spot in ε.

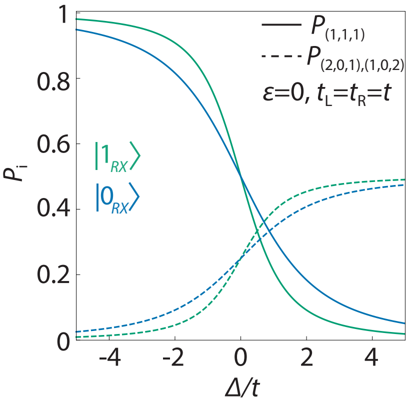

Figure 3.11 RX spin and charge character. Probabilities $\mathrm{P}_{(1,1,1)}$ (solid lines), $\mathrm{P}_{(2,0,1)}$ and $\mathrm{P}_{(1,0,2)}$ (dashed lines), as defined in the text, for $|0_{\mathrm{RX}}\rangle$ (blue) and $|1_{\mathrm{RX}}\rangle$ (green) as a function of Δ/t. The plot is obtained for $t_{\mathrm{L}} = t_{\mathrm{R}} = t$ and $\varepsilon = 0$.

In the limit $\Delta \ll -t_{\mathrm{L,R}}$ the qubit states are of spin character, as they have predominantly the same $(1,1,1)$ charge configurations, $\mathrm{P}_{(1,1,1)} \gg \mathrm{P}_{(2,0,1)}, \mathrm{P}_{(1,0,2)}$ (see Fig. 3.11). Since both qubit states have the same total spin and spin z-component of $1/2$, the qubit energy is not determined by an external magnetic field but rather by the exchange interaction between the $|0_{\mathrm{RX}}\rangle$ and $|1_{\mathrm{RX}}\rangle$ spin states via virtual tunneling to the asymmetric charge states (Taylor et al., 2013). In this regime, the qubit is minimally influenced by charge noise, but also has a small electrical dipole moment as discussed in subsection 5.1.2. In the other extreme where $\Delta \gg t_{\mathrm{L,R}}$, the occupation probabilities in Fig. 3.11 are dominated by the $(2,0,1)$ and $(1,0,2)$ charge configurations. The RX qubit states are therefore of charge character and the qubit can be interpreted as a charge qubit with an excess electron either in the right or left quantum dot and the middle quantum dot acting as a tunnel barrier that is tunable with Δ. Such a qubit has a strong electric dipole moment (see subsection 5.1.2) and is susceptible to charge noise. For the most experiments presented in this thesis, we operate the RX qubit in the intermediate regime $|\Delta| \lesssim t_{\mathrm{L,R}}$.

In this paragraph we derive an approximate expression for the RX qubit Hamiltonian in the regime $\Delta \ll -t_{\mathrm{L,R}}$, $\varepsilon \approx 0$, where its spin character becomes apparent. There, the contribution of $(1,0,2)$ and $(2,0,1)$ to the qubit states can be treated perturbatively by applying a Schrieffer-Wolff transformation (Bravyi et al., 2011) to the RX qubit Hamiltonian from Eq. (3.13). We obtain a Heisenberg Hamiltonian (Russ et al., 2015a)

$$\hat{\mathrm{H}}_{\mathrm{Heis}} = \mathrm{J}_{\mathrm{L}} \hat{\mathbf{S}}_{\mathrm{L}} \cdot \hat{\mathbf{S}}_{\mathrm{M}} + \mathrm{J}_{\mathrm{R}} \hat{\mathbf{S}}_{\mathrm{M}} \cdot \hat{\mathbf{S}}_{\mathrm{R}}, \tag{3.19}$$

where $\mathrm{J}_{\mathrm{L}} = t_{\mathrm{L}}^2/(-\Delta-\varepsilon)$ and $\mathrm{J}_{\mathrm{R}} = t_{\mathrm{R}}^2/(-\Delta+\varepsilon)$ are the exchange energies and $\hat{\mathbf{S}}_{\mathrm{i}}$ are the left (L), middle (M) and right (R) quantum dot spin operators. In terms of the basis states $|\tilde{0}_{\mathrm{RX}}\rangle$ and $|\tilde{1}_{\mathrm{RX}}\rangle$ from Eq. (3.12) the Heisenberg Hamiltonian in Eq. (3.19) can be expressed as (Russ et al., 2015a)

$$\hat{\mathrm{H}}'_{\mathrm{Heis}} = \frac{\mathrm{J}}{2}\hat{\sigma}_z - \frac{\sqrt{3}}{2} j \hat{\sigma}_x, \tag{3.20}$$

with the Pauli operators $\hat{\sigma}_z = |\tilde{1}_{\mathrm{RX}}\rangle \langle \tilde{1}_{\mathrm{RX}}| - |\tilde{0}_{\mathrm{RX}}\rangle \langle \tilde{0}_{\mathrm{RX}}|$, $\hat{\sigma}_x = |\tilde{0}_{\mathrm{RX}}\rangle \langle \tilde{1}_{\mathrm{RX}}| + |\tilde{1}_{\mathrm{RX}}\rangle \langle \tilde{0}_{\mathrm{RX}}|$ and the exchange energies $\mathrm{J} = (\mathrm{J}_{\mathrm{L}} + \mathrm{J}_{\mathrm{R}})/2$ and $j = (\mathrm{J}_{\mathrm{L}} - \mathrm{J}_{\mathrm{R}})/2$. By transforming Eq. (3.20) to its eigenbasis, we obtain an expression for the general RX qubit Hamiltonian from Eq. (3.14), which is valid in the regime $\Delta \ll -t_{\mathrm{L,R}}$, $\varepsilon \approx 0$ as

$$\hat{\mathrm{H}}_{\mathrm{RX}} \approx \frac{1}{2}\mathrm{E}_{\mathrm{RX}}\tilde{\hat{\sigma}}_{\mathrm{z}}, \tag{3.21}$$

with $\mathrm{E}_{\mathrm{RX}} = \sqrt{\mathrm{J}^2 + 3j^2}$ and $\tilde{\hat{\sigma}}_{\mathrm{z}}$ defined in the eigenbasis of Eq. (3.20). For $j = 0$, $\tilde{\hat{\sigma}}_{\mathrm{z}}$ is given by the Pauli matrix $\hat{\sigma}_{\mathrm{z}}$ from Eq. (3.20). Hence for $j = 0$ the logical RX qubit states are $|0_{\mathrm{RX}}\rangle = |\tilde{0}_{\mathrm{RX}}\rangle$ and $|1_{\mathrm{RX}}\rangle = |\tilde{1}_{\mathrm{RX}}\rangle$.

3.2.4 Few-electron triple quantum dot

We use the depletion gate technique introduced in subsection 3.1.1 to define a TQD. The gate electrode voltages V_{i} indicated in Fig. 3.12(a) tune the TQD potential landscape shown in Fig. 3.12(b).

The gate design is adapted from Refs. Medford et al., 2013a,b, where in contrast to other linear TQD designs in GaAs (Schröer et al., 2007, Gaudreau et al., 2009, Granger et al., 2010, Takakura et al., 2010) a single gate [horizontal gate in Fig. 3.12(a)] is used to define a potential barrier in one spatial direction. We observe that the presence of this barrier allows a high level of control over the interdot tunnel couplings by either tuning the interdot gate potentials $\mathrm{V}_{\mathrm{tL,tR}}$ or the reservoir gate voltages $\mathrm{V}_{\mathrm{rL,rR}}$, where the latter are found to be most effective for reaching large interdot tunnel couplings $t_{\mathrm{L,R}}$ of the order of 10 GHz.

We detect the TQD charge occupation with a QPC. By tuning the TQD plunger gates, the charge occupation changes as shown in the charge stability diagram in Fig. 3.13(a)

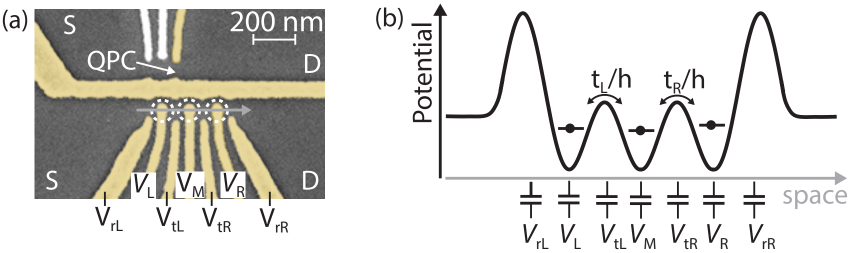

Figure 3.12 Formation of a TQD. (a) False-colored SEM picture of an exemplary gate structure to form a TQD (dashed circles) and a QPC by applying negative voltages V_{i} to the colored gate electrodes. Reservoirs for electrons are indicated as S and D. The corresponding idealized potential landscape in (b) that traps electrons spatially in three minima can be controlled with the voltages from (a).

as a function of the left and the right plunger gate voltages $\mathrm{V_L}$ and $\mathrm{V_R}$, respectively. If the middle quantum dot is empty, we observe charge transition lines with two different slopes in the charge stability diagram. These lines correspond to charge transitions between either the left or the right quantum dot and their respective reservoir. We reach the $(0, 0, 0)$ charge regime and sequentially load single electrons to the left and right quantum dots by increasing $\mathrm{V_L}$ and $\mathrm{V_R}$. By tuning the middle plunger gate voltage $\mathrm{V_M}$ more positive, we observe a charge transition line with a third slope in Fig. 3.13(b), which corresponds to loading the first electron into the middle quantum dot. Among the few electron charge configurations in Fig. 3.13(c) we identify $(1, 1, 1)$, $(2, 0, 1)$ and $(1, 0, 2)$. This demonstrates, that the TQD can be tuned to the relevant charge configurations for the RX qubit. In section 7.2 we further discuss the gate tuning that is necessary to implement the RX qubit in the desired parameter regime $\varepsilon \approx 0$, $|\Delta| \lesssim t_{\mathrm{L,R}}$ with a qubit energy of the order of a few GHz.

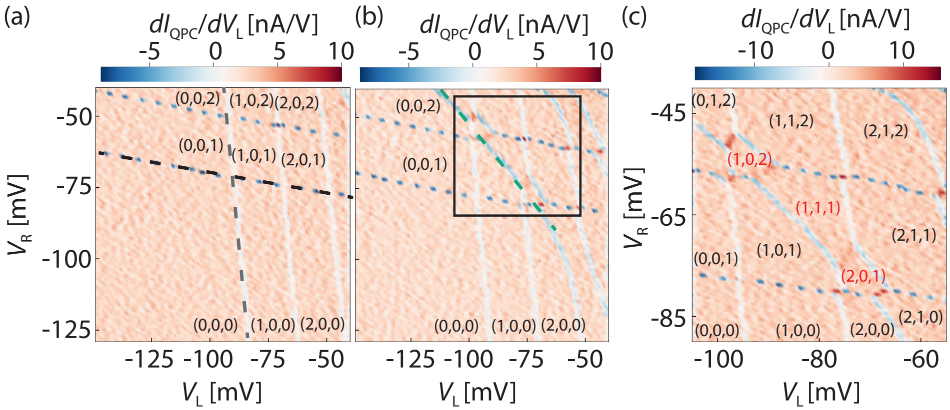

Figure 3.13 TQD charge stability diagrams. Differential QPC current as a function of $\mathrm{V_L}$ and $\mathrm{V_R}$. Regions with a stable charge occupation are labelled. Exemplary charge transition lines between the reservoirs and the left, middle or right quantum dots are marked as dashed gray, green or black lines, respectively. (a) $\mathrm{V_M} = -60\,\mathrm{mV}$ (b) $\mathrm{V_M} = -40\,\mathrm{mV}$. (c) Magnified view of the region marked with a black square in (b).

3.3 Superconducting qubit

The solid-state qubits discussed so far were built by localizing single electrons in quantum dots. This implementation allows control at the level of the electron wave function and minimizes the interaction with other degrees of freedom in the qubit environment that could cause qubit decoherence. For charge carriers in superconductors, i.e. Cooper pairs, the isolation from decohering degrees of freedom is to a large extent inherent as Cooper pairs are well separated in energy from dissipative channels by the superconducting gap (Clarke et al., 2008). In addition, a microscopic level of control, as with quantum dots, is not required since all Copper pairs occupy the same macroscopic state. The basic idea behind the superconducting qubit used in this thesis, which is a transmon qubit (Koch et al., 2007), is to form a tunnel barrier between two superconductors by using an insulating material and to encode the quantum information into states with excess Copper pairs on either side of the barrier (Nakamura et al., 1999). This can be considered analogous to a DQD charge qubit, where electrons are used instead of Cooper pairs and a DQD tunnel barrier replaces the insulator.

In subsection 3.3.1 we introduce both the tunnel barrier for Cooper pairs, known as Josephson junction, as well as a superconducting loop connecting two Josephson junctions by following in parts Ref. Stockklauser, 2017. Consecutively we briefly introduce the transmon qubit in subsection 3.3.2. More details about the physics of Josephson junctions devices can for example be found in Refs. Tinkham, 1996, Gross, 2006. Basic theoretical introductions to the transmon and superconducting qubits in general are provided for instance in Refs. Devoret et al., 2005, Clarke et al., 2008, Girvin, 2014.

3.3.1 Superconducting quantum interference device

A tunnel barrier for Cooper pairs can be realized by sandwiching a thin insulating material between two superconductors as illustrated in Fig. 3.14(a). For a sufficiently thin barrier (typically a few nm) the wave functions of the states in both superconductors overlap such that Cooper pairs can coherently tunnel across the barrier. The barrier is referred to as Josephson junction and its working principle is based on the two Josephson equations (Tinkham, 1996)

$$\mathrm{I} = \mathrm{I_c} \sin(\phi) \quad \text{and} \quad \dot{\phi} = 2e\mathrm{V}/\hbar, \tag{3.22}$$

where I is the supercurrent (current carried by Cooper pairs) across the junction, $\mathrm{I_c}$ is the maximum supercurrent of the junction, ϕ is a gauge-invariant difference between the phases of the superconducting states in both superconductors and V is a voltage difference applied across the junction. Using Faraday's law $V = -L\dot{I}$, the Josephson equations imply that the junction has an inductance

$$L_J = \frac{L_{J,0}}{\cos(\phi)} \tag{3.23}$$

with $L_{J,0} = \Phi_0/(2\pi I_c)$, where $\Phi_0 = h/(2e)$ is the flux quantum. By rewriting Eq. (3.23) with Eq. (3.22) as

$$L_J = \Phi_0/\left(2\pi\sqrt{I_c^2 - I^2}\right) \tag{3.24}$$

we find that the Josephson inductance is nonlinear. L_J is referred to as kinetic inductance (Devoret et al., 2005) as the energy

$$E = \int VI dt = -E_J \cos(\phi), \tag{3.25}$$

stored in this inductance is the kinetic energy of Cooper pairs tunneling across the junction. The term $E_J = I_c\Phi_0/(2\pi)$ is called Josephson energy.

A superconducting loop connecting two Josephson junctions forms a superconducting quantum interference device (SQUID) illustrated in Fig. 3.14(b). The phase differences across both junctions are linked due to the flux quantization in a superconducting loop, which originates from the requirement that the wave function needs to be single valued. For two identical junctions and by neglecting the inductance of the

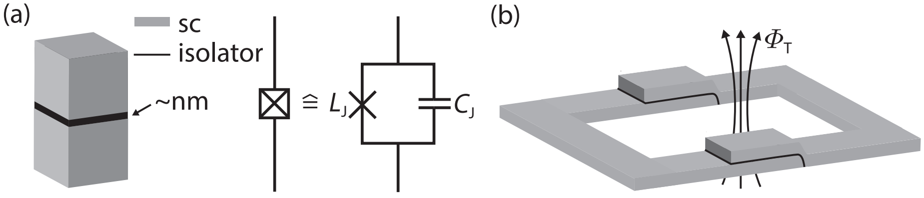

Figure 3.14 Josephson junction and SQUID. (a) Two superconductors (sc) are separated by a few nm thick insulating layer. This forms a Josephson junction that is symbolized as a crossed square, which corresponds to a Josephson inductance L_J in parallel to a capacitance C_J. (b) Superconducting loop that contains two Josephson junctions (SQUID). Φ_T denotes an external magnetic flux.

loop, the maximum supercurrent through the SQUID is given as (Gross, 2006)

$$\mathrm{I}_{\mathrm{c}}^{(\mathrm{SQ})} = 2\mathrm{I}_{\mathrm{c}}|\cos(\pi\Phi_{\mathrm{T}}/\Phi_0)|, \tag{3.26}$$

which is tunable with an applied flux $\Phi_{\mathrm{T}} = \mathrm{A}\mathrm{B}_{\perp}$, where A is the area enclosed by the SQUID loop and $\mathrm{B}_{\perp}$ is the magnitude of the perpendicular magnetic field through the loop. Following the derivation for a single Josephson junction above, this results in a flux-tunable SQUID inductance

$$\mathrm{L}_{\mathrm{J}}^{(\mathrm{SQ})} = \mathrm{L}_{\mathrm{J,max}}^{(\mathrm{SQ})}|\cos(\pi\Phi_{\mathrm{T}}/\Phi_0)|^{-1} \tag{3.27}$$

and Josephson energy

$$\mathrm{E}_{\mathrm{J}}^{(\mathrm{SQ})} = \mathrm{E}_{\mathrm{J,max}}^{(\mathrm{SQ})}|\cos(\pi\Phi_{\mathrm{T}}/\Phi_0)| \tag{3.28}$$

with $\mathrm{L}_{\mathrm{J,max}}^{(\mathrm{SQ})} = \mathrm{L}_{\mathrm{J}}/2$ and $\mathrm{E}_{\mathrm{J,max}}^{(\mathrm{SQ})} = 2\mathrm{E}_{\mathrm{J}}$.

3.3.2 Transmon qubit

A linear inductor in parallel to a capacitor realizes a harmonic oscillator with degenerate transition frequencies (see subsection 4.1.1). Due to its non-linear inductance, a Josephson junction can be used to build an anharmonic oscillator, where this degeneracy is lifted to form an effective dissipationless two-level system in a superconducting state called superconducting qubit (Shnirman et al., 1997).

The circuit diagram of the superconducting qubit used in this thesis is depicted in Fig. 3.15(a). It consists of a SQUID that connects a superconducting island via Josephson junctions to a reservoir. The SQUID is connected in parallel to a shunt capacitor with capacitance C_{B}. Another capacitor C_{g} connects to a voltage V_{g}, with which Cooper pairs can be induced on the island. The system Hamiltonian can be written as (Koch et al., 2007)

$$\hat{\mathrm{H}}_{\mathrm{T}} = 4\mathrm{E}_{\mathrm{C}}^{(\mathrm{T})}(\hat{n} - n_{\mathrm{g}})^2 - \mathrm{E}_{\mathrm{J}}^{(\mathrm{SQ})}\cos(\hat{\phi}), \tag{3.29}$$

where $\mathrm{E}_{\mathrm{C}}^{(\mathrm{T})} = e^2/[2(\mathrm{C}_{\mathrm{J}}^{(\mathrm{SQ})} + \mathrm{C}_{\mathrm{B}} + \mathrm{C}_{\mathrm{g}})]$ is the Coulomb charging energy for transferring a single electron to the island and $\mathrm{C}_{\mathrm{J}}^{(\mathrm{SQ})}$ is the total capacitance of the junctions. The operators $\hat{n}$ and $\hat{\phi}$ are canonical conjugate variables that represent the number of excess Cooper pairs on the island as well as the superconductor phase difference ϕ. The dispersion of the three lowest energy eigenstates of Eq. (3.29) are shown in Fig. 3.15(b) for two different ratios of $\mathrm{E}_\mathrm{J}^{(\mathrm{SQ})}/\mathrm{E}_\mathrm{C}^{(\mathrm{T})}$. The logical qubit states $|0_\mathrm{T}\rangle$ and $|1_\mathrm{T}\rangle$ are defined as the ground and first excited states of the system with energies E_0 and E_1, respectively. By increasing $\mathrm{E}_\mathrm{J}^{\mathrm{SQ}}/\mathrm{E}_\mathrm{C}^{(\mathrm{T})}$ the energy spectrum in Fig. 3.15(b) becomes flat, which reduces the effect of charge noise acting on the qubit via n_g. In this regime, the qubit is referred to as transmon and the qubit energy is approximately given as (Koch et al., 2007)

$$\mathrm{E}_\mathrm{T} \equiv \mathrm{E}_1 - \mathrm{E}_0 \approx \sqrt{8\mathrm{E}_\mathrm{C}^{(\mathrm{T})}\mathrm{E}_\mathrm{J}^{(\mathrm{SQ})}} - \mathrm{E}_\mathrm{C}^{(\mathrm{T})}. \tag{3.30}$$

With increasing $\mathrm{E}_\mathrm{J}^{(\mathrm{SQ})}/\mathrm{E}_\mathrm{C}^{(\mathrm{T})}$, the absolute anharmonicity $\mathrm{E}_{12} - \mathrm{E}_{01} \approx \mathrm{E}_\mathrm{C}^{(\mathrm{T})}$ and hence the two-level character of the qubit decreases, since $\mathrm{E}_{01} \equiv \mathrm{E}_1 - \mathrm{E}_0$ and $\mathrm{E}_{12} \equiv \mathrm{E}_2 - \mathrm{E}_1$ are the energies for the transitions $|0_\mathrm{T}\rangle \rightarrow |1_\mathrm{T}\rangle$ and $|1_\mathrm{T}\rangle \rightarrow |2_\mathrm{T}\rangle$, respectively. In this thesis we use a transmon in the regime $50 \lesssim \mathrm{E}_\mathrm{J}^{(\mathrm{SQ})}/\mathrm{E}_\mathrm{C}^{(\mathrm{T})} \lesssim 80$. In the basis of its eigenstates $|k_\mathrm{T}\rangle$, Eq. (3.29) becomes

$$\hat{\mathrm{H}}_\mathrm{T} = \sum_{k=0}^{\mathrm{N}} \mathrm{E}_\mathrm{k}\hat{\mathrm{A}}_{\mathrm{k,k}}, \tag{3.31}$$

where we introduced the operator $\hat{\mathrm{A}}_{k,l} = |k_\mathrm{T}\rangle\langle l_\mathrm{T}|$.

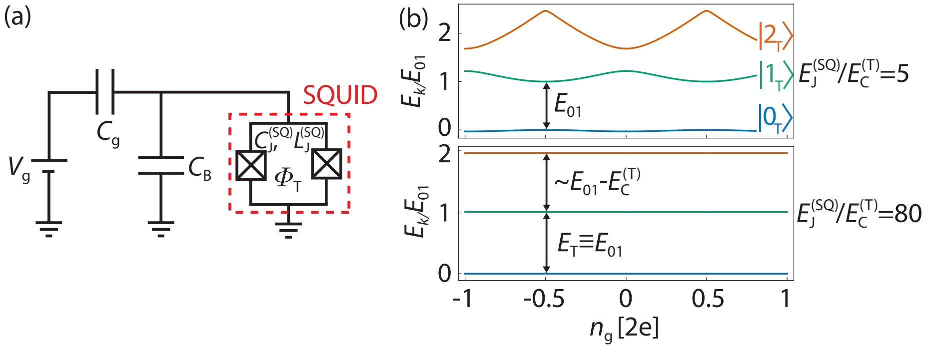

Figure 3.15 Transmon schematic and energy spectrum. (a) Circuit model of a transmon qubit. (b) Energies E_k of the eigenstates $|k_\mathrm{T}\rangle$ of Eq. (3.29) as a function of the offset charge n_g calculated according to Ref. Koch et al., 2007 for different $\mathrm{E}_\mathrm{J}^{(\mathrm{SQ})}/\mathrm{E}_\mathrm{C}^{(\mathrm{T})}$ in the top and bottom panel. The energies are normalized by the $|0_\mathrm{T}\rangle \rightarrow |1_\mathrm{T}\rangle$ transition energy E_{01} and offset such that the minimum of E_0 is at $\mathrm{E}_k/\mathrm{E}_{01} = 0$. The transmon qubit energy E_T corresponds to E_{01} (Koch et al., 2007).

Chapter 4

Superconducting microwave resonators

In the course of this thesis we study the interaction of the qubits introduced in chapter 3 with single microwave photons. Thereby, the photons are stored in the quantum system presented in this chapter. It is a superconducting on-chip microwave resonator, that exhibits a harmonic energy spectrum with single quanta of the electromagnetic field (photons) as the excitations. Once resonator and qubits are coupled, this spectrum can become anharmonic as we will discuss chapter 5.

In section 4.1 we introduce theoretical concepts that allow to describe the three different types of superconducting microwave resonators used in this thesis. The first resonator is an Al coplanar waveguide transmission line resonator, which has a characteristic impedance of $50\,\Omega$. Among others, the characteristic impedance determines the magnitude of the voltage fluctuations in the resonator ground state, i.e. the vacuum state. This magnitude can be increased in order to enhance the qubit-photon coupling strength, which is discussed in chapter 5. Another potential benefit of a high impedance resonator is its smaller size compared to a $50\,\Omega$ resonator with the same resonance frequency. We present two different resonators, where a high characteristic impedance ($> 1\,\mathrm{k}\Omega$) is either achieved by using the high distributed kinetic inductance of a thin and narrow superconducting NbTiN wire or by employing the high local kinetic inductance of an array of SQUIDs. The $50\,\Omega$ and SQUID array resonators are based on the designs in Refs. Göppl et al., 2008, Frey, 2013 and Ref. Stockklauser, 2017, respectively. They are briefly overviewed in section 4.2 and subsection 4.3.2. For the NbTiN resonator, which was developed in this thesis based on similar work in Ref. Samkharadze et al., 2016, the fabrication and characterization is explained in detail in subsection 4.3.1. This resonator is resilient to external magnetic fields of the order of a tesla, which is in contrast to the other two resonators.

4.1 Theoretical concepts

The three different types of resonator that are used for the experiments in this thesis can be described as transmission line resonators. In subsection 4.1.1 we explain basic theoretical concepts of transmission lines and present a quantum mechanical description of transmission line resonators. We then introduce the quantum mechanical input-output theory framework in subsection 4.1.2, which we subsequently use in subsection 4.1.3 to derive equations for the resonator spectra and photon numbers. We thereby also discuss the resonator decay rates and quality factors that are related to internal and external loss channels.

4.1.1 Transmission line resonator

Transmission lines are electrical structures that support the propagation of electromagnetic waves. For the microwave frequencies from 4 to 8 GHz that are used in this thesis, the wavelength of the propagating waves is of the order of centimeters (in vacuum). Transmission lines can, for instance, be realized in a coplanar waveguide (CPW) geometry that is shown in Fig. 4.1(a). It consists of a center conductor of width w separated by a distance s from two extended ground planes. This metallic structure of thickness

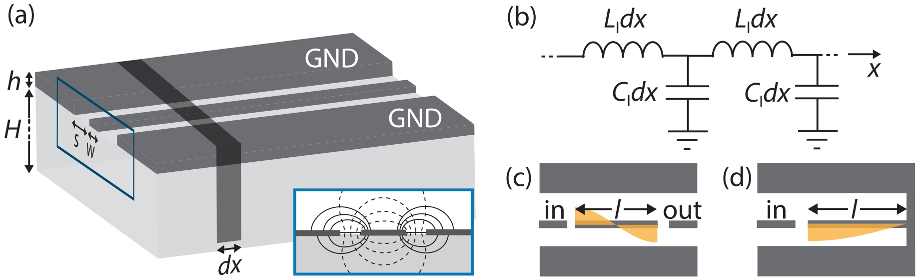

Figure 4.1 Transmission line. (a) Illustration of a coplanar waveguide (dark gray) consisting of a metallic center conductor and extended ground planes (GND) on top of a substrate (light gray). The cross-sectional cut framed with a blue rectangle is depicted on the bottom right corner. There, the transverse electric and magnetic fields of the electromagnetic wave in the CPW are shown qualitatively as solid and dashed lines, respectively (Wolff, 2006). (b) Lumped element circuit for a section of length dx from (a). The inductance and capacitance per unit length are $\mathrm{L_l}$ and $\mathrm{C_l}$, respectively. (c)-(d) Schematic illustration of a $\lambda/4$ resonator in (c) and a $\lambda/2$ resonator in (d). The voltage profile of the fundamental resonance mode is indicated.

h is patterned on top of a substrate of thickness H. In this thesis, $\mathrm{H} \approx 500\,\mu\mathrm{m}$ and w, s and h are of the order of micrometers. To minimize resistive losses, we pattern the transmission line from a superconducting material. The spatial dependence of voltages and currents along such a lossless transmission line can be modelled with a lumped-element representation of an infinitesimal transmission line section of length dx as shown in Fig. 4.1(b). This section consists of an inductance per unit length $\mathrm{L_l}$ in parallel to a capacitance to unit length $\mathrm{C_l}$ to ground (Pozar, 2005).

We follow Refs. Girvin, 2014, Laloy, 2010 to derive the wave equation for the transmission line. We start by defining the variable

$$\Phi(x,t) = \int_{-\infty}^{t} d\tau \mathrm{V}(x,\tau), \tag{4.1}$$

where $\mathrm{V}(x,t) = \partial_t \Phi(x,t)$ is the position- and time-dependent voltage on the transmission line. The voltage drop over a section of length dx is therefore $-dx\partial_x\partial_t\Phi(x,t)$. By employing Faraday's law we find that the magnetic flux through $\mathrm{L_l}$ is $-dx\partial_x\Phi(x,t)$. This determines the position- and time-dependent current $\mathrm{I}(x,t)$ as

$$\mathrm{I}(x,t)\mathrm{L_l}\,dx = -dx\partial_x\Phi(x,t). \tag{4.2}$$

With this relation we can write the system Lagrangian as

$$\mathscr{L} = \int dx \left[\frac{\mathrm{C_l}}{2}(\partial_t\Phi)^2 - \frac{1}{2\mathrm{L_l}}(\partial_x\Phi)^2 \right], \tag{4.3}$$

where the two terms in the equation represent the charging energy for $\mathrm{C_l}$ and the magnetic energy stored in $\mathrm{L_l}$. The Euler-Lagrange equation leads to the wave equation

$$v_{\mathrm{ph}}^2 \partial_x^2 \Phi - \partial_t^2 \Phi = 0, \tag{4.4}$$

where $v_{\mathrm{ph}} = 1/\sqrt{\mathrm{L_l C_l}}$ is the phase velocity of the transmission line waves. The characteristic impedance of the transmission line is defined as

$$\mathrm{Z} \equiv \sqrt{\frac{\mathrm{L_l}}{\mathrm{C_l}}}, \tag{4.5}$$

which is the ratio of voltage and current amplitudes for waves propagating in the same direction.

By leaving one end of a transmission line open or shorting it to ground, we can impose spatial boundary conditions on the voltage and current waves and form a resonator as we will show below. Electromagnetic radiation can be coupled into an open end by coupling this end capacitively to another transmission line, which is in this context referred to as a port [see Figs. 4.1(c)-(d)].

In the following we consider a transmission line of length l with two open ends as depicted in Fig. 4.1(c). We neglect the capacitive influence of the coupled ports and follow in parts Refs. Girvin, 2014, Stockklauser et al., 2017 to introduce the quantum mechanical description of this system. The current needs to vanish at the open ends of the transmission line at $x = 0$ and $x = l$. This implies $\partial_x \Phi(x,t)|_{x=0,t} = 0$ and $\partial_x \Phi(x,t)|_{x=l,t} = 0$. The solution of Eq. (4.4) can therefore be written in terms of spatial normal modes with wave number $k_n = n\pi/l$ as

$$\Phi(x,t) = \sum_{n=0}^{\infty} \xi_n(t)\cos(k_n x), \tag{4.6}$$

where $\xi_n(t)$ are time-dependent functions describing the magnitude of mode n. By substituting Eq. (4.6) into Eq. (4.4), the Lagrangian becomes

$$\mathscr{L} = \sum_{n=0}^{\infty} \left[\frac{\mathrm{C}}{2}(\partial_t \xi_n)^2 - \frac{1}{2\mathrm{L}}\xi_n^2 \right], \tag{4.7}$$

where every summation term can be identified as the Lagrangian for a lumped element circuit consisting of an inductor $\mathrm{L} = 2l\mathrm{L}_\mathrm{l}/(n^2\pi^2)$ in parallel to a capacitor $\mathrm{C} = \mathrm{C}_\mathrm{l} l/2$. The momentum conjugate to ξ_n is the charge

$$q_n = \mathrm{C}\partial_t \xi_n \tag{4.8}$$

with which we obtain the system Hamiltonian from the Lagrangian in Eq. (4.7) as

$$\mathrm{H} = \sum_{n=0}^{\infty} \left[\frac{q_n^2}{2\mathrm{C}} + \frac{\xi_n^2}{2\mathrm{L}} \right]. \tag{4.9}$$

We now promote the classical conjugate quantities q_n and ξ_n to quantum mechanical operators, which obey the canonical commutation relation

$$[\hat{q}_n, \hat{\xi}_n] = -i\hbar \tag{4.10}$$

and are related to the annihilation and creation operators $\hat{a}_n$ and $\hat{a}_n^\dagger$ as

$$\hat{\xi}_n = \sqrt{\frac{\hbar \mathrm{Z_r}}{n\pi}}(\hat{a}_n + \hat{a}_n^\dagger) \tag{4.11}$$

and

$$\hat{q}_n = -i\sqrt{\frac{\hbar n\pi}{4\mathrm{Z_r}}}(\hat{a}_n - \hat{a}_n^\dagger), \tag{4.12}$$

where

$$\mathrm{Z_r} \equiv \sqrt{\mathrm{L_l}/\mathrm{C_l}} \tag{4.13}$$

is the characteristic impedance of the transmission line segment of length l. With this definition, the Hamiltonian from Eq. (4.9) becomes the quantum mechanical operator

$$\hat{\mathrm{H}} = \sum_{n=1}^{\infty} \hbar\omega_{\mathrm{r},n}\left(\hat{a}_n^\dagger \hat{a}_n + \frac{1}{2}\right), \tag{4.14}$$

which is a sum over the Hamiltonian of harmonic oscillators. Here, the harmonic oscillators represent resonances in the transmission line at resonance frequencies

$$\omega_{r,n} = \pi n/(l\sqrt{\mathrm{L_l C_l}}). \tag{4.15}$$

The operators $\hat{a}_n$ and $\hat{a}_n^\dagger$ annihilate and create photon excitations in the transmission line at frequency $\omega_{r,n}$. The transmission line therefore acts as a resonator with a degenerate excitation spectrum for every mode n as $\hat{a}_n^\dagger \hat{a}_n$ in Eq. (4.14) is the photon number operator. The mode n is the n-th harmonic and corresponds to a standing electromagnetic wave in the transmission line, which has voltage maxima at the ends and n voltage nodes. If only the fundamental (1st harmonic) is relevant, we omit the index n and write the Hamiltonian in Eq. (4.14) as

$$\hat{\mathrm{H}}_\mathrm{r} = \hbar\omega_\mathrm{r}\left(\hat{a}^\dagger \hat{a} + \frac{1}{2}\right). \tag{4.16}$$

The transmission line resonator with two open ends is referred to as $\lambda/2$ resonator, as $\lambda/2 = l$ for the fundamental mode [see Fig. 4.1(c)].

For a transmission line with one open end and one end shorted to ground, above derivation yields the Hamiltonian from Eq. (4.14) with the mode frequencies $\omega_{r,n} =$

$(2n-1)\pi/(2l\sqrt{\mathrm{L}_l\mathrm{C}_l})$. Such a transmission line structure is shown in Fig. 4.1(d). It forms a $\lambda/4$ resonator with a voltage node and anti-node at the shorted and open ends, respectively. The higher order modes are odd multipliers of $\lambda/4$.

To quantify the voltage at the anti-node for a transmission line resonator, we first express the wave equation solution from Eq. (4.4) in terms of operators as

$$\hat{\Phi}(x) = \sum_{n=0}^{\infty} \hat{\xi}_n \cos(k_n x). \tag{4.17}$$

By inserting Eq. (4.17) into Eq. (4.1) and using (4.8) and (4.12), the voltage operator becomes

$$\hat{\mathrm{V}}(x) = \sum_{n=1}^{\infty} \hat{\mathrm{V}}_n(x) = \partial_t \hat{\Phi}(x) = -i \sum_{n=1}^{\infty} \sqrt{\frac{\hbar\omega_{\mathrm{r},n}}{\mathrm{C}_\mathrm{l} l}} \cos(k_n x)(\hat{a}_n - \hat{a}_n^\dagger). \tag{4.18}$$

This implies that the root mean square of the voltage vacuum fluctuations at the voltage anti-node in the resonator are

$$\mathrm{V}_{\mathrm{ZPF},n} \equiv \sqrt{\langle 0| \, |\hat{\mathrm{V}}(x=0)|^2 \, |0\rangle} = \sqrt{\frac{\hbar\omega_{\mathrm{r},n}}{\mathrm{C}_\mathrm{l} l}} = \sqrt{\frac{\hbar \mathrm{Z}_\mathrm{r}}{\pi n}} \omega_{\mathrm{r},n}, \tag{4.19}$$

where we used Eqns. (4.13) and (4.15) to rewrite the expression. For the fundamental resonator mode, we again omit the index n and define $\mathrm{V}_{\mathrm{ZPF}} \equiv \mathrm{V}_{\mathrm{ZPF},1}$. Note that Eq. (4.19) equally holds for $\lambda/2$ and $\lambda/4$ resonators.

4.1.2 Input-Output formulation for cavities

In this section we follow in parts Refs. Walls et al., 2008, Laloy, 2010, Girvin, 2014 to introduce a theoretical description of a dissipative quantum system that consists of a cavity interacting with external fields. This theory is referred to as input-output theory and was initially derived in the context of optical cavities (Collett et al., 1984). It is used to calculate the spectral response of the resonators in sections 4.2-4.3 and is generalized in chapter 5 to the situation where a qubit interacts with the cavity mode.

We consider a single-port cavity shown in Fig. 4.2 that contains a single mode and is described by the Hamiltonian $\hat{\mathrm{H}}_{\mathrm{cav}}$. The mode is coupled via a partially transmitting

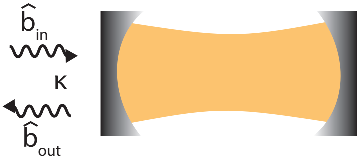

Figure 4.2 Cavity input-output model. Schematic illustration of a single-sided cavity that is coupled to input (in) and output (out) fields represented by the operators $\hat{b}_{\text{in,out}}$ at coupling rate κ.

mirror to an external field. We model the external field with the Hamiltonian

$$\hat{\mathrm{H}}_{\text{bath}} = \hbar \int_{-\infty}^{\infty} d\omega \omega \hat{b}^{\dagger}(\omega)\hat{b}(\omega), \tag{4.20}$$

which describes a bath of harmonic oscillators at angular frequencies ω, where $\hat{b}^{\dagger}(\omega)$ $[\hat{b}(\omega)]$ is the corresponding creation (annihilation) operator and $[\hat{b}(\omega_1), \hat{b}^{\dagger}(\omega_2)] = \delta(\omega_1 - \omega_2)$ ensures that the oscillators are independent. The interaction between the cavity mode and the bath is modeled as a dissipative process at coupling rate κ. Using rotating wave approximation (RWA), it is formally described by the interaction Hamiltonian

$$\hat{\mathrm{H}}_{\text{int}} = i\hbar\sqrt{\frac{\kappa}{2\pi}} \int_{-\infty}^{\infty} d\omega [\hat{b}(\omega)\hat{a}^{\dagger} - \hat{a}\hat{b}^{\dagger}(\omega)], \tag{4.21}$$

where the cavity mode creation and annihilation operators are $\hat{a}^{\dagger}$ and $\hat{a}$, respectively. Above Hamiltonians define the total system Hamiltonian as

$$\hat{\mathrm{H}}_{\text{sys}} = \hat{\mathrm{H}}_{\text{cav}} + \hat{\mathrm{H}}_{\text{bath}} + \hat{\mathrm{H}}_{\text{int}}. \tag{4.22}$$

We can now write the Heisenberg equation of motion for the bath operator $\hat{b}(\omega)$

$$\partial_t \hat{b}(t,\omega) = \frac{i}{\hbar}[\hat{\mathrm{H}}_{\text{sys}}, \hat{b}(\omega)] = -i\omega\hat{b}(\omega) + \sqrt{\frac{\kappa}{2\pi}}\hat{a} \tag{4.23}$$

as well as for the cavity mode operator $\hat{a}$:

$$\partial_t \hat{a}(t) = \frac{i}{\hbar}[\hat{\mathrm{H}}_{\text{cav}}, \hat{a}] - \sqrt{\frac{\kappa}{2\pi}} \int_{-\infty}^{\infty} d\omega \hat{b}(t,\omega). \tag{4.24}$$

Equation (4.23) can be solved as

$$\hat{b}(t,\omega) = e^{-i\omega(t-t_0)}\hat{b}_0(\omega) + \sqrt{\frac{\kappa}{2\pi}}\int_{t_0}^{t} dt' e^{-i\omega(t-t')}\hat{a}(t') \tag{4.25}$$

by assuming that at time $t_0 < t$, which is before cavity and bath interact, the bath is described by $\hat{b}_0(\omega) = \hat{b}(t = t_0, \omega)$. The first term in Eq. (4.25) corresponds to the free time evolution of the bath modes and the second term quantifies cavity modes that are radiated into the bath. By inserting Eq. (4.25) into Eq. (4.24) one can derive the time evolution of the intra-cavity field as

$$\partial_t \hat{a} = \frac{i}{\hbar}[\hat{\mathrm{H}}_{\mathrm{cav}}, \hat{a}] - \frac{\kappa}{2}\hat{a} + \sqrt{\kappa}\hat{b}_{\mathrm{in}}(t), \tag{4.26}$$

where the operator

$$\hat{b}_{\mathrm{in}}(t) \equiv -\frac{1}{\sqrt{2\pi}}\int_{-\infty}^{\infty} d\omega e^{-i\omega(t-t_0)}\hat{b}_0(\omega) \tag{4.27}$$

represents the cavity input field, i.e. a field from the bath that propagates towards the cavity. Equation (4.26) can be interpreted as the equation of motion for a damped cavity mode that is driven by the cavity input field.

The Heisenberg equation of motion (4.23) for the bath operator can equivalently be solved with the boundary condition $\hat{b}_1(\omega) = \hat{b}(t = t_1, \omega)$, where $t_1 > t$ is a time after the interaction. One obtains

$$\partial_t \hat{a} = \frac{i}{\hbar}[\hat{\mathrm{H}}_{\mathrm{cav}}, \hat{a}] + \frac{\kappa}{2}\hat{a} - \sqrt{\kappa}\hat{b}_{\mathrm{out}}(t), \tag{4.28}$$

where

$$\hat{b}_{\mathrm{out}}(t) \equiv \frac{1}{\sqrt{2\pi}}\int_{-\infty}^{\infty} d\omega e^{-i\omega(t-t_1)}\hat{b}_1(\omega) \tag{4.29}$$

describes the field propagating away from the cavity after the interaction. We combine Eqns. (4.26) and (4.28) to relate input- and output fields as

$$\hat{b}_{\mathrm{in}}(t) + \hat{b}_{\mathrm{out}}(t) = \sqrt{\kappa}\hat{a}(t). \tag{4.30}$$

The main results of above derivation in Eq. (4.26) and (4.30) can be generalized to the coupling of the cavity mode at rate κ_i to multiple fields that are described by $\hat{b}_{\mathrm{in},i}(t)$

and $\hat{b}_{\mathrm{out},i}(t)$. There, we obtain

$$\begin{aligned} \partial_t \hat{a} &= \frac{i}{\hbar}[\hat{\mathrm{H}}_{\mathrm{cav}}, \hat{a}] - \left(\sum_i \frac{\kappa_i}{2}\right)\hat{a} + \sum_i \sqrt{\kappa_i}\hat{b}_{\mathrm{in},i}(t), \\ \hat{b}_{\mathrm{in},i}(t) + \hat{b}_{\mathrm{out},i}(t) &= \sqrt{\kappa_i}\hat{a}(t)\ \forall i. \end{aligned} \tag{4.31}$$

4.1.3 Resonator spectrum and photon number

We use the input-output theory framework presented in subsection 4.1.2 to calculate the spectroscopic response of the transmission line resonators that are relevant in this thesis. We denote dissipative interaction of the resonator mode with the external field at its ports as external resonator decay rate κ_{ext}, while dissipation that is not related to this external field as internal resonator decay rate κ_{int}. The origin of the latter is among others due to loss mechanisms in the resonator material and the substrate. We treat internal photon loss in the input-output theory formalism as an additional port with $\hat{b}_{\mathrm{in,int}} = 0$ (Laloy, 2010).

We start with the derivation of the spectrum of the $\lambda/4$ resonator depicted in Fig. 4.3(a). Using the resonator Hamiltonian in Eq. (4.16), the input-output theory relations in Eq. (4.31) read as

$$\partial_t \hat{a} = -i\omega_{\mathrm{r}}\hat{a} - \frac{\kappa_{\mathrm{ext}} + \kappa_{\mathrm{int}}}{2}\hat{a} + \sqrt{\kappa_{\mathrm{ext}}}\hat{b}_{\mathrm{in},1}(t), \tag{4.32}$$

$$\hat{b}_{\mathrm{in},1}(t) + \hat{b}_{\mathrm{out},1}(t) = \sqrt{\kappa_{\mathrm{ext}}}\hat{a}(t). \tag{4.33}$$

This system of equations can be solved by Fourier transformation, where $\partial_t \hat{a}(t) \rightarrow$

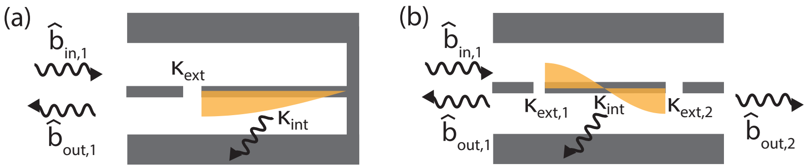

Figure 4.3 Resonator models. Schematic illustration of a $\lambda/4$ and $\lambda/2$ resonator in (a) and (b), respectively. The field operators $\hat{b}_{\mathrm{in,out}}$ and resonator decay rates $\kappa_{\mathrm{ext,int}}$ are discussed in the text.

$-i\omega\hat{a}(\omega)$. Hence, we arrive at the spectroscopic resonator response

$$\frac{\hat{b}_{\mathrm{out},1}(\omega)}{\hat{b}_{\mathrm{in},1}(\omega)} = \frac{(\kappa_{\mathrm{ext}} - \kappa_{\mathrm{int}}) + 2i(\omega - \omega_{\mathrm{r}})}{(\kappa_{\mathrm{ext}} + \kappa_{\mathrm{int}}) - 2i(\omega - \omega_{\mathrm{r}})}, \tag{4.34}$$

which is probed in experiment with a classical coherent drive at frequency $\omega = \omega_{\mathrm{p}}$. We therefore replace the quantum operators $\hat{b}_{\mathrm{in/out},1}$ with the complex valued quantities $b_{\mathrm{in},1}$ and $b_{\mathrm{out},1}$ that represent the complex amplitude of a coherent state. The ratio $b_{\mathrm{out},1}/b_{\mathrm{out},1}$ is equivalent to the experimentally determined reflection coefficient S_{11} and we obtain by rewriting Eq. (4.34)

$$\mathrm{S}_{11}(\omega_{\mathrm{p}}) \equiv \frac{b_{\mathrm{out},1}}{b_{\mathrm{in},1}} = \frac{\kappa_{\mathrm{ext}}}{\kappa_{\mathrm{r}}/2 - i(\omega_{\mathrm{p}} - \omega_{\mathrm{r}})} - 1, \tag{4.35}$$

where $\kappa_{\mathrm{r}} \equiv \kappa_{\mathrm{int}} + \kappa_{\mathrm{ext}}$ defines the total resonator decay rate.

For $\kappa_{\mathrm{ext}} > \kappa_{\mathrm{int}}$ a resonator is considered overcoupled as photons are lost at a higher rate through the ports compared to internal loss mechanisms. It is undercoupled in the reversed situation, i.e. $\kappa_{\mathrm{ext}} < \kappa_{\mathrm{int}}$. The situation $\kappa_{\mathrm{ext}} = \kappa_{\mathrm{int}}$ is referred to as critical coupling. The decay rate κ_{ext} is a design parameter, which depends among others on the capacitance $\mathrm{C_c}$ between the resonator and its ports. For a single-port resonator one can derive (Castellanos-Beltran, 2002)

$$\kappa_{\mathrm{ext}} = \frac{4}{\pi}\omega_{\mathrm{r}}^3 \mathrm{C_c^2 Z_r Z_{port}}, \tag{4.36}$$

where $\mathrm{Z_{port}}$ the characteristic impedance of the capacitively coupled port. Resonators are often also characterized in terms of the internal, external and loaded quality factors defined as $\mathrm{Q_{int}} \equiv \omega_r/\kappa_{\mathrm{int}}$, $\mathrm{Q_{ext}} \equiv \omega_r/\kappa_{\mathrm{ext}}$ and $\mathrm{Q_{ld}} \equiv \omega_r/\kappa_{\mathrm{r}}$.

Since the resonator is coupled to a classical coherent tone at its port, it is in a coherent state $|\alpha\rangle$, which has a Poissonian photon number distribution with average $\bar{n} = \langle\alpha|\,\hat{a}^\dagger\hat{a}\,|\alpha\rangle = |\alpha|^2$ (Girvin, 2014) that is given as (Laloy, 2010)

$$\bar{n} = \frac{4\kappa_{\mathrm{ext}}}{\hbar\omega_{\mathrm{r}}(\kappa_{\mathrm{int}} + \kappa_{\mathrm{ext}})^2}\mathrm{P_{in}}, \tag{4.37}$$

where $\mathrm{P_{in}}$ is the power of the resonator input tone.

Next, we derive the spectrum of the $\lambda/2$ resonator shown in Fig. 4.3(b) that is symmetrically coupled ($\kappa_{\mathrm{ext},1} = \kappa_{\mathrm{ext},2} \equiv \kappa_{\mathrm{ext}}/2$) and probed in transmission from port 1 to 2. We extend the calculation from above to two ports and set $\hat{b}_{\mathrm{in},2} = 0$ to obtain the complex transmitted amplitude

$$\mathrm{S}_{21}(\omega_\mathrm{p}) \equiv \frac{b_{\mathrm{out},2}}{b_{\mathrm{in},1}} = \frac{\kappa_\mathrm{ext}}{\kappa_\mathrm{r} - 2i(\omega_\mathrm{p} - \omega_\mathrm{r})}. \tag{4.38}$$

Hence, the transmitted power

$$|\mathrm{S}_{21}|^2(\omega_\mathrm{p}) = \frac{(\kappa_\mathrm{ext}/2)^2}{(\omega_\mathrm{p} - \omega_\mathrm{r})^2 + (\kappa_\mathrm{r}/2)^2}, \tag{4.39}$$

has a Lorentzian lineshape with a full width at half maximum (FWHM) κ_r. Again, κ_ext depends on the resonator design. One can derive (Castellanos-Beltran, 2002)

$$\kappa_\mathrm{ext} = \frac{2}{\pi} \omega_\mathrm{r}^3 \mathrm{C}_\mathrm{c}^2 \mathrm{Z}_\mathrm{r} \mathrm{Z}_\mathrm{port}. \tag{4.40}$$

The averaged number of photons becomes in this case (Laloy, 2010)

$$\bar{n} = \frac{2\kappa_\mathrm{ext}}{\hbar\omega_\mathrm{r}(\kappa_\mathrm{int} + \kappa_\mathrm{ext})^2} \mathrm{P}_\mathrm{in}. \tag{4.41}$$

4.2 Al coplanar waveguide $\lambda/2$ resonator (50 Ω)

In this section we provide a short introduction to the design and the characterization of an Al coplanar waveguide $\lambda/2$ resonator that is employed for the experiments presented in chapter 8. This resonator is adapted from prior work in Refs. Göppl et al., 2008, Göppl, 2009, Frey, 2013, where we refer to for more details.

4.2.1 Resonator design

The resonator in Fig. 4.4 is a CPW type $\lambda/2$ resonator. The geometry parameters $w = 10\,\mu\mathrm{m}$ and $s = 7.1\,\mu\mathrm{m}$ that were defined in Fig. 4.1(a), are chosen such that we obtain $\mathrm{Z}_\mathrm{r} = \sqrt{\mathrm{L}_\mathrm{l}/\mathrm{C}_\mathrm{l}} \approx 50\,\Omega$, where we used $\mathrm{L}_\mathrm{l} = 445\,\mathrm{nH/m}$ and $\mathrm{C}_\mathrm{l} = 174\,\mathrm{pF/m}$ according to Ref. Mc Mahill, 2009. From the resonator length $l = 10.34\,\mathrm{mm}$ we estimate $\nu_\mathrm{r} = 5.50\,\mathrm{GHz}$ with Eq. (4.15).

The resonator is fabricated as a $h \approx 200\,\mathrm{nm}$ thick film of Al on top of a GaAs/AlGaAs heterostructure. Fabrication details can be found in Appendix C.2. Before depositing the resonator, the 2DEG is removed in the surrounding area by wet etching the top part of the heterostructure. Otherwise it would act as a resistive shunt to ground that induces a significant resonator loss (Frey, 2013) since the distance of the center conductor to

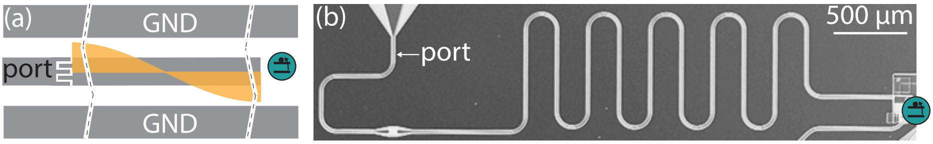

Figure 4.4 50 Ω resonator schematic and picture. (a) Schematic illustration of a coplanar waveguide $\lambda/2$ resonator that is capacitively coupled to a microwave port on one side and a qubit on the other side. (b) False-colored optical micrograph of the resonator from (a) that is fabricated from Al (dark gray) on top of GaAs (white).

the 2DEG of ≈ 90 nm is much smaller than its distance s to the ground planes. The resonator is at one end coupled with a finger capacitor to a 50 Ω transmission line. At the other open end the resonator couples capacitively to a qubit, which is omitted in this section but discussed in detail in chapter 8.

4.2.2 Resonator characterization

To fit to the in-phase $\tilde{\mathrm{I}}$ and quadrature $\tilde{\mathrm{Q}}$ components of the measured resonator reflectance spectrum in Fig. 4.5(a), we consider the bare resonator reflectance $\mathrm{S}_{11} \equiv \tilde{\mathrm{I}} + i\tilde{\mathrm{Q}}$

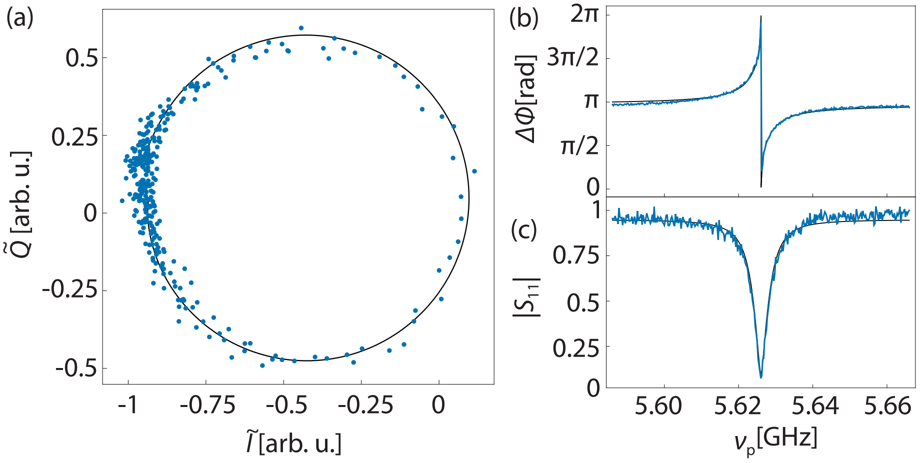

Figure 4.5 50 Ω resonator characterization. (a) Theory fit to the data (points) in the $\tilde{\mathrm{I}} - \tilde{\mathrm{Q}}$ plane using $\mathrm{S}_{11,\mathrm{meas}}$ in Eq. (4.42). (b)-(c) Data and theory curve calculated from (a) using the equality $\mathrm{S}_{11} \equiv |\mathrm{S}_{11}| e^{i\Delta\Phi}$.

given for a single-port resonator in Eq. (4.35) as well as the influence of the experimental setup. The fit function is therefore of the form (Frey, 2013)

$$S_{11,\mathrm{meas}}(\nu_\mathrm{p}) = (a + b \cdot \delta x) S_{11}(\nu_\mathrm{p}) e^{i(\nu \cdot \delta x + \Theta)} + (\tilde{I}_0 + i\tilde{Q}_0), \tag{4.42}$$

with $\delta x = (\nu_\mathrm{p} - \nu_\mathrm{r})/\nu_\mathrm{r}$. The fit parameters a, b, v and Θ account for the attenuation and phase change of the reflected signal due to the microwave lines of the setup and $\tilde{I}_0 + i\tilde{Q}_0$ is a frequency-independent offset.

From the fit in Fig. 4.5(a) we extract that the resonator is overcoupled, because $\kappa_\mathrm{int}/2\pi = 3.0\,\mathrm{MHz}$ ($Q_\mathrm{int} \approx 1880$) and $\kappa_\mathrm{ext}/2\pi = 3.8\,\mathrm{MHz}$ ($Q_\mathrm{ext} \approx 1480$). The resonance frequency $\nu_\mathrm{r} = 5.63\,\mathrm{GHz}$ is in good agreement with above theoretical estimate.

4.3 High impedance resonators (> 1 kΩ)

The magnitude of the vacuum voltage fluctuations V_ZPF of a transmission line resonator is according to Eq. (4.19) proportional to $\omega_\mathrm{r}\sqrt{Z_\mathrm{r}}$. It can therefore be enhanced using a high impedance resonator, i.e. a resonator with $Z_\mathrm{r} \gg 50\,\Omega$. Here we use the approach to enhance $Z_\mathrm{r} = \sqrt{L_\mathrm{l}/C_\mathrm{l}}$ by increasing the resonator inductance per unit length L_l, which is the sum of the magnetic inductance $L_\mathrm{l,mag}$ and the kinetic inductance per unit length $L_\mathrm{l,kin}$:

$$L_\mathrm{l} = L_\mathrm{l,mag} + L_\mathrm{l,kin} \tag{4.43}$$

While the magnetic (geometric) inductance can be associated with the magnetic energy stored in a conductor in the presence of a current, the kinetic inductance origins from the energy stored in the motion of the charge carriers. Although $L_\mathrm{l,mag}$ depends on the resonator geometry, it cannot be increased significantly. For the resonator in section 4.2 we estimate $L_\mathrm{l,geom} \approx 1\,\mathrm{pH}/\mu\mathrm{m}$ (Mc Mahill, 2009), which is on the same order of magnitude for a submicron width w of the center conductor. In contrast to the magnetic inductance, the kinetic inductance allows to increase L_l significantly. While $L_\mathrm{l,kin}$ is negligible for a normal conductor compared to the magnetic inductance since electron transport is dominated by scattering, it can become the dominant contribution in a superconductor.

In particular the high kinetic inductance of submicron sized thin wires of a:InO (Dupré et al., 2017), AlO_x (Rotzinger et al., 2017, Zhang et al., 2019), NbN (Niepce et al., 2019), NbTiN (Samkharadze et al., 2016) and TiN (Coumou et al., 2013) have been used to build high impedance microwave resonators with $Z_r \gg 1\,\mathrm{k}\Omega$ and Q_{int} of the order of 10^4 at the level of single photons. A superconducting wire of width w, length l and superconducting gap Δ_{sc} has the kinetic inductance (Annunziata et al., 2010)

$$L_{\mathrm{l,kin}} = \frac{R_{\square}\hbar}{\pi w \Delta_{\mathrm{sc}}} \frac{1}{\tanh(\frac{\Delta_{\mathrm{sc}}}{2k_{\mathrm{B}}T})}, \tag{4.44}$$

which becomes large for a disordered superconductor due to its high normal state sheet resistance per square $R_{\square}$. Note that for the $h \approx 200\,\mathrm{nm}$ thick CPW Al resonator in section 4.2 disorder is small and $L_{\mathrm{l,kin}}$ is negligible (Göppl et al., 2008). In subsection 4.3.1 we present a high impedance $\lambda/2$ CPW resonator fabricated with a narrow center conductor from a thin film of NbTiN.

Another method to engineer a high kinetic inductance in superconductors relies on the use of the Josephson inductance of a Josephson junction, which provides a local (almost point-like) kinetic inductance of the order of $1\,\mathrm{nH}/\mu\mathrm{m}^2$ (Devoret et al., 2005). An array of Josephson junctions can be used to build a high impedance microwave resonator (Masluk et al., 2012). If SQUIDs are used instead of Josephson junctions, the inductance per unit length and consequently the resonance frequency is tunable via an external magnetic flux (Altimiras et al., 2013, Stockklauser et al., 2017) threading the SQUIDs. The single-photon quality factor and characteristic impedance for these resonators are comparable to the values quoted above for the narrow and thin wire resonators. We introduce this resonator type in subsection 4.3.2.

4.3.1 NbTiN coplanar waveguide $\lambda/2$ resonator

In subsections 4.3.1.1 and 4.3.1.2 we present the design and fabrication of a high impedance NbTiN resonator that is used for the experiments in chapters 6-7. In subsection 4.3.1.3 we characterize test resonator structures with different geometries at different temperatures. We also compare the measurements with a simulation model. Finally we discuss the resonator magnetic field resilience in subsection 4.3.1.4.

4.3.1.1 Resonator design

A schematic and an optical micrograph of the resonator is shown in Fig. 4.6. It is a $\lambda/2$ resonator in a CPW geometry that is patterned as a $h \approx 15\,\mathrm{nm}$ thick film of NbTiN on top of a commercially available GaAs substrate. Note that if a 2DEG is required on the chip, the GaAs is replaced by the heterostructure, which has to be etched in

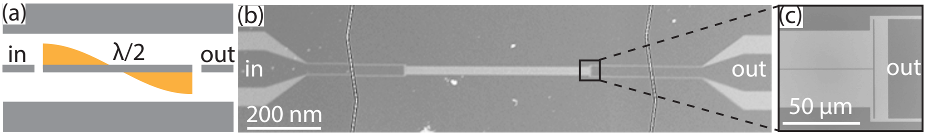

Figure 4.6 NbTiN test resonator design. (a) $\lambda/2$ coplanar-waveguide type resonator that couples capacitively to input (in) and output (out) transmission lines. (b) False-colored optical micrograph of the resonator from (a), which is patterned as a NbTiN layer (dark gray) on top of GaAs (light gray). (c) Zoom into the region outlined with a black square in (b).

the resonator region as it was discussed in section 4.2. The center conductor of the resonator has a width that is of the order of hundreds of nanometers in order to provide a high kinetic inductance (see subsection 4.3). The resonator length is of the order of $l \approx 1\,\mathrm{mm}$ and is separated by $s \approx 25\,\mu\mathrm{m}$ from the resonator ground planes. This distance is larger by a factor of ≈ 3.5 compared to the $50\,\Omega$ resonator in section 4.2, which also contributes to an increase of $\mathrm{Z_r} \propto 1/\sqrt{\mathrm{C_l}}$ since $\mathrm{C_l}$ is reduced. As indicated in Fig. 4.6(c), we use a t-shaped capacitor geometry to couple the resonator capacitively to input and output transmission lines that are designed as $\mathrm{Z_{port}} \approx 50\,\Omega$.

4.3.1.2 Resonator fabrication

For details about the fabrication process we refer to Appendix C.3. We sputter NbTiN from a NbTi target in an argon(Ar)/nitrogen(N) atmosphere on top of GaAs. We then pattern the resonator structure using electron beam lithography (EBL) with a positive resist. As shown in Fig. 4.7(a) the developed resist covers the resonator center conductor, the transmission lines as well as the ground planes. Since the center conductor is of submicron width and millimeter length, we expose the resist using a 100 keV EBL system with automatic proximity correction and a laser-interferometer controlled stage. In the next step, we remove the NbTiN in the regions that are not covered by the resist using reactive ion etching (RIE) with a sulfur hexafluoride (SF_6) plasma.

In the regions that were not covered by the resist during etching we observe an undesired irregular structure in the SEM image in Fig. 4.7(b), which was absent before the RIE processing steps. This structure cannot be removed by cleaning with organic solvents or water or by modifying the RIE process parameters such as changing the power, the gas pressure or adding Ar to the plasma. We therefore further investigate

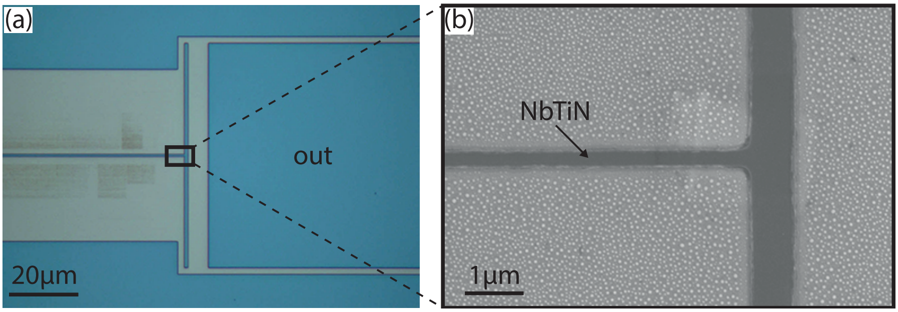

Figure 4.7 NbTiN resonator during processing. (a) Optical micrograph of a resonator region similar to Fig. 4.6 (c) after the reactive ion etching. NbTiN on a GaAs substrate is covered with resist (blue). (b) SEM image of the area marked with a black rectangle in (a).

the topography of this structure to find out whether it is etched into the bare GaAs or whether it is a material deposited on top of GaAs. If the latter was not superconducting, it would be a potential loss channel for the resonator photons.

We prepattern test samples with a photolithography mask such that the samples contain two different regions: NbTiN sputtered on GaAs and bare GaAs. Subsequently we etch these samples while protecting them partially with a resist layer. In the protected region, which is for $y < 0$ in Fig. 4.8(a), we measure with an atomic force microscope (AFM) a film height of $h \approx 15\,\mathrm{nm}$ for NbTiN. In the etched (former NbTiN and bare GaAs) regions, the height signal is constant. In a magnified AFM image in Fig. 4.8(b) the undesired irregular structure is visible in both the former GaAs and NbTiN regions. We extract from the height profile [panel on the right in Fig. 4.8(b)], that this structure is both below and above the GaAs reference level (see $y < 0$). This suggests, that during the RIE step both etching of GaAs as well as redeposition of an unknown material compound on the GaAs surface occurs. This compound may contain elements from the SF_6 plasma as well as from GaAs and NbTiN. It likely contains elements from NbTiN, since we do not observe the irregular structure in a separate experiment, where we use the RIE process to etch a bare GaAs sample (without NbTiN). Further investigation for example with x-ray photoelectron spectroscopy is necessary to identify the material composition of the irregular structure. This could help to develop an etching or cleaning process for this structure.

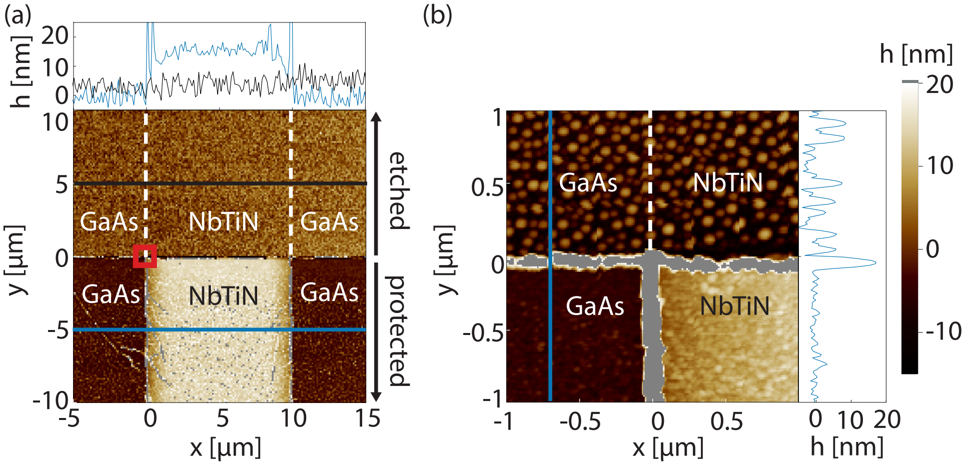

Figure 4.8 AFM of RIE etched NbTiN on GaAs. AFM measurement of the height $h(x, y)$ of a NbTiN structure on top of GaAs after etching. The structure was protected by a resist layer for $y < 0$ and etched for $y > 0$. The borders of the (former) NbTiN region that was exposed during the etching process are indicated by white dashed lines. Height data outside the color scale is shown in gray. (a) The top panel indicates cuts at y as depicted with horizontal lines in the bottom panel. (b) Magnified view of the area outlined with a red square in (a). The height profile in the panel on the right was measured along the vertical blue line.

4.3.1.3 Resonator characterization

In this section we present measurements of test resonators with different geometry parameters w and l that were fabricated in independent fabrication rounds. The resonance frequency is according to Eqns. (4.15) and (4.43) given as

$$\nu_\mathrm{r} = \frac{1}{2l\sqrt{\mathrm{L}_{\mathrm{kin},\square}\mathrm{C}_\mathrm{l}/w}}, \tag{4.45}$$

where we omitted the negligible contribution of the magnetic inductance and $\mathrm{L}_{\mathrm{kin},\square} = \mathrm{L}_{\mathrm{l,kin}}w$ is the kinetic inductance per square. Most of the measurements in this section are carried out in a dipstick setup at $\mathrm{T} \approx 5\,\mathrm{K}$. This measurement temperature is a significant fraction of the critical temperature of the NbTiN film of $\mathrm{T_c} \approx 9\,\mathrm{K}$[1]. As we will show below, the internal quality factor is likely limited by resistive losses due to

---

[1] We determined $\mathrm{T_c}$ for one NbTiN film in a 4-point measurement with a Physical Property Measurement System.

thermally excited quasi particles (Schuster, 2007). We nevertheless use the dipstick setup, which has a short cooling cycle compared to a dilution refrigerator, since the goal of the measurements presented in this section is a basic characterization of NbTiN test resonators and the reproducibility of their fabrication process in order to design a resonator with a desired resonance frequency ν_r and characteristic impedance Z_r.

The dipstick setup is equipped with a pair of RF lines without attenuation or amplification stages. We therefore use a resonator input power $P_\mathrm{in} \approx -75\,\mathrm{dBm}$ to measure the resonator transmission $|S_{21}|^2$ with a vector network analyzer. This input power is far above the single photon level (Göppl et al., 2008). We estimate an averaged number of photons $\bar{n} \approx 10^6$ with Eq. (4.41), which would in principle result in an enhanced quality factor compared to measurements at the single photon level, where the quality factor can be limited by parasitic two-level systems (TLSs) (Gao et al., 2008, O'Connell et al., 2008). This power dependence is however not relevant for the dipstick measurements, where the internal quality factor is likely limited by temperature. An exemplary resonator transmission spectrum for two different temperatures in the dipstick is shown in Fig. 4.9(a). Note that the transmission is corrected for the bare setup transmission in the absence of the resonator.
We observe the fundamental resonance as well as the second harmonic. By increasing T, the resonances shift to lower frequencies since $L_\mathrm{l,kin}$ increases with T according to Eq. (4.44). From a fit of Eq. (4.39) to the spectrum of the fundamental resonance in Fig. 4.9(b) we extract the resonator parameters ν_r, Q_int and Q_ld that are shown for various test resonators in Table 4.10. The table indicates that $Q_\mathrm{int} \ll 10^3$ for all test resonators measured in the dipstick setup.

To investigate the influence of temperature on Q_int, we measure one resonator that was previously measured in the dipstick in Fig. 4.9(a)-(b) also in a dilution refrigerator setup (Stockklauser, 2017) at $T \approx 10\,\mathrm{mK}$. This setup is similar to the one presented in chapter 2 and allows to probe the resonator transmission at the single photon level. The corresponding fundamental resonance in Fig. 4.9(c) is narrower compared to the higher temperature resonance of the same resonator in Fig. 4.9(b), where we obtained $Q_\mathrm{int}(4.8\,\mathrm{K}) \approx 720$ (see Table 4.10). Since the setup related transmission offset is not known for the dilution refrigerator setup, a Lorentzian fit to the resonance in Fig. 4.9(c) only allows to directly extract $Q_\mathrm{ld}(10\,\mathrm{mK}) \approx 890$ and $\nu_\mathrm{r} = 2.96\,\mathrm{GHz}$. We calculate $Q_\mathrm{int}(10\,\mathrm{mK}) = [1/Q_\mathrm{ld} - 1/Q_\mathrm{int}]^{-1}(10\,\mathrm{mK})$ by converting $Q_\mathrm{ext}(4.8\,\mathrm{K}) \approx 1310$ obtained from the Fig. 4.9(b) fit to $Q_\mathrm{ext}(10\,\mathrm{mK}) \approx 1230$ using $Q_\mathrm{ext} \propto 1/(\sqrt{L_{\mathrm{kin},\square}}\,\nu_r^2)$ according to Eqns. (4.40) and (4.45). Note that we explain the extraction of $L_{\mathrm{kin},\square}$ below. We

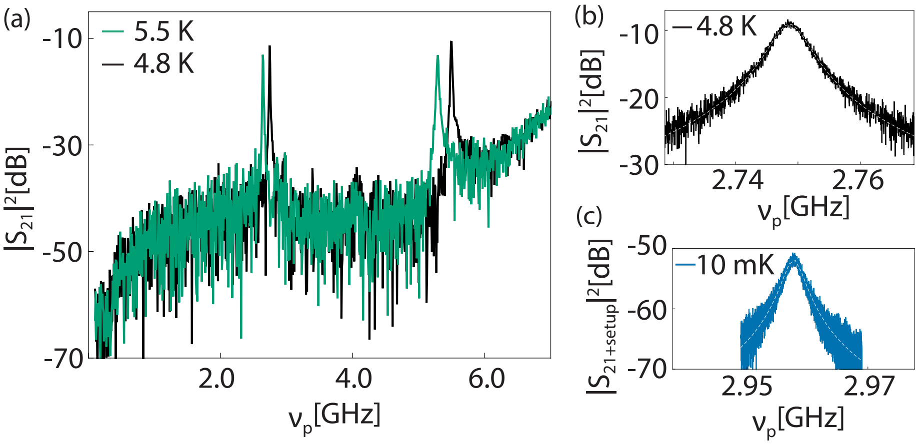

Figure 4.9 Test resonator spectral response. Frequency spectrum of NbTiN test resonator sample 1 (see Table 4.10). (a) Transmitted power $|S_{21}|^2$ as a function of probe frequency ν_p for two different temperatures. (b) Fundamental resonance from (a) with Lorentzian fit (dashed line). (c) Spectrum around the fundamental resonance frequency measured in a dilution refrigerator with a base plate temperature of 10 mK. The frequency range for ν_p is the same as in (b). We indicate $|S_{21+\mathrm{setup}}|^2$, which is the transmitted power that is not corrected for an (unknown) offset due to the experimental setup.

obtain[2] $Q_{\mathrm{int}}(10\,\mathrm{mK}) \approx 3220 \gg Q_{\mathrm{int}}(4.8\,\mathrm{K}) \approx 720$. This supports our claim, that Q_{int} is limited by temperature for the dipstick measurement.

# s	# fab	$l\,[\mu\mathrm{m}]$	$w\,[\mathrm{nm}]$	T [K]	ν_r [GHz]	Q_{ld}	Q_{int}	$L_{\mathrm{kin},\square}$ [pH]	Z_r [kΩ]
1	1	2105	350	4.8	2.75	470	720	40	1.3
1	1	2105	350	0.01	2.96	890	3220	34	1.2
2	1	1710	350	5.7	3.28	310	410	42	1.3
3	2	1206	590	5.0	5.47	240	330	47	1.1
4	2	1206	366	5.2	4.37	220	340	47	1.4
5	3	1124	145	4.7	3.06	350	580	49	2.3
6	4	1124	60	4.8	1.96	470	620	47	3.5

Figure 4.10 Test resonators parameter table. Resonator parameters ν_r, Q_{int} and Q_{ext} are extracted from measurements, $L_{\mathrm{kin},\square}$ and Z_r are obtained from simulations (see text). The table indicates parameters for multiple samples (s) and fabrication (fab) rounds measured in a dipstick ($T \approx 5$ K) and dilution refrigerator ($T \approx 10$ mK) setup.

---

[2] If we assume an error for the calibration of the dipstick setup transmission of ±1 dB, we calculate $2200 \lesssim Q_{\mathrm{int}} \lesssim 3700$.

The maximal $Q_{int} \approx 3220$ in Table 4.10 is well below 10^4, which was instead reported for $50\,\Omega$ Al CPW resonators fabricated on GaAs in Ref. Frey, 2013. There, $Q_{int} \approx 10^4$ was found as an upper limit and attributed to the piezoelectricity of GaAs, which causes resonator losses by phonon excitations. Although a systematic study of $Q_{int}(10\,\mathrm{mK})$ for multiple NbTiN resonators would be necessary for a fully conclusive statement that $Q_{int} \ll 10^4$ for the NbTiN resonators, we would like to discuss possible origins for the reduced Q_{int} in the case of NbTiN compared to Al resonators. One potential source of dissipation is the irregular structure of an unknown material compound that was discussed in subsection 4.3.1.2. In addition, the material quality of the NbTiN film can have a notable influence on Q_{int} (Burnett et al., 2017). Since the film is sputtered in a system which is used for various different materials, including magnetic materials, impurities in the film can cause local non-superconducting regions in the resonator center conductor or in the ground planes that lead to dissipation. Note that in principle high quality NbTiN films can be fabricated that allow for $Q_{int} \gg 10^4$ as demonstrated in Ref. Samkharadze et al., 2016 for high impedance NbTiN resonators with a similar geometry as in this thesis.

We perform microwave simulations with *Sonnet* to reproduce the measured ν_r for the test resonators in Table 4.10 by adjusting $L_{kin,\square}$ for every resonator. We observe a maximum deviation of $L_{kin,\square}$ between the fabrication rounds of about 20%, which we suspect to be mainly due to a physical difference in the NbTiN films. While reproducibility is challenging for thin disordered films (Kroll et al., 2018), recent experiments in our group with a sputtering system dedicated for Nb and NbTiN indicate a significant increase in the reproducibility of $L_{kin,\square}$.

Finally, we discuss the characteristic impedance Z_r of the resonators, which is calculated in Table 4.10 as $Z_r = 2\nu_r L_{kin,\square} l/w$ using Eqns. (4.13) and (4.45). The NbTiN test resonators in the table are high impedance with a maximum $Z_r \approx 3.5\,\mathrm{k}\Omega$ for $w \approx 60\,\mathrm{nm}$. Note that Z_r is temperature dependent since $L_{kin,\square}$ depends on Δ_{sc} according to Eq. (4.44). We use the approximation (Sigrist, 2016)

$$\Delta_{sc}(T) \approx \Delta_{sc}(0)\tanh\left(1.74\sqrt{(T_c - T)/T}\right) \tag{4.46}$$

with $\Delta_{sc}(0) = 1.76 k_B T_c$ to obtain $L_{kin,\square}(50\,\mathrm{mK})/L_{kin,\square}(4.8\,\mathrm{K}) = 0.84$. This ratio is equivalent to the resonance frequency ratio $[\nu_r(4.8\,\mathrm{K})/\nu_r(50\,\mathrm{mK})]^2$ [see Eq. (4.45)], for which we calculate 0.86 for sample 1 in Table 4.10 in good agreement with the theoretical value of 0.84. The resonator impedance therefore decreases for the measurement in a dilution refrigerator compared to the dipstick measurement by about

10%.

Above characterization measurements demonstrate that we can fabricate high impedance NbTiN resonators with $L_{\mathrm{kin},\square}$ and Z_r comparable to values for similar resonators reported in literature (Samkharadze et al., 2016, 2018). In addition, the reproducibility of the fabrication allows to sufficiently target Z_r and ν_r with the resonator design.

4.3.1.4 Resonator magnetic field dependence

In this section we discuss the dependence of the resonance frequency and quality factor of a NbTiN resonator on a parallel external magnetic field. The data presented in this section is obtained for the resonator that is employed for the experiments in chapter 6. The resonator design is similar to the design of the test resonators above. The measurements were performed with a single axis magnet at $T \approx 10\,\mathrm{mK}$ in the setup from chapter 2. At zero magnetic field, we measure a resonance frequency $\nu_r = 8.33\,\mathrm{GHz}$ and a loaded quality factor $Q_{\mathrm{ld}} \approx 80$ ($\kappa_r/(2\pi) = 101\,\mathrm{MHz}$). Possible explanations for the significant reduction of Q_{ld} compared to the test resonator characterization measurements in subsection 4.3.1.3 are discussed in subsection 6.1.1.

By applying a magnetic field to a type-II superconductor such as NbTiN, regions of normal conductance that are surrounded by a supercurrent are induced[3]. If free to move, these vortices cause dissipation at microwave frequencies. The generation of vortices is suppressed for parallel field alignment if the extent of the film in the direction of the field is much smaller than the penetration length λ (Kuit et al., 2008, Samkharadze et al., 2016, Kroll et al., 2018). This situation applies to the center conductor of the NbTiN resonator, which has a width of $w \approx 300\,\mathrm{nm}$. Since $R_\square$ is not known for the NbTiN film, we use $\lambda = \sqrt{\hbar R_\square h/[\pi\mu_0\Delta_{\mathrm{sc}}(0)]}$ (Kroll et al., 2018) together with Eq. (4.44) to obtain the penetration length $\lambda \approx \sqrt{L_{\mathrm{kin},\square} h/\mu_0} \approx 730\,\mathrm{nm}$, with the estimated $L_{\mathrm{kin},\square} \approx 45\,\mathrm{pH}/\square$, the film thickness $h \approx 15\,\mathrm{nm}$ and the vacuum permeability μ_0.

By ramping a magnetic field B that is applied approximately parallel to the sample from 0 to 2 T, we observe a reduction of Q_{ld} by about 35% in Fig. 4.11(a). While the resonance can still clearly be resolved at $B = 2\,\mathrm{T}$, better magnetic field resilience has been reported for thin film NbTiN resonators in Refs. Samkharadze et al., 2016, Kroll et al., 2018. We suspect that the decrease of Q_{ld} in Fig. 4.11(a) has two origins.

---

[3] Note that also films of type-I superconductors support vortex nucleation. This requires that the coherence length of the bulk material exceeds the film thickness and that the magnetic field is applied perpendicular to the film (Song et al., 2009).

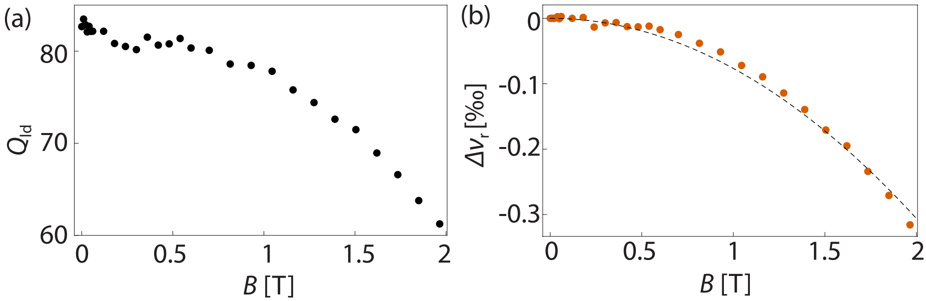

Figure 4.11 Resonator magnetic field dependence. Dependence of the loaded quality factor Q_{ld} in (a) and the relative resonance frequency shift $\Delta\nu_r$ (see text) in (b) on a parallel external magnetic field B.

First, dissipation can be induced by vortices that are generated in the resonator ground planes. Second, the magnetic field is likely not aligned perfectly parallel with respect to the resonator since a single axis magnet is used. By increasing the distance to the ground planes (Samkharadze et al., 2016), by engineering artificial pinning sites in the ground planes (Kroll et al., 2018) or by using a three-axis magnet to achieve a better B-field alignment, we expect the magnetic field resilience to improve.

We also measure the relative resonance frequency shift $\Delta\nu_r \equiv [\nu_r(B) - \nu_r(B = 0)]/\nu_r(B = 0)$ as a function of parallel magnetic field in Fig. 4.11(b). Since quasiparticles are induced in a magnetic field, the Cooper pair density n_c is reduced with increasing B. This leads to an enhancement of $L_{kin,\square} \propto 1/n_c$ (Meservey et al., 1969) and therefore to a reduction of $\nu_r \propto 1/\sqrt{L_{kin,\square}}$ with increasing B. The magnetic field dependence can be modelled with $\Delta\nu_r = -\frac{\pi}{48}h^2e^2D/(\hbar k_B T_c)B^2$ (Samkharadze et al., 2016), where e is the elementary charge and D the quasiparticle diffusion constant (Day et al., 2003). We observe good agreement of this model with the data in Fig. 4.11(b) for $D \approx 0.3\,\mathrm{cm^2s^{-1}}$, which is similar to previously reported values in Refs. Semenov et al., 2006, Samkharadze et al., 2016, Kroll et al., 2018.

4.3.2 Al SQUID array $\lambda/4$ resonator

In this section we provide a brief introduction to the high impedance SQUID array resonator that is used for the experiments presented in chapter 8. For more details we refer to Ref. Stockklauser, 2017, where the design, characterization and theoretical background of a SQUID array resonator with very similar parameters is discussed.

4.3.2.1 Resonator design

The resonator is illustrated in Fig. 4.12. It is fabricated with a 30 keV EBL system by using a bilayer resist and depositing 35 nm and 110 nm of Al in a shadow evaporation process. Fabrication details are given in Appendix C.2. The resonator consists of a linear array of 34 SQUIDs that is shunted to ground at one end and capacitively coupled to a read-out port at the other open end. Note that the SQUID array is also capacitively coupled to two qubits at the open end, which will be relevant in chapter 8. The resonator can be modeled as a distributed element $\lambda/4$ resonator as demonstrated in Ref. Stockklauser, 2017. Due to the nonlinear current dependence of the Josephson inductance [see Eq. (3.24)], the resonator exhibits a dependence on the SQUID array current, i.e. on the number of photons in the resonator. For the resonator operation in this thesis with an average photon number $\bar{n} \ll 1$, the SQUID array Hamiltonian for the fundamental mode can be approximated by the single mode harmonic oscillator Hamiltonian in Eq. (4.16) (Stockklauser, 2017).

To estimate the SQUID array characteristic impedance, we model the resonator as a distributed element with total in-line inductance $L_l l$ and capacitance $C_l l$ to ground per unit length. We obtain $L_l l \approx 30\,\mathrm{nH}$ from the room temperature resistance of a SQUID array resonator with the same fabrication process parameters and extract $C_l l = 16\,\mathrm{fF}$ from an electrostatic simulation. This results in $Z_r = \sqrt{L_l/C_l} \approx 1.37\,\mathrm{k\Omega}$, which is a rough estimate for the minimum characteristic impedance. Note that the inductance of a SQUID [see Eq. (3.27)] and consequently Z_r increases in the presence of an external magnetic flux.

We estimate the SQUID array resonance frequency ν_r by modeling it close to resonance as lumped element resonator with inductance $L = 8lL_l/\pi^2$ and capacitance $C = C_l l/2$ (valid for a $\lambda/4$ resonator)(Castellanos-Beltran, 2002). We now consider

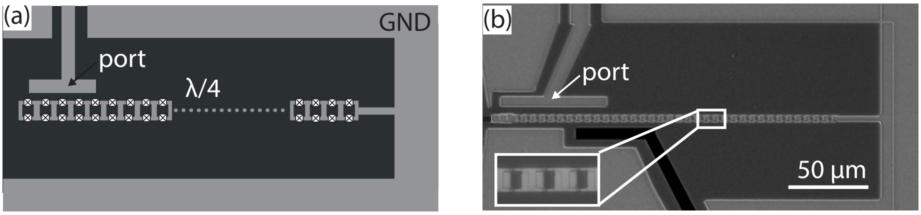

Figure 4.12 SQUID array resonator. Schematic illustration (a) and false-colored optical micrograph (b) of a SQUID array resonator that is connected to ground (GND) at one end and capacitively coupled to a port at the other end. The regions marked in black will be relevant in chapter 8.

the capacitive coupling of the SQUID array to the probe line as well as to the qubits, which gives rise to an extra localized capacitance $C_{exc} \approx 11.1\,\mathrm{fF}$ that adds up to C in the lumped element model. The resonance frequency can therefore be approximated as $\nu_r \approx 1/[2\pi\sqrt{L(C+C_{exc})}] \approx 7.38\,\mathrm{GHz}$. This is an estimate for the maximum resonance frequency of the SQUID array resonator, since the SQUID inductance increases and hence ν_r decreases by applying an external magnetic flux.

4.3.2.2 Resonator characterization

We measure the SQUID array resonator reflectance spectrum in Fig. 4.13(a) as a function of an external magnetic flux Φ_{cr} and observe for every value of flux a minimum in $|S_{11}|$ once the probe frequency ν_p is on resonance with the SQUID array resonator ($\nu_p = \nu_r$). The resonance frequency changes as a function of magnetic flux and reaches a maximum at $\nu_p \approx 6.5\,\mathrm{GHz}$ in reasonable agreement with above rough theoretical estimate. Note that ν_r can be further decreased below $\nu_r \approx 5.7\,\mathrm{GHz}$ observed in Fig. 4.13(a) by increasing the flux range (see chapter 8).

Since we operate the SQUID array resonator in regime where only the fundamental mode is relevant, its reflectance spectrum is identical to the single-port cavity spectrum derived in subsection 4.1.2. Analog to the $50\,\Omega$ Al resonator we use Eq. (4.42), which also considers the experimental setup, to fit to the SQUID array resonator S_{11} reflectance spectrum. The comparison for the amplitude and phase of S_{11} in Fig. 4.13(c) is best fit for $\nu_r = 5.894\,\mathrm{GHz}$, $\kappa_{ext}/(2\pi) = 2.4\,\mathrm{MHz}$ ($Q_{ext} \approx 2460$) and $\kappa_{int}/(2\pi) = 4.6\,\mathrm{MHz}$ ($Q_{ext} \approx 1280$).

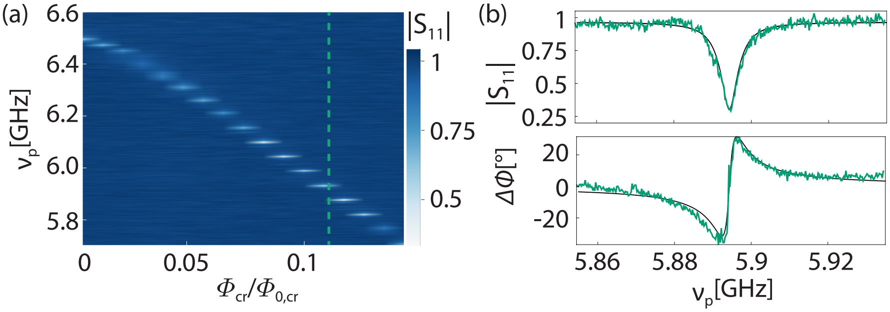

Figure 4.13 SQUID array resonator reflectance spectrum. (a) Reflected amplitude $|S_{11}|$ as a function of global magnetic flux Φ_{cr} normalized by the SQUID array flux periodicity $\Phi_{0,cr}$. (b) Amplitude and phase response of the resonator (green) with theory fit (black) at the position indicated with a dashed line in (a).

4.4 Conclusion and outlook

We presented three different types of superconducting microwave resonators in this chapter. The $50\,\Omega$ Al coplanar waveguide resonator as well as the high impedance SQUID array resonator were adapted from prior work. The NbTiN resonator, for which the design and fabrication was developed in this work, was found to provide a quality factor of the order of 10^3 at mK temperatures and a magnetic field resilience in a parallel field of up to $2\,\mathrm{T}$. The quality factor is potentially limited by fabrication residues as well as by the material quality of the NbTiN film. While the latter issue is already addressed in ongoing work with a new sputter system, further optimization of the fabrication process is necessary. The magnetic field resilience can possibly be improved by designing vortex pinning sites (Kroll et al., 2018) and by optimizing the magnetic field alignment with respect to the sample.

Chapter 5

Hybrid circuit quantum electrodynamics

The interaction between the quantized electromagnetic field and charged matter quantum systems, presented in chapter 3, is described with quantum electrodynamics (Walls et al., 2008). In cavity quantum electrodynamics (cavity QED) this interaction is realized by positioning the quantum system inside a cavity. There, the cavity confines the electromagnetic field at the level of single photons and restricts the number of allowed modes. Cavity QED experiments were pioneered with atoms and photons in either the microwave (Raimond et al., 2001) or the optical (Mabuchi et al., 2002) domain.

The magnitude of the interaction in cavity QED is characterized by the coupling rate between light and matter. If this rate exceeds the rate of the decoherence mechanisms in both sub-systems, the system is in the strong coupling regime. As a result, a coherent light-matter state is formed once qubit and cavity are on resonance (Thompson et al., 1992). Even in the dispersive regime, the cavity experiences a frequency shift that depends on the state of the atoms (Blais et al., 2004). The strong coupling regime is therefore appealing not only for the study of quantum effects at a fundamental level but also in the context of quantum information processing (Mabuchi et al., 2002).

In this thesis we use a solid state analog of cavity QED, which combines the quantum systems presented in chapters 3 and 4. The corresponding chip design is shown for the case of a double-sided superconducting transmission line resonator and a single qubit in Fig. 5.1. The qubit is ideally placed at the anti-node of the voltage standing mode in the resonator in order to maximize the electric dipole coupling strength between the resonator vacuum fluctuations and the qubit states. This design was proposed (Blais et al., 2004) and first experimentally realized (Wallraff et al., 2004) using superconducting circuits as the qubit (superconducting qubit), where it is referred to as circuit QED architecture. In case qubits other than superconducting qubits are employed, the term hybrid circuit QED is commonly used (Burkard et al., 2019).

In the first part of this chapter we present the theoretical framework of hybrid circuit QED that is necessary to understand the experiments in chapters 6-8. We thereby start in section 5.1 by deriving the corresponding interaction Hamiltonians for the three different types of solid state qubits used in this thesis. We then introduce in section 5.2 two Hamiltonians that describe the system in Fig. 5.1 in the absence of decoherence in the case of one or two qubits coupled to the same resonator. While the first situation applies to the experiments in chapters 6 and 7, the latter case will be relevant in chapter 8.

In the second part of this chapter we provide in section 5.3 a brief introduction into theoretical models that include dissipative interactions with the environment. For resonator photons, this interaction consists of an engineered coupling rate to the resonator ports and an internal photon loss rate. For the qubits, the random fluctuations of the environment result in qubit decoherence, i.e. a randomization of the phase relation between the qubit states (Burkard, 2001). Decoherence mechanisms for the three different qubits used in this work are discussed in section 5.4 with a focus on the RX qubit.

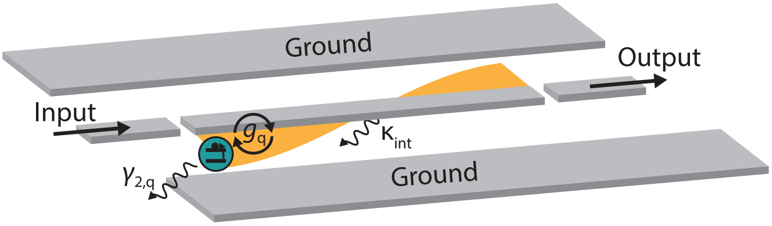

Figure 5.1 Circuit QED architecture. Schematic illustration of an exemplary chip design that is used for circuit QED experiments (Blais et al., 2004). A qubit (green) couples at rate g_q to the voltage fluctuations (yellow) at one end of a superconducting transmission line resonator (gray), which has extended ground planes. Dissipation is indicated as a qubit decoherence rate $\gamma_{2,q}$ and a cavity decay rate κ_{int}. Input and output transmission lines connect the system to the external circuitry.

5.1 Qubit-resonator coupling

In this section we first derive a general Hamiltonian for the electric dipole interaction between a qubit and the vacuum fluctuations of the resonator electric field. Subsequently we treat the specific case of a charge qubit, a RX qubit and a transmon.

The interaction between the qubit electric dipole moment and the cavity electric field is described by (Srinivasa et al., 2016)

$$\hat{\mathrm{H}}_{\mathrm{q,int}} = -\hat{\mathbf{d}} \cdot \hat{\mathbf{E}} \tag{5.1}$$

with the dipole operator $\hat{\mathbf{d}}$ and the cavity electric field operator $\hat{\mathbf{E}} = \mathbf{E}_{\mathrm{ZPF}}(\hat{a} + \hat{a}^{\dagger})$. The magnitude of the electric field $|\mathbf{E}_{\mathrm{ZPF}}|$ at the qubit is proportional to the voltage vacuum fluctuations $\mathrm{V}_{\mathrm{ZPF}}$ of the fundamental mode in the resonator. The electric field can drive the transition between the qubit ground state $|0_{\mathrm{q}}\rangle$ and excited state $|1_{\mathrm{q}}\rangle$ at a rate given by the coupling strength (Girvin, 2014)

$$g_{\mathrm{q}} \equiv 1/\hbar \, \langle 0_{\mathrm{q}}| \, \hat{\mathbf{d}} \cdot \mathbf{E}_{\mathrm{ZPF}} \, |1_{\mathrm{q}}\rangle \, . \tag{5.2}$$

We use Eq. (5.2) to write the Hamiltonian in Eq. (5.1) as

$$\hat{\mathrm{H}}_{\mathrm{q,int}} = \hbar g_{\mathrm{q}} (\hat{a} + \hat{a}^{\dagger}) \hat{\sigma}_x , \tag{5.3}$$

with $\hat{\sigma}_x = |0_{\mathrm{q}}\rangle \langle 1_{\mathrm{q}}| + |1_{\mathrm{q}}\rangle \langle 0_{\mathrm{q}}|$. Since the qubit frequencies by far exceed the coupling strengths in our experiments ($\omega_{\mathrm{q}} \gg g_{\mathrm{q}}$), we perform a rotating wave approximation (RWA) that simplifies Eq. (5.3) to

$$\hat{\mathrm{H}}_{\mathrm{q,int}} = \hbar g_{\mathrm{q}} (\hat{a} \hat{\sigma}_+ + \hat{a}^{\dagger} \hat{\sigma}_-) \tag{5.4}$$

with the qubit raising operator $\hat{\sigma}_+ = (\hat{\sigma}_x + i \hat{\sigma}_y)$ and the lowering operator $\hat{\sigma}_- = (\hat{\sigma}_x - i \hat{\sigma}_y)$. In the following subsections we derive an interaction Hamiltonian of this form for the charge qubit and the RX qubit as well as for the transmon.

Note that we introduced high impedance resonators in section 4.3 as they have strong voltage vacuum fluctuations $\mathrm{V}_{\mathrm{ZPF}} \propto \sqrt{\mathrm{Z}_{\mathrm{r}}}$ and, consequently, a high qubit-photon coupling strength. This implication is quantified in Eq. (5.2), where $g_{\mathrm{q}} \propto |\mathbf{E}_{\mathrm{ZPF}}|$.

5.1.1 Double quantum dot charge qubit-resonator coupling

We realize a coupling of charge qubit and resonator photons by electrically connecting the left plunger gate to the resonator as depicted in Fig. 5.2. The resonator voltage fluctuations therefore couple via the detuning parameter to the qubit. This coupling is described by the Hamiltonian (Srinivasa et al., 2016)

$$\hat{\hat{\mathrm{H}}}_{\mathrm{int,CQ}} = \hbar g_{\mathrm{CQ}}^{(0)}(\hat{a}+\hat{a}^{\dagger})(\hat{n}_{\mathrm{L}}-\hat{n}_{\mathrm{R}}), \tag{5.5}$$

with the left and right quantum dot number operators $\hat{n}_{\mathrm{L}}$ and $\hat{n}_{\mathrm{R}}$, respectively. By rewriting Eq. (5.5) in the charge qubit eigenbasis $\{|0_{\mathrm{CQ}}\rangle, |1_{\mathrm{CQ}}\rangle\}$ and performing a RWA we obtain the interaction Hamiltonian in the form (Stockklauser, 2017)

$$\hat{\mathrm{H}}_{\mathrm{int,CQ}} = \hbar g_{\mathrm{CQ}}^{(0)} \sin(\theta)(\hat{a}^{\dagger}\hat{\sigma}_{-}+\hat{a}\hat{\sigma}_{+}). \tag{5.6}$$

We now relate the charge qubit coupling strength $g_{\mathrm{CQ}}^{(0)}$ to the electrostatics of the DQD by following Ref. Koski, 2019. Among others this gives experimental access to the coupling strength by choosing a certain DQD gate design. We consider the DQD and its gate lines as capacitively coupled metallic objects. The electrostatic energy of the DQD can then be written as (Wiel et al., 2002)

$$\mathrm{E}_{\mathrm{DQD}}(n_{\mathrm{L}}, n_{\mathrm{R}}) = \mathrm{U}_{\mathrm{L}}(n_{\mathrm{L}}-n_{\mathrm{gL}})^2 + \mathrm{U}_{\mathrm{R}}(n_{\mathrm{R}}-n_{\mathrm{gR}})^2 + \mathrm{U}_{\mathrm{LR}}(n_{\mathrm{L}}-n_{\mathrm{gL}})(n_{\mathrm{R}}-n_{\mathrm{gR}}), \tag{5.7}$$

where $\mathrm{U}_{\mathrm{L(R)}}$ is the left (right) dot charging energy and U_{LR} describes the interdot charging energy. In analogy to the electrostatic terms in the Hubbard Hamiltonian in Eq. (3.8), $n_{\mathrm{gL(R)}}$ is the gate number that quantifies the charge induced on the left (right) quantum dot by capacitive coupling to the gate potentials. We can therefore

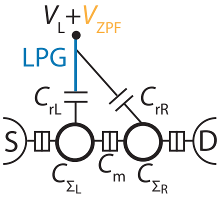

Figure 5.2 Charge qubit-resonator coupling. Schematic illustration of the coupling of the resonator zero-point voltage fluctuations $\mathrm{V}_{\mathrm{ZPF}}$ via the left plunger gate (blue) to the DQD. Note that only capacitances that are relevant for the derivation in the text are labelled.

express the qubit detuning parameter as

$$\delta = \mathrm{E}_{\mathrm{DQD}}(n_{\mathrm{L}}+1, n_{\mathrm{R}}-1) - \mathrm{E}_{\mathrm{DQD}}(n_{\mathrm{L}}, n_{\mathrm{R}}). \tag{5.8}$$

The charging energies relate to the capacitances of the system via the equality

$$\begin{pmatrix} \mathrm{U_L} & \mathrm{U_{LR}}/2 \\ \mathrm{U_{LR}}/2 & \mathrm{U_R} \end{pmatrix} = \frac{e^2}{2} \begin{pmatrix} \mathrm{C}_{\Sigma_\mathrm{L}} & -\mathrm{C_m} \\ -\mathrm{C_m} & \mathrm{C}_{\Sigma_\mathrm{R}} \end{pmatrix}^{-1}, \tag{5.9}$$

where $\mathrm{C_m}$ is the interdot capacitance and $\mathrm{C}_{\Sigma_{\mathrm{L(R)}}}$ the total left (right) dot capacitance, which includes the respective dot capacitances to the reservoirs and the gates as well as $\mathrm{C_m}$. We solve Eq. (5.9) and obtain $\mathrm{U_{L(R)}} = e^2 \mathrm{C}_{\Sigma_{\mathrm{R(L)}}}/[2(\mathrm{C}_{\Sigma_\mathrm{L}}\mathrm{C}_{\Sigma_\mathrm{R}} - \mathrm{C_m^2})]$ as well as $\mathrm{U_{LR}} = e^2\mathrm{C_m}/(\mathrm{C}_{\Sigma_\mathrm{L}}\mathrm{C}_{\Sigma_\mathrm{R}} - \mathrm{C_m^2})$. A voltage V on the left plunger gate couples via the capacitances $\mathrm{C_{rL(R)}}$ (see Fig. 5.2) to $n_{\mathrm{gL(R)}}$. We write this capacitive coupling as

$$n_{\mathrm{gL(R)}} = -\mathrm{C_{rL(R)}}\mathrm{V}/|e|. \tag{5.10}$$

The influence of the resonator voltage fluctuations on δ is therefore given as

$$\Delta\delta(\mathrm{V_{ZPF}}) \equiv \delta(\mathrm{V} = \mathrm{V_{ZPF}}) - \delta(\mathrm{V} = 0). \tag{5.11}$$

We calculate this quantity for the ideal case of equal quantum dots ($\mathrm{C}_\Sigma = \mathrm{C}_{\Sigma_{\mathrm{L(R)}}}$) by inserting Eqns. (5.7)-(5.10) into Eq. (5.11). We obtain

$$\Delta\delta(\mathrm{V_{ZPF}}) = \frac{\mathrm{C_{rL}} - \mathrm{C_{rR}}}{\mathrm{C}_\Sigma + \mathrm{C_m}} e\mathrm{V_{ZPF}} = \alpha_\delta e \mathrm{V_{ZPF}}, \tag{5.12}$$

where α_δ is the left plunger gate lever arm on the detuning. Finally, we express the coupling strength in terms of the capacitances:

$$g_{\mathrm{CQ}}^{(0)} = \frac{e}{\hbar}\alpha_\delta \mathrm{V_{ZPF}} = \frac{e}{\hbar}\frac{\mathrm{C_{rL}} - \mathrm{C_{rR}}}{\mathrm{C}_\Sigma + \mathrm{C_m}} \mathrm{V_{ZPF}}. \tag{5.13}$$

We extract that the coupling strength is maximal for $\mathrm{C}_\Sigma = \mathrm{C_{rL}} + \mathrm{C_m}$ and $\mathrm{C_{rR}} = 0$, in which case $\alpha_\delta = 1/(1 + 2\mathrm{C_m}/\mathrm{C_{rL}})$.

5.1.2 RX qubit-resonator coupling

The RX qubit couples capacitively to the resonator in the same manner as the DQD charge qubit by extending the left plunger gate to the resonator. This is schematically illustrated in Fig. 5.3. The interaction Hamiltonian between the RX qubit and the resonator photons can be expressed as

$$\hat{\hat{\mathrm{H}}}_{\mathrm{int,RX}} = \hbar g^{(0)}_{\mathrm{c,RX}}(\hat{n}_{\mathrm{L}} - \hat{n}_{\mathrm{R}} + \upsilon\hat{n}_{\mathrm{M}})(\hat{a} + \hat{a}^{\dagger}), \tag{5.14}$$

where $\hat{n}_{\mathrm{L}}$, $\hat{n}_{\mathrm{M}}$ and $\hat{n}_{\mathrm{R}}$ are the left, middle and right quantum dot number operators, respectively. The term $g^{(0)}_{\mathrm{c,RX}}$ is the bare charge-photon coupling strength discussed below and the parameter υ accounts for cross capacitance-effects, i.e. tuning the left dot plunger gate potential affects both the left-right dot charge asymmetry ε as well as the middle dot detuning Δ. Note that the Hamiltonian in Eq. (5.14) is equivalent to the interaction Hamiltonian

$$\hat{\hat{\mathrm{H}}}^{*}_{\mathrm{int,RX}} = 2\hbar g^{(0)}_{\mathrm{c,RX}}(\hat{n}_{\mathrm{L}} + \alpha\hat{n}_{\mathrm{M}})(\hat{a} + \hat{a}^{\dagger}) \tag{5.15}$$

quoted in Ref. Landig et al., 2018 by omitting an irrelevant energy offset $g^{(0)}_{\mathrm{c,RX}}\mathbb{1}$ and using the definition $\alpha \equiv (\upsilon + 1)/2$.

For $\upsilon = 0$, Eq. (5.14) takes the same form as the DQD charge qubit Hamiltonian in Eq. (5.5) since the resonator only tunes ε. This motivates to express Eq. (5.14) in terms of the lever arms α_{ε} and α_{Δ} that quantify the left plunger gate coupling to ε and Δ:

$$\hat{\hat{\mathrm{H}}}_{\mathrm{int,RX}} = e\mathrm{V}_{\mathrm{ZPF}}\alpha_{\varepsilon}(\hat{n}_{\mathrm{L}} - \hat{n}_{\mathrm{R}} + \frac{\alpha_{\Delta}}{\alpha_{\varepsilon}}\hat{n}_{\mathrm{M}})(\hat{a} + \hat{a}^{\dagger}). \tag{5.16}$$

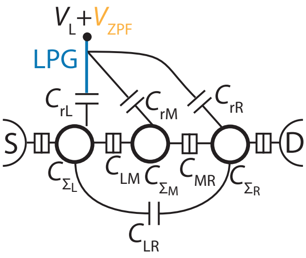

Figure 5.3 RX qubit-resonator coupling. Illustration of the capacitive coupling of $\mathrm{V}_{\mathrm{ZPF}}$ via the left plunger gate (blue) to the DQD. Relevant capacitances for the derivation in the text are indicated.

By comparing Eqns. (5.14) and (5.16) we find $\upsilon = \alpha_\Delta/\alpha_\varepsilon$ and therefore $\alpha = (\alpha_\Delta + \alpha_\varepsilon)/(2\alpha_\varepsilon)$ since $\alpha = (\nu + 1)/2$. We determine α_Δ and α_ε experimentally with the measurements presented in section 7.2 and obtain $\alpha = 0.4$.

In the following we relate the RX qubit interaction Hamiltonian to the TQD capacitances, i.e. we express α_Δ and α_ε in terms of the capacitances. We thereby follow the same approach as for the DQD charge qubit in subsection 5.1.1. The TQD electrostatic energy is given according to the Hubbard Hamiltonian from Eq. (3.8) as

$$\mathrm{E}(n_\mathrm{L}, n_\mathrm{M}, n_\mathrm{R}) = \sum_{i\in\{\mathrm{L,M,R}\}} \mathrm{U}_i(\hat{n}_i - n_{gi})^2 + \sum_{i\neq j} \mathrm{U}_{ij}(\hat{n}_i - n_{gi})(\hat{n}_q - n_{gj}). \tag{5.17}$$

The charging energies are defined via the capacitance matrix as

$$\begin{pmatrix} \mathrm{U_L} & \mathrm{U_{LM}}/2 & \mathrm{U_{LR}}/2 \\ \mathrm{U_{LM}}/2 & \mathrm{U_M} & \mathrm{U_{MR}}/2 \\ \mathrm{U_{LR}}/2 & \mathrm{U_{MR}}/2 & \mathrm{U_R}/2 \end{pmatrix} = \frac{e^2}{2} \begin{pmatrix} \mathrm{C}_{\Sigma_\mathrm{L}} & -\mathrm{C_{LM}} & -\mathrm{C_{LR}} \\ -\mathrm{C_{LM}} & \mathrm{C}_{\Sigma_\mathrm{M}} & -\mathrm{C_{MR}} \\ -\mathrm{C_{LR}} & -\mathrm{C_{MR}} & \mathrm{C}_{\Sigma_\mathrm{R}} \end{pmatrix}^{-1}, \tag{5.18}$$

where C_{Σ_i} is the total capacitance of dot i and C_{ij} is the mutual capacitance of dots i and j. By applying a voltage V to the left plunger gate in Fig. 5.3, the capacitive effect on dot $i \in \{\mathrm{L, M, R}\}$ is

$$n_\mathrm{gi} = -\mathrm{C_{ri}}\mathrm{V}/|e| \tag{5.19}$$

with the resonator (left plunger) gate capacitance $\mathrm{C}_{\mathrm{r}i}$ to dot i. The resonator voltage vacuum fluctuations on the left plunger gate therefore affect Δ and ε as

$$\Delta\varepsilon(\mathrm{V_{ZPF}}) = \varepsilon(\mathrm{V} = \mathrm{V_{ZPF}}) - \varepsilon(\mathrm{V} = 0) = \alpha_\varepsilon e \mathrm{V_{ZPF}} \tag{5.20}$$

and

$$\Delta[\Delta(\mathrm{V_{ZPF}})] = \Delta(\mathrm{V} = \mathrm{V_{ZPF}}) - \Delta(\mathrm{V} = 0) = \alpha_\Delta e \mathrm{V_{ZPF}}. \tag{5.21}$$

We can now express the lever arms α_Δ and α_ε as a function of the TQD capacitances by using Eqns. (5.17)-(5.21) as well as the definitions of the qubit detuning parameters $\varepsilon = 1/2[\mathrm{E}(1,0,2) - \mathrm{E}(2,0,1)]$ and $\Delta = \mathrm{E}(1,1,1) - 1/2[\mathrm{E}(1,0,2) + \mathrm{E}(2,0,1)]$ from Eq. (3.9). For the case of identical quantum dots that are symmetrically coupled, we define $\mathrm{C_m} \equiv \mathrm{C_{LM}} = \mathrm{C_{MR}}$ and $\mathrm{C}_\Sigma \equiv \mathrm{C}_{\Sigma_\mathrm{L}} = \mathrm{C}_{\Sigma_\mathrm{R}}$. In this situation the mutual capacitance of the middle quantum dot with the left and right dots is the same such that we can write

$\mathrm{C}_{\Sigma_\mathrm{M}} = \mathrm{C}_\Sigma + \mathrm{C}_\mathrm{m}$. In addition we neglect the mutual left-right dot coupling ($\mathrm{C}_\mathrm{LR} = 0$) and arrive at the analytic expressions

$$\alpha_\varepsilon = \frac{\mathrm{C}_\mathrm{rL} - \mathrm{C}_\mathrm{rR}}{\mathrm{C}_\Sigma} \tag{5.22}$$

and

$$\alpha_\Delta = \frac{2\mathrm{C}_\mathrm{rM} - \mathrm{C}_\mathrm{rR} - \mathrm{C}_\mathrm{rL}}{2(2\mathrm{C}_\mathrm{m} + \mathrm{C}_\Sigma)}. \tag{5.23}$$

To gain a qualitative understanding for Eqns. (5.22)-(5.23) we consider two limiting cases. First, if the left plunger gate couples equally to the left and right quantum dots, $\mathrm{C}_\mathrm{rL} = \mathrm{C}_\mathrm{rR}$, the left-right detuning lever arm α_ε is zero. Second, in case the left plunger gate coupling to the middle quantum dot is equal to the mean of its couplings to the left and right dots $[\mathrm{C}_\mathrm{rM} = (\mathrm{C}_\mathrm{rL} + \mathrm{C}_\mathrm{rR})/2]$, we obtain $\alpha_\Delta = 0$.

We now return to the interaction Hamiltonian from Eq. (5.14), apply a RWA and express it in the RX qubit eigenbasis $\{|0_\mathrm{RX}\rangle, |1_\mathrm{RX}\rangle\}$ such that it takes the form

$$\hat{\mathrm{H}}_\mathrm{int,RX} = \hbar g_\mathrm{RX}(\hat{a}^\dagger\hat{\sigma}_- + \hat{a}\hat{\sigma}_+) \tag{5.24}$$

with the spin-photon coupling strength

$$g_\mathrm{RX} = \left[c_2^{(1_\mathrm{RX})}c_2^{(0_\mathrm{RX})*} - \frac{\upsilon+1}{2}\left(c_3^{(1_\mathrm{RX})}c_3^{(0_\mathrm{RX})*} + c_2^{(1_\mathrm{RX})}c_2^{(0_\mathrm{RX})*}\right)\right] g_\mathrm{c,RX}^{(0)}. \tag{5.25}$$

The coefficients $c_{2/3}^{(0_\mathrm{RX}/1_\mathrm{RX})}$ were defined in Eq. (3.15). They quantify the contribution of the basis states with asymmetric charge configuration $(1,0,2)$ and $(2,0,1)$ to the qubit states.

Next, we investigate the dependence $g_\mathrm{RX}(\Delta)$, since the qubit parameter Δ is mostly tuned in our experiments. For a symmetric RX qubit tunnel coupling configuration ($t_\mathrm{L} = t_\mathrm{R} = t$) and at the sweet spot $\varepsilon = 0$ (see subsection 3.2.2) the coupling strength in Eq. (5.25) be expressed analytically as

$$g_\mathrm{RX} = \frac{\sqrt{3}t^2}{[(2t^2+\Delta^2-\Delta\sqrt{2t^2+\Delta^2})(6t^2+\Delta^2-\Delta\sqrt{6t^2+\Delta^2})]^{1/2}} g_\mathrm{c,RX}^{(0)}. \tag{5.26}$$

The analytic result is illustrated for $t/h = 9\,\mathrm{GHz}$ as the solid line in Fig. 5.4. We observe an increase of g_RX with Δ. For maximum tunnel coupling asymmetries in this work of about 20%, the analytic equation is a good approximation for the numerical result.

The latter is shown as the solid line in Fig. 5.4 and was evaluated at the sweet spot in ε which is a function of Δ due to the tunnel coupling asymmetry.

In the regime where $\Delta \gg t_{\mathrm{L,R}}$, Eq. (5.26) reduces to (Landig et al., 2018)

$$g_{\mathrm{RX}} = \left(1 - \frac{t^2}{\Delta^2}\right) g^{(0)}_{\mathrm{c,RX}} + \mathcal{O}(t^4/\Delta^4) \tag{5.27}$$

with a maximal coupling strength $g^{(0)}_{\mathrm{c,RX}}$, which we refer to as charge-photon coupling strength because the qubit states are mainly composed of the asymmetric charge configurations $(1,0,2)$ and $(2,0,1)$ (see discussion in subsection 3.2.3). Such a charge qubit between the left and right quantum dots has a strong electric dipole moment which makes it susceptible to charge noise as discussed in subsection 5.4.1.2. The quadratic term ($\propto t^2/\Delta^2$) in Eq. (5.27) is due to the mixing, mediated by exchange interaction, of the charge-qubit states with the spin-qubit states defined in the $(1,1,1)$ charge subspace. By decreasing Δ, this mixing and hence the electric dipole moment decreases. We mainly operate the qubit in the regime $|\Delta| \lesssim t_{\mathrm{L,R}}$, where we take a linear expansion of Eq. (5.26) to obtain

$$g_{\mathrm{RX}} = \left[\frac{1}{2} + \frac{\sqrt{2}}{24}(3+\sqrt{3})\frac{\Delta}{t}\right] g^{(0)}_{\mathrm{c,RX}} + \mathcal{O}(\Delta^2/t^2). \tag{5.28}$$

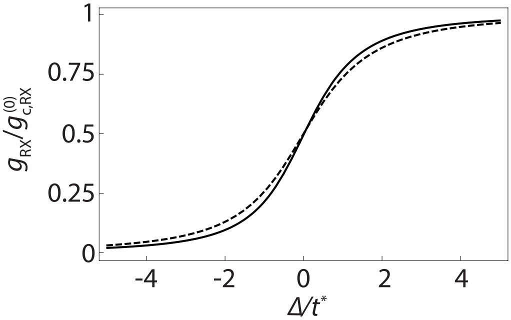

Figure 5.4 Δ-dependent RX qubit coupling strength. RX qubit coupling strength g_{RX} normalized by the charge coupling strength $g^{(0)}_{\mathrm{c,RX}}$ as a function of Δ/t^*, where $t^*/h = 9\,\mathrm{GHz}$. The solid line is the numerical result for $t_{\mathrm{L}}/h = 10\,\mathrm{GHz}$ and $t_{\mathrm{R}}/h = 8\,\mathrm{GHz}$ by evaluating Eq. (5.25) at the sweet spot in ε, where $\partial \mathrm{E}_{\mathrm{RX}}/\partial\varepsilon = 0$. The dashed line shows the analytic result using Eq. (5.26) with $t/h = 9\,\mathrm{GHz}$. The maximum difference of analytical and numerical calculation is 4% of $g^{(0)}_{\mathrm{c,RX}}$.

Finally, in the limit $\Delta \ll -t_{\mathrm{L,R}}$, the electric dipole moment of the qubit and hence g_{RX} eventually vanishes as the qubit states have the same $(1,1,1)$ charge configuration and are minimally influenced by charge noise (see discussion in subsection 3.2.3). In this regime, Eq. (5.26) takes the form

$$g_{\mathrm{RX}} = \frac{\sqrt{3}}{2}\left(\frac{t}{\Delta}\right)^2 g_{\mathrm{c,RX}}^{(0)} + \mathcal{O}(t^4/\Delta^4). \tag{5.29}$$

5.1.3 Transmon-resonator coupling

A transmon can be coupled to a resonator via a capacitive coupling as illustrated in Fig. 5.5. This coupling mechanism is described by the Hamiltonian (Koch et al., 2007)

$$\hat{\tilde{\mathrm{H}}}_{\mathrm{int,T}} = 2\frac{\mathrm{C_g}}{\mathrm{C}_\Sigma} e\mathrm{V_{ZPF}}\hat{n}(\hat{a} + \hat{a}^\dagger), \tag{5.30}$$

with the total capacitance $\mathrm{C}_\Sigma = \mathrm{C}_\mathrm{J}^{(\mathrm{SQ})} + \mathrm{C_g} + \mathrm{C_B}$. In the basis of the transmon states $|k_\mathrm{T}\rangle$ and by considering coupling of nearest-neighbor states we obtain (Koch et al., 2007)

$$\hat{\mathrm{H}}_{\mathrm{int,T}} = \sum_{k=0}^{\mathrm{N}} g_{\mathrm{T},k}(|k_\mathrm{T}\rangle\langle(k+1)_\mathrm{T}| + |(k+1)_\mathrm{T}\rangle\langle k_\mathrm{T}|)(\hat{a} + \hat{a}^\dagger) \tag{5.31}$$

with $g_{\mathrm{T},k} \approx \sqrt{k+1}\,g_\mathrm{T}$. The quantity $g_\mathrm{T} = 2\frac{\mathrm{C_g}}{\mathrm{C}_\Sigma} e\mathrm{V_{ZPF}}\langle 0_\mathrm{T}|\,\hat{n}\,|1_\mathrm{T}\rangle$ is the coupling strength between the two lowest levels of the transmon and the resonator. It depends via the Matrix element $\langle 0_\mathrm{T}|\,\hat{n}\,|1_\mathrm{T}\rangle$ on $\mathrm{E}_\mathrm{J}^{(\mathrm{SQ})}$ and therefore on Φ_T. We define it for zero transmon flux as $g_\mathrm{T}^{(0)} \equiv g_\mathrm{T}(\Phi_\mathrm{T} = 0)$. In the two-level approximation and considering RWA, Eq. (5.31) reduces to

$$\hat{\mathrm{H}}_{\mathrm{int,T}} = g_\mathrm{T}(\hat{a}^\dagger\hat{\sigma}_- + \hat{a}\hat{\sigma}_+). \tag{5.32}$$

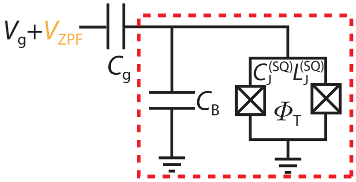

Figure 5.5 Schematic illustration of transmon-resonator coupling. The resonator voltage vacuum fluctuations $\mathrm{V_{ZPF}}$ couple capacitively to the transmon (highlighted with a red rectangle) via the capacitance $\mathrm{C_g}$.

5.2 Idealized hybrid circuit QED Hamiltonians

In this section we present the Hamiltonians that model the single and two qubit hybrid circuit QED system as a closed quantum system. We discuss the eigenstates of the Hamiltonians for resonant and dispersive qubit-photon interaction. For the latter case we introduce a spectroscopy technique that is frequently used for the experiments in chapters 7 and 8. For a more detailed discussion of the theory presented in this section we refer to Refs. Blais et al., 2004, 2007.

5.2.1 Jaynes-Cummings model

The coupled quantum system of a single qubit and a single resonator mode is described by the Jaynes-Cummmings Hamiltonian (Walls et al., 2008)

$$\hat{\mathrm{H}}_{\mathrm{JC}} = \hbar\omega_{\mathrm{r}}(\hat{a}^{\dagger}\hat{a} + \frac{1}{2}) + \frac{\hbar\omega_{\mathrm{q}}}{2}\hat{\sigma}_z + \hbar g_{\mathrm{q}}(\hat{a}\hat{\sigma}_+ + \hat{a}^{\dagger}\hat{\sigma}_-), \tag{5.33}$$

where the first and second terms are the Hamiltonians of the resonator and the qubit that were introduced in chapters 4 and 3, respectively. The third term is the interaction Hamiltonian from Eq. (5.4).

The energy spectrum of the Jaynes-Cummings Hamiltonian for resonant qubit-resonator interaction ($\omega_{\mathrm{r}} = \omega_{\mathrm{q}}$) is depicted in Fig. 5.6(a). The qubit ground ($|0_{\mathrm{q}}\rangle$) and excited ($|1_{\mathrm{q}}\rangle$) states hybridize with the resonator eigenstates $|n_{\mathrm{r}}\rangle$ to form the dressed states

$$|\Psi_{\pm,n}\rangle_{\mathrm{res},2} = (|n_{\mathrm{r}}, 0_{\mathrm{q}}\rangle \pm |(n-1)_{\mathrm{r}}, 1_{\mathrm{q}}\rangle)/\sqrt{2}, \tag{5.34}$$

where the subscript of $|\Psi_{\pm,n}\rangle_{\mathrm{res},2}$ indicates the resonant interaction of two quantum systems. The states $|\Psi_{\pm,n}\rangle_{\mathrm{res},2}$ are separated in energy by $2g_{\mathrm{q}}\sqrt{n+1}$. Since the energy separation depends on the number n of excitations in the system, this realizes an anharmonic energy spectrum. In this thesis we are limited to the single-photon limit, such that the relevant states are $|\pm\rangle_{\mathrm{res},2} \equiv |\Psi_{\pm,1}\rangle_{\mathrm{res},2} = (|1_{\mathrm{r}}, 0_{\mathrm{q}}\rangle \pm |0_{\mathrm{r}}, 1_{\mathrm{q}}\rangle)/\sqrt{2}$, which are formed by an equal superposition of a single excitation in either the resonator or the qubit. The states separation $2g_{\mathrm{q}}$ is referred to as vacuum Rabi mode splitting. It determines the rate at which the excitation is coherently exchanged between the qubit and the resonator. If this rate exceeds the cavity decay rate κ_{r} and the qubit decoherence rate $\gamma_{2,\mathrm{q}}$, the system is in the strong coupling limit and the vacuum Rabi mode splitting can be resolved spectroscopically. While κ_{r} was discussed in chapter 4, we consider qubit decoherence in this chapter in section 5.4. A more specific requirement for the observation of the vacuum Rabi mode splitting is $2g_\mathrm{q} > \kappa_\mathrm{r}/2 + \gamma_{2,\mathrm{q}}$.

If qubit and resonator are detuned by $|\Delta_\mathrm{qr}| \equiv |\omega_\mathrm{q} - \omega_\mathrm{r}| \gg g_\mathrm{q}$, the dispersive limit is realized. In this regime, the Jaynes-Cummings Hamiltonian can be approximated by the Hamiltonian (Schuster, 2007)

$$\hat{\mathrm{H}}_\mathrm{JC,disp} = \hbar(\omega_\mathrm{r} + \chi\hat{\sigma}_z)(\hat{a}^\dagger\hat{a} + \frac{1}{2}) + \frac{\hbar\omega_\mathrm{q}}{2}\hat{\sigma}_z, \tag{5.35}$$

where $\chi \equiv g_\mathrm{q}^2/\Delta_\mathrm{qr}$ is the dispersive shift. The spectrum of this Hamiltonian is shown in Fig. 5.6(b). We extract from the figure that the resonator resonance frequency is shifted by $-\chi$ or $+\chi$ if the qubit is in the ground or excited state, respectively. This qubit-state-dependent resonator shift, which relates to the first $\hat{\sigma}_z$ term in Eq. (5.35), is used in chapters 2 and 4 to experimentally determine the qubit energy spectroscopically if qubit and resonator are detuned.

The idea of this so-called two-tone spectroscopy measurement (Schuster et al., 2005) is to apply a first tone at frequency ω_p in order to probe the resonator transmission (or reflection) on resonance with the dispersively shifted resonator frequency $\omega_\mathrm{r} - \chi$. In addition, a second tone at frequency ω_d is applied either directly to the

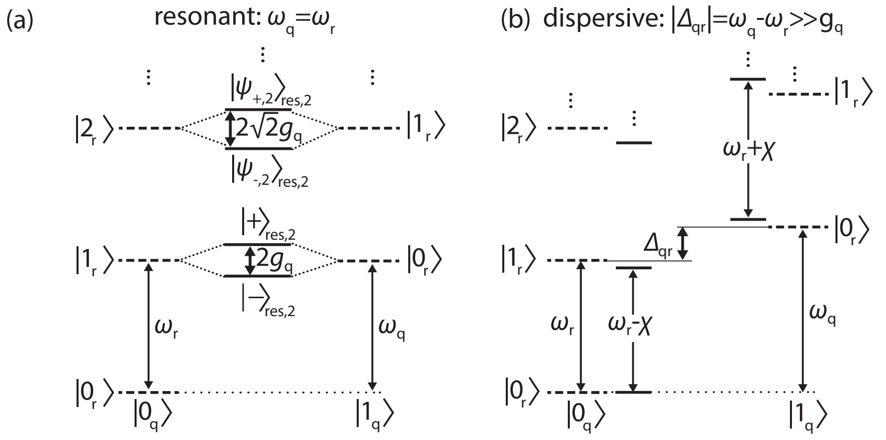

Figure 5.6 Jaynes-Cummings ladder. The dashed lines are the resonator photon number eigenstates $|n_\mathrm{r}\rangle$ for a mode frequency ω_r and the qubit in the ground (left) or excited (right) state, where ω_q is the qubit transition frequency. The solid lines represent the eigenstates of the Jaynes-Cummings Hamiltonian. The resonant and dispersive situations are depicted in (a) and (b), respectively.

qubit or via the resonator. This second tone is often referred to as drive tone or spectroscopy tone. If drive tone and qubit are on resonance ($\omega_\mathrm{d} = \omega_\mathrm{q}$), the drive saturates the qubit transition such that the qubit is in a mixed state. The expectation value of $\hat{\sigma}_z$ in Eq. (5.35) is therefore zero and the resonator resonance shifts back to its bare (uncoupled) value ω_r. This frequency shift is detected as a probe tone response, i.e. a change in the transmitted (or reflected) probe signal, since the probe at $\omega_\mathrm{p} = \omega_\mathrm{r} - \chi$ is no longer on resonance with the resonator.

The probe tone response has a Lorentzian lineshape with a half width at half maximum (HWHM) $\delta\nu_\mathrm{q}$ that depends on the drive tone generator power $\mathrm{P}_\mathrm{gen,d}$ as (Schuster et al., 2005)

$$\delta\nu_\mathrm{q} = \sqrt{[\gamma_{2,\mathrm{q}}/(2\pi)]^2 + \eta \mathrm{P}_\mathrm{gen,d}}, \tag{5.36}$$

where η is a constant. By measuring $\delta\nu_\mathrm{q}$ for multiple $\mathrm{P}_\mathrm{gen,d}$ and performing a linear fit to $\delta\nu_\mathrm{q}^2(\mathrm{P}_\mathrm{gen,d})$, one can extract $\gamma_{2,\mathrm{q}}$ experimentally from the extrapolation of the fit to zero drive power.

The Hamiltonian in Eq. (5.35) can equivalently be written as (Schuster, 2007)

$$\hat{\mathrm{H}}_\mathrm{JC,disp} = \hbar\omega_\mathrm{r}\left(\hat{a}^\dagger\hat{a} + \frac{1}{2}\right) + \frac{\hbar}{2}\left[\omega_\mathrm{q} + \chi\left(2\hat{a}^\dagger\hat{a} + 1\right)\right]\hat{\sigma}_z, \tag{5.37}$$

where the qubit experiences a vacuum-induced Lamb shift χ as well as an ac Stark shift $2\chi n$, i.e. a photon number n dependent frequency shift. We use the time averaged ac Stark shift $2\chi\bar{n}$, where $\bar{n} = \langle\hat{a}^\dagger\hat{a}\rangle$ is the averaged number of resonator photons, to determine the average number of photons in the resonator in chapter 7.

5.2.2 Tavis-Cummings model

We now extend above discussion to the case of two qubits $j = \{1, 2\}$ with states $|0/1_{\mathrm{q}_j}\rangle$ and transition frequencies ω_{q_j}. The qubits are coupled with coupling strengths g_{q_j} to the same resonator mode. Similar to Eq. (5.33) the Hamiltonian of the system can be expressed as

$$\hat{\mathrm{H}}_\mathrm{TC} = \hbar\omega_\mathrm{r}\left(\hat{a}^\dagger\hat{a} + \frac{1}{2}\right) + \sum_{j=1,2}\frac{\hbar\omega_{\mathrm{q}_\mathrm{j}}}{2}\hat{\sigma}_{z_j} + \sum_{j=1,2}\hbar g_{\mathrm{q}_j}(\hat{a}\hat{\sigma}_{+_j} + \hat{a}^\dagger\hat{\sigma}_{-_j}), \tag{5.38}$$

where $\hat{\sigma}_{+_j}$ and $\hat{\sigma}_{-_j}$ are the raising and lowering operators of qubit j, respectively. The Hamiltonian in Eq. (5.38) is referred to as Tavis-Cummings Hamiltonian (Tavis et al., 1968). We now restrict the discussion to a single excitation in the system, which is relevant for our experiments.

If both qubits and the resonator are on resonance ($\omega_\mathrm{r} = \omega_{\mathrm{q}_1} = \omega_{\mathrm{q}_2}$), which is depicted schematically in Fig. 5.7 (a), we can write Eq. (5.38) as (Woerkom et al., 2018)

$$\hat{\mathrm{H}}_\mathrm{TC} = \begin{array}{cc} \begin{array}{ccc} |0_{\mathrm{q}_1}0_{\mathrm{q}_2}1_\mathrm{r}\rangle & |1_{\mathrm{q}_1}0_{\mathrm{q}_2}0_\mathrm{r}\rangle & |0_{\mathrm{q}_1}1_{\mathrm{q}_2}0_\mathrm{r}\rangle \end{array} & \\ \left(\begin{array}{ccc} 0 & \hbar g_{\mathrm{q}_1} & 0 \\ \hbar g_{\mathrm{q}_1} & 0 & \hbar g_{\mathrm{q}_2} \\ 0 & \hbar g_{\mathrm{q}_2} & 0 \end{array}\right) & \begin{array}{c} |0_{\mathrm{q}_1}0_{\mathrm{q}_2}1_\mathrm{r}\rangle \\ |1_{\mathrm{q}_1}0_{\mathrm{q}_2}0_\mathrm{r}\rangle \\ |0_{\mathrm{q}_1}1_{\mathrm{q}_2}0_\mathrm{r}\rangle \end{array} \end{array}, \tag{5.39}$$

where we omitted the energy offset $\hbar\omega_\mathrm{r}$ and assumed that both qubits are coupled to the same phase of the resonator voltage mode, which is the case in our experiments in chapter 8. The eigenstates of Eq. (5.39) read as

$$\begin{aligned} |0\rangle_{\mathrm{res},3} &= \frac{1}{g_{\mathrm{q}_{12}}}(g_{\mathrm{q}_1}|0_{\mathrm{q}_1}1_{\mathrm{q}_2}0_\mathrm{r}\rangle - g_{\mathrm{q}_2}|1_{\mathrm{q}_1}0_{\mathrm{q}_2}0_\mathrm{r}\rangle), \\ |-\rangle_{\mathrm{res},3} &= \frac{1}{\sqrt{2}g_{\mathrm{q}_{12}}}(g_{\mathrm{q}_2}|0_{\mathrm{q}_1}1_{\mathrm{q}_2}0_\mathrm{r}\rangle + g_{\mathrm{q}_1}|1_{\mathrm{q}_1}0_{\mathrm{q}_2}0_\mathrm{r}\rangle - g_{\mathrm{q}_{12}}|0_{\mathrm{q}_1}0_{\mathrm{q}_2}1_\mathrm{r}\rangle) \\ |+\rangle_{\mathrm{res},3} &= \frac{1}{\sqrt{2}g_{\mathrm{q}_{12}}}(g_{\mathrm{q}_2}|0_{\mathrm{q}_1}1_{\mathrm{q}_2}0_\mathrm{r}\rangle + g_{\mathrm{q}_1}|1_{\mathrm{q}_1}0_{\mathrm{q}_2}0_\mathrm{r}\rangle + g_{\mathrm{q}_1 2}|0_{\mathrm{q}_1}0_{\mathrm{q}_2}1_\mathrm{r}\rangle), \end{aligned} \tag{5.40}$$

where $g_{\mathrm{q}_{12}} = \sqrt{g_{\mathrm{q}_1}^2 + g_{\mathrm{q}_2}^2}$ is the collective coupling strength that is enhanced for two qubits by a factor of $\sqrt{2}$ compared to the single qubit case discussed above since $g_{\mathrm{q}_{12}} = \sqrt{2}g_{\mathrm{q}_1}$ for equal qubit-resonator couplings ($g_{\mathrm{q}_1} = g_{\mathrm{q}_2}$). As shown in Fig. 5.7(b), the two states $|\pm\rangle_{\mathrm{res},3}$ are split in energy by $2g_{\mathrm{q}12}$. They can be excited by the resonator, while the state $|\pm\rangle_{\mathrm{res},3}$ only contains the vacuum state $|0_\mathrm{r}\rangle$ [see Eq. (5.40)] and is

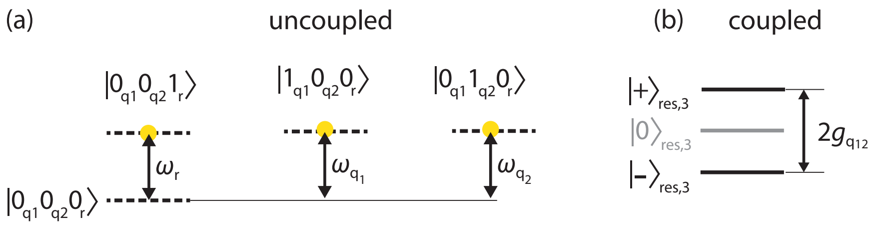

Figure 5.7 Tavis-Cummings Hamiltonian energy diagram. The system contains a single excitation. Energy diagram of the uncoupled and coupled states in (a) and (b), respectively. The state that is dark for the resonator is shown in gray.

therefore dark for the resonator.

If both qubits are detuned by $|\Delta_{\mathrm{rq_j}}| \equiv |\omega_{\mathrm{r}} - \omega_{\mathrm{q_j}}| \gg g_{\mathrm{q_j}}$ from the resonator, they can interact via virtual microwave photon excitations in the resonator. In this regime, the Tavis-Cummings Hamiltonian from Eq. (5.38) is approximately given by the dispersive Hamiltonian (Blais et al., 2007)

$$\begin{aligned}\hat{\mathrm{H}}_{\mathrm{TC,disp}} =& \hbar(\omega_{\mathrm{r}} + \chi_{\mathrm{q}1}\hat{\sigma}_{z_1} + \chi_{\mathrm{q}2}\hat{\sigma}_{z_2})\hat{a}^{\dagger}\hat{a} + \sum_{j=1,2}\frac{\hbar\omega_{\mathrm{q_j}}}{2}\hat{\sigma}_{z_j} + \\ & \hbar\mathrm{J}(\hat{\sigma}_{+_1}\hat{\sigma}_{-_2} + \hat{\sigma}_{-_1}\hat{\sigma}_{+_2})\end{aligned}. \tag{5.41}$$

We infer from the first term that the resonator resonance frequency depends on the state of both qubits via the expression $\chi_{\mathrm{q_j}}\hat{\sigma}_{z_j}$. Among others, this state-dependent shift of the bare resonator resonance by $\chi_{\mathrm{q_j}} \equiv g_{\mathrm{q_j}}^2/\Delta_{\mathrm{rq_j}}$ allows two-tone spectroscopy that was introduced in subsection 5.2.1. The quantity $\mathrm{J} \equiv g_{\mathrm{q_1}} g_{\mathrm{q_2}}(1/\Delta_{\mathrm{rq_1}} + 1/\Delta_{\mathrm{rq_2}})/2$ in Eq. (5.41) is referred to as exchange coupling strength since it determines the rate at which both qubits exchange excitations via virtual photons in the resonator.

If the dressed frequencies $\tilde{\omega}_{\mathrm{q}_j} \equiv \omega_{\mathrm{q}_j} + \chi_j$ of both qubits are on resonance ($\tilde{\omega}_{\mathrm{q_1}} = \tilde{\omega}_{\mathrm{q_2}}$), the Hamiltonian in Eq. (5.41) can be written after subtracting the energy offset $\hbar\omega_{\mathrm{r}}$ as (Woerkom et al., 2018)

$$\hat{\mathrm{H}}_{\mathrm{TC,disp}} = \begin{array}{cc} \begin{array}{cc} |0_{\mathrm{q_0}}1_{\mathrm{q_1}}\rangle & |1_{\mathrm{q_0}}0_{\mathrm{q_1}}\rangle \end{array} & \\ \left(\begin{array}{cc} 0 & \hbar\mathrm{J} \\ \hbar\mathrm{J} & 0 \end{array}\right) & \begin{array}{c} |0_{\mathrm{q_0}}1_{\mathrm{q_1}}\rangle \\ |1_{\mathrm{q_0}}0_{\mathrm{q_1}}\rangle \end{array} \end{array}. \tag{5.42}$$

The eigenstates $|\pm\rangle_{\mathrm{disp,3}} = 1/\sqrt{2}(|0_{\mathrm{q_0}}1_{\mathrm{q_1}}\rangle \pm |1_{\mathrm{q_0}}0_{\mathrm{q_1}}\rangle)$ of the Hamiltonian are entangled two-qubit states, i.e. states that cannot be written as product of states. Both states are separated in energy by the exchange splitting $2\mathrm{J} = 2g_{\mathrm{q_1}}g_{\mathrm{q_2}}/\Delta_{\mathrm{r}}$ with $\Delta_{\mathrm{r}} \equiv \omega_{\mathrm{r}} - \omega_{\mathrm{q_j}}$ [1].

---

[1] This definition of the detuning parameter Δ_{r} neglects the shift χ_{q_j}, which is a reasonable assumption in the dispersive regime since $|\Delta_{\mathrm{rq}_j}| \geq 10g_{\mathrm{q}_j}$ leads to a relative error $\chi_{\mathrm{q}_j}/|\Delta_{\mathrm{rq}_j}| \approx 1\%$.

5.3 Hybrid circuit QED description with dissipation

The Jaynes-Cummings and Tavis-Cummings Hamiltonians that were considered so far in this chapter describe a closed quantum system. This is an idealized model since it does not take the dissipative interaction of the quantum system with its environment into account. In subsections 5.3.1 and 5.3.2 we present two approaches to include dissipation in the theoretical description by considering an open quantum system.

5.3.1 Quantum master equation

This section is mostly based on the theory developed by Clemens Müller, which is used to describe our two-qubit experiments presented in chapter 8. A dissipative quantum system can be modeled by describing the time evolution of its density matrix ρ with a quantum master equation that reads as (Walls et al., 2008)

$$\dot{\rho} = -\frac{\mathrm{i}}{\hbar}\left[\hat{\mathrm{H}}_{\mathrm{sys}}, \rho\right] + \sum_k \hat{\mathscr{L}}_k \rho, \tag{5.43}$$

where $\hat{\mathrm{H}}_{\mathrm{sys}}$ is the total Hamiltonian of the system and $\hat{\mathscr{L}}_k \rho$ describes different dissipative channels. In our case, the total Hamiltonian consists of the Hamiltonian of the closed resonator-qubit quantum system as well as of a Hamiltonian that considers the coupling of the resonator with its probe tone, i.e. the reflection or transmission of the probe signal. The latter is taken into account through the scattering Lindblad Hamiltonian (SLH) cascaded quantum systems approach (Combes et al., 2017, Müller et al., 2017a, Woerkom et al., 2018). An introduction to this formalism is beyond the scope of this experimental thesis and we refer the interested reader to Ref. Combes et al., 2017. Qualitatively speaking, the probe tone is added to the quantum master equation via the input-output theory formalism presented in subsection 4.1.2. In essence, one obtains

$$\hat{\mathrm{H}}_{\mathrm{sys}} = \hat{\mathrm{H}}_{\mathrm{TC}} + \hat{\mathrm{H}}_{\mathrm{p}}, \tag{5.44}$$

where $\hat{\mathrm{H}}_{\mathrm{TC}}$ is the Tavis-Cummings Hamiltonian from subsection 5.2.2 and H_{p} is probe tone Hamiltonian that reads in the rotating frame at the probe frequency as

$$\hat{\mathrm{H}}_{\mathrm{p}} = \frac{\hbar}{2i}\sqrt{\frac{\kappa_{\mathrm{ext}}}{2}} \sum_{m\in\{\mathrm{L},\mathrm{R}\}} (b_{\mathrm{in},m}\hat{a}^{\dagger} - b^{*}_{\mathrm{in},m}\hat{a}), \tag{5.45}$$

where we assumed a two-port resonator which can be probed from the left (L) or right (R) side with a classical coherent tone of amplitude $b_{\mathrm{in},m}$. Note the similarity between this Hamiltonian and the Hamiltonian in Eq. (4.21) that described the interaction of the cavity mode with a bath of harmonic oscillators. The probe tone also contributes the dissipative term

$$\hat{\mathscr{L}}_{\mathrm{SLH}}\rho = \hat{\mathscr{D}}[\hat{b}_{\mathrm{out,R}}]\rho + \hat{\mathscr{D}}[\hat{b}_{\mathrm{out,L}}]\rho \tag{5.46}$$

to the master equation (5.43), as it describes the decay of the resonator mode into the probe field. Note that the relation (Combes et al., 2017)

$$\hat{b}_{\mathrm{out},m} = \sqrt{\frac{\kappa_{\mathrm{ext}}}{2}}\,\hat{a} + b_{\mathrm{in},m}\mathbb{1} \tag{5.47}$$

for the operator $\hat{b}_{\mathrm{out},m}$ is similar to the corresponding input-output theory relation in Eq. (4.30)[2]. Note also that the operator $\hat{\mathscr{D}}[\hat{\mathscr{O}}] = \hat{\mathrm{O}}\rho\hat{\mathrm{O}}^{\dagger} - (\hat{\mathrm{O}}^{\dagger}\hat{\mathrm{O}}\rho + \rho\hat{\mathrm{O}}^{\dagger}\hat{\mathrm{O}})/2$ in Eq. (5.46) is the Lindblad superoperator.

The internal resonator decay adds the additional dissipative term

$$\hat{\mathscr{L}}_{\mathrm{r}}\rho = \kappa_{\mathrm{int}}\hat{\mathscr{D}}[\hat{a}]\rho, \tag{5.48}$$

to the quantum master equation (5.43). The last contribution to dissipation in the master equation describes the qubit interaction with its environment. Using Born-Markov approximation one obtains

$$\hat{\mathscr{L}}_{\mathrm{q}}\rho = \gamma_{1,\mathrm{q}}\hat{\mathscr{D}}[\hat{\sigma}_{-_{\mathrm{q}}}]\rho + \frac{1}{2}\gamma_{\varphi,\mathrm{q}}\hat{\mathscr{D}}[\hat{\sigma}_{z_{\mathrm{q}}}]\rho, \tag{5.49}$$

where $\gamma_{1,\mathrm{q}}$ is the qubit relaxation rate and $\gamma_{\varphi,\mathrm{q}}$ the qubit pure dephasing rate. To gain some intuition about this result we note that the relaxation term couples to the dissipator of the qubit annihilation operator $\hat{\sigma}_{-_{\mathrm{q}}}$, while the dephasing rate is contained in the term that describes the coupling of the environment to the qubit energy via the Pauli operator $\hat{\sigma}_{z_{\mathrm{q}}}$. The relaxation and pure dephasing rates add up to the qubit decoherence rate $\gamma_{2,\mathrm{q}}$ as

$$\gamma_{2,\mathrm{q}} = \frac{\gamma_{1,\mathrm{q}}}{2} + \gamma_{\varphi,\mathrm{q}}. \tag{5.50}$$

---

[2] The different sign for the second term on the right hand side in Eq. (5.47) compared to Eq. (4.30) is due to a different sign convention in Ref. Combes et al., 2017 compared to Ref. Walls et al., 2008, where the latter was followed in subsection 4.1.2.

Note that we take relaxation and dephasing into account either phenomenologically or with a noise model as discussed in section 5.4.

We can now calculate the amplitude of the field reflected from the resonator as

$$b_{\mathrm{out},m} = \mathrm{Tr}\left\{\hat{b}_{\mathrm{out},m}\rho\right\} \quad , \tag{5.51}$$

where ρ is the solution of the total master equation, including the drive and the decay terms.

For the spectroscopy experiments conducted in this thesis, we are only interested in the steady state of the system and therefore solve the master equation (5.43) with the constraint $\dot{\rho} = 0$. Note that if the resonator is measured in reflection, we obtain $\mathrm{S}_{11} = b_{\mathrm{out},m}/b_{\mathrm{in},m}$ from Eq. (5.51) as discussed for a single-port cavity in subsection 4.1.2.

5.3.2 Input-Output theory

Another approach to describe a dissipative quantum system theoretically is given by input-output theory. This approach can be used equivalently to the quantum master equation to describe a hybrid circuit QED system if the resonator probe tone is weak such that it does not introduce additional excitations into the system (Mi, 2018).

In this section we follow Refs. Petersson et al., 2012, Burkard et al., 2016 to derive the transmission through a two-port resonator that is coupled to a single qubit. The system Hamiltonian is given by the Jaynes-Cummings Hamiltonian from Eq. (5.33), which can be transformed into a frame rotating at the probe tone frequency ω_{p} such that we obtain

$$\hat{\mathrm{H}}_{\mathrm{sys}} = \hbar\Delta_{\mathrm{rp}}\hat{a}^{\dagger}\hat{a} + \frac{\hbar\Delta_{\mathrm{qp}}}{2}\hat{\sigma}_z + \hbar g_{\mathrm{q}}(\hat{a}\hat{\sigma}_+ + \hat{a}^{\dagger}\hat{\sigma}_-), \tag{5.52}$$

where $\Delta_{\mathrm{rp}} \equiv \omega_{\mathrm{r}} - \omega_{\mathrm{p}}$ and $\Delta_{\mathrm{qp}} \equiv \omega_{\mathrm{q}} - \omega_{\mathrm{p}}$ are the resonator–probe-tone and the qubit–probe-tone detunings, respectively. As for the input-output calculation for a bare resonator in subsection 4.1.2, the next step is to write down the Heisenberg equations of motion for the operators $\hat{a}$ and σ_-:

$$\dot{\hat{a}} = \frac{i}{\hbar}[\hat{\mathrm{H}}_{\mathrm{sys}} + \hat{\mathrm{H}}_{\mathrm{diss}}, \hat{a}] \quad \text{and} \quad \dot{\hat{\sigma}}_- = \frac{i}{\hbar}[\hat{\mathrm{H}}_{\mathrm{sys}} + \hat{\mathrm{H}}_{\mathrm{diss}}, \hat{\sigma}_-]. \tag{5.53}$$

Thereby, $\hat{\mathrm{H}}_{\mathrm{diss}}$ captures the dissipative channels that result in the qubit decoherence rate $\gamma_{2,\mathrm{q}}$ as well as the internal and external resonator decay rates rates κ_{int} and $\kappa_{1,2} =$

$\kappa_{\mathrm{ext}}/2$. For a single input field described by $\hat{a}_{\mathrm{in},1}$, the equations of motion become

$$\begin{aligned} \dot{\hat{a}} &= -i\Delta_{\mathrm{rp}}\hat{a} - ig_{\mathrm{q}}\hat{\sigma}_{-} - \frac{\kappa_{\mathrm{r}}}{2}\hat{a} + \sqrt{\kappa_1}\hat{a}_{\mathrm{in},1}, \\ \dot{\hat{\sigma}}_{-} &= -i\Delta_{\mathrm{qp}}\hat{\sigma}_{-} - ig_{\mathrm{q}}(p_{|0_{\mathrm{q}}\rangle} - p_{|1_{\mathrm{q}}\rangle})\hat{a} - \gamma_{2,\mathrm{q}}\hat{\sigma}_{-} \end{aligned} . \tag{5.54}$$

The thermal occupation probabilities $p_{|0(1)_{\mathrm{q}}\rangle}$ of the qubit ground (excited) state are given as

$$p_{|0(1)_{\mathrm{q}}\rangle} = 1/\sum_j e^{(\mathrm{E}_{|0(1)_{\mathrm{q}}\rangle} - \mathrm{E}_j)/(k_{\mathrm{B}}\mathrm{T})}, \tag{5.55}$$

where $\mathrm{E_j}$ describes the energy of every state of the quantum system, which forms the qubit, that can be thermally occupied at temperature T. For $k_{\mathrm{B}}\mathrm{T} \ll \mathrm{E}_{\mathrm{q}}$, the ground state occupation $p_{|0_{\mathrm{q}}\rangle}$ dominates.

If we neglect the quantum fluctuations at the resonator port that is not probed ($\hat{a}_{\mathrm{in},2} = 0$), we obtain with Eq. (4.31) $\hat{a}_{\mathrm{out},2} = \sqrt{\kappa_2}\hat{a}$ and can calculate the resonator transmission S_{21}, where we replace the field operators as in subsection 4.1.2 with the corresponding coherent states amplitudes:

$$\mathrm{S}_{21} = \frac{-i\sqrt{\kappa_1\kappa_2}}{\Delta_{\mathrm{rp}} - i\frac{\kappa_{\mathrm{r}}}{2} + g_{\mathrm{q}}\chi_{\mathrm{e}}}. \tag{5.56}$$

The term

$$\chi_{\mathrm{e}} = \frac{g_{\mathrm{q}}(p_{|0_{\mathrm{q}}\rangle} - p_{|1_{\mathrm{q}}\rangle})}{-\Delta_{\mathrm{qp}} + i\gamma_{2,\mathrm{q}}}, \tag{5.57}$$

can be identified as the electric susceptibility of the qubit, which modifies the resonator transmission compared to the uncoupled situation. We note that for equal ground and excited state occupation probabilities the susceptibility vanishes, since the incoherent interaction of the qubit with the thermal bath results in a fully mixed state $\rho = \frac{1}{2}\mathbb{1}$ with vanishing coherence.

5.4 Qubit decoherence

There are multiple dissipative channels for the qubit coherence that have a different physical origin. They are characterized by their respective noise spectra. While high-frequency noise at the qubit energy causes relaxation, low-frequency noise tunes the qubit energy, which leads to dephasing. Note that if the fluctuations in the latter case occur on a time scale that is long compared to the relaxation rate but short compared to the measurement time, they are still observed as an ensemble dephasing (Schuster, 2007).

In this section we focus on the relevant dissipative channels for the RX qubit, where we introduce corresponding noise models in subsection 5.4.1, since the RX qubit coherence is studied in chapters 7 and 8. The charge qubit and transmon decoherence is discussed in less depth in subsection 5.4.2. In subsection 5.4.3 we explain the effect of two qubit decoherence mechanisms that are related to noise in the resonator and therefore generally apply to a coupled qubit-resonator system.

5.4.1 RX qubit decoherence

In chapters 7 and 8 we study the dependence of the RX qubit decoherence rate on Δ at the sweet spot in ε. The dominant decoherence mechanisms are magnetic noise in the qubit host material as well as charge noise. In this section we present models for both mechanisms. For a more general discussion of decoherence in three-electron spin qubits we refer to Refs. Mehl et al., 2013, Russ et al., 2017.

5.4.1.1 Magnetic noise

In the following we first discuss the physical origin and basic properties of magnetic-noise-induced decoherence. Subsequently we report the corresponding noise model developed by José Carlos Abadillo-Uriel and presented in Ref. Landig et al., 2019a.

Basic concepts

The RX qubit is implemented in the $S = S_z = 1/2$ subspace of the full three-electron Hilbert space. If a magnetic noise source couples equally to all three electrons, it leaves the qubit states unaffected. The RX qubit is therefore referred to as decoherence free subspace (DFS) qubit. While the DFS protects the qubit against fluctuations in the global magnetic field, the qubit is still affected by local magnetic field noise. Local magnetic fields are present in the quantum dots due to the spin of the nuclei in the

GaAs host material. These fields are unavoidable since the stable isotopes of Ga (^{69}Ga and ^{71}Ga) and the naturally occurring isotope of As (^{75}As) do not have an even number of neutrons and protons and consequently possess a finite magnetic moment. The interaction of an electron in a quantum dot with its nuclear spin environment is described by the hyperfine Hamiltonian (Hanson et al., 2007)

$$\hat{\mathrm{H}}_{\mathrm{HF}} = g\mu_{\mathrm{B}}\hat{\mathbf{B}}_{\mathrm{N}} \cdot \hat{\mathbf{S}}, \tag{5.58}$$

with the electron spin operator and g-factor $\hat{\mathbf{S}}$ and g, respectively. The operator $\hat{\mathbf{B}}_{\mathrm{N}}$ describes the magnetic field produced by N nuclei in the quantum dot. This field is referred to as Overhauser field and can be expressed as (Russ et al., 2017)

$$\hat{\mathbf{B}}_{\mathrm{N}} = \frac{1}{g\mu_{\mathrm{B}}} \sum_{k=1}^{\mathrm{N}} \mathrm{A}_k \hat{\mathbf{I}}_k, \tag{5.59}$$

where $\hat{\mathbf{I}}_k$ denotes the nuclear spin operator. The hyperfine interaction constant A_k in Eq. (5.59) is proportional to the probability density of the electron wave function at the location of the nucleus (Slichter, 1990). The Hamiltonian in Eq. (5.58) therefore describes contact interaction, which gives the dominant contribution for the coupling between and electron and a nucleus for 2DEG electrons in GaAs (Coish et al., 2009), since the conduction band of GaAs is s-type.

While for fully polarized nuclear spins the Overhauser field is $|\langle\hat{\mathbf{B}}_{\mathrm{N,max}}\rangle| \approx 5\,\mathrm{T}$ (Hanson et al., 2007), the spins are practically unpolarized in our experiments due to the small Zeeman splitting of the nuclear spin levels. In thermal equilibrium at 30 mK we obtain $|\langle\hat{\mathbf{B}}_{\mathrm{N}}\rangle| \approx 13\,\mathrm{mT}$ (Hanson et al., 2007, Coish et al., 2009) for the maximum external magnetic field of 200 mT that is used to operate the RX qubit in this thesis. The nuclear spins are therefore randomly oriented and we can treat the Overhauser field as a classical magnetic field that has a magnitude and a direction described by a Gaussian probability distribution with standard deviation $\sigma_{\mathrm{HF}} = 1/\sqrt{\mathrm{N}}|\langle\hat{\mathbf{B}}_{\mathrm{N,max}}\rangle|$ (Merkulov et al., 2002). For a typical number of nuclei of $\mathrm{N} \approx 10^6$ that interact with an electron in a quantum dot, we calculate $\sigma_{\mathrm{HF}} \approx 5\,\mathrm{mT}$.

If the Overhauser field was constant in time, it would influence the electron in a predictable manner (Hanson et al., 2007). The field however is time dependent, such that the phase of the electron becomes randomized. For a single electron spin, this pure dephasing time can be calculated as (Hanson et al., 2007)

$$\mathrm{T}_{2,\mathrm{HF}}^{*} = \sqrt{2}\hbar/(g\mu_{\mathrm{B}}\sigma_{\mathrm{HF}}) \approx 8\,\mathrm{ns} \tag{5.60}$$

by averaging the free time-evolution of the electron over different Overhauser magnetic field realizations (ensemble average), which are given by the Gaussian probability distribution. Since the time scale of the nuclear field fluctuations are slow compared to the electron dynamics, the electron spin coherence can be prolonged by using, for example, spin-echo techniques that refocus the electron spin on time scales that are fast compared to the temporal changes in the Overhauser field (Bluhm et al., 2011). For the time averaged measurements presented in this thesis the picture of the ensemble average applies. Note that in the presence of an external magnetic field, magnetic field fluctuations parallel and perpendicular to the quantization axis are distinguished. For magnetic fields larger than about 100 mT, the contribution of the latter in the direction of the (tilted) spin quantization axis is negligible (Hanson et al., 2007) however they can cause spin-flip processes for smaller magnetic fields.

Quantitative noise model

Above discussion was restricted to one electron in a single quantum dot. In the following we present a model for hyperfine-induced decoherence for the RX qubit as a function of the external magnetic field, which can be divided into two different channels: decoherence within the $\mathrm{S}_z = 1/2$ subspace of the qubit, associated with magnetic field fluctuations parallel to the quantization axis, and leakage towards the $\mathrm{S}_z = -1/2$ subspace, associated with magnetic field fluctuations perpendicular to the external field direction.

First, we follow Refs. Hung et al., 2014, Fei et al., 2015 to analyze the effects of decoherence within the $\mathrm{S}_z = 1/2$ subspace, which, as we show below, is the leading source of magnetically-induced decoherence. We define the local differences in the magnetic field along the quantization axis due to the hyperfine interaction in the left (L), middle (M) and right (R) quantum dot as $\delta\mathrm{B}_\mathrm{l} \equiv \mathrm{B}^z_\mathrm{L} - \mathrm{B}^z_\mathrm{M}$ and $\delta\mathrm{B}_\mathrm{r} \equiv \mathrm{B}^z_\mathrm{M} - \mathrm{B}^z_\mathrm{R}$. In these terms, the Hamiltonian due to magnetic field fluctuations reads in the basis $\{|\tilde{0}_\mathrm{RX}\rangle, |\tilde{1}_\mathrm{RX}\rangle, |\tilde{2}_\mathrm{RX}\rangle, |\tilde{3}_\mathrm{RX}\rangle, |\tilde{4}_\mathrm{RX}\rangle\}$ defined in Eq. (3.12) as

$$\hat{\mathrm{H}}_{\delta\mathrm{B}_z} = \frac{1}{2} g\mu_\mathrm{B} \begin{pmatrix} \frac{2}{3}(\delta\mathrm{B}_\mathrm{l} - \delta\mathrm{B}_\mathrm{r}) & \frac{1}{\sqrt{3}}(\delta\mathrm{B}_\mathrm{l} + \delta\mathrm{B}_\mathrm{r}) & 0 & 0 & -\frac{\sqrt{2}}{3}(\delta\mathrm{B}_\mathrm{l} - \delta\mathrm{B}_\mathrm{r}) \\ \frac{1}{\sqrt{3}}(\delta\mathrm{B}_\mathrm{l} + \delta\mathrm{B}_\mathrm{r}) & 0 & 0 & 0 & \sqrt{\frac{2}{3}}(\delta\mathrm{B}_\mathrm{l} + \delta\mathrm{B}_\mathrm{r}) \\ 0 & 0 & -\delta\mathrm{B}_\mathrm{r} & 0 & 0 \\ 0 & 0 & 0 & -\delta\mathrm{B}_\mathrm{l} & 0 \\ -\frac{\sqrt{2}}{3}(\delta\mathrm{B}_\mathrm{l} - \delta\mathrm{B}_\mathrm{r}) & \sqrt{\frac{2}{3}}(\delta\mathrm{B}_\mathrm{l} + \delta\mathrm{B}_\mathrm{r}) & 0 & 0 & \frac{1}{3}(\delta\mathrm{B}_\mathrm{l} - \delta\mathrm{B}_\mathrm{r}) \end{pmatrix}. \tag{5.61}$$

The Hamiltonian couples the different spin configurations of the $(1,1,1)$ states $|\tilde{0}_\mathrm{RX}\rangle$,

$|\tilde{1}_{\mathrm{RX}}\rangle$ and $|\tilde{4}_{\mathrm{RX}}\rangle$. We assume that the magnetic field fluctuations in all three dots follow the Gaussian probability distribution

$$\mathrm{P}(\delta\mathrm{B}_l,\delta\mathrm{B}_r)=\frac{1}{2\pi\sigma_{\mathrm{HF}}^2}e^{-(\delta\mathrm{B}_l^2+\delta\mathrm{B}_r^2)/(2\sigma_{\mathrm{HF}}^2)}. \tag{5.62}$$

To calculate the dephasing rate due to the hyperfine interaction $\gamma_{\varphi,\mathrm{RX}}^{\mathrm{HF}}$ we assume that the Overhauser field is quasistatic compared to the qubit dynamics. The time evolution of the density matrix is therefore given as

$$\dot{\rho}=-\frac{\mathrm{i}}{\hbar}[\hat{\tilde{\mathrm{H}}}_{\mathrm{Hub}}+\hat{\tilde{\mathrm{H}}}_{\delta\mathrm{B}_z},\rho], \tag{5.63}$$

where the tilde in $\hat{\tilde{\mathrm{H}}}_{\mathrm{Hub}}$ and $\hat{\tilde{\mathrm{H}}}_{\delta\mathrm{B}_z}$ indicates that we have performed a transformation to the basis that diagonalizes the unperturbed Hubbard Hamiltonian $\hat{\mathrm{H}}_{\mathrm{Hub}}$, as defined in Eq. (3.13) at the relevant RX qubit working point. To evaluate the decay of the coherence, we assume the following initial state

$$|\psi_0\rangle=\frac{1}{\sqrt{2}}(|0\rangle+|1\rangle). \tag{5.64}$$

We now assume that the noise due to fluctuating hyperfine fields $\delta\mathrm{B}_\mathrm{l}$ and $\delta\mathrm{B}_\mathrm{r}$ is uncorrelated. It is therefore possible to average the value of the coherence using the probability distribution given in Eq. (5.62). Hence, we obtain for the average value of the density matrix:

$$\langle\rho(t)\rangle=\int\frac{d(\delta\mathrm{B}_l)d(\delta\mathrm{B}_r)}{2\pi\sigma_{\mathrm{HF}}^2}\rho(t,\delta\mathrm{B}_l,\delta\mathrm{B}_r)e^{-(\delta\mathrm{B}_l^2+\delta\mathrm{B}_r^2)/2\sigma_{\mathrm{HF}}^2} \tag{5.65}$$

The value of $\gamma_{\varphi,\mathrm{RX}}^{\mathrm{HF}}$ is then determined by Gaussian decay of the coherence term in the density matrix:

$$|\langle\rho_{01}\rangle|=\frac{1}{2}e^{-\left(\gamma_{\varphi,\mathrm{RX}}^{\mathrm{HF}}t\right)^2}. \tag{5.66}$$

Below, we first derive an analytical formula for the decoherence rate under the assumption that it mainly arises due to pure dephasing within the qubit subspace. For simplicity, we also assume symmetric tunnel couplings $t_\mathrm{L}=t_\mathrm{R}=t$. Later, we show how the numerical results based on Eq. (5.65) validate the assumptions made.

For a given working point we can approximate the qubit dynamics using the two-state Hamiltonian

$$\hat{\mathrm{H}}=\frac{\hbar\omega_{\mathrm{RX}}}{2}\hat{\sigma}_z+\big(h_l(\Delta,t)\delta\mathrm{B}_l+h_r(\Delta,t)\delta\mathrm{B}_r\big)\hat{\sigma}_z, \tag{5.67}$$

where $h_{l,r}$ are the prefactors of $\delta \mathrm{B}_l$ and $\delta \mathrm{B}_r$ in the basis that diagonalizes $\hat{\mathrm{H}}_{\mathrm{Hub}}$ [see Eq. (3.13)], after projecting onto the qubit subspace. These prefactors can be calculated analytically at the sweet spot in ε ($\varepsilon = 0$) for a given Δ and t, giving $h_l = -h_r$ with

$$h_l = \frac{g\mu_{\mathrm{B}}}{24}\Big[-4 + \Delta\Big(\frac{3}{\sqrt{2t^2+\Delta^2}} + \frac{1}{\sqrt{6t^2+\Delta^2}}\Big)\Big]. \tag{5.68}$$

Inserting the two-level Hamiltonian Eq. (5.67) in Eq. (5.63), and applying Eqs. (5.64)-(5.66) we get

$$\gamma^{\mathrm{HF}}_{\varphi,\mathrm{RX}} = \frac{\sqrt{h_l^2 + h_r^2}\,\sigma_{\mathrm{HF}}}{\sqrt{2}\hbar}, \tag{5.69}$$

which gives with Eq. (5.68) the analytic expression

$$\gamma^{\mathrm{HF}}_{\varphi,\mathrm{RX}} = \frac{|g|\mu_{\mathrm{B}}\sigma_{\mathrm{HF}}}{24\hbar}\Big[4 - \Delta\Big(\frac{3}{\sqrt{\Delta^2+2t^2}} + \frac{1}{\sqrt{\Delta^2+6t^2}}\Big)\Big]. \tag{5.70}$$

The resulting dependence of $\gamma^{\mathrm{HF}}_{\varphi,\mathrm{RX}}$ on Δ is shown in Fig. 5.8(a) for $\sigma_{\mathrm{HF}} = 5\,\mathrm{mT}$ as estimated above. By decreasing Δ, the contribution of the $(1,1,1)$ states to the RX

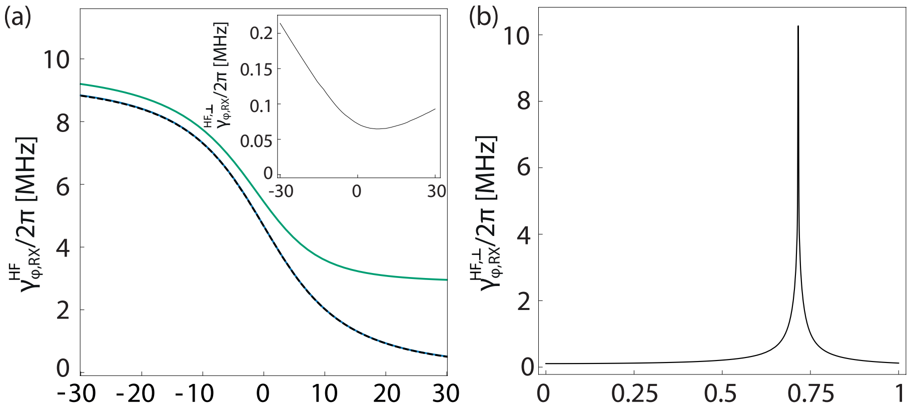

Figure 5.8 Hyperfine-induced RX qubit decoherence. The graphs are obtained for $\sigma_{\mathrm{HF}} = 5\,\mathrm{mT}$ and $g = -0.4$. (a) Analytic solutions ($t/h = 9\,\mathrm{GHz}$ in black) and numerical calculations ($t_{\mathrm{R}}/h = t_{\mathrm{L}}/h = 9\,\mathrm{GHz}$ in blue, $t_{\mathrm{L}}/h = 9.91\,\mathrm{GHz}$ and $t_{\mathrm{R}}/h = 8.26\,\mathrm{GHz}$ in green) of $\gamma^{\mathrm{HF}}_{\varphi,\mathrm{RX}}$ as a function of Δ. Inset: Contribution $\gamma^{\mathrm{HF},\perp}_{\varphi,\mathrm{RX}}$ to decoherence from the field fluctuations perpendicular to the spin quantization axis for $t_{\mathrm{R}}/h = t_{\mathrm{L}}/h = 9\,\mathrm{GHz}$. **b** Perpendicular contribution to decoherence as a function of the external magnetic field for $t_{\mathrm{R}}/h = t_{\mathrm{L}}/h = 9\,\mathrm{GHz}$ and $\Delta/h = -10\,\mathrm{GHz}$.

qubit states increases (see subsection 3.2.3) and consequently the hyperfine-induced decoherence rate is enhanced. In the limit $\Delta \rightarrow -\infty$, we obtain $\gamma_{\varphi,\mathrm{RX}}^{\mathrm{HF}} = g\mu_{\mathrm{B}}\sigma_{\mathrm{HF}}/(3\hbar)$, which translates into a similar dephasing time $\mathrm{T}_{2,\mathrm{HF}}^{*} = 1/\gamma_{\varphi,\mathrm{RX}}^{\mathrm{HF}} = 17\,\mathrm{ns}$ compared to the estimate for a single electron spin in Eq. (5.60).

We also numerically evaluate the integral in Eq. (5.65) for the full five-dimensional basis set, following the procedure described in Ref. Fei et al., 2015, allowing us to also obtain results for asymmetric tunnel couplings. Numerical and analytical result of $\gamma_{\varphi,\mathrm{RX}}^{\mathrm{HF}}$ for $t_{\mathrm{L}}/h = t_{\mathrm{R}}/h = 9\,\mathrm{GHz}$ as a function of Δ are identical as shown by the blue and black lines in Fig. 5.8(a). The green line in Fig. 5.8(a) indicates the numerical result of $\gamma_{\varphi,\mathrm{RX}}^{\mathrm{HF}}$ for a tunnel coupling asymmetry $|(t_{\mathrm{L}} - t_{\mathrm{R}})|/t_{\mathrm{L}} \approx 20\%$. It agrees in the regime $\Delta/h \leq -7.5\,\mathrm{GHz}$ within $\approx 5\%$ with the analytical calculation for an averaged tunnel coupling ($t/h = (t_{\mathrm{L}} + t_{\mathrm{R}})/2h \approx 9.1\,\mathrm{GHz}$), which overlaps within the resolution of the plot with the black line in Fig. 5.8(a) that is shown for $t/h = 9.0\,\mathrm{GHz}$. Note that this small relative error of analytical and numerical results for asymmetric tunnel couplings motivates to use the analytical formula to fit to decoherence data in chapters 7 and 8.

Next, we consider the hyperfine fields that are perpendicular to the spin quantization axis, which mix states from the qubit subspace ($\mathrm{S}_z = 1/2$) with states from the opposite spin subspace ($\mathrm{S}_z' = -1/2$). This form of leakage is expected to be the dominating decoherence channel when the global magnetic field is suppressed (Hung et al., 2014). However, since the cavity response does not depend on the spin subspace where the qubit is defined, the impact of this mechanism on the qubit linewidth is non-trivial. For instance, the resonator mediates the interaction between qubit states, but there is no coupling between the pair of states with $\mathrm{S}_z = +1/2$ and the pair of states with $\mathrm{S}_z = -1/2$. This means that if there was a magnetic-noise-induced error that transforms the qubit state from $|0_{\mathrm{RX}}\rangle^{+}$ to $|0_{\mathrm{RX}}\rangle^{-}$, where the superscript $\pm$ indicates the spin subspace, the cavity response and the interactions mediated by the resonator would be unaffected. A hyperfine-induced bit-flip from $|0_{\mathrm{RX}}\rangle^{\pm}$ to $|1_{\mathrm{RX}}\rangle^{\mp}$ however would have an impact on the cavity response linewidth.

To analyze this bit-flip decoherence mechanism we consider the contribution of the in-plane components of the magnetic field noise ($\delta \mathrm{B}_x, \delta \mathrm{B}_y$). We then follow the same numerical procedure used to study fluctuations of the B_z field in Ref. Fei et al., 2015. However, we only consider the interaction terms that mix states with $\mathrm{S}_z' = \mathrm{S}_z \pm 1$. The estimated contribution $\gamma_{\varphi,\mathrm{RX}}^{\mathrm{HF},\perp}$ of the perpendicular Overhauser fields to the qubit decoherence is shown in the inset in Fig. 5.8(a) for $\mathrm{B} = 0$ and as a function of B_z at $\Delta/h = -10\,\mathrm{GHz}$ in Fig. 5.8(b). It is negligible at $\mathrm{B} = 0$, where $|0_{\mathrm{RX}}\rangle^{\pm}$ and $|1_{\mathrm{RX}}\rangle^{\mp}$ are split by the qubit energy. The decoherence rate $\gamma_{\varphi,\mathrm{RX}}^{\mathrm{HF},\perp}$ however becomes significant once the states $|0_{\mathrm{RX}}\rangle^{-}$ and $|1_{\mathrm{RX}}\rangle^{+}$ are close in energy at around $B_z = 700\,\mathrm{mT}$ and can consequently be mixed by the hyperfine fields.

5.4.1.2 Charge noise

Charge noise is due to electric field fluctuations from uncontrolled degrees of freedom that couple to the RX qubit. It is either externally introduced via the TQD gate electrodes or intrinsic of the qubit host material. The latter typically has a $1/f$ spectral density (Dial et al., 2013), which can be attributed to an ensemble of two-level fluctuators with a Lorentzian spectrum (Paladino et al., 2014) that couple to the qubit. Possible explanations for the physical origin of this charge noise in GaAs heterostructures include trapping of charges during cooldown due to leakage from the gate electrodes to the 2DEG (Buizert et al., 2008) as well as charged trap sites induced during fabrication (Hitachi et al., 2013). The dominant low frequency components of the $1/f$ charge noise couple via the RX qubit charge asymmetry parameter ε and the detuning parameter Δ to the qubit energy and hence dephase the qubit. While first order dephasing is suppressed at the sweet spot in ε, where $\partial E_{\mathrm{RX}}/\partial\varepsilon = 0$ (Russ et al., 2015a), second order charge noise that couples to the curvature of the qubit dispersion can still have a significant contribution to dephasing depending on the noise magnitude (Russ et al., 2015a).

The second source of charge noise are the TQD gate lines, that introduce thermal noise to the RX qubit. Note that significant contribution to this noise could be related to evanescent electromagnetic waves in the near field of the gates that reach the qubit (Volokitin et al., 2007), which is referred to as evanescent-wave Johnson noise. The thermal-noise spectral density can be derived by considering that the gate lines represent an impedance Z for the qubit, which is a source of voltage noise with spectral density (Callen et al., 1951, Clerk et al., 2010)

$$S_V(\omega) = 2\Re[Z(\omega)]\frac{\hbar\omega}{1-e^{-\hbar\omega/(k_B T)}} \tag{5.71}$$

that is derived from a quantum treatment of thermal noise[3]. For $\hbar\omega > k_B T$, the spec-

---

[3] The quantum mechanical derivation considers the vacuum fluctuations, which is in contrast to the Johnson-Nyquist equation for thermal noise, where $S_{V,JN}(\omega) = 2\Re[Z(\omega)]\hbar\omega/(\exp[\hbar\omega/(k_B T)]-1)$ (Nyquist, 1928) is obtained. While $S_{V,JN}$ decreases with ω, S_V shows an increase, which was observed experimentally for Josephson junctions in Ref. Koch et al., 1981. A discussion about this different behavior can for example be found in Ref. Kish et al., 2016. In the classical limit $k_B T \gg \hbar\omega$, both derivations yield the same white noise spectrum $S_V = S_{V,JN} = 2\Re[Z(\omega)]k_B T$ [note that $S_{V,JN}(\omega) + S_{V,JN}(-\omega) = 4\Re[Z(\omega)]k_B T$ is the engineering convention (Clerk et al., 2010)].

trum is approximately linear in ω and called ohmic[4]. The high frequency components of the thermal noise couple via the electric dipole moment to the qubit and lead to relaxation (Langsjoen et al., 2012, Poudel et al., 2013). The low frequency contribution is smaller but can still dephase the qubit (Premakumar et al., 2018).

Another intrinsic source of charge noise are phonons, which couple to the qubit electric dipole moment (Russ et al., 2017) causing relaxation. We identify two dominant mechanisms in GaAs (Gasser et al., 2009). First, acoustic phonons couple to the qubit via a deformation potential that is a result of phonon-induced strain, which modifies the electronic structure in the host material. Second, GaAs is piezoelectric and therefore acoustic phonons induce electric fields that lead to qubit-phonon coupling. A theoretical model for phonon-induced relaxation for the RX qubit is presented in Ref. Taylor et al., 2013. It is however not applicable to our experiments, since the model is restricted to the regime $\Delta \ll -t_{\mathrm{L,R}}$, where the Schrieffer-Wolff transformation (see subsection 3.2.3) is valid.

It is likely that all three above-mentioned charge noise sources have a notable contribution to the RX qubit decoherence. To distinguish their contribution, time-resolved experiments could be performed. These experiments allow to extract relaxation and dephasing rates as a function of the qubit energy and consequently to map out the underlying noise spectrum (Dial et al., 2013). Such an analysis is not possible in our experiments where we measure time-averaged decoherence rates. Instead we use the approach to describe the qubit decoherence due to charge noise with the least possible number of free parameters while still finding reasonable agreement with our experimental observations. We therefore consider relaxation induced by ohmic noise, which we model as

$$\gamma_{1,\mathrm{RX}}^{\mathrm{th}} = \beta\, \omega_{\mathrm{RX}} \left| \frac{g_{\mathrm{RX}}}{g_{\mathrm{c,RX}}^{(0)}} \right|^2 , \tag{5.72}$$

where β is a fit parameter that encodes the noise spectral power and the absolute magnitude of its coupling to the RX qubit and ω_{RX} is the level splitting of the RX qubit. The factor $(|g_{\mathrm{RX}}|/|g_{\mathrm{c,RX}}^{(0)}|)^2$ ensures the proper scaling with Δ for the charge noise coupling.

---

[4] A noise spectrum $S(\omega) \propto \omega^s$ is referred to as ohmic for $s = 1$, sub-ohmic for $s < 1$ (e.g. $1/f$ noise) and super-ohmic for $s > 1$ (Shnirman et al., 2002).

5.4.2 Charge qubit and transmon decoherence

Since the logical qubit states of a charge qubit have a different charge distribution, the qubit is prone to charge noise, which has the same physical origin as for the RX qubit (see subsection 5.4.1.2). In contrast to the RX qubit, it is however not influenced by magnetic field fluctuations. By working at the sweet spot ($\delta = 0$), dephasing due to low-frequency charge noise is reduced. Recently, the decoherence rates for GaAs charge qubits has been decreased by three orders of magnitude (Scarlino et al., 2019b,a) down to a few MHz compared to earlier experiments (Frey et al., 2012, Basset et al., 2013) by engineering the DQD electrostatics such that the qubit electric dipole moment is reduced (Scarlino et al., 2019a). Similar decoherence rates have been reported for Si/SiGe charge qubits and were attributed to the gate design, to low intrinsic charge noise due to a high quality host material (Mi et al., 2017c) as well as to a reduction of externally induced noise by on-chip filtering the quantum dot gate lines (Mi et al., 2017a). In contrast to the RX qubit, the charge qubit decoherence is in this thesis not subject to intensive studies. We therefore follow earlier work with charge qubits in GaAs in Refs. Frey et al., 2012, Stockklauser et al., 2017, Woerkom et al., 2018 and use a charge noise model with a white spectrum. There, the relaxation and dephasing rates are determined as (Frey, 2013)

$$\gamma_{1,\mathrm{CQ}} = \gamma^{(b)}_{\varphi,\mathrm{CQ}} \sin(\theta)^2 + \gamma^{(b)}_{1,\mathrm{CQ}} \cos(\theta)^2 \tag{5.73}$$

$$\gamma_{\varphi,\mathrm{CQ}} = \gamma^{(b)}_{\varphi,\mathrm{CQ}} \cos(\theta)^2 + \gamma^{(b)}_{1,\mathrm{CQ}} \sin(\theta)^2. \tag{5.74}$$

They depend on the qubit mixing angle θ that was defined in subsection 3.1.3 as well as on the bare relaxation and dephasing rates $\gamma^{(b)}_{1,\mathrm{CQ}}$ and $\gamma^{(b)}_{\varphi,\mathrm{CQ}}$, respectively. The charge qubit decoherence rate is then given as $\gamma_{2,\mathrm{CQ}} = \gamma_{1,\mathrm{CQ}}/2 + \gamma_{\varphi,\mathrm{CQ}}$.

While the decoherence rate of the charge and RX qubit is of the order of MHz, two to three orders of magnitude lower rates are routinely achieved for transmon qubits (Andersen et al., 2019). This is likely related to the significantly lower susceptibility of the transmon to charge noise (see subsection 3.3.2) and to the inherent decoherence protection by the superconducting gap (Clarke et al., 2008). One of the possibly limiting decoherence mechanisms for state-of-the-art transmons is parasitic coupling to two-level defects (Müller et al., 2017b) that reside for example in the oxide of the Josephson junctions or at interfaces of dielectrics (Wang et al., 2015). The coherence of the transmon used in this thesis is limited by Purcell decay through the coupled resonator and is taken into account phenomenologically.

5.4.3 Resonator-related decoherence mechanisms

5.4.3.1 Measurement-induced dephasing

While the ac Stark shift introduced in subsection 5.2.1 can be used to measure the averaged number of photons in the resonator and to calibrate the resonator probe line attenuation, it also introduces a decoherence mechanism. Since the resonator photons are in a coherent state, there are fluctuations (shot noise) in the number of photons, which translate via the ac Stark shift into fluctuations of the qubit transition frequency that dephase the qubit. This so-called measurement-induced dephasing (MID) occurs at a rate (Gambetta et al., 2006)

$$\Gamma_{\mathrm{MID}} = \frac{2\bar{n}\kappa_{\mathrm{r}}\chi^2}{\kappa^2/4 + \chi^2 + \Delta_{\mathrm{rp}}^2}, \tag{5.75}$$

where $\Delta_{\mathrm{rp}} \equiv \nu_{\mathrm{r}} - \nu_{\mathrm{p}}$ is the detuning of the probe tone from the resonator resonance and the definition of the other quantities can be found in subsection 5.2.1. For $\kappa \gg \chi$ one recovers the result $\Gamma_{\mathrm{MID}} = 8\bar{n}\chi^2/\kappa_{\mathrm{r}}$ that is typically quoted in literature (see e.g. Ref. Schuster et al., 2005).

5.4.3.2 Purcell decay

The presence of the resonator has another effect on the qubit coherence. Its vacuum fluctuations stimulate qubit relaxation if the qubit and the resonator are on resonance. This phenomenon is named Purcell effect (Purcell et al., 1946) and leads to qubit relaxation at rate (Sete et al., 2014)

$$\Gamma_{\mathrm{P}} = \frac{\kappa_{\mathrm{r}}}{2} - \frac{\sqrt{2}}{2}\sqrt{-\mathrm{A} + \sqrt{\mathrm{A}^2 + (\kappa\Delta_{\mathrm{qr}})^2}} \tag{5.76}$$

with $\mathrm{A} \equiv \Delta_{\mathrm{qr}}^2 + 4g_{\mathrm{q}}^2 - \kappa_{\mathrm{r}}^2/4$. If qubit and resonator are detuned ($|\Delta_{\mathrm{qr}}| > 0$), Purcell decay can be suppressed. In the limit of large qubit resonator detuning $|\Delta_{\mathrm{qr}}| \gg g_{\mathrm{q}}, \kappa_{\mathrm{r}}$, we obtain $\Gamma_{\mathrm{P}} = \kappa_{\mathrm{r}} g_{\mathrm{q}}^2/\Delta_{\mathrm{qr}}^2$, which is typically used in the context of circuit QED (Sete et al., 2014).

Chapter 6

Microwave detection of two-electron double quantum dot spin states

Single electrons confined in quantum dots reveal quantum effects at a fundamental level (Kastner, 1992). The electron wave function can be engineered to investigate phenomena due to the Pauli exclusion principle, like exchange interaction (Tarucha et al., 1996) or spin blockade (see subsection 3.1.4). To deduce information about such phenomena, one can couple the system to electron reservoirs and measure the resulting current (Nowack et al., 2007) or utilize a charge sensor to infer information about the charge state of the system (Elzerman et al., 2003, Barthel et al., 2010). An alternative approach is to probe the photon transmission through a microwave cavity coupling weakly to the electronic states in the quantum dots (Childress et al., 2004, Burkard et al., 2016). This approach has been used to study charge related phenomena (Frey et al., 2012, Petersson et al., 2012, Delbecq et al., 2011, Toida et al., 2013, Deng et al., 2015) and valley physics (Mi et al., 2017b) in quantum dots.

In this chapter we present experiments where we use such a setup with a magnetic field resilient resonator to investigate singlet-triplet spin physics in a DQD with the resonator only. We utilize the fact, that in contrast to the spin-triplet states, spin-singlet states have a finite electric susceptibility and therefore couple to microwave photons (Zheng et al., 2019, Petersson et al., 2012). We then apply an external magnetic field to detect the transition from a spin-singlet to a spin-triplet ground state. In previous experiments, where low-frequency resonant circuits were used (Schroer et al., 2012, House et al., 2015, Betz et al., 2015), this transition was observed in the dispersive regime only. We tune the qubit energy above or below the resonator energy and perform both resonant and dispersive spectroscopy. Subsequently, we map the two-electron singlet-triplet crossover at finite magnetic field with resonant spectroscopy without the need of pulsed gate operations (Petta et al., 2005).

We also present experiments where we apply a source-drain bias and measure the resonator response of the non-equilibrium steady state. With this method, we detect the spin blockade previously observed in transport experiments (Ono et al., 2002, Johnson et al., 2005a) and discover an unconventional spin blockade that involves the absorption of resonator photons.

This chapter is structured as follows: In sections 6.1 and 6.2 we discuss experimental details and basic characterization measurements, respectively. Subsequently we present results for zero and finite bias measurements in sections 6.3-6.4 and compare the latter to a rate-equation model. In most parts of this chapter we closely follow our letter:

Cavity-Detected Spin Blockade in a Few-Electron Double Quantum Dot
A. J. Landig, J. V. Koski, P. Scarlino, C. Reichl, W. Wegscheider, A. Wallraff, K. Ensslin, and T.Ihn, PRL **122**, 213601 (2019)

6.1 Experimental details

In this section we introduce the sample and provide a summary of the sample fabrication. We also discuss the degradation of the resonator quality factor compared to experiments in subsection 4.3.1.3.

6.1.1 Sample

The experiments are performed in the setup presented in chapter 2 with the sample shown in Fig. 6.1. We define a DQD by local electrostatic depletion of the 2DEG in a GaAs/AlGaAs heterostructure with Au gate electrodes. The gate electrodes are designed to be in close proximity in order to prevent regions of floating 2DEG between gate lines, which were found to cause instabilities in the DQD electrostatic potential. A source-drain bias V_{sd} can be applied to the DQD. The voltages V_L and V_R control the charge occupation of the DQD, which is detected with a QPC. V_T is used to tune the interdot tunnel coupling.

One of the gate electrodes [orange in Fig.6.1(a)] is electrically connected close to one end of a $\lambda/2$ CPW resonator with a resonance frequency $\nu_r = 8.33\,\text{GHz}$, a total linewidth $\kappa_r/2\pi = 101\,\text{MHz}$ ($Q_{ld} \approx 80$) and an estimated characteristic impedance $Z_r \approx 1.3\,\text{k}\Omega$. A DC voltage can be applied to this gate line via a DC bias line that

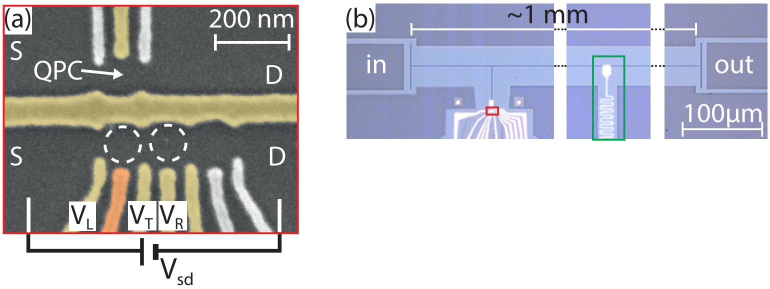

Figure 6.1 Sample. (a) False-colored scanning electron micrograph of the DQD region. A DQD (circles) is formed with the gate lines marked in color. One of the gate lines (orange) extends to the microwave resonator. Source (S) and drain (D) ohmic contacts are marked. A voltage V_{sd} can be applied over the DQD. (b) False-colored optical micrograph indicating NbTiN (dark blue), bare GaAs (light blue) and Au (yellow). The resonator (in) and output (out) ports are labelled. The position of the DQD and the region for DC bias of the resonator are marked with a red and green rectangle, respectively.

electrically connects to the resonator center conductor at half the resonator length (Frey, 2013) [see green rectangle in Fig. 6.1(b)]. The resonator is fabricated from a $h \approx 15\,\mathrm{nm}$ thick and $w \approx 300\,\mathrm{nm}$ wide film of NbTiN, which makes it resilient to parallel magnetic fields of up to $\mathrm{B} = 2\,\mathrm{T}$ (see subsection 4.3.1.4). For the experiments presented in this work, the number of photons in the resonator is about one.

6.1.2 Resonator quality factor

The zero magnetic field quality factor $Q_{ld} \approx 80$ found in subsection 6.1.1 is one order of magnitude lower compared to the value obtained for NbTiN test resonators with a similar resonator design in subsection 4.3.1.3. In the following we discuss two possible explanations for this significant reduction.

First, since the resonator extends to the DQD region, parasitic capacitive coupling between the resonator and the DC gate lines can lead to additional photon loss via these lines. This loss mechanism can be reduced, for example, by engineering low-pass filters for the gate lines (Mi et al., 2017a).

Second, the reduced Q_{ld} may be related to the voltage bias line that was not present for the NbTiN test resonators. This line is fabricated as a $\approx 3.1\,\mathrm{mm}$ long and $\approx 300\,\mathrm{nm}$ wide meander of a Ti(3 nm)/Au(25 nm) film, which provides a high impedance environment for the resonator photons due to the large resistance per unit length of $R_l \approx 5.5\,\mathrm{M\Omega/m}$. To minimize the loss of resonator photons via the bias line, it would ideally be connected to the minimum impedance point of the resonator (Chen et al., 2011), which is the position of the node of the resonator voltage mode. For the fundamental mode of a symmetrically coupled $\lambda/2$ resonator, this voltage node is at half the resonator length. Since the resonator line that extends to the DQD [see Fig. 6.1(b)] can modify the voltage mode profile, the location of the voltage node is potentially offset from the ideal position. Consequently, the resonator impedance at the connection point to the bias line, which is at half the resonator length for the sample in Fig. 6.1(b), would not be minimal. This would increases the photon loss via the bias line. To mitigate this effect in the future, simulations of the resonator voltage profile could be performed, where the design of the DQD fine gates is probably relevant since they couple capacitively to the resonator. Alternative experimental approaches are to symmetrize the system by coupling the resonator to a second DQD at the opposite end of the resonator or to increase the bias line impedance via its geometry or by the choice of a material with a larger specific resistivity such as platinum (Van Woerkom et al., 2017).

A significant reduction of Q_{int} due to the bias line was not reported for a $50\,\Omega$ resonator in Ref. Frey, 2013. We suspect that the positioning of the bias line is more critical for high impedance resonators compared to $50\,\Omega$ resonators, since the voltage fluctuations in the latter are smaller.

6.1.3 Sample fabrication

The sample fabrication starts by patterning a global marker structure with a 100 keV EBL system on top of the heterostructure. All subsequent steps are aligned with respect to these markers. Consecutively, we define a mesa structure for the DQD and its source and drain leads by photolitography and wet etching. The etching depth of ≈ 80 nm exceeds the depth of the Si dopant layer to ensure that the 2DEG is removed in the etched areas. In the following processing step, we contact the remaining 2DEG electrically by patterning ohmic contacts at the edges of the mesa with photolithography, followed by evaporating layers of germanium (Ge), Au and nickel (Ni), which are subsequently annealed. We then use photolithography to define the macroscopic gate line structure as well as several pads that will serve as electrical connections between NbTiN and EBL defined Au structures. Subsequently we evaporate Ti(5 nm)/Au(55 nm), where Ti serves as an adhesion layer. Next, the NbTiN regions are sputtered on top of a photolithographically defined structure. We then partially remove the NbTiN with RIE in regions that are patterned with the 100 keV EBL system in order to define the resonator structure. In the last step, we evaporate the DQD fine gates as a Ti(3 nm)/Au(25 nm) layer on an EBL defined structure. Note that for this last step we use a 30 keV EBL system that provides a sufficient precision within a write field size of $200 \times 200\,\mu\mathrm{m}^2$. For more details about the fabrication process we refer to Appendix C.1.

6.2 Basic characterization

We set $\mathrm{V_{sd}} = 0$, $\mathrm{B} = 0$ and tune the DQD into a regime where the relevant charge states are $(0,1)$, $(0,2)$, $(1,1)$ and $(1,2)$. As introduced in subsection 3.1.3, the tunnel coupled $(0,2)$ and $(1,1)$ charge states with singlet spin configuration form a charge qubit. The qubit energy $\mathrm{E_q} = \sqrt{\delta^2 + (2t)^2}$ can be tuned electrostatically: the voltages $\mathrm{V_L}$ and $\mathrm{V_R}$ control the bare energy detuning $\delta = \mathrm{E}(1,1) - \mathrm{E}(0,2)$ of the $(0,2)$ and $(1,1)$ charge states, and the voltage $\mathrm{V_T}$ in Fig. 6.1(a) determines the tunnel coupling t. For $2t \leq h\nu_\mathrm{r}$, the qubit and resonator energies intersect at the resonant detuning values $\delta_\pm = \pm\sqrt{(h\nu_\mathrm{r})^2 - (2t)^2}$ [see top panel in Fig. 6.2(a)].

By probing the resonator transmission $|\mathrm{S}_{21}|^2$ at the bare resonance frequency ν_r as a

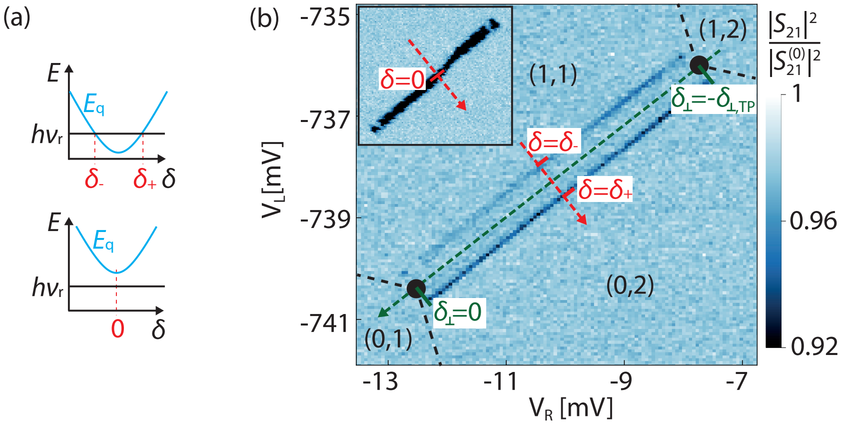

Figure 6.2 Charge qubit dispersion and resonator response. (a) Bare charge qubit energy $\mathrm{E_q}$ (blue) and resonator energy $h\nu_\mathrm{r}$ (black) as a function of δ for $2t < h\nu_\mathrm{r}$ (top) and $2t > h\nu_\mathrm{r}$ (bottom). (b) Resonator transmission $|\mathrm{S}_{21}|^2$ on resonance as a function of $\mathrm{V_L}$ and $\mathrm{V_R}$ at $\mathrm{B} = 0$ and $\mathrm{V_{sd}} = 0$ normalized by the background value $|\mathrm{S}_{21}^{(0)}|^2$. The interdot tunnel coupling is $t/h = 3.4\,\mathrm{GHz}$ ($2t < h\nu_\mathrm{r}$) for the main figure and $t/h = 4.5\,\mathrm{GHz}$ ($2t > h\nu_\mathrm{r}$) for the inset. Changing voltages along the dashed green line or the dashed red line independently tunes $\delta_\perp$ or δ, respectively. The two triple points are each marked with a black dot.

function of $\mathrm{V_L}$ and $\mathrm{V_R}$, we observe two lines with reduced transmission at $\delta = \delta_\pm$ in the main panel in Fig. 6.2(b). They are due to electric dipole interaction of the resonator electric field with the charge qubit in the DQD, causing a shift of the resonator resonance frequency (Childress et al., 2004). Note that the measurement in Fig. 6.2(b) is identical to the measurement in Fig. 3.5(a), where the QPC response was indicated instead of the resonator transmission. For $2t > h\nu_\mathrm{r}$, the resonator interacts dispersively with the qubit [bottom panel in Fig. 6.2(a)], evident as a single line with reduced transmission at $\delta = 0$ in the inset of Fig. 6.2(b). In the following we refer to the reduced transmission as the "resonator response". As expected, the resonator response in Fig. 6.2(b) is visible once the charge qubit is isolated from the reservoirs. This is for $-\delta_{\perp,\mathrm{TP}} < \delta < 0$, where $\delta_\perp = 0.5[\mathrm{E}(1,1)+\mathrm{E}(0,2)]-\mathrm{E}(0,1)$ ranges between the triple points. Here, we extract $\delta_{\perp,\mathrm{TP}} \simeq 510\,\mu\mathrm{eV}\,(123\,\mathrm{GHz})$.

To characterize the coupled qubit-resonator system, we measure in Fig. 6.3 the in-phase $\tilde{\mathrm{I}}$ and quadrature $\tilde{\mathrm{Q}}$ components of the complex resonator transmission amplitude $\mathrm{S}_{21} = \tilde{\mathrm{I}} + i\tilde{\mathrm{Q}}$ for multiple tunnel gate voltages $\mathrm{V_T}$ along the δ-axis marked in red in Fig. 6.2(b), i.e. for $\delta_\perp \simeq -\delta_{\perp,\mathrm{TP}}/2$. Note that the x-axes in Fig. 6.3 are converted into energy with the lever arm $\alpha_\delta = 0.046 \pm 0.005$, which was extracted from charge stability diagram measurements. The parameters $\tilde{\mathrm{I}}$ and $\tilde{\mathrm{Q}}$ in Fig. 6.3 are calculated from the raw data as follows. We measure the amplitude $\hat{\mathrm{V}}$ and phase difference $\Delta\phi$ of the microwave signal transmitted through the resonator with the heterodyne detection setup presented in chapter 2. We then define $\tilde{\mathrm{I}} \equiv \Re[\hat{\mathrm{V}}/\hat{\mathrm{V}}_0 \cdot e^{i(\Delta\phi-\Delta\phi_0)}]$ and $\tilde{\mathrm{Q}} \equiv \Im[\hat{\mathrm{V}}/\hat{\mathrm{V}}_0 \cdot e^{i(\Delta\phi-\Delta\phi_0)}]$, where $\hat{\mathrm{V}}_0$ is the background signal measured at $\delta \gg 0$ and $\Delta\phi_0$ is a setup related phase offset.

To describe the experimental data in Fig. 6.3 theoretically, we use the input-output model derived in subsection 5.3.2 together with the white-noise decoherence model from subsection 5.4.2. The theoretical transmission amplitude S_{21} relates to the experimentally measured quantities in Fig. 6.3 according to $\tilde{\mathrm{I}} = \Re[|\mathrm{S}_{21}|/\mathrm{S}_{21}^{(0)} \cdot e^{i\arg(\mathrm{S}_{21})}]$ and $\tilde{\mathrm{Q}} = \Im[|\mathrm{S}_{21}|/\mathrm{S}_{21}^{(0)} \cdot e^{i\arg(\mathrm{S}_{21})}]$, where $\mathrm{S}_{21}^{(0)} = |\mathrm{S}_{21}(g_{\mathrm{CQ}}^{(0)} \to 0)|$ is obtained for zero qubit-resonator coupling. We perform a simultaneous fit to thirteen $\tilde{\mathrm{I}}$ and $\tilde{\mathrm{Q}}$ datasets (in parts shown in Fig. 6.3), which are obtained for different $\mathrm{V_T}$. Free parameters that are the same for all datasets are $\gamma_{1,\mathrm{CQ}}^{(\mathrm{b})}$, $\gamma_{\varphi,\mathrm{CQ}}^{(\mathrm{b})}$ (defined in subsection 5.4.2) and $\mathrm{T_e}$. The coupling strength $g_{\mathrm{CQ}}^{(0)}$ and the tunnel coupling t are additional free parameters, which can, however, vary for the datasets: $\mathrm{G_{CQ}} \equiv \{g_{\mathrm{CQ},1}^{(0)}, g_{\mathrm{CQ},2}^{(0)}, ..., g_{\mathrm{CQ},13}^{(0)}\}$, $\tilde{\mathrm{T}} = \{t_1, t_2, ..., t_{13}\}$. We obtain $\gamma_{1,\mathrm{CQ}}^{(\mathrm{b})}/2\pi \simeq 84\,\mathrm{MHz}$, $\gamma_{\varphi,\mathrm{CQ}}^{(\mathrm{b})}/2\pi \simeq 315\,\mathrm{MHz}$, $\mathrm{T_e} \simeq 60\,\mathrm{mK}$, the tunnel couplings as specified in Fig. 6.3 and an averaged coupling strength $g_{\mathrm{CQ}}^{(0)}/2\pi = 28 \pm 2\,\mathrm{MHz}$ with the error being the standard deviation of the fitted values in $\mathrm{G_{CQ}}$. For all qubit configurations analyzed in this work beyond the thirteen mentioned above, we perform a simultaneous fit to $\tilde{\mathrm{I}}$ and $\tilde{\mathrm{Q}}$ with the free parameters t and $g_{\mathrm{CQ}}^{(0)}$, where we use

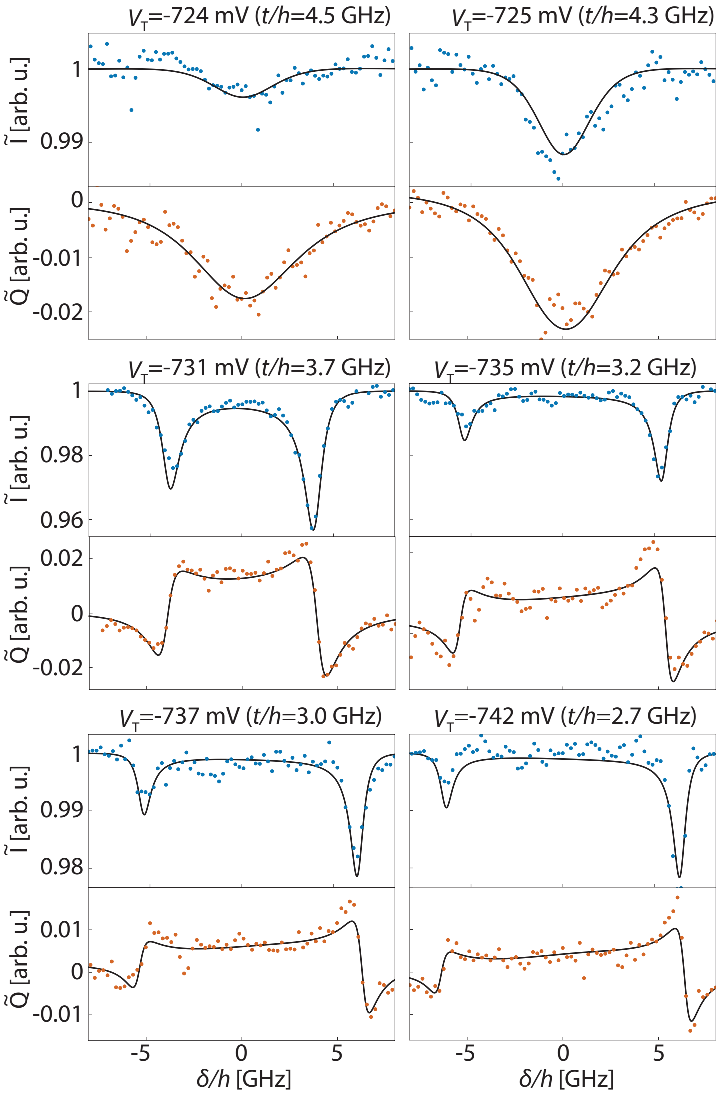

Figure 6.3 Qubit parameter extraction. In-phase $\tilde{\mathrm{I}}$ (blue) and quadrature $\tilde{\mathrm{Q}}$ (orange) components of complex resonator transmission amplitude probed on resonance as a function of δ. The corresponding tunnel gate voltages V_T and extracted tunnel couplings t are indicated. The solid lines are a fit to an input-output theory model.

the constraint $g_{\mathrm{CQ}}^{(0)}/2\pi \in [26, 30]\,\mathrm{MHz}$. Since $g_{\mathrm{CQ}}^{(0)} \ll \gamma_{2,\mathrm{CQ}}, \kappa_{\mathrm{r}}$, the resonator acts as a weakly coupled probe that does not influence the DQD states coherently (Koski et al., 2018).

6.3 Zero bias measurements

In this section we present measurements performed at zero source-drain bias. We report the experimental signature of the system transitioning from a spin-singlet to a spin-triplet state as a function of magnetic field in subsection 6.3.1 and subsequently use this signature in subsection 6.3.2 to map the singlet-triplet intersection point. We also discuss singlet-triplet mixing and the influence of the magnetic field on tunnel coupling in subsections 6.3.3 and 6.3.4, respectively.

6.3.1 Resonator spin blockade

We probe the resonator at $\nu_{\mathrm{p}} \simeq \nu_{\mathrm{r}}$ as a function of δ and B for $\delta_{\perp} \simeq -\delta_{\mathrm{TP}}/2$ and $\mathrm{V}_{\mathrm{sd}} = 0$. Note that the dependence $\nu_r(\mathrm{B})$ (see subsection 4.3.1.4) was approximately accounted for, since $|\nu_r(\mathrm{B}) - \nu_p(\mathrm{B})| \leq \kappa_{\mathrm{r}}(\mathrm{B})/10$ within the magnetic field range from 0 to 1.8 T, which is relevant for our experiments. In Figure 6.4(a) we show the experimental result for dispersive interaction ($2t > h\nu_{\mathrm{r}}$). Like in the inset of Fig. 6.2(b), we observe a single dip in the transmission at $\delta = 0$ for $\mathrm{B} = 0$. The dip vanishes along a slanted line at $\mathrm{B} \simeq 1\,\mathrm{T}$ in Fig. 6.4(a). For resonant interaction ($2t < h\nu_{\mathrm{r}}$) in Fig. 6.4(b), the two transmission dips at $\mathrm{B} = 0$ [cf. Fig. 6.2(b)] vanish at different magnetic fields. The simulations in Figs. 6.4(b)-(c) obtained from the transmission amplitude in Eq. (5.56) together with the thermal state occupation in Eq. (5.55) are in good qualitative agreement with the corresponding experimental results in Figs. 6.4(a)-(b). We use the values for the parameters $g_{\mathrm{CQ}}^{(0)}, \gamma_{1,\mathrm{CQ}}^{(\mathrm{b})}, \gamma_{\varphi,\mathrm{CQ}}^{(\mathrm{b})}$ and T_e obtained from the fits in section 6.2 as well as the g-factor $g = -0.4$ (Nowack et al., 2007) for the calculation. We also take the magnetic field dependence of the resonator linewidth $\kappa_{\mathrm{r}}(\mathrm{B})$ and the resonance frequency $\nu_r(\mathrm{B})$ into account (see subsection 4.3.1.4). Note that the small jumps of the transmission minima in Fig. 6.4(a)-(b) with δ as a function of B are due to sample instabilities and therefore not captured by the simulations.

We explain the observation in Figs. 6.4(a)-(b) qualitatively by considering the spin character of the two electron DQD states. The relevant spin-singlet states $(0,2)\mathrm{S}$ and $(1,1)\mathrm{S}$ as well as the spin-triplet states $(1,1)\mathrm{T}_0$, $(1,1)\mathrm{T}_+$ and $(1,1)\mathrm{T}_-$ were in introduced in subsection 3.1.4. In Fig. 6.4(e) and Fig. 6.4(f) we show the singlet-triplet energy spectrum as a function of δ for $2t > h\nu_r$ and for $2t < h\nu_r$, respectively. The resonator weakly probes the ground state of the system at the detuning values $\delta = \delta_\pm$ and $\delta = 0$ for $2t < h\nu_\mathrm{r}$ and $2t \geq h\nu_\mathrm{r}$, respectively. For B = 0, the ground state of the system is

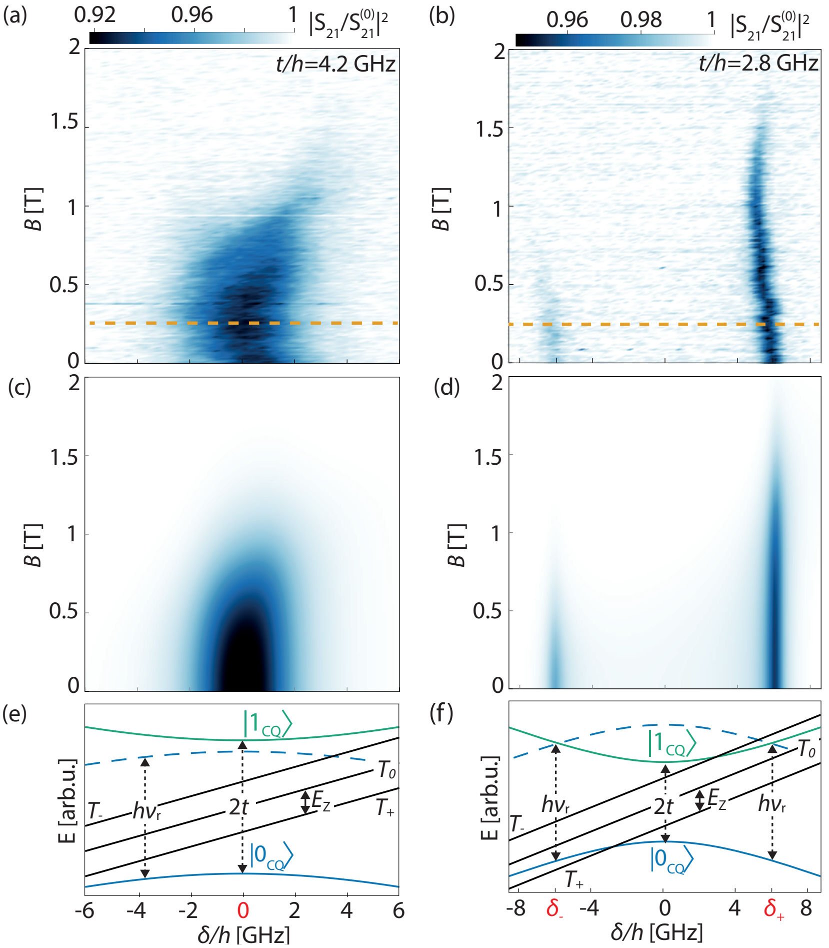

Figure 6.4 Zero bias magnetic field dependence. Left (right) column: $2t > h\nu_\mathrm{r}$ ($2t < h\nu_\mathrm{r}$). (a)-(b) Normalized resonator transmission at $\nu_\mathrm{p} \simeq \nu_\mathrm{r}$. $|S_{21}^{(0)}|^2$ is the bare resonator transmission for a given B. The data obtained from a cut at the orange dashed lines is shown in Fig. 6.5. (c)-(d) Input-output theory calculation for the parameters in (a)-(b). (e)-(f) Singlet-triplet energy spectrum as a function of δ for B = 300 mT. The dashed line indicates the qubit ground state energy offset by the resonator energy.

the qubit ground state $|0_{\mathrm{CQ}}\rangle$. When increasing the magnetic field, $(1,1)\mathrm{T}_{+}$ is lowered in energy with respect to $|0_{\mathrm{CQ}}\rangle$ by the Zeeman energy $\mathrm{E_Z}$ and eventually becomes the ground state at $\delta = 0$ and at $\delta = \delta_{\pm}$. As $(1,1)\mathrm{T}_{+}$ has no electrical dipole moment, the resonator response at $\delta = 0$ in Fig. 6.4(a) and at $\delta = \delta_{\pm}$ in Fig. 6.4(b) vanishes. In the following we call this phenomenon “spin blockade of the resonator response” in analogy to the spin-blockade phenomenon in electron transport (Ono et al., 2002).

6.3.2 Singlet-triplet intersection point

Figures 6.5(a)-(b) show cuts of the data in Figs. 6.4(a)-(b) at $\mathrm{B} = 300\,\mathrm{mT}$. The transmission as a function of δ has a Lorentzian lineshape with either a single dip of amplitude A_0^2 at $\delta = 0$ for $2t \geq h\nu_{\mathrm{r}}$ in Fig. 6.5(a) or two dips of amplitudes $\mathrm{A}_{\pm}^2$ at $\delta = \delta_{\pm}$ for $2t < h\nu_{\mathrm{r}}$ in Fig. 6.5(b). Note that the δ—position of the minima is a free fitting parameter to account for the sample instabilities discussed in the context of Fig. 6.4(a)-(b).

The magnetic field dependence of A_0^2 and $\mathrm{A}_{\pm}^2$ is depicted in Fig. 6.6(a). We use a Fermi Golden rule approach to describe the observed behavior theoretically, since the resonator acts as a weak probe for singlet state transitions. In this picture, the Fermi Golden rule determines the rate at which a photon in the resonator and qubit interact as

$$\Gamma_{\mathrm{ph}-|0_{\mathrm{CQ}}\rangle} = \frac{2\pi}{\hbar} |\langle 1_{\mathrm{CQ}}| \hat{\mathrm{H}}_{\mathrm{int,CQ}} |0_{\mathrm{CQ}}\rangle|^2 p_{|0_{\mathrm{CQ}}\rangle} = \frac{2\pi}{\hbar} \left(g_{\mathrm{CQ}}^{(0)}\right)^2 \sin(\theta)^2 p_{|0_{\mathrm{CQ}}\rangle} \tag{6.1}$$

with the electric dipole interaction Hamiltonian $\hat{\mathrm{H}}_{\mathrm{int,CQ}}$ from Eq. (5.6) and the ground state occupation probability $p_{|0_{\mathrm{CQ}}\rangle}$. If the qubit is in the ground state, it can be excited by absorbing a photon from the resonator. We can model this process with a classical

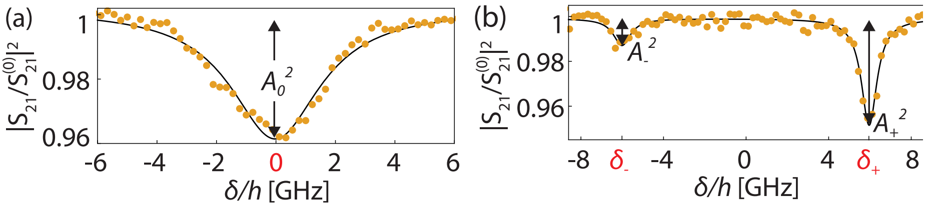

Figure 6.5 Extraction of response amplitude. (a) Cut of the data in Fig. 6.4(a) at $\mathrm{B} = 300\,\mathrm{mT}$. A_0^2 is extracted from a Lorentzian fit (solid line). (b) Cut of Fig. 6.4(b) at $\mathrm{B} = 300\,\mathrm{mT}$ with two Lorentzian fits (solid line) of amplitudes $\mathrm{A}_{\pm}^2$ at $\delta \approx \delta_{\pm}$.

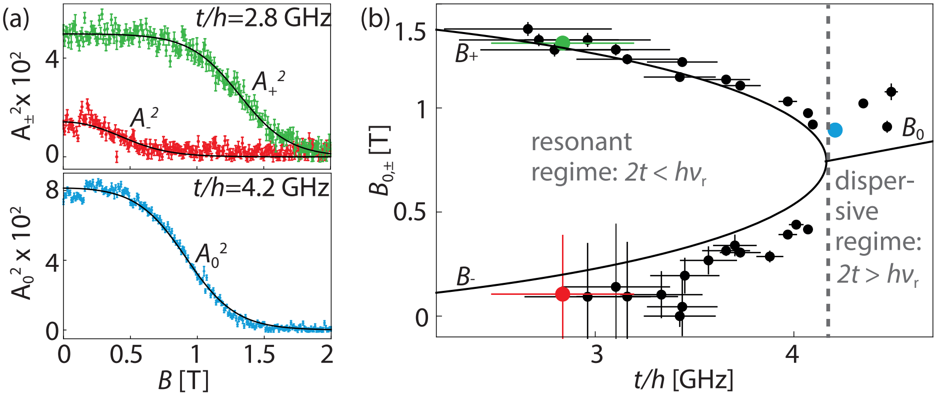

Figure 6.6 Singlet-triplet intersection fields. (a) $A_0^2(B)$ (blue), $A_+^2(B)$ (green) and $A_-^2(B)$ (red) with standard errors and theory fits (solid lines). (b) $B_0(t)$ and $B_\pm(t)$ compared to theory (solid line). The data points extracted from the fits in (a) are marked in color. The error bars in t account for the δ lever arm error. For $B_{0,+}$ we show the standard errors of the fits as in (a), for B_- maximum error estimates from repeated measurements.

rate equation. The resonator can have one or zero photons with probabilities p_1 or p_0, respectively. In addition to resonator-qubit interaction, the number of photons in the resonator decreases at rate κ_{int} by decay in the resonator. In steady state, the rate equation is

$$\dot{p}_1 = \Gamma_P p_0 - (\Gamma_{\text{ph}-|0_{\text{CQ}}\rangle} + \kappa_{\text{int}}) p_1 = 0, \tag{6.2}$$

where Γ_P is the rate at which the resonator probe tone feeds photons into the resonator. With $p_0 = 1 - p_1$, we arrive at

$$p_1 = \frac{\Gamma_P}{\Gamma_{\text{ph}-|0_{\text{CQ}}\rangle} + \Gamma_P + \kappa_{\text{int}}}. \tag{6.3}$$

The transmission of a two-port coupled resonator is given as

$$|S_{21}|^2 \propto \frac{\kappa_{\text{ext}}}{2} p_1 = \frac{\Gamma_P \kappa_{\text{ext}}/2}{\Gamma_{\text{ph}-|0_{\text{CQ}}\rangle} + \Gamma_P + \kappa_{\text{int}}}. \tag{6.4}$$

For $\Gamma_{ph-|0_{\text{CQ}}\rangle} \ll \kappa_{\text{int}}, \Gamma_P$, we finally obtain with Eqns. (6.1) and (6.4)

$$|S_{21}|^2 \propto 1 - C p_{|0_{\text{CQ}}\rangle}, \tag{6.5}$$

where C is a constant. We now express the occupation probability of $|0_{\mathrm{CQ}}\rangle$ in thermal equilibrium from Eq. (5.55) as

$$p_{|0_{\mathrm{CQ}}\rangle}(\mathrm{B}_\delta) = 1/\left(1 + e^{\frac{-g\mu_{\mathrm{B}}\mathrm{B}_\delta}{k_{\mathrm{B}}\mathrm{T}_{\mathrm{e}}}} + e^{\frac{-g\mu_{\mathrm{B}}(\mathrm{B}_\delta - \mathrm{B})}{k_{\mathrm{B}}\mathrm{T}_{\mathrm{e}}}} + e^{\frac{-g\mu_{\mathrm{B}}(\mathrm{B}_\delta + \mathrm{B})}{k_{\mathrm{B}}\mathrm{T}_{\mathrm{e}}}}\right),$$

where B_δ is the $|0_{\mathrm{CQ}}\rangle - (1,1)\mathrm{T}_+$ intersection field at δ, i.e. for $\mathrm{B} > \mathrm{B}_\delta$, $(1,1)\mathrm{T}_+$ is lower in energy than $|0_{\mathrm{CQ}}\rangle$ at δ. From a fit of $\mathrm{C} \cdot p_{|0_{\mathrm{CQ}}\rangle}$ to the data in Fig. 6.6(a) we extract B_+ at δ_+ and B_- at δ_- for resonant interaction (top panel) and B_0 at $\delta = 0$ for dispersive interaction (bottom panel). The constant C as well as B_0 and $\mathrm{B}_\pm$ are free parameters. Fixed parameters are $g = -0.4$, the electron temperature $\mathrm{T}_{\mathrm{e}} \simeq 60\,\mathrm{mK}\,(1.3\,\mathrm{GHz})$ and t obtained from the input-output theory fit at $\mathrm{B} = 0$ discussed in the context of Fig. 6.3.

A summary of the analysis for multiple t is shown in Fig. 6.6(b). We obtain three branches for the three $|0_{\mathrm{CQ}}\rangle - (1,1)\mathrm{T}_+$ intersection fields B_+, B_- and B_0. The values of $g\mu_{\mathrm{B}}\mathrm{B}_\pm$ are a direct spectroscopic measurement of the $|0_{\mathrm{CQ}}\rangle - (1,1)\mathrm{T}_+$ intersection point. The theory curve in Fig. 6.6(b) is calculated from the singlet-triplet energy spectrum. There is a good agreement between this model and the experimental data over a large range of t.

6.3.3 Influence of singlet-triplet mixing

In this section we discuss the observation of a non-monotonic decrease of A_-^2 with magnetic field, which we relate to singlet-triplet mixing. The observation is shown in two exemplary datasets for different tunnel couplings in Fig. 6.7(a). With increasing magnetic field we observe a dip in A_-^2 (red arrow) followed by a peak (orange arrow). Note that this behavior is also observed for $\mathrm{A}_-^2(\mathrm{B})$ in the top panel in Fig. 6.6(a). Since our fit function $\mathrm{A}_-(\mathrm{B}) = \mathrm{C} \cdot p_{|0_{\mathrm{CQ}}\rangle}(\mathrm{B})$ is monotonically decreasing with B it deviates from the experimentally observed structure [see black line in Fig. 6.7(a)]. This leads to a systematic error for B_- that is obtained from the fits [see Fig. 6.6(b)].

The extracted dip and peak positions for various tunnel couplings are indicated in Fig. 6.7(b). The theory curve for B_-, i.e. the $|0_{\mathrm{CQ}}\rangle - (1,1)\mathrm{T}_+$ intersection field at negative resonant detuning δ_-, overlaps with the experimental peak positions. Hence, the observed structure could be related to $|0_{\mathrm{CQ}}\rangle - (1,1)\mathrm{T}_+$ mixing [see black circle in inset of Fig. 6.7(a)]. We suspect that the hybridization results in a reduced charge noise sensitivity of the qubit, since $(1,1)\mathrm{T}_+$ has equal charge distributions. As a consequence, the qubit coherence is increased and we observe an enhanced signal in the resonator response (peak in A_-^2).

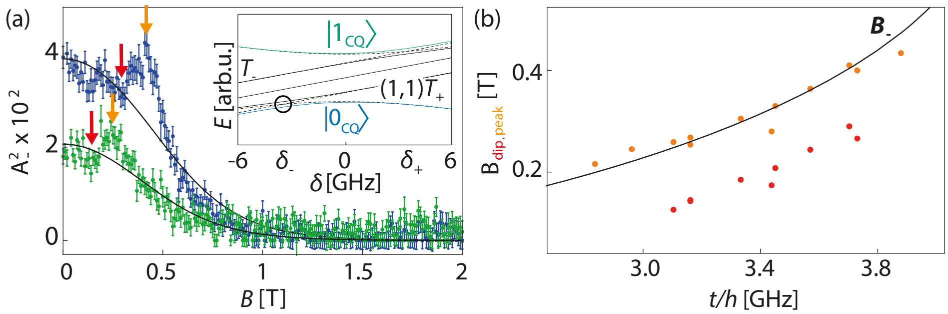

Figure 6.7 Signature of singlet-triplet mixing. (a) Magnetic field dependence of A^2_- (points) with fit (solid line) for $t/h = 3.2\,\mathrm{GHz}$ in green and $t/h = 3.7\,\mathrm{GHz}$ in blue. Inset: Singlet-triplet spectrum for $t/h = 3.7\,\mathrm{GHz}$ and $\mathrm{B} = \mathrm{B}_-$ as a function of detuning δ as solid (dashed) lines in the presence (absence) of singlet-triplet mixing. The point where $|0_{\mathrm{CQ}}\rangle$ and $(1,1)\mathrm{T}_+$ form an avoided crossing is marked with a circle. (b) Positions of peak and dip structures in $\mathrm{A}_-(\mathrm{B})^2$ as a function of tunnel coupling t.

6.3.4 Magnetic-field-dependent tunnel coupling

In this section we discuss a feature observed in the data in Fig. 6.4(a), which is a splitting of the transmission dip in two at $\mathrm{B} \simeq 1\mathrm{T}$. We attribute this effect to a dependence of the tunnel coupling on the magnetic field. As the magnetic field increases, the wave functions tend to localize, decreasing the tunnel coupling. The visibility of this effect is pronounced in Fig. 6.4(a), where $2t = 8.4\,\mathrm{GHz} \gtrsim \nu_\mathrm{r} = 8.33\,\mathrm{GHz}$ at $\mathrm{B} = 0$. In Fig. 6.8 we simulate the resonator response as in Fig. 6.4(c), however with a magnetic-field-dependent tunnel coupling $t(\mathrm{B})/h = t(\mathrm{B}=0)/h - 0.1\,\mathrm{GHz/T} \times \mathrm{B}$. The simulation result qualitatively agrees with the experimental observation of split peaks in Fig. 6.4(a).

6.4 Finite bias measurements

We investigate the coupled DQD-resonator system for $t/h = 3.7\,\mathrm{GHz}$ ($2t < h\nu_\mathrm{r}$) at $\mathrm{B} = 800\,\mathrm{mT}$ in the presence of positive and negative source-drain bias with $|\mathrm{V}_\mathrm{sd}| = 300\,\mu\mathrm{V}$ by measuring the resonant resonator transmission. Note that the DC current through the DQD is below the limit that can be detected with our setup ($\simeq 1\,\mathrm{pA}$). The dominant energy scales for the measurements are $\delta_{\perp,\mathrm{TP}}$ and $e\mathrm{V}_\mathrm{sd}$ since $\delta_{\perp,\mathrm{TP}} > e\mathrm{V}_\mathrm{sd} \gg h\nu_r > 2t > \mathrm{E}_\mathrm{Z} > k_\mathrm{B}\mathrm{T}_\mathrm{e}$.

This section is structured as follows: We present experiments at positive and negative

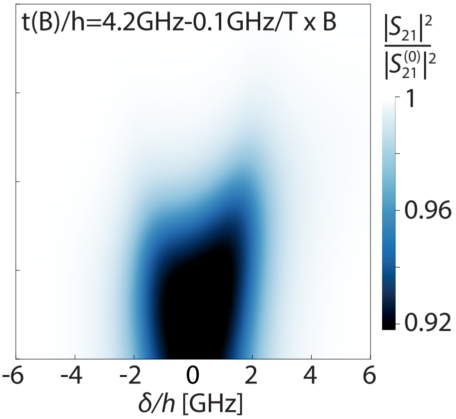

Figure 6.8 Simulation with $t(\mathrm{B})$. Input-output theory simulation of the resonator transmission identical to Fig. 6.4(c) except for the tunnel coupling dependence $t(\mathrm{B})/h = 4.2\,\mathrm{GHz} - 0.1\,\mathrm{GHz/T} \times \mathrm{B}$.

bias voltage in subsections 6.4.1 and 6.4.2, respectively. These measurements are subsequently described theoretically in subsection 6.4.3. In subsection 6.4.4 we compare experiment with simulation.

6.4.1 Positive source-drain bias

We measure the resonant resonator transmission as a function of $\delta_\perp$ and δ for $\mathrm{V}_{\mathrm{sd}} = 300\,\mu\mathrm{V}$ in Fig. 6.9. The bias window is relevant where transport through the DQD that involves the $(0,1)$ (region A) and $(1,2)$ (region C) charge states occurs. At $\delta = 0$, the extent of the bias window in $\delta_\perp$ is $e\mathrm{V}_{\mathrm{sd}}$. We observe a resonator response in Fig. 6.9 at $\delta = \delta_\pm$ like in the thermal case [cf. Fig. 6.2(b)]. However, the response is suppressed in certain intervals of $\delta_\perp$. While most properties of the signal are immediately evident from the corresponding energy diagrams, we highlight several regimes in Fig. 6.9 and schematically illustrate the tunneling processes leading to the observations in these regions in Figs. 6.10-6.11. Unless stated otherwise we omit the hybridization of the $(0,2)$ and $(1,1)$ charge states as well as the Zeeman splitting of $(0,1)$ and $(1,2)$ for the qualitative discussion below, but consider them in the simulations.

We first discuss region B in Fig. 6.9. There, the DQD has a two-electron ground state and the bias is irrelevant. Hence, the zero bias situation discussed in section 6.3 applies: we observe a resonator response at δ_+ and spin blockade of the resonator response at δ_- (cf. Fig. 6.4(b) for $\mathrm{B} \gtrsim 0.5\,\mathrm{T}$).

The spin blockade of the resonator response is lifted in the region outlined in green in Fig. 6.9 by increasing $\delta_\perp$ such that $(0,1)$ is within the bias window (region A). At $\delta_\perp \simeq -|eV_{sd}/2| + h\nu_r/2$ (green star in Fig. 6.9), the electrochemical potential of $(1,1)T_+$ is aligned with μ_{dr} as indicated in Fig. 6.10(a). Hence, the tunneling sequence $(1,1)T_+ \rightarrow (0,1) \rightarrow (0,2)S$ is possible [1.-2. in Fig. 6.10(a)], which leaves the system in $(0,2)S$ that can make a transition to $(1,1)S$ by photon emission into the resonator or by phonon emission into the substrate [3. in Fig. 6.10(a)]. When increasing $\delta_\perp$, the DQD electrochemical potentials indicated in Fig. 6.10(a) rise. The above tunneling sequence is possible until $\delta_\perp \simeq |eV_{sd}/2| - h\nu_r/2$, where the electrochemical potential of $(0,2)S$ is on resonance with μ_s (upper edge of green region in Fig. 6.9). For larger $\delta_\perp$, $(0,1) \rightarrow (0,2)S$ is suppressed and the $(0,1)$ state becomes the ground state of the system, which does not interact with the resonator.

For symmetric tunneling rates Γ_{rL} to the left and Γ_{rR} to the right reservoir, both region A and region C in Fig. 6.9 would have the same resonator response, as transport cycles of electrons that involve $(0,1)$ (region A) are symmetric to transport cycles of holes that involve $(1,2)$ (region C). We have chosen asymmetric rates $\Gamma_{rR} \gg \Gamma_{rL}$ for our measurements such that Γ_{rL} is comparable to the spin-flip rate Γ_{sf}. This allows us to quantify the ratio Γ_{sf}/Γ_{rL} in subsection 6.4.4. For positive bias, where electrons enter the DQD from the right lead [cf. Fig. 6.10(a)], the asymmetry leads to a dominant population of the $(1,2)$ charge state in region C, which does not interact with the

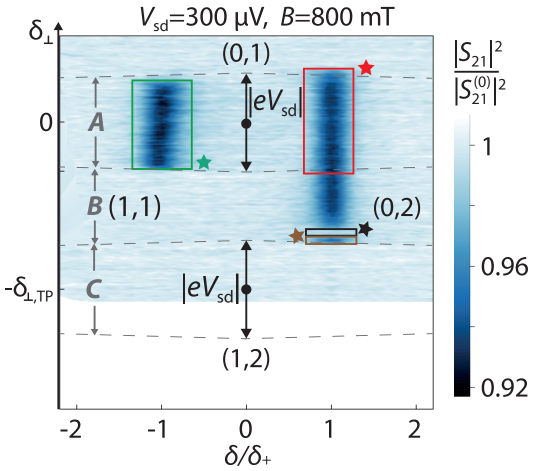

Figure 6.9 Positive bias data. Normalized resonator transmission at $\nu_p \simeq \nu_r$ as a function of δ/δ_+ and $\delta_\perp$ for $B = 800\,\mathrm{mT}$, $t/h = 3.7\,\mathrm{GHz}$ and $V_{sd} = 300\,\mu\mathrm{V}$. The dots indicate the zero bias triple points.

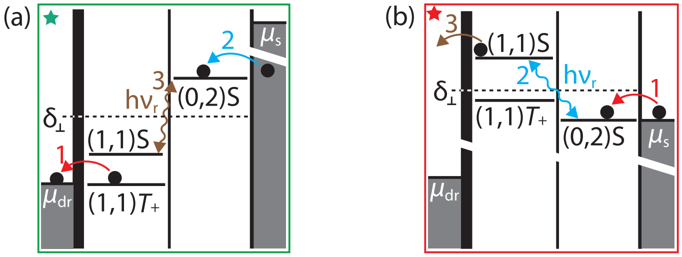

Figure 6.10 DQD diagrams for positive bias. Energy level diagrams with the source (μ_s), drain (μ_{dr}) and DQD state electrochemical potentials at $\delta_\perp$ indicated by the corresponding star in Fig. 6.9. The DQD states electrochemical potentials are shown with respect to $(0,1)$.

resonator.

Next we consider the region at δ_+ marked in red in Fig. 6.9, where the spin blockade of the resonator response is lifted. At $\delta_\perp = |eV_{sd}/2| + h\nu_r/2$ labelled with a red star in Fig. 6.9, $\mu[(0,2)S] = \mu_s$ such that the transition $(0,1) \rightarrow (0,2)S$ is possible by tunneling into the DQD from the right lead [1. in Fig. 6.10(b)]. As a next step, the absorption of a resonator photon leaves the DQD in $(1,1)S$ [2. in Fig. 6.10(b)]. Hence, a resonator response is visible. The tunneling cycle is completed, because an electron can tunnel from the DQD to the left lead, resulting in a $(0,1)$ charge state [3. in Fig. 6.10(b)]. By decreasing $\delta_\perp$, above tunneling cycle is possible until $(1,1)S$ is resonant with μ_{dr} at $\delta_\perp = -|eV_{sd}/2| - h\nu_r/2$ [lower boundary of red rectangle in Fig. 6.9]. For smaller $\delta_\perp$, $(0,1)$ is outside the bias window and a resonator response is visible due to thermal occupation of the DQD states.

By further decreasing $\delta_\perp$, the resonator response vanishes in the region indicated in black in Fig. 6.9 due to the spin blockade usually considered in transport experiments, which is however here triggered by the absorption of a resonator photon. At $\delta_\perp \simeq -\delta_{\perp,TP} + |eV_{sd}/2| + h\nu_r/2$ marked with a black star in Fig. 6.9 and shown in Fig. 6.11(a), an electron can enter the DQD from the right lead and occupy $(1,2)$ because $\mu[(1,2)_{11S}] = \mu_s$ [2. in Fig. 6.11(a)]. This tunneling process is triggered by absorption of a resonator photon which excites the $(0,2)S$ to $(1,1)S$ transition [1. in Fig. 6.11(a)]. In a subsequent step, an electron can tunnel out to the right lead and leave the system in $(1,1)T_+$ [3. in Fig. 6.11(a)]. Consequently, the system is spin blocked in $(1,1)T_+$, as it can only make a transition to $(0,2)S$ by a spin-flip [4. in Fig. 6.11(a)]. Since $(1,1)T_+$ is higher in energy than $(0,2)S$, this corresponds to the transport spin blockade situation. We refer to this spin blockade as unconventional spin blockade,

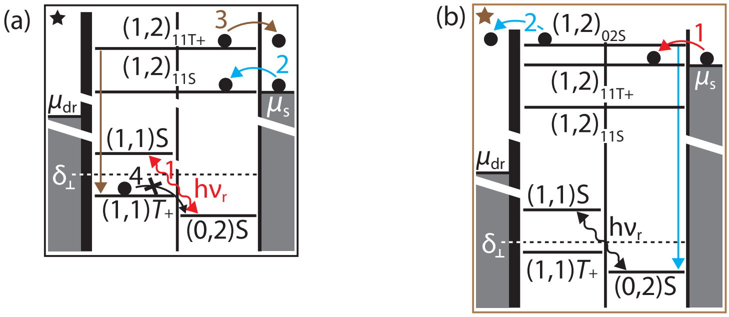

Figure 6.11 Positive bias DQD diagrams. DQD energy level diagrams at $\delta_\perp$ marked by the corresponding star in Fig. 6.9. The DQD states electrochemical potentials are shown with respect to $(0,1)$ for the two electron states and with respect to state x for the three-electron states $(1,2)_x$. Transitions involving a spin-flip are marked with a cross.

because it occurs due to the presence of resonator photons.

For smaller $\delta_\perp$, tunneling into $(1,1)\mathrm{T}_+$ is possible until $\mu[(1,2)_{11\mathrm{T}+}] = \mu_\mathrm{s}$. This level alignment occurs at the lower boundary of the black rectangle in Fig. 6.9, which is equivalent to the position of the brown star in the same figure. At this $\delta_\perp$, the transport spin blockade is lifted, since $(1,1)\mathrm{T}_+ \to (1,2)$ [1. in Fig. 6.11(b)] is possible. In a subsequent tunneling process the resonator sensitive state $(0,2)$S can be occupied by tunneling out to the left lead [2. in Fig. 6.11(b)].

We continue the discussion for $\delta_\perp$ below the lower boundary of the brown rectangle in Fig. 6.9, where the resonator response is absent due to asymmetric tunnel couplings to the reservoirs. At the lower boundary of the brown rectangle, $\mu[(1,2)_{02\mathrm{S}}] = \mu_s$. Consequently, $(0,2)$S can make a transition to $(1,2)$ via the low right reservoir barrier due to the hybridization of $(0,2)$ and $(1,1)$. Since also $\mu[(1,2)_{11\mathrm{S}}] < \mu_s$ [see Fig. 6.11(b)], both resonator sensitive states $(1,1)$S and $(0,2)$S can make a transition to the resonator insensitive state $(1,2)$. The state $(1,2)$ is mainly occupied due to asymmetric tunneling rates $\Gamma_{\mathrm{rL}} \ll \Gamma_{\mathrm{rR}}$ to the leads: tunneling out of $(1,2)$ is only possible via the left lead, which occurs at a low rate Γ_{rL} compared to tunneling into $(1,2)$ via the right reservoir barrier at rate Γ_{rR}.

6.4.2 Negative source-drain bias

Figure 6.12 shows the resonant resonator transmission for negative bias $V_{sd} = -300\,\mu V$ as a function of $\delta_\perp$ and δ. We observe a similar resonator response as for positive bias (see Fig. 6.9) and highlight certain regions in $\delta_\perp$, where the corresponding tunneling processes are illustrated in Figs. 6.13-6.14 and explained qualitatively below. In analogy to the positive bias measurement, the bias window is relevant in Fig. 6.12 in regions A and C and not relevant in region B, where the resonator response is present (absent) at δ_+ (δ_-) as in Fig. 6.9.

We first explain the absence of a resonator response in region A in Fig. 6.12, which is due to the asymmetric tunneling barriers $\Gamma_{rR} \gg \Gamma_{rL}$ to the leads discussed in subsection 6.4.1, where for the same reason the response was absent in region C in Fig. 6.9. In region A, $(0,1)$ is within the bias window. For negative bias as in Fig. 6.12, where electrons leave the DQD to the right lead (cf. Fig. 6.13), the asymmetry leads to a dominant occupation of the resonator insensitive $(0,1)$ state.

Next, we discuss the absence of a resonator response due to resonator spin blockade in region C at δ_- marked with a gray rectangle in Fig. 6.12. Within region B, the DQD states are thermally occupied and we observe spin blockade of the resonator response at δ_-, where $(1,1)T_+$ is the ground state. By decreasing $\delta_\perp$ to lie within the region

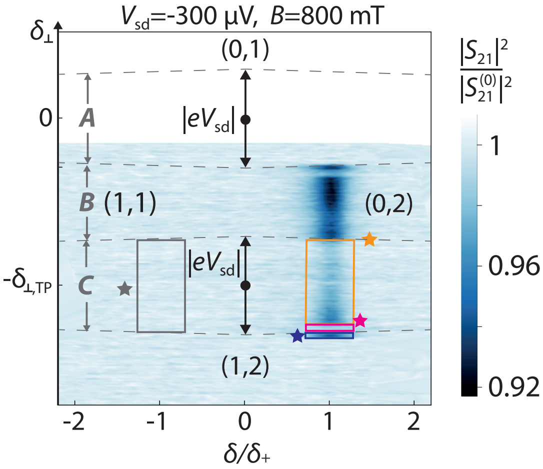

Figure 6.12 Negative bias data. Normalized resonant resonator transmission as a function of δ/δ_+ and $\delta_\perp$ for $V_{sd} = -300\,\mu V$, $B = 800\,mT$ and $t/h = 3.7\,GHz$. The triple points are indicated as dots.

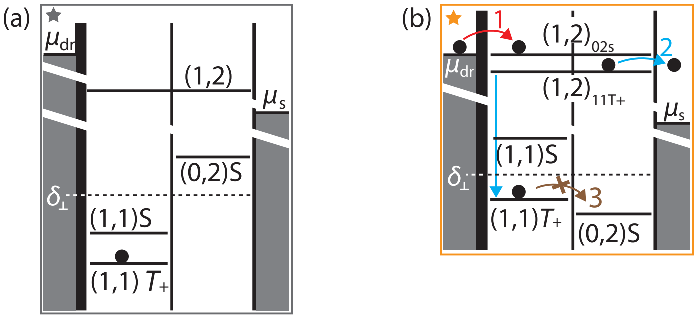

Figure 6.13 DQD diagrams for negative bias. Energy level diagram of the DQD at $\delta_\perp$ indicated with a corresponding star in Fig. 6.12. The electrochemical potentials of the DQD states are depicted with respect to $(0,1)$ for the two-electron states and with respect to the state x for the three-electron states $(1,2)_x$. A cross marks transitions that involve a spin-flip.

marked with a gray rectangle, transitions that involve $(1,2)$ are within the bias window [see Fig. 6.13(a)]. However, the transition $(1,1)\mathrm{T}_+ \rightarrow (1,2)$ is not possible since the tunneling process would require an electron to tunnel into the DQD from the right reservoir, which is not possible as a first order process for negative bias. Consequently, we also observe spin blockade of the resonator response in the region marked in gray in Fig. 6.12 because $(1,1)\mathrm{T}_+$ is occupied.

We now continue the discussion with the region marked with an orange rectangle in Fig. 6.12, where we observe the signature of transport spin blockade in the resonator response. In this region, transport through the DQD that involves $(1,2)$ is possible. At $\delta_\perp \simeq -\delta_{\perp,\mathrm{TP}} + |e\mathrm{V}_{\mathrm{sd}}/2|$ (orange star), the transition $(0,2)\mathrm{S} \rightarrow (1,2)$ is resonant with μ_{dr}, i.e. $\mu_{\mathrm{dr}} = \mu[(1,2)_{02\mathrm{S}}]$. Hence, an electron can enter the DQD from the left lead [1. in Fig. 6.13(b)]. Since $\mu[(1,2)_{11\mathrm{T}+}] \geq \mu_{\mathrm{s}}$, $(1,2)$ can make a transition to $(1,1)\mathrm{T}_+$ by tunneling out to the right reservoir [2. in Fig. 6.13(b)]. As a result, the system is spin blocked in $(1,1)\mathrm{T}_+$, which realizes the transport spin blockade situation as $(1,1)\mathrm{T}_+$ is higher in energy than $(0,2)\mathrm{S}$. Consequently, we observe a reduced resonator response, which is however nonzero as Γ_{rL} is comparable to the spin-flip rate Γ_{sf}. Therefore, the spin-flip processes $(1,1)\mathrm{T}_+ \rightarrow (0,2)\mathrm{S}$ [3. in Fig. 6.13(b)] and the tunneling cycle $(0,2)\mathrm{S} \rightarrow (1,2) \rightarrow (1,1)\mathrm{T}_+$ [1.-2. in Fig. 6.13(b)] have similar event frequencies and $(1,1)\mathrm{T}_+$ and $(0,2)\mathrm{S}$ are occupied with similar probabilities. For symmetric reservoir barriers, the transport spin blockade would also be visible in region A, where $(0,1)$ is within the bias window (see simulation in subsection 6.4.4).

In the region outlined in magenta in Fig. 6.12, the resonator response is further suppressed compared to the orange region because the occupation of $(1,1)\mathrm{T}_+$ is further increased due to the presence of an additional tunneling sequence that involves the absorption of a resonator photon. At $\delta_\perp \simeq -\delta_{\perp,\mathrm{TP}} - |e\mathrm{V}_{\mathrm{sd}}/2| + h\nu_r/2$, indicated with a magenta star in Fig. 6.12, $\mu[(1,2)_{11\mathrm{S}}] = \mu_s$ such that $(1,2)$ can be occupied by an electron tunneling into the DQD via the low right reservoir barrier [2. in Fig. 6.14(a)]. This process involves a prior absorption of a resonator photon to excite $(0,2)\mathrm{S}$ to $(1,1)\mathrm{S}$ [1. in Fig. 6.14(a)]. In a next step, the transition $(1,2) \rightarrow (1,1)\mathrm{T}_+$ [3. in Fig. 6.14(a)] is possible, as $\mu[(1,2)_{11\mathrm{T}+}] > \mu_s$. Consequently, $(1,1)\mathrm{T}_+$ can be occupied via two tunneling sequences. It is $(1,1)\mathrm{S} \rightarrow (1,2) \rightarrow (1,1)\mathrm{T}_+$ as well as $(0,2)\mathrm{S} \rightarrow (1,2) \rightarrow (1,1)\mathrm{T}_+$ that was explained for the orange region in the previous paragraph. This increases the occupation probability of $(1,1)\mathrm{T}_+$ and leads to a further suppression of the resonator response in the region outlined in magenta in Fig. 6.12, compared to the orange region in the same figure.

We now discuss the region indicated in blue in Fig. 6.12, where the transport spin blockade is lifted. At the lower boundary of the magenta region, which is equivalent to the upper boundary of the blue region [blue star in Fig. 6.12], $\mu[(1,2)_{11\mathrm{T}+}]$ is on resonance with the right reservoir (μ_s). Hence, the transport spin blockade is lifted: $(1,1)\mathrm{T}_+$ can transition into $(1,2)$ in a first step [1. in Fig. 6.14(b)] and $(0,2)\mathrm{S}$ is occupied in a second tunneling event by an electron leaving the DQD to the right reservoir [2. in Fig. 6.14(b)]. Note that hybridization of $(1,1)\mathrm{S}$ and $(0,2)\mathrm{S}$ is necessary for the latter process to occur. Otherwise, $(0,2)$ and $(1,2)$ would only be coupled via tunneling in from the left but not via tunneling out to the right reservoir.

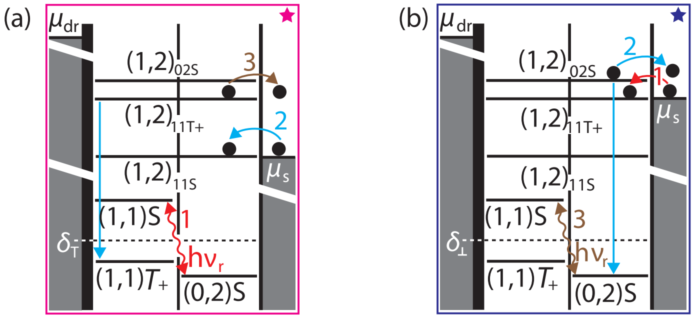

Figure 6.14 Negative bias DQD energy diagrams. DQD energy level diagrams referring to the $\delta_\perp$ positions marked with a star in Fig. 6.12. The notation is otherwise the same as in Fig. 6.13.

6.4.3 Rate-equation model

To describe the observations in subsections 6.4.1 and 6.4.2 theoretically, we set up a rate-equation model for electron transport through the DQD. We consider the charge configurations $(0,1)$, $(0,2)$, $(1,1)$ and $(1,2)$ that were relevant in these sections as well as spin to arrive at the basis states

$$\begin{gathered}\{(0,\uparrow),(0,\downarrow),(\uparrow,\uparrow),(\downarrow,\downarrow),\\ (1,1)\mathrm{T}_0,|0_{\mathrm{CQ}}\rangle,|1_{\mathrm{CQ}}\rangle,(\uparrow,2),(\downarrow,2)\}\end{gathered} \tag{6.6}$$

that are relevant for our model, where $(\uparrow,2)$ and $(\downarrow,2)$ are states with a singlet in the right quantum dot. The basis state's energies are parametrized according to

$$\begin{aligned}
\mathrm{E}_{(0,\uparrow)} &= -\delta_\perp - \frac{1}{2}\mathrm{E}_\mathrm{Z},\\
\mathrm{E}_{(0,\downarrow)} &= -\delta_\perp + \frac{1}{2}\mathrm{E}_\mathrm{Z},\\
\mathrm{E}_{(\uparrow,\uparrow)} &= \delta/2 - \mathrm{E}_\mathrm{Z},\\
\mathrm{E}_{(\downarrow,\downarrow)} &= \delta/2 + \mathrm{E}_\mathrm{Z},\\
\mathrm{E}_{\mathrm{T}_0} &= \delta/2,\\
\mathrm{E}_{|0_{\mathrm{CQ}}\rangle} &= -\sqrt{t^2+(\delta/2)^2},\\
\mathrm{E}_{|1_{\mathrm{CQ}}\rangle} &= \sqrt{t^2+(\delta/2)^2},\\
\mathrm{E}_{(\uparrow,2)} &= \delta_{\perp,\mathrm{TP}} + \delta_\perp - \frac{1}{2}\mathrm{E}_\mathrm{Z},\\
\mathrm{E}_{(\downarrow,2)} &= \delta_{\perp,\mathrm{TP}} + \delta_\perp + \frac{1}{2}\mathrm{E}_\mathrm{Z}.
\end{aligned} \tag{6.7}$$

The rate equation for transitions between the DQD states i can generally be written as (Ihn, 2010)

$$\frac{dp_i}{dt} = \sum_{i'} (\mathrm{W}_{i'\to i} p_{i'} - \mathrm{W}_{i\to i'} p_i) \tag{6.8}$$

with the steady state condition $dp_i/dt = 0$ for all states i. The term p_i in Eq. (6.8) is the occupation probability of state i. The transition rates from state i' to i are

$$\begin{aligned}\mathrm{W}_{i'\to i} =& \Gamma^{i'i}_{\mathrm{rL},0} f_\mathrm{L}(\Delta\mathrm{E}^-_{i'i}) + \Gamma^{i'i}_{\mathrm{rR},0} f_\mathrm{R}(\Delta\mathrm{E}^+_{i'i}) + \\ & (\Gamma^{i'i}_{\mathrm{sf},0} + \Gamma^{i'i}_{\mathrm{rel},0}) e^{-\Delta\mathrm{E}_{i'i}/k_\mathrm{B}\mathrm{T}} + \Gamma^{i'i}_{\mathrm{exc},0}.\end{aligned} \tag{6.9}$$

The first two terms in Eq. (6.9) describe transitions involving the left (right) reservoir with Fermi distribution f_{L} (f_{R}). The term $\Delta \mathrm{E}^{\pm}_{i'i} = \mathrm{E}_i - \mathrm{E}'_i \pm e\mathrm{V}_{\mathrm{sd}}/2$ quantifies the energy cost for the transition from state i' with energy E'_i to state i with energy E_i at symmetric bias voltage V_{sd}. The coupling rates $\Gamma^{i'i}_{\mathrm{rL},0}$ ($\Gamma^{i'i}_{\mathrm{rR},0}$) to the left (right) reservoirs depend on the respective bare reservoir tunneling rate Γ_{rL} (Γ_{rR}). For example, $(1,1)\mathrm{T}_0$ couples at rate $\Gamma^{\mathrm{T}_0,(0,\uparrow)}_{\mathrm{rL},0} = \Gamma_{\mathrm{rL}}/2$ with $(0,\uparrow)$ via the left reservoir, due to the fact that it has with equal probability an up or down spin electron in the left dot.

Overall we obtain in the basis of Eq. (6.6) for tunneling to the left reservoir

$$\Gamma_{\mathrm{rL},0} = \Gamma_{\mathrm{rL}} \begin{pmatrix} 0 & 0 & 1 & 0 & \frac{1}{2} & \frac{\cos(\zeta)^2}{2} & \frac{\sin(\zeta)^2}{2} & 0 & 0 \\ 0 & 0 & 0 & 1 & \frac{1}{2} & \frac{\cos(\zeta)^2}{2} & \frac{\sin(\zeta)^2}{2} & 0 & 0 \\ 1 & 0 & 0 & 0 & 0 & 0 & 0 & 0 & 0 \\ 0 & 1 & 0 & 0 & 0 & 0 & 0 & 0 & 0 \\ \frac{1}{2} & \frac{1}{2} & 0 & 0 & 0 & 0 & 0 & 0 & 0 \\ \frac{\cos(\zeta)^2}{2} & \frac{\cos(\zeta)^2}{2} & 0 & 0 & 0 & 0 & 0 & \sin(\zeta)^2 & \sin(\zeta)^2 \\ \frac{\sin(\zeta)^2}{2} & \frac{\sin(\zeta)^2}{2} & 0 & 0 & 0 & 0 & 0 & \cos(\zeta)^2 & \cos(\zeta)^2 \\ 0 & 0 & 0 & 0 & 0 & \sin(\zeta)^2 & \cos(\zeta)^2 & 0 & 0 \\ 0 & 0 & 0 & 0 & 0 & \sin(\zeta)^2 & \cos(\zeta)^2 & 0 & 0 \end{pmatrix} \tag{6.10}$$

with $\zeta \equiv \theta/2$ and the mixing angle $\cos(\theta) = -\delta/\mathrm{E}_{\mathrm{CQ}}$ that was defined in subsection 3.1.3. For tunneling processes that involve the right reservoir we arrive at

$$\Gamma_{\mathrm{rR},0} = \Gamma_{\mathrm{rR}} \begin{pmatrix} 0 & 0 & 0 & 0 & 0 & \sin(\zeta)^2 & \cos(\zeta)^2 & 0 & 0 \\ 0 & 0 & 0 & 0 & 0 & \sin(\zeta)^2 & \cos(\zeta)^2 & 0 & 0 \\ 0 & 0 & 0 & 0 & 0 & 0 & 0 & 1 & 0 \\ 0 & 0 & 0 & 0 & 0 & 0 & 0 & 0 & 1 \\ 0 & 0 & 0 & 0 & 0 & 0 & 0 & \frac{1}{2} & \frac{1}{2} \\ \sin(\zeta)^2 & \sin(\zeta)^2 & 0 & 0 & 0 & 0 & 0 & \frac{\cos(\zeta)^2}{2} & \frac{\cos(\zeta)^2}{2} \\ \cos(\zeta)^2 & \cos(\zeta)^2 & 0 & 0 & 0 & 0 & 0 & \frac{\sin(\zeta)^2}{2} & \frac{\sin(\zeta)^2}{2} \\ 0 & 0 & 1 & 0 & \frac{1}{2} & \frac{\cos(\zeta)^2}{2} & \frac{\sin(\zeta)^2}{2} & 0 & 0 \\ 0 & 0 & 0 & 1 & \frac{1}{2} & \frac{\cos(\zeta)^2}{2} & \frac{\sin(\zeta)^2}{2} & 0 & 0 \end{pmatrix}. \tag{6.11}$$

Spin-flip processes from state i' to i are phenomenologically accounted for in Eq. (6.9) by the term $\Gamma^{i'i}_{\mathrm{sf},0} e^{-\Delta \mathrm{E}_{i'i}/k_{\mathrm{B}}\mathrm{T}}$, where $\Delta \mathrm{E}_{i'i} = 0$ for $\mathrm{E}_i < \mathrm{E}'_i$ and $\Delta \mathrm{E}_{i'i} = \mathrm{E}_i - \mathrm{E}'_i$ otherwise. Hence, spin-flips are exponentially suppressed if $\mathrm{E}_i > \mathrm{E}'_i$. The bare spin-flip rate Γ_{sf} is related to $\Gamma_{\mathrm{sf},0}^{i'i}$ via

$$\Gamma_{\mathrm{sf},0} = \Gamma_{\mathrm{sf}} \begin{pmatrix} 0 & 1 & 0 & 0 & 0 & 0 & 0 & 0 & 0 \\ 1 & 0 & 0 & 0 & 0 & 0 & 0 & 0 & 0 \\ 0 & 0 & 0 & 0 & 1 & \cos(\zeta)^2 & \sin(\zeta)^2 & 0 & 0 \\ 0 & 0 & 0 & 0 & 1 & \cos(\zeta)^2 & \sin(\zeta)^2 & 0 & 0 \\ 0 & 0 & 1 & 1 & 0 & \cos(\zeta)^2 & \sin(\zeta)^2 & 0 & 0 \\ 0 & 0 & \cos(\zeta)^2 & \cos(\zeta)^2 & \cos(\zeta)^2 & 0 & 0 & 0 & 0 \\ 0 & 0 & \sin(\zeta)^2 & \sin(\zeta)^2 & \sin(\zeta)^2 & 0 & 0 & 0 & 0 \\ 0 & 0 & 0 & 0 & 0 & 0 & 0 & 0 & 1 \\ 0 & 0 & 0 & 0 & 0 & 0 & 0 & 1 & 0 \end{pmatrix}. \tag{6.12}$$

The term $\Gamma_{\mathrm{rel},0}^{i'i} e^{-\Delta \mathrm{E}_{i'i}/k_\mathrm{B}\mathrm{T}}$ in Eq. (6.9) considers qubit relaxation from $|1_\mathrm{CQ}\rangle$ to $|0_\mathrm{CQ}\rangle$ at rate $\Gamma_{\mathrm{rel},0}^{|1_\mathrm{CQ}\rangle,|0_\mathrm{CQ}\rangle} \equiv \gamma_{1,\mathrm{CQ}}^{(\mathrm{b})}/2\pi = 84\,\mathrm{MHz}$. Similarly to the spin-flip process discussed above, $\Delta \mathrm{E}_{i'i} = 0$ for $\mathrm{E}_i < \mathrm{E}_i'$ and $\Delta \mathrm{E}_{i'i} = \mathrm{E}_i - \mathrm{E}_i'$ otherwise.

The last term in Eq. (6.9) describes $|0_\mathrm{CQ}\rangle$ to $|1_\mathrm{CQ}\rangle$ excitation via absorption of a resonator photon. The corresponding rate $\Gamma_\mathrm{exc} \equiv \Gamma_{\mathrm{exc},0}^{|0_\mathrm{CQ}\rangle,|1_\mathrm{CQ}\rangle}$ depends on the number of photons in the resonator and is a free parameter in our simulations.

We solve Eq. (6.8) in steady state with the constraint $\sum_i p_i = 1$ for the qubit ground (excited) state occupation probability $p_{|0_\mathrm{CQ}\rangle}$ ($p_{|1_\mathrm{CQ}\rangle}$). This result is used to simulate the resonator transmission with the input-output theory result from Eq. (5.56).

6.4.4 Simulation results

Using the rate-equation model derived in the previous subsection we simulate the resonator response for the experimental parameters of the positive and negative bias measurements that were shown in Fig. 6.9 and Fig. 6.12, respectively. The free parameters for the simulation are Γ_rL, Γ_rR, Γ_sf and Γ_exc. For the parameters $g_\mathrm{CQ}^{(0)}$, $\gamma_{1,\mathrm{CQ}}^{(\mathrm{b})}$, $\gamma_{\varphi,\mathrm{CQ}}^{(\mathrm{b})}$, $\delta_{\perp,\mathrm{TP}}$ and T_e the values extracted in section 6.2 are used.

The simulation results depicted in Fig. 6.15 are in good agreement with the corresponding experimental observations in Figs. 6.9 and Figs. 6.12. We thereby choose $\Gamma_\mathrm{rR}/\Gamma_\mathrm{rL} \geq 100$ for the simulations such that the simulated resonator response is absent in region C for positive bias in agreement with the experimental result in Fig. 6.9. The ratio $\Gamma_\mathrm{sf}/\Gamma_\mathrm{rL} \simeq 1$ is determined by the experimental magnitude of the resonator response in the transport spin blockade situation for negative bias [orange region in Fig. 6.12]. We can therefore quantitatively estimate the tunneling rates as typical spin-flip rates for our experimental parameters are of the order of MHz (Danon, 2013). The remaining free parameter Γ_{exc} in the simulations mainly influences the simulated resonator response in the two regions outlined in black in Fig. 6.9 and in magenta in Fig. 6.12 where $|0_{\mathrm{CQ}}\rangle$ to $|1_{\mathrm{CQ}}\rangle$ excitations due to resonator photons trigger the spin blockade. We set $\Gamma_{\mathrm{exc}} = 5\,\mathrm{MHz}$ in all simulations to qualitatively reproduce the response in these two regions.

It was pointed out in subsections 6.4.1 and 6.4.2 that the resonator response is absent in region C in Fig. 6.9 and region A in Fig. 6.12 due to asymmetric reservoir couplings $\Gamma_{\mathrm{rL}} \ll \Gamma_{\mathrm{rR}}$. This claim is supported by the simulation results for symmetric reservoir couplings $\Gamma_{\mathrm{rL}} = \Gamma_{\mathrm{rR}} = 100\,\mathrm{MHz}$ in the insets of Fig. 6.15. Both simulation results are symmetric in $\delta_\perp$.

In the following we discuss the two regions highlighted with rectangles in Fig. 6.15, where experiment and simulation deviate. First, the positions of the upper and lower boundary of the region marked with a green rectangle in Fig. 6.15(a) and Fig. 6.9 are not in agreement. At $\delta_\perp \simeq |eV_{\mathrm{sd}}/2| + h\nu_r/2$, marked with a green star in Fig. 6.15(a), a resonator response is visible in the simulation. At this value of $\delta_\perp$, (1,1)S is resonant

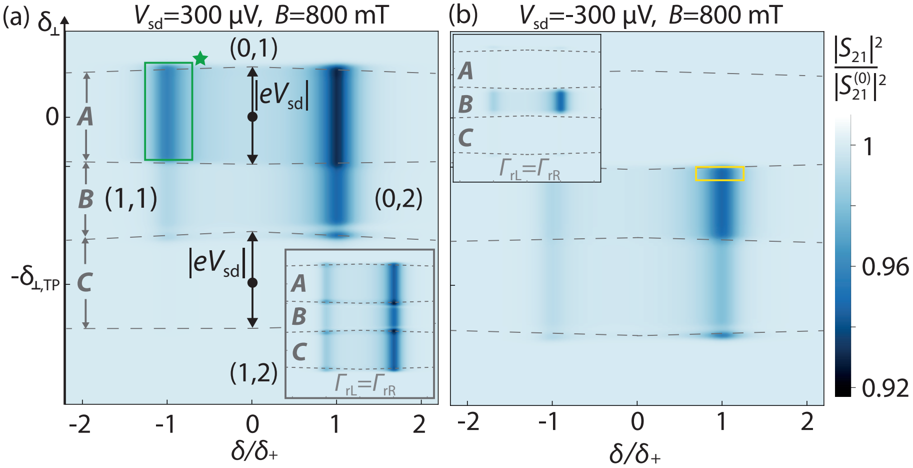

Figure 6.15 Positive and negative bias simulation. Rate equation simulation of the resonator transmission as a function of δ and $\delta_\perp$ for $V_{\mathrm{sd}} = 300\,\mu\mathrm{V}$ in (a) and $V_{\mathrm{sd}} = -300\,\mu\mathrm{V}$ in (b). The simulation parameters for both panels are $B = 800\,\mathrm{mT}$, $\Gamma_{\mathrm{rR}} = 100\,\mathrm{MHz}$, $\Gamma_{\mathrm{rL}} = 1\,\mathrm{MHz}$, $\Gamma_{\mathrm{sf}} = 1.3\,\mathrm{MHz}$, $\Gamma_{\mathrm{exc}} = 5.0\,\mathrm{MHz}$, $t/h = 3.7\,\mathrm{GHz}$, and $\delta_{\perp,\mathrm{TP}} = 510\,\mu\mathrm{eV}$. Inset: simulation parameters as in the main panels except for symmetric reservoir couplings $\Gamma_{\mathrm{rL}} = \Gamma_{\mathrm{rR}} = 100\,\mathrm{MHz}$. The axes and plot ranges of the insets are identical to the main figures.

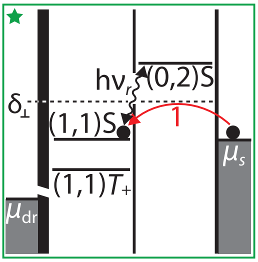

Figure 6.16 Negative bias DQD diagram. DQD energy level diagram with electrochemical potentials depicted with respect to $(0,1)$. The diagram indicates tunneling processes at $\delta_\perp$ marked with a green star in Fig. 6.15(a).

with the right reservoir as shown in Fig. 6.16. Due to the hybridization of $(1,1)$S and $(0,2)$S, the transition $(0,1) \rightarrow (1,1)$ is possible by tunneling into the DQD from the right reservoir and a resonator sensitive state is occupied. By decreasing $\delta_\perp$, a resonator response starts being visible at $\delta_\perp < |eV_{\mathrm{sd}}/2|$ in the experiment in Fig. 6.9. A possible explanation for this discrepancy of experiment and simulation is an interdependence of $\delta_\perp$ and δ in the experiment. Consequently, the resonator response at δ_- is shifted in $\delta_\perp$ with respect to the signal at δ_+. Our claim is supported by the fact, that the total length in $\delta_\perp$ of the blue regions is approximately the same in experiment (Fig. 6.9) and simulation [Fig. 6.15(a)]. Second, a resonator response is present in the region outlined in yellow in the simulation in Fig. 6.15(b) but absent in the experiment in Fig. 6.12. A possible origin of this discrepancy is higher order tunneling processes via the low barrier to the right reservoir. Such processes are not considered in our theoretical model.

Finally, we present simulation results for different ratios of the slow tunneling rate Γ_{rL} and the spin-flip rate Γ_{sf} for negative source-drain bias. In the region marked in orange in Fig. 6.12 a reduced resonator signal was observed due to transport spin blockade. The signal is finite, as the spin-flip rate is comparable to the left reservoir tunneling rate. It was argued in subsection 6.4.2, that the magnitude of the finite response depends for asymmetric couplings $\Gamma_{\mathrm{rL}} \ll \Gamma_{\mathrm{rR}}$ on the ratio $\Gamma_{\mathrm{sf}}/\Gamma_{\mathrm{rL}}$: there is a weak (strong) resonator response for $\Gamma_{\mathrm{sf}}/\Gamma_{\mathrm{rL}} \ll 1$ ($\Gamma_{\mathrm{sf}}/\Gamma_{\mathrm{rL}} \gg 1$). Fig. 6.17 shows the simulation result for different values of $\Gamma_{\mathrm{sf}}/\Gamma_{\mathrm{rL}}$. The orange region from Fig. 6.12 is indicated in Fig. 6.17 with the same color. We observe that for $\Gamma_{\mathrm{sf}}/\Gamma_{\mathrm{rL}} = 10$ in Fig. 6.17(b) compared to $\Gamma_{\mathrm{sf}}/\Gamma_{\mathrm{rL}} = 1.3$ in Fig. 6.17(a), the magnitude of the resonator response in the orange region increases. This observation is due to the rate of the spin-

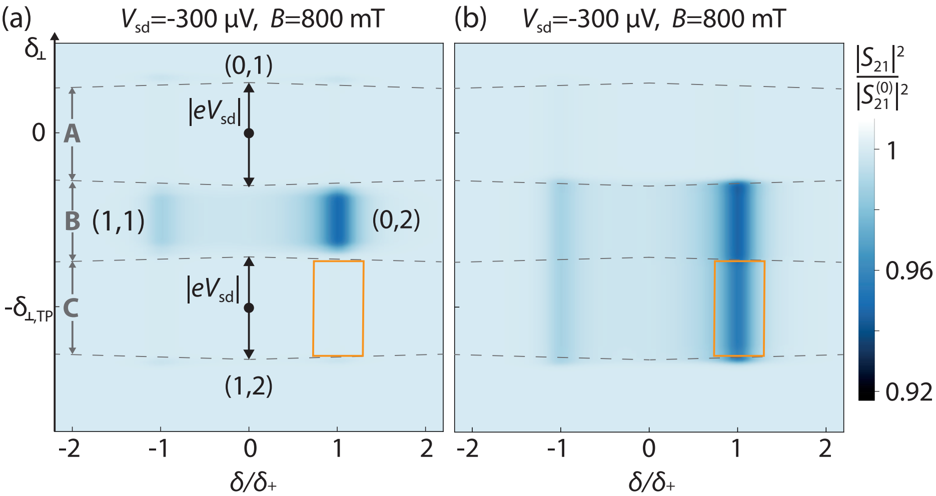

Figure 6.17 Influence of spin-flip rate on simulation. (a) Simulation result identical to the inset of Fig. 6.15(b): $\Gamma_{\mathrm{rR}} = 100\,\mathrm{MHz}$, $\Gamma_{\mathrm{rL}} = 1\,\mathrm{MHz}$, $\Gamma_{\mathrm{sf}} = 1.3\,\mathrm{MHz}$, $t/h = 3.7\,\mathrm{GHz}$, $\delta_{\perp,\mathrm{TP}} = 510\,\mu\mathrm{V}$, $\Gamma_{\mathrm{exc}} = 5.0\,\mathrm{MHz}$. (b) Simulation parameters as in (a) except for $\Gamma_{\mathrm{sf}} = 13\,\mathrm{MHz}$. The region marked in orange in (a) and (b) is identical to the region with the same color in Fig. 6.12.

flip process $(1,1)\mathrm{T}_+ \rightarrow (0,2)\mathrm{S}$ dominating over the rate of $(0,2)\mathrm{S} \rightarrow (1,2) \rightarrow (1,1)\mathrm{T}_+$, such that the occupation of $(1,1)\mathrm{T}_+$ is reduced.

6.5 Conclusion and outlook

In this chapter we have studied spin physics in a few electron DQD using a weakly coupled microwave resonator as a probe in the resonant and dispersive regime. We observed spin blockade of the resonator response and mapped out the two-electron singlet-triplet crossover in continuous wave experiments without pulsed gate operations. In finite bias measurements we observed the conventional transport spin blockade as well as an unconventional spin blockade triggered by resonator photons. Signatures in the finite bias data gave direct access to relevant qubit parameters that are not easily accessible in transport experiments in the few electron regime: the symmetry of the reservoir tunneling barriers and their ratio to the spin-flip rate.

The experiments presented in this work can be implemented in any other material system to investigate spin-dependent material properties like spin-orbit coupling, spin relaxation rates or the g-factor. By increasing the qubit-photon coupling strength to the strong coupling limit, fast read-out of spin states has been demonstrated after the submission of this work in Ref. Zheng et al., 2019, which is a requirement for a spin qubit based quantum processor. Future work could also focus on studying the spin physics of more complex quantum states in multi quantum dot systems such as two dimensional arrays of quantum dots (Mortemousque et al., 2018) that provide a promising route towards a scalable spin qubit device.

Chapter 7

Coherent spin-photon coupling using a resonant exchange qubit

The ability to transmit quantum information over long distances is desirable for quantum information processors (DiVincenzo, 2000). Circuit QED provides a well-established platform to connect distant qubits (Majer et al., 2007). Strong coupling has been realized with superconducting qubits (Wallraff et al., 2004) and recently, the coherence properties of charge qubits in semiconductor quantum dots have improved sufficiently to achieve strong coupling (Bruhat et al., 2018, Mi et al., 2017c, Stockklauser et al., 2017). Even better coherence is expected by transferring the quantum information from electron charge to spin (Hanson et al., 2007, Zwanenburg et al., 2013). This approach comes with a major challenge as the coupling of photons to spins is several orders of magnitude weaker than the coupling to charge (Schoelkopf et al., 2008). The challenge can be resolved by introducing an electric dipole moment to the spin states. For single-electron spin qubits, spin and charge are coupled by using materials with strong spin-orbit interaction (Petersson et al., 2012), devices with ferromagnetic leads (Viennot et al., 2015), or a magnetic field gradient generated by an on-chip micromagnet (Pioro-Ladrière et al., 2008, Hu et al., 2012, Beaudoin et al., 2016). A different approach is realized with the resonant exchange (RX) qubit (Medford et al., 2013a,b, Gaudreau et al., 2012, Taylor et al., 2013, Russ et al., 2015a), where spin exchange interaction couples two states with an equal three-electron charge distribution and equal total spin, but different spin arrangement. This interaction also gives rise to an electrical dipole moment that enables coherent qubit-photon coupling.

In this chapter we demonstrate strong coupling between single microwave photons in a NbTiN high impedance resonator and a RX qubit hosted in GaAs by using hybrid circuit QED (Srinivasa et al., 2016, Russ et al., 2015b). We resolve the vacuum Rabi mode splitting with a coupling strength of $g_{\text{RX}}/2\pi \approx 31\,\text{MHz}$ and a qubit decoherence of $\gamma_{2,\text{RX}}/2\pi \approx 20\,\text{MHz}$. We tune the decoherence electrostatically and obtain a minimal $\gamma_{2,\text{RX}}/2\pi \approx 10\,\text{MHz}$ for $g_{\text{RX}}/2\pi \approx 23\,\text{MHz}$. The dependence of the qubit-photon coupling strength on the tunable electric dipole moment of the qubit is measured directly using the ac Stark effect. Our demonstration of strong spin-photon interaction is an important step towards coherent long-distance coupling of spin qubits. It is one of three independent works that were published around the same time. In the other two studies in Refs. Mi et al., 2018, Samkharadze et al., 2018 strong spin-photon coupling was demonstrated for a double quantum dot single-electron spin qubit in Si.

The structure of this chapter is as follows: We present details of the sample in section 7.1 before we explain the electrostatic tuning of the TQD into the RX regime in section 7.2. We then discuss the experimental signature of qubit-photon interaction in the resonator and report the observation of the vacuum Rabi mode splitting in sections 7.3 and 7.4, respectively. In sections 7.5-7.6 we characterize the electrostatic tunability of the qubit decoherence and extract the qubit–photon coupling strength from the ac Stark shift. Finally, we study the RX qubit in large magnetic fields that are of the order of a few tesla in section 7.7.

The content of this chapter follows in most parts our article:

Coherent spin-photon coupling using a resonant exchange qubit
A. J. Landig, J. V. Koski, P. Scarlino, U.C. Mendes, A. Blais, C. Reichl, W. Wegscheider,
A. Wallraff, K. Ensslin and T. Ihn, Nature **560** (2018)

7.1 Sample

Figure 7.1 shows optical and scanning electron micrographs of our hybrid quantum device. It was fabricated with the techniques explained in subsection 6.1.3 and mounted in the experimental setup presented in chapter 2. Electrons are trapped in a TQD structure (see three dashed circles) by electrostatic confinement created by Au gates [Fig. 7.1(c)] on top of a GaAs/AlGaAs heterostructure. The electrostatic potentials of the left, middle and right quantum dots are tuned with the respective plunger gate voltages V_L, V_M and V_R. A QPC acts as a charge sensor that allows us to determine the TQD charge configuration. We configure a RX qubit in the TQD as discussed in detail in section 7.2.

To couple the qubit to microwave photons, the plunger gate of the left quantum dot extends to the superconducting microwave resonator as shown in Fig. 7.1(b). The left plunger gate is also DC-biased via a resistive Au line, which is connected to the middle of the resonator center conductor. The coupling strength g_{RX} between qubit and resonator photons is proportional to the square root of the characteristic impedance $\sqrt{Z_r}$ of the resonator [see Eq. (4.13)]. It is enhanced by fabricating the resonator with a thin ($\sim 15\,\mathrm{nm}$) and narrow ($\sim 300\,\mathrm{nm}$) center conductor from the high kinetic-inductance material NbTiN (Samkharadze et al., 2016). We estimate $Z_r = \sqrt{L_l/C_l} \sim 1.3\,\mathrm{k}\Omega$, with the resonator inductance (capacitance) $L_l \sim 150\,\mu\mathrm{H/m}$ ($C_l \sim 90\,\mathrm{pF/m}$) per unit length, resulting in a coupling strength enhancement by a factor of 5 compared to a standard

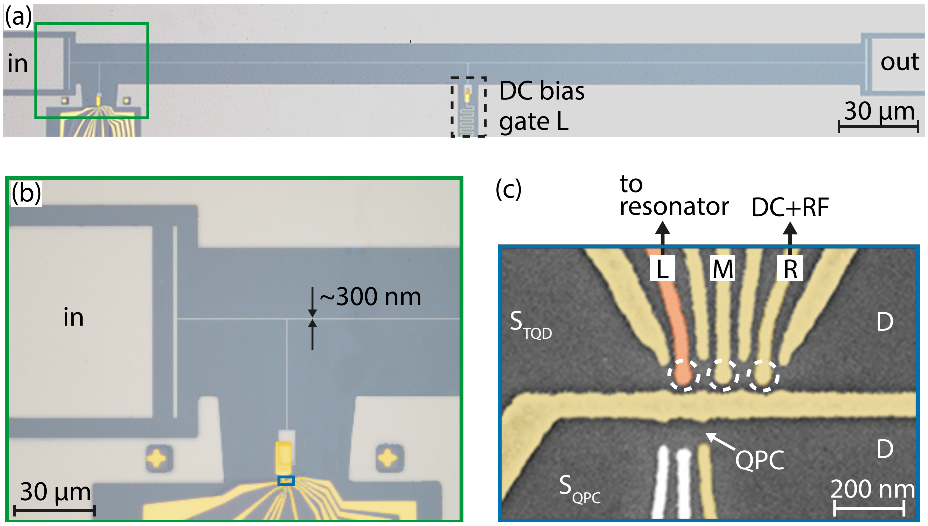

Figure 7.1 Hybrid quantum device. (a) Optical micrograph of the device showing the resonator that is capacitively coupled to the input (in) and output (out) transmission lines. The region for DC bias that connects to the center of the resonator is indicated in black. (b) Magnified image of the region outlined in green in (a). The width of the resonator center conductor is indicated and the resonator extension to the TQD (blue rectangle) is visible. (c) False-colored scanning electron micrograph of the TQD gate structure defined by electron beam lithography. The two white gates are kept at zero voltage in our experiments. The gate highlighted in orange is electrically connected to the resonator. The approximate positions of the left, middle and right quantum dots are indicated by dashed white circles. Their corresponding plunger gates are labelled as (L), (M) and (R). The right plunger gate is biased with DC and microwave signals. The TQD and the QPC have separate ohmic source contacts (S_{TQD} and S_{QPC}) and a common drain contact (D).

impedance-matched $Z_r = 50\,\Omega$ resonator. Our choice of material and design allows us to operate the resonator in the presence of an external magnetic field applied parallel to the resonator plane (Samkharadze et al., 2016). In the experiments described here, we apply a magnetic field of $B = 200\,\mathrm{mT}$.

From the resonator transmission spectrum we determine its resonance frequency $\nu_r = 4.38\,\mathrm{GHz}$ and linewidth $\kappa_r/2\pi = 47.1\,\mathrm{MHz}$ ($Q_{ld} \approx 93$) at an average resonator photon occupation of less than one. For a discussion of possible reasons for the comparably low quality factor we refer to subsection 6.1.2. Note that one important difference in the design of the resonator used in this chapter compared to the resonator in chapter 6 is the smaller distance of the resonator extension, which connects to the dot [see Fig. 7.1(b)], with respect to the resonator end ($\approx 37\,\mu$m instead of $\approx 105\,\mu$m). This enhances the amplitude of the voltage fluctuations that couple to the qubit.

7.2 TQD tuning into the RX regime

The spin qubit is formed by tuning the TQD into the three-electron regime. Figure 7.2(a) shows the charge stability diagram of the TQD, as measured by the charge detector. This data set is similar to Fig. 3.13(a), however with larger interdot tunnel couplings.

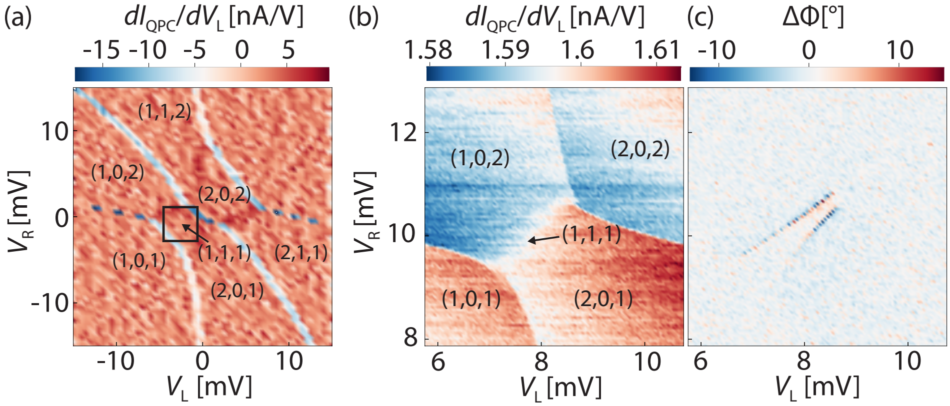

Figure 7.2 QPC and resonator signal in left-right basis. (a)-(b) TQD charge stability diagram in the few-electron regime as a function of left and right plunger gate voltages with $V_{rL} = -610\,\mathrm{mV}$, $V_{rR} = -611\,\mathrm{mV}$, $V_M = -53.7\,\mathrm{mV}$ in (a) and $V_{rL} = -629\,\mathrm{mV}$, $V_{rR} = -631\,\mathrm{mV}$, $V_M = -56.2\,\mathrm{mV}$ in (b). The black rectangle in (a) outlines the measurement region in (b)-(c). (c) Relative phase of the signal transmitted through the resonator (phase response) by probing it on resonance within the same parameter range as in (b).

To realize the desired RX working point $\varepsilon \approx 0$ and $|\Delta| \lesssim t_{\mathrm{L,R}}$ with $t_{\mathrm{L,R}}/h \approx 8\,\mathrm{GHz}$, we tune $(2,0,1)$, $(1,0,2)$ and $(1,1,1)$ close to their degeneracy point by adjusting the middle plunger gate potential $\mathrm{V_M}$. We also increase the tunnel couplings by tuning the left and right reservoir gate potentials $\mathrm{V_{rL}}$ and $\mathrm{V_{rR}}$ (see Fig. 3.12) more negative. As a result, we observe a phase shift in the transmitted resonator signal in Fig. 7.2(c), which is due to the interaction of the resonator with the RX qubit as discussed below.

For the measurements in Fig. 7.2, $\mathrm{V_L}$ and $\mathrm{V_R}$ were swept independently. In order to measure in the basis of the RX qubit parameters $\varepsilon = \frac{1}{2}[\mathrm{E}(1,0,2)-\mathrm{E}(2,0,1)]$ and $\Delta = \mathrm{E}(1,1,1)-\frac{1}{2}[\mathrm{E}(2,0,1)+\mathrm{E}(1,0,2)]$, which were defined in subsection 3.2.1, combinations of all three plunger gate potentials need to be tuned along the measurement axes. To realize this basis change, we first measure the TQD charge stability diagram as a function of $\mathrm{V_L}-\mathrm{V_R}$ and $\mathrm{V_L}+\mathrm{V_R}$ in Fig. 7.3(a). The resulting QPC response is rotated with respect to the measurement in Fig. 7.2(a). The position of the $(1,1,1)$ region in Fig. 7.3(a) depends on the middle plunger gate voltage $\mathrm{V_M}$ (not shown). By analyzing this position as a function of $\mathrm{V_M}$, we define the voltage detunings ε' and Δ', which independently tune the left-right dot detuning and the detuning of the middle dot with respect to the left and right quantum dots, respectively. These voltage de-

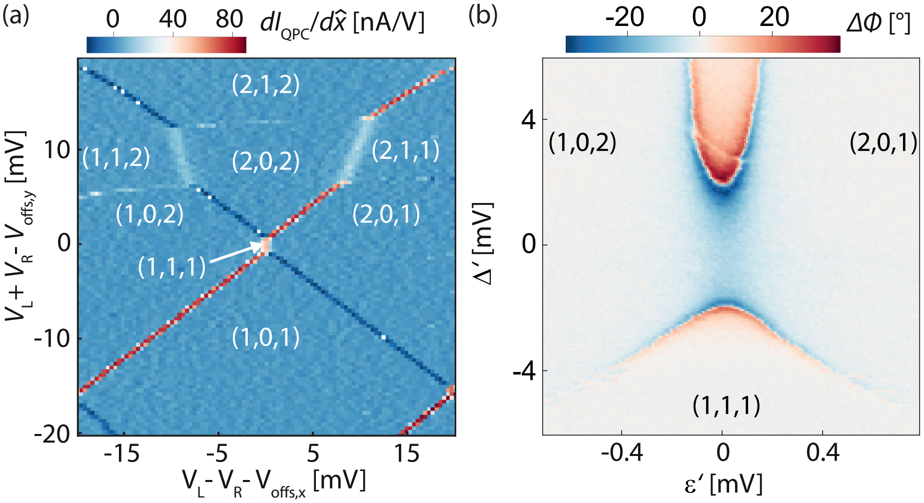

Figure 7.3 Change of measurement basis. (a) Differential QPC current as a function of combinations of left and right plunger gate voltages. $\mathrm{V_{offs,x}}$ and $\mathrm{V_{offs,y}}$ are voltage offsets, $\hat{x}$ is the quantity on the x-axis. (b) Resonator phase response on resonance as a function of the parameters Δ' and ϵ' that are defined in the text.

tunings are related to the plunger gate voltages as follows: $V_L = V_{L,offs} + (\Delta' + \varepsilon')/2$, $V_M = V_{M,offs} - 2/3\Delta'$,$V_R = V_{R,offs} + (\Delta' - \varepsilon')/2$, where $V_{i,offs}$ is a voltage offset on plunger gate i. By probing the resonator transmission on resonance in this new measurement basis, we observe the phase shift shown in Fig. 7.3(b). This observation is explained by the dependence of the RX qubit energy E_{RX} on ε' and Δ' (see subsection 3.2.2). We observe a phase shift whenever the qubit and the resonator approach a resonance $E_{RX} = h\nu_r$. When the resonance is crossed, the phase changes sign. We discuss this signature of the RX qubit in the resonator phase signal in more detail in the following section.

7.3 Qubit-resonator interaction

We concluded in the previous section that the resonator acts as a probe of the RX qubit energy spectrum at the resonator energy. The theoretically expected lines of constant qubit energy as a function of detuning Δ and asymmetry ε for symmetric tunnel couplings ($t = t_L = t_R$) are indicated in Fig. 7.4(a). Among others we observe the DSS, which is a saddle point in energy, at $\varepsilon = \Delta = 0$. The measurement in Fig. 7.3(b) therefore reproduces one of the theoretically expected energy contours shown in Fig. 7.4(a). We map the voltage axes Δ' and ϵ' from Fig. 7.3(b) to their corresponding energy axes Δ and ϵ as shown in Fig. 7.4(a) with the analysis explained in the following paragraph.

First, we extract the zero-phase positions $\{\epsilon'_r, \Delta'_r\}$ in Fig. 7.3(b), where the resonance condition $E_{RX}(\Delta'_r + \Delta'_{r,offs}, \alpha_\Delta, \varepsilon'_r + \varepsilon'_{r,offs}, \alpha_\varepsilon, t_L, t_R) = h\nu_r$ applies. The parameters $\Delta'_{r,offs}$ and $\varepsilon'_{r,offs}$ are voltage offsets, α_ε and α_Δ are lever arms that relate the resonant energy detunings Δ_r and ε_r to the resonant voltage detunings according to $\Delta_r = \alpha_\Delta e \Delta'_r$ and $\varepsilon_r = \alpha_\varepsilon e \varepsilon'_r$. By numerically diagonalizing the RX qubit Hamiltonian [see Eq. (3.13)], we solve above resonance condition for the function $\varepsilon'_r(\Delta'_r, \Delta'_{r,offs}, \alpha_\Delta, \varepsilon'_{r,offs}, \alpha_\varepsilon, t_L, t_R, \nu_r)$, which we fit to the $\{\epsilon'_r, \Delta'_r\}$ data set. For fitting to a single dataset we choose $\Delta'_{r,offs}$, α_Δ, $\varepsilon'_{r,offs}$, α_ε, t_L and t_R as free parameters. Figure 7.4(b) shows the result of this analysis for the dataset from Fig. 7.3(b).

We map different energy contour lines by changing the tunnel coupling. This is realized experimentally by changing the electrical potential of the gate lines between the plunger gates [see Fig. 7.1(c)]. We obtain the magnitude of both tunnel barriers for Figs. 7.4(b)-(d) with a fit to the resonance positions of the phase response data (see previous paragraph). A simultaneous fit to the three datasets in Fig. 7.4(b)-(d) reduces the number of free parameters, since we assume that the lever arms α_ϵ and α_Δ are the same for all datasets. We obtain an excellent agreement between theoretical and

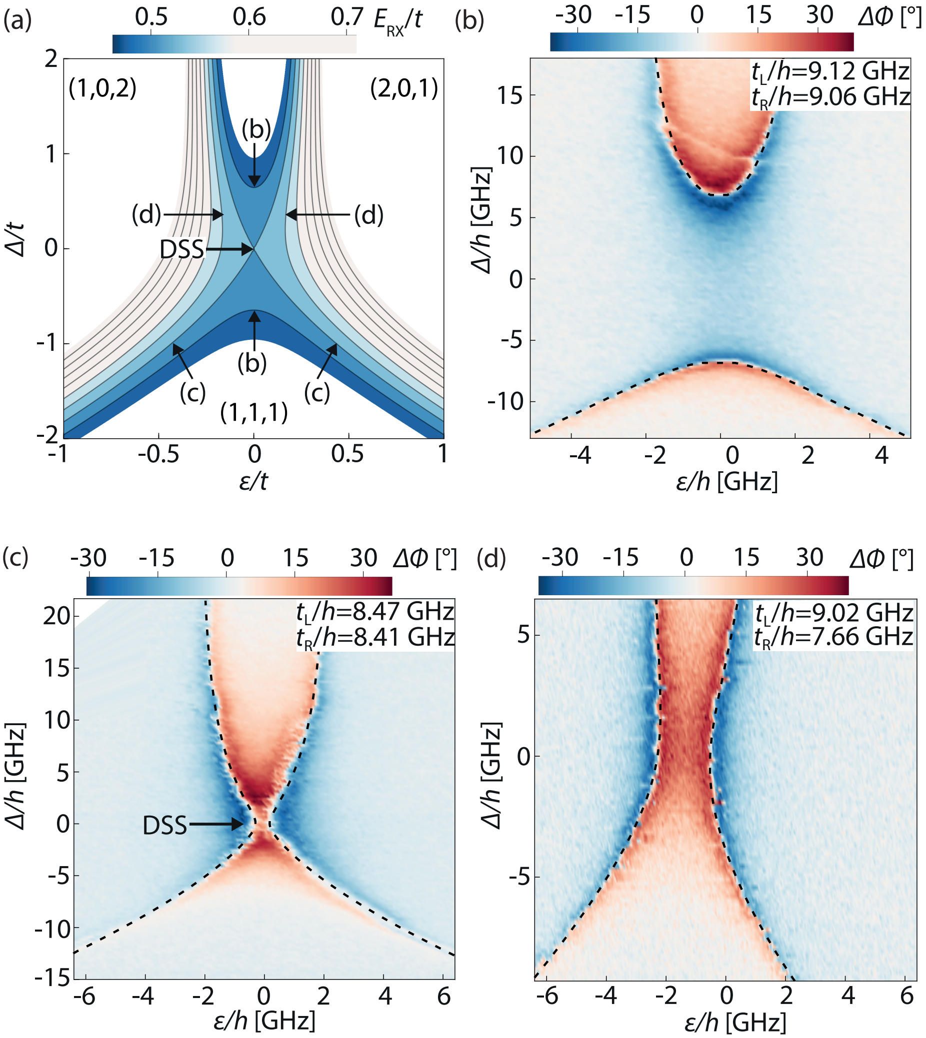

Figure 7.4 (a) Contour plot of the normalized qubit energy E_{RX}/t for symmetric tunnel coupling t as a function of detuning parameters ε/t and Δ/t. The energy contours as probed in (b)-(d) are labelled. DSS marks the position of the double sweet spot. The energetically favored three-electron charge configurations are indicated. (b)-(d) Resonator phase response measured on resonance for different tunnel coupling configurations t_L and t_R. The dashed lines indicate a fit to the theory model. Note that since the tunnel coupling is asymmetric in (d), the resonator response is shifted and tilted with respect to the contour labelled as (d) in (a).

measured resonance conditions as indicated by the dashed black line in Fig. 7.4(b)-(d). The tunability of the resonator-qubit resonance position via the tunnel coupling allows us to observe qubit-photon interaction at the DSS in Fig. 7.4(c). Note that, as observed in Fig. 7.4(d), the DSS is shifted for asymmetric barriers (Russ et al., 2015a).

7.4 Vacuum Rabi mode splitting

To further characterize the strength of the resonator-qubit interaction, we tune the qubit to a similar tunnel coupling configuration as in Fig. 7.4(c), such that qubit and resonator are resonant at the DSS. We measure the resonator transmission spectra as a function of ε at the single sweet spot in Δ in Fig. 7.5(a) and as a function of Δ at the single sweet spot in ϵ in Fig. 7.5(b). Both transmission spectra show a clear anti-

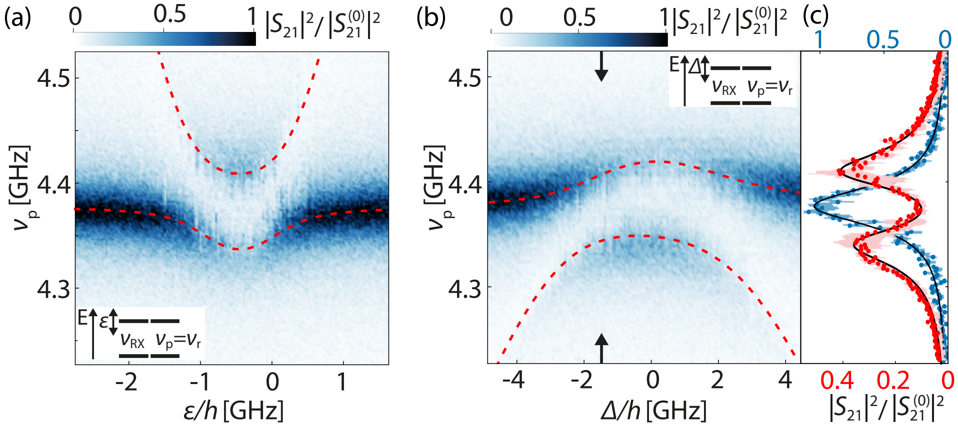

Figure 7.5 Vacuum Rabi mode splitting. (a) Resonator transmission $|S_{21}|^2$ normalized by the maximum transmission on resonance $|S_{21}^{(0)}|^2$ as a function of probe frequency ν_p and ε for $\Delta/h = 0.23\,\mathrm{GHz}$, $t_L/h = 8.25\,\mathrm{GHz}$ and $t_R/h = 8.64\,\mathrm{GHz}$. (b) Normalized resonator transmission as a function of ν_p and detuning Δ for asymmetry $\varepsilon/h = -1.03\,\mathrm{GHz}$ and tunnel couplings $t_L/h = 9.04\,\mathrm{GHz}$ and $t_R/h = 7.99\,\mathrm{GHz}$. The insets in (a) and (b) illustrate the measurement configuration. The dashed lines in (a) and (b) are the eigenenergies of the coupled qubit-resonator system. (c) Normalized resonator transmission as a function of ν_p for uncoupled (blue) and coupled (red) configuration at $\Delta/h = -1.44\,\mathrm{GHz}$ showing a strong spin-photon coupling vacuum Rabi mode splitting. The standard deviation of repeated measurements is indicated as a shaded region. The solid black lines are a fit to an input-output theory model (Collett et al., 1984).

crossing of qubit and resonator over a large range of detuning Δ and asymmetry ε. This anti-crossing is apparent from the cut at constant Δ in Fig. 7.5(c), where we observe two distinct peaks in the transmission spectrum (red data points). This observation is in clear contrast to the resonator transmission spectrum in the situation where RX qubit and resonator are detuned energetically. In this case, we observe a single peak in the resonator spectrum as indicated by the blue data points in Fig. 7.5(c). The splitting of the resonator resonance into two well separated peaks, known as the vacuum Rabi mode splitting (see subsection 5.2.1), is the characteristic fingerprint of strong coherent hybridization of a single microwave photon in the resonator and the spin qubit in the TQD. From a fit of the vacuum Rabi splitting to input-output theory, we extract the qubit-photon coupling strength $g_{\mathrm{RX}}/2\pi = (31.4 \pm 0.3)\,\mathrm{MHz}$ and the qubit decoherence rate $\gamma_{2,\mathrm{RX}}/2\pi = (19.6 \pm 0.5)\,\mathrm{MHz}$. As a result, our quantum device operates in the strong coupling regime, which is supported by the fact that the approximate peak separation is larger than the peaks width, i.e. $2g_{\mathrm{RX}} > \kappa_{\mathrm{r}}/2 + \gamma_{2,\mathrm{RX}}$. Note that the extracted spin-photon coupling strength corresponds to a charge-photon coupling strength $g^{(0)}_{\mathrm{c,RX}}/2\pi = 71\,\mathrm{MHz}$ (see subsection 5.1.2). At the RX qubit working point where the vacuum Rabi mode splitting was measured, the composition of the RX qubit states is dominated by states with $(1,1,1)$ charge configuration ($\mathrm{P}_{(1,1,1)} > \mathrm{P}_{(2,0,1)} + \mathrm{P}_{(1,0,2)}$) (see subsection 3.2.3). A majority of the quantum information is therefore stored in the spin degree of freedom.

The transmission spectra in Fig. 7.5(a)-(b) also show that the DSS of the qubit is a saddle point in energy: in Fig. 7.5(a) we observe an energy minimum of the qubit around $\varepsilon \approx 0$, in Fig. 7.5(b) the qubit energy has a maximum around $\Delta \approx 0$.

7.5 RX qubit decoherence

To further characterize the spin qubit, we now consider the shift of the resonator frequency due to resonator-qubit coupling in the dispersive regime, where the qubit-resonator detuning is much larger than the qubit-photon coupling strength (Schuster et al., 2005). We perform the two-tone spectroscopy method that was introduced in subsection 5.2.1 by applying a probe tone at frequency $\nu_{\mathrm{p}} = \nu_{\mathrm{r}}$ to the resonator and a spectroscopy tone at frequency ν_{dRX} to the right plunger gate, indicated in Fig. 7.1(c). By sweeping both the detuning Δ and the spectroscopy frequency ν_{dRX}, we trace the spectroscopic qubit signal in the resonator phase signal in Fig. 7.6(a). It resembles the Δ-dependence of the qubit energy observed in Fig. 7.5(b) and calculated in Fig. 7.4(a), and shows good agreement with theory (dashed line). Note that for the measurement in Fig. 7.6(a), ε is set to the energy minimum of the qubit (single sweet spot).

As explained in subsection 5.2.1, the qubit decoherence $\gamma_{2,\mathrm{RX}}/2\pi$ is equal to the HWHM $\delta\nu_{\mathrm{RX}}$ of the spectroscopic dip in the phase signal [right panel of Fig. 7.6(a)] in the limit of zero drive power ($\mathrm{P}_{\mathrm{gen,dRX}} \to 0$). For finite drive power, such as in Fig. 7.6(a), the spectroscopic signal is power broadened. We define the HWHM $\overline{\delta\nu_{\mathrm{RX}}}$ as the average

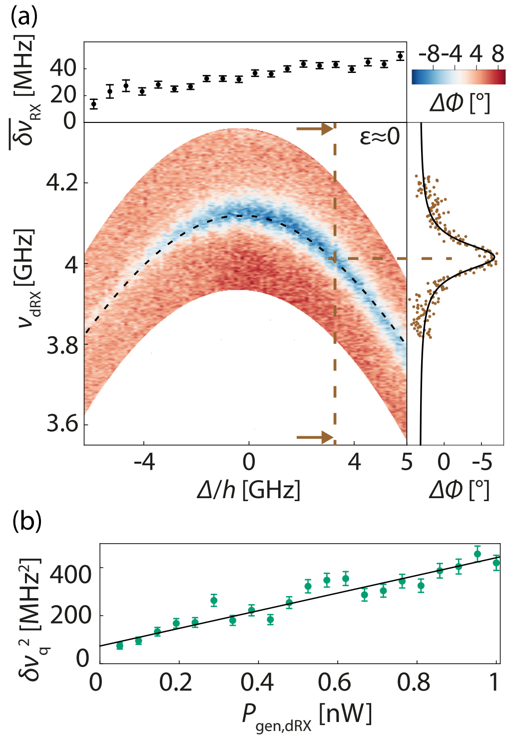

Figure 7.6 Two-tone spectroscopy. (a) Phase response of the resonator probed on resonance as a function of spectroscopy frequency ν_{dRX} and detuning Δ around the DSS for tunnel couplings $t_{\mathrm{L}}/h = 8.10\,\mathrm{GHz}$ and $t_{\mathrm{R}}/h = 7.86\,\mathrm{GHz}$, a drive generator power of $\mathrm{P}_{\mathrm{gen,dRX}} = 0.75\,\mathrm{nW}$ and a resonator photon occupation of less than one. The theoretically expected position of the phase response minima is indicated by a dashed line. In the panel on the right, a Lorentzian with a HWHM $\delta\nu_{\mathrm{RX}}$ (black line) is fit to a cut of the phase response (brown points). The panel on the top shows $\overline{\delta\nu_{\mathrm{RX}}}$, which is the average of $\delta\nu_{\mathrm{RX}}$ over five subsequent cuts along Δ with its standard error. (b) Dependence of $\delta\nu_{\mathrm{RX}}^2$ (with standard errors) on drive generator power $\mathrm{P}_{\mathrm{gen,dRX}}$ measured at $\Delta/h = -8.03\,\mathrm{GHz}$ and at the single sweet spot in asymmetry ε for $t_{\mathrm{L}}/h = 8.74\,\mathrm{GHz}$ and $t_{\mathrm{R}}/h = 8.12\,\mathrm{GHz}$. The solid line is a fit to the expected linear dependence.

of $\delta\,\nu_{\mathrm{RX}}$ for five subsequent cuts along the Δ-direction in Fig. 7.6(a) and observe an increase of $\overline{\delta\,\nu_{\mathrm{RX}}}$ with increasing Δ, as illustrated in the top panel in Fig. 7.6(a).

To disentangle the effects of power broadening and qubit decoherence on $\delta\,\nu_{\mathrm{RX}}$, we extract $\gamma_{2,\mathrm{RX}}$ in Fig. 7.7(a) by measuring $\delta\,\nu_{\mathrm{RX}}$ as a function of the power of the spectroscopy tone [see Fig. 7.6(b)] for different Δ and three different sets of tunnel coupling configurations. Note that we estimate Purcell decay with Eq. (5.76) and measurement-induced dephasing with Eq. (5.75) to be at least one order of magnitude smaller than $\gamma_{2,\mathrm{RX}}/2\pi$ in Fig. 7.7(a). For a high admixture of asymmetric charge states, we measure a maximum decoherence rate $\gamma_{2,\mathrm{RX}}/2\pi \sim 30\,\mathrm{MHz}$. For a more $(1,1,1)$-like character of the spin qubit, we extract a minimum decoherence rate $\gamma_{2,\mathrm{RX}}/2\pi \approx 10\,\mathrm{MHz}$, which corresponds to a dephasing time $\mathrm{T}_2^\star = 1/\gamma_{2,\mathrm{RX}} = 16\,\mathrm{ns}$. This measurement demonstrates that storing the quantum information in the spin degree of freedom increases the qubit coherence.

We model the RX qubit decoherence as $\gamma_{2,\mathrm{RX}} \equiv \gamma_{1,\mathrm{RX}}^{\mathrm{th}}/2 + \gamma_{\varphi,\mathrm{RX}}^{\mathrm{HF}}$, where the first and second terms are relaxation due to ohmic charge noise and Overhauser field induced dephasing, respectively. Both noise contributions were introduced in subsection 5.4.1. Theory and experiment in Fig. 7.7(a) are in good agreement for a standard deviation of the Overhauser fields of $\sigma_{\mathrm{HF}} = 3.51\,\mathrm{mT}$, which agrees with previously reported values

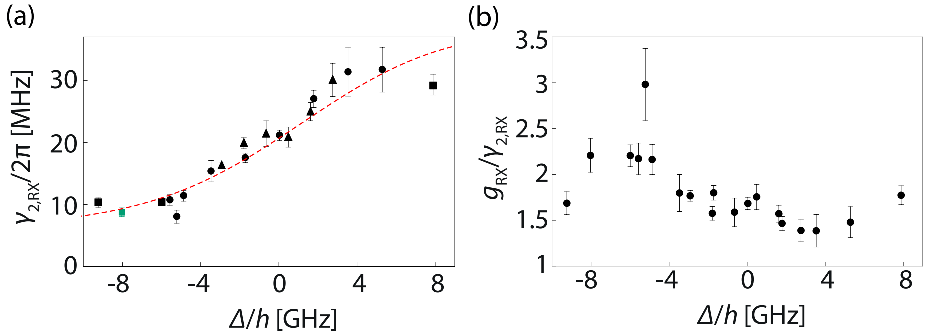

Figure 7.7 RX decoherence and optimal working point. (a) Extracted qubit decoherence $\gamma_{2,\mathrm{RX}}/2\pi$ with standard errors as a function of Δ for three different tunnel coupling configurations (■ $t_{\mathrm{L}}/h = 8.74\,\mathrm{GHz}$, $t_{\mathrm{R}}/h = 8.12\,\mathrm{GHz}$, ▲ $t_{\mathrm{L}}/h = 7.47\,\mathrm{GHz}$, $t_{\mathrm{R}}/h = 7.77\,\mathrm{GHz}$, • $t_{\mathrm{L}}/h = 8.10\,\mathrm{GHz}$, $t_{\mathrm{R}}/h = 7.86\,\mathrm{GHz}$). $\gamma_{2,\mathrm{RX}}$ obtained from the linear fit in Fig. 7.6(b) is shown in green. The red dashed line is a fit of a decoherence model (see subsection 5.4.1), which yields the charge noise parameter $\beta = 129.4$ and the width of the hyperfine field $\sigma_{\mathrm{B}} = 3.51\,\mathrm{mT}$. (b) Ratio of RX qubit coupling strength as extracted from theory over decoherence rate for the data points from (a).

for a resonant exchange qubit (Malinowski et al., 2017) and other spin qubits in GaAs (Petta et al., 2005, Johnson et al., 2005b, Koppens et al., 2005, 2006, Koppens et al., 2008). Our measurement in Fig. 7.7(a) therefore suggests that the RX qubit coherence is limited by hyperfine interaction in the GaAs host material.

While $\gamma_{2,\mathrm{RX}}$ increases with Δ in Fig. 7.7(a), the qubit-photon coupling strength increases since the contribution of $(1,0,2)$ and $(2,0,1)$ charge configurations to the qubit states and therefore the qubit electric dipole moment is enhanced. This suggests the existence of an optimal working point for the qubit, where the ratio $g_{\mathrm{RX}}/\gamma_{2,\mathrm{RX}}$ is maximal. We use the theory model for g_{RX} from subsection 5.1.2 to calculate this ratio for the data set in Fig. 7.7(a). We find in Fig. 7.7(b) that $g_{\mathrm{RX}}/\gamma_{2,\mathrm{RX}}$ is enhanced in the spin dominated regime with a maximum of ≈ 2.2 at $\Delta/h \approx -6\,\mathrm{GHz}$, which is about 40% larger compared to the averaged value of 1.6 obtained for a dominant charge character of the qubit ($\Delta > 0$).

7.6 RX qubit-photon coupling strength

In above section we assumed the validity of the theoretical prediction for the dependence of g_{RX} on Δ that was derived in subsection 5.1.2. In this section we extract this dependence from experiment by measuring the ac Stark shift. We also show that the average photon number in the resonator is well below one for the measurement of the Rabi splitting.

In the dispersive regime, the qubit frequency ν_{RX} shifts as a function of the average number of photons $\bar{n}$ in the resonator, which linearly depends on the resonator generator power $\mathrm{P}_{\mathrm{gen,r}}$. In addition, there is a Lamb shift of the qubit frequency due to the coupling to vacuum fluctuations. This results in the dressed qubit frequency [see Eq. (5.37)]

$$\tilde{\nu}_{\mathrm{RX}} = \nu_{\mathrm{RX}} + (2\bar{n}+1)(g_{\mathrm{RX}}/2\pi)^2/(\nu_{\mathrm{RX}} - \nu_{\mathrm{r}}). \tag{7.1}$$

In Fig. 7.8(a), we observe the frequency shift due to the ac Stark shift in the spectroscopic qubit signal measured at $\Delta/h = -6.02\,\mathrm{GHz}$ and $\varepsilon/h = -0.26\,\mathrm{GHz}$. We fit a function of the form

$$\tilde{\nu}_{\mathrm{RX}}(\mathrm{P}_{\mathrm{gen,p}}) = a\mathrm{P}_{\mathrm{gen,p}} + b \tag{7.2}$$

to the resonator generator power $\mathrm{P}_{\mathrm{gen,p}}$ dependent positions $\tilde{\nu}_{\mathrm{RX}}$ of the dressed qubit.

Note that we extract $\tilde{\nu}_{\mathrm{RX}}$ as the minimum of a Lorentzian fit to the phase response at constant $\mathrm{P}_{\mathrm{gen,p}}$ in Fig. 7.8(a). Using Eqns. (7.1) and (7.2) we obtain the bare qubit frequency as

$$\nu_{\mathrm{RX}} = \frac{1}{2}\left(b - \sqrt{-4(g_{\mathrm{RX}}/2\pi)^2 + (b-\nu_{\mathrm{r}})^2} + \nu_{\mathrm{r}}\right), \tag{7.3}$$

which allows to determine the photon number calibration factor

$$\alpha_{\bar{n}} \equiv n/\mathrm{P}_{\mathrm{gen,r}} = a(\nu_{\mathrm{RX}} - \nu_{\mathrm{r}})/(2(g_{\mathrm{RX}}/2\pi)^2) \tag{7.4}$$

for a known coupling strength g_{RX}. To determine the coupling strength, we measure the resonator frequency shift as a function of ε [as in Fig. 7.5(a)] at the RX qubit operation point ($\Delta/h = -6.02\,\mathrm{GHz}$) that was used for the ac Stark shift measurement in

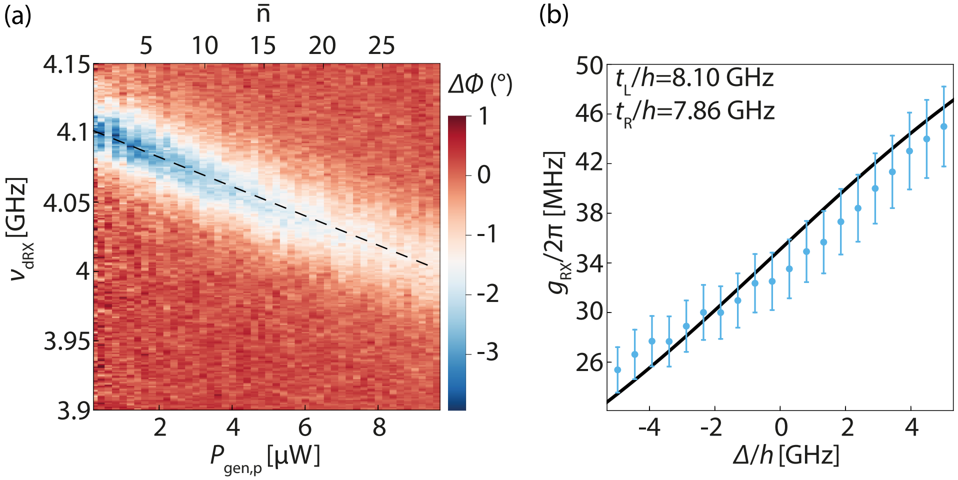

Figure 7.8 ac Stark shift. (a) Phase response as a function of spectroscopy frequency ν_{dRX} and resonator probe generator power $\mathrm{P}_{\mathrm{gen,p}}$. The resonator power is converted to the average number of photons in the resonator $\bar{n}$. The generator of the drive gate is set to a power of $\mathrm{P}_{\mathrm{gen,dRX}} = 0.25\,\mathrm{nW}$, the resonator is probed on resonance. The qubit parameters are tunnel couplings $t_{\mathrm{L}}/h = 8.74\,\mathrm{GHz}$ and $t_{\mathrm{R}}/h = 8.12\,\mathrm{GHz}$, detuning $\Delta/h = -6.02\,\mathrm{GHz}$ and asymmetry $\varepsilon/h = -0.26\,\mathrm{GHz}$. The position of the phase response minima are indicated with a dashed line. (b) Spin-qubit photon coupling strength g_{RX} with errors from the photon number calibration as a function of Δ (points) compared to the theory prediction (line) for ε close to the single sweet spot.

Fig. 7.8(a). We then obtain g_{RX} from the theory model which agrees with the frequency shift measurement.

We measure the ac Stark shift as in Fig. 7.8(a) for a second RX qubit configuration where $\{t_{\mathrm{L}}/h = 8.10\,\mathrm{GHz},\ t_{\mathrm{R}}/h = 7.86\,\mathrm{GHz},\ \Delta/h = -0.07\,\mathrm{GHz},\ \varepsilon/h = -0.1\,\mathrm{GHz}\}$ and perform the above analysis for this second data set. We extract the photon number calibration for both measurements independently and obtain an averaged value $\alpha_{\bar{\mathrm{n}}} = (2.6 \pm 0.4) \times 10^{-3}$ photons/nW. The vacuum Rabi splitting shown in Fig. 7.5(c) was recorded for $\mathrm{P}_{\mathrm{gen,p}} = 100\,\mathrm{nW}$. We can therefore reliably claim that for this measurement the average number of photons in the resonator is on the order of ~ 0.3. This confirms that we indeed achieved a strong hybridization of the spin qubit with single microwave photons.

With the known calibration factor $\alpha_{\bar{n}}$, the ac Stark shift gives direct access to the qubit-photon coupling strength since we obtain with Eqns. (7.1) and (7.2)

$$g_{\mathrm{RX}}/2\pi = \sqrt{-a(a - 2\alpha_{\bar{n}} b + 2\alpha \nu_{\mathrm{r}})}/2\alpha_{\bar{n}}. \tag{7.5}$$

By measuring the ac Stark shift as a function of Δ we extract an increases of g_{RX} with increasing Δ in Fig. 7.8(b). This increase in coupling strength, however, comes at the cost of an increase in qubit decoherence [see Fig. 7.7(a)]. The theoretically predicted coupling strength shown as a solid line in Fig. 7.8(b) agrees with our experimental observation.

7.7 Role of the $\mathrm{S}_z = 3/2$ state

In this paragraph we discuss the influence of the $\mathrm{S}_{\mathrm{z}} = 3/2$ state on the resonator response as observed in Figs. 7.4(b)-(d) at external magnetic fields $\mathrm{B} \geq 1\,\mathrm{T}$. For the experiments presented so far in this chapter, an external magnetic field of $\mathrm{B} = 200\,\mathrm{mT}$ was applied. For this choice of magnetic field, the state with $\mathrm{S}_{\mathrm{z}} = 3/2$ is more than $h \times 1\,\mathrm{GHz}$ higher in energy than the qubit states. When introducing B, the energy difference between the qubit states ($\mathrm{S}_{\mathrm{z}} = 1/2$) and the $\mathrm{S}_{\mathrm{z}} = 3/2$ state is changed by the Zeeman splitting $\mathrm{E}_{\mathrm{Z}} = g\mu_{\mathrm{B}}\mathrm{B}$.

In Fig. 7.9 we probe the resonator on resonance and sweep Δ and ε as for the measurements in Figs. 7.4(b)-(d)[1]. As we increase the external magnetic field from 1T to 2.5T in Fig. 7.9(a)-(d), the phase response signal in the resonator vanishes for

---

[1] The measurements in Figs. 7.4(b)-(d) were performed with a second sample, which has the same design as the first sample that was used for the experiments in the previous sections of this chapter. Both samples were processed at the same time and show similar qubit, resonator and qubit-resonator parameters.

negative Δ. This is expected when the $S_z = 3/2$ state, which does not couple to the resonator, becomes the ground state. The intersection of the $S_z = 3/2$ state with the qubit ground state is commonly used to read out the state of the RX qubit with RF reflectometry (Medford et al., 2013a,b, Malinowski et al., 2017). The thermal window

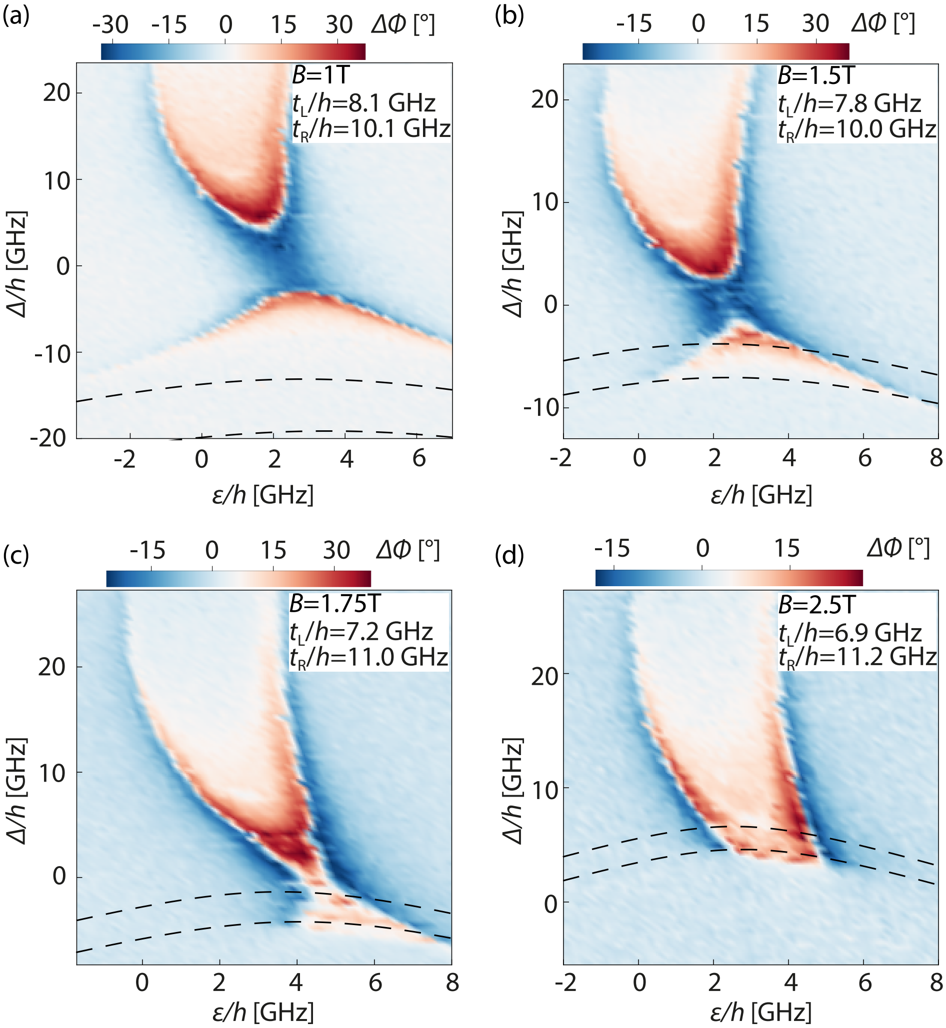

Figure 7.9 Resonator response for $B \geq 1\,T$. (a)-(d) Resonator phase response probed on resonance as a function of Δ and ε for different external magnetic fields B. The two dashed lines indicate the intersections $E_{3/2} = E_{|0_{RX}\rangle} + k_B T$ (bottom) and $E_{3/2} = E_{|0_{RX}\rangle} - k_B T$ (top), where $E_{3/2}$ is the $S_z = 3/2$ state energy, $k_B T$ the thermal energy for 30 mK and $E_{|0_{RX}\rangle}$ the qubit ground state energy.

for this intersection point is indicated by two dashed lines in Fig. 7.9(a)-(d). Within this window, the thermal occupation of the qubit ground state and the $S_z = 3/2$ state is expected to change significantly. The theory curves are calculated from the qubit energy spectrum and are in agreement with the experiment. Note that the change in the tunnel couplings $t_{\mathrm{L,R}}$ in Fig. 7.9(a)-(d) is due to the magnetic field since the electrostatic configuration of the qubit is unchanged.

7.8 Conclusion and outlook

The experiments presented in this chapter demonstrate the coherent coupling of a resonant exchange qubit to single microwave photons using hybrid circuit QED. The TQD spin-qubit arises from exchange interaction, which couples spin and charge independent of the host material. Other spin-qubit implementations are restricted to materials with strong spin-orbit interaction (Petersson et al., 2012) or require additional components such as ferromagnets (Viennot et al., 2015, Mi et al., 2018, Samkharadze et al., 2018) for the spin-charge hybridization. Furthermore, the TQD spin-qubit is versatile as all its parameters can be controlled electrostatically. For these reasons, it is possible to move our architecture to material systems with minimal hyperfine interaction, such as graphene (Trauzettel et al., 2007) or isotopically purified Si (Zwanenburg et al., 2013) without the necessity to deposit ferromagnetic materials, which is generally undesirable in the presence of a superconductor. By doing so, we expect the qubit coherence to improve by at least one order of magnitude.

Chapter 8

Coherent long-distance spin-qubit–transmon coupling

A future quantum processor will benefit from the advantages of different qubit implementations (Acín et al., 2018). Two prominent workhorses of solid state qubit implementations are spin- and superconducting qubits. While spin qubits have a high anharmonicity, a small footprint (Hanson et al., 2007) and promise long coherence times (Veldhorst et al., 2014, Yoneda et al., 2018, Russ et al., 2018), superconducting qubits allow fast and high fidelity read-out and control (Barends et al., 2014, Walter et al., 2017). A coherent link, which couples both qubit systems controllably over distances exceeding the physical size of the qubit, typically hundreds of nanometers, by several orders of magnitude is required to create an integrated scalable quantum device. An architecture to provide such a long-distance link is circuit QED, where long-distance coupling (Majer et al., 2007, Sillanpää et al., 2007) enables two-qubit gate operations (DiCarlo et al., 2009). Recently, coherent qubit-photon coupling was demonstrated for spin qubits (Mi et al., 2018, Samkharadze et al., 2018, Landig et al., 2018) in few electron quantum dots. However, coupling a spin qubit to another distant qubit has not yet been shown. One major challenge for an interface between spin and superconducting qubits is that spin qubits typically require large magnetic fields (Loss et al., 1998, Petta et al., 2005), to which superconductors are not resilient (Luthi et al., 2018).

We overcome this challenge by using a resonant exchange qubit. The qubit is implemented in a GaAs triple quantum dot at zero magnetic field without reducing its coherence compared to the measurements at finite magnetic field presented in chapter 7. The quantum link is realized with a frequency-tunable high impedance SQUID array resonator (Stockklauser et al., 2017), which couples the RX and the superconducting qubit coherently over a distance of a few hundred micrometers. We tune the RX qubit coupling strength to the resonator and its decoherence rate electrically and find that their ratio is comparable to previously reported values for spin qubits in Si (Mi et al., 2018, Samkharadze et al., 2018). We demonstrate coherent coupling between the two qubits first by resonant and then by virtual photon exchange in the high impedance resonator. For the latter coupling mechanism we tune the RX qubit into different regimes, where the qubit states have either a dominant spin or charge character.

The structure of this chapter is as follows: In sections 8.1 and 8.2 we present the sample and characterize both qubits as well as their individual interaction with the SQUID array resonator before we demonstrate resonant qubit-qubit interaction in section 8.3. Subsequently we characterize the RX qubit in section 8.4 at various working points in terms of the ratio of qubit-photon coupling strength over decoherence rate. Finally, we demonstrate virtual-photon-mediated RX qubit-transmon interaction in section 8.5 at four of these operation points.

The content of this chapter is closely related to our following preprint:

Coherent long-distance spin-qubit–transmon coupling
A. J. Landig, J. V. Koski, P. Scarlino, C. Müller, J. C. Abadillo-Uriel, B. Kratochwil, C. Reichl, W. Wegscheider, S. N. Coppersmith, Mark Friesen, A. Wallraff, T. Ihn, and K. Ensslin, arXiv: 1903.04022 (2019)

8.1 Experimental details

8.1.1 Sample

Figure 8.1 shows a schematic illustration and an optical micrograph of our sample. The microwave read-out scheme is also depicted in the figure. The sample design is similar to Ref. Scarlino et al., 2019b, where a semiconductor charge qubit was used instead of a spin qubit. The experiments are performed in the setup from chapter 2.

In the following we describe the four quantum systems of the sample. The superconducting qubit we use is a transmon (see subsection 3.3.2) as its Josephson energy exceeds the charging energy by about two orders of magnitude (see characterization in subsection 8.2.2). As shown in Fig. 8.1(b) and Fig. 8.2(a) and introduced in subsection 3.3.2, the transmon consists of an Al SQUID grounded on one side and connected in parallel to a shunt capacitor. We tune the transition frequency ν_{T} between the transmon ground $|0_{\mathrm{T}}\rangle$ and first excited state $|1_{\mathrm{T}}\rangle$ by changing the flux Φ_{T} through the SQUID loop with an on-chip flux line.

The transmon and the RX qubit are capacitively coupled to the same end of a SQUID array resonator, which we denote as coupling resonator in the following, with electric dipole coupling strengths g_{T} and g_{RX}, respectively. The other end of the coupling resonator is connected to DC ground. The resonator was introduced and characterized in section 4.3.2. Its resonance frequency ν_{cr} can be tuned from $\approx 4-6.8\,\mathrm{GHz}$ within the detection bandwidth of our measurement setup with a magnetic flux Φ_{cr} produced by a coil mounted close to the sample (see section 2.5). The resonator characteristic

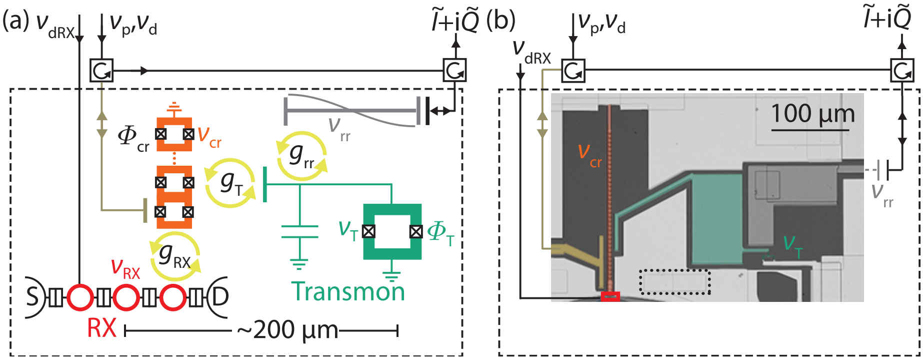

Figure 8.1 Sample. (a) Schematic of sample and measurement scheme. Microwave signals at frequencies ν_{p} (probe) and ν_{d} (drive) are routed with circulators as indicated by arrows. The reflected signal $\tilde{\mathrm{I}}+\mathrm{i}\tilde{\mathrm{Q}}$ at ν_{p} is measured. The sample (dashed line) contains four quantum systems with transition frequencies ν_i: a coupling resonator that consists of an array of SQUID loops (ν_{cr}, orange), a RX qubit (ν_{RX}, red), a transmon (ν_{T}, green) and a read-out resonator (ν_{rr}, gray). Empty black double-rectangles indicate electron tunnel barriers separating the three quantum dots (red circles) as well as the source (S) and drain (D) electron reservoirs. A drive tone at frequency ν_{dRX} can be applied to one of the dots. Crossed squares denote the Josephson junctions of SQUIDs. Yellow arrows indicate the coupling between the quantum systems with coupling strengths g_i. Φ_{cr} and Φ_{T} denote coupling resonator and transmon flux, respectively. (b) Optical micrograph of the relevant part of the sample (dashed region) that was schematically shown in (a). The measurement schematic is identical to (a). The micrograph is false colored with the same color code as in (a): SQUID array (coupling) resonator in orange with corresponding drive and probe port in yellow, transmon in green, one end of the $50\,\Omega$ (read-out) resonator in gray. GaAs in highlighted in black and grounded Al in white. The position of the TQD is outlined with a red rectangle. The dotted region is discussed in subsection 8.1.2.

impedance $Z_{\mathrm{cr}} \approx 1.37\,\mathrm{k\Omega}$ (for $\nu_{\mathrm{cr}} \approx 6.8\,\mathrm{GHz}$[1]) enhances its coupling strength to both qubits compared to a $50\,\Omega$ resonator. The transmon flux Φ_{T} has a negligible effect on ν_{cr}.

Figure 8.1 indicates that the transmon is also capacitively coupled to a $50\,\Omega$ $\lambda/2$ coplanar waveguide resonator. Throughout this article, we refer to this resonator as the read-out resonator, because it allows us to independently probe the transmon without populating the coupling resonator with photons. The read-out resonator is shown to the full extent in Fig. 8.2(c). Its design and characterization was discussed in section 4.2. It has a bare resonance frequency $\nu_{\mathrm{rr}} = 5.62\,\mathrm{GHz}$ and a total photon decay rate $\kappa_{\mathrm{rr}}/2\pi = 5.3\,\mathrm{MHz}$.

Coupling and read-out resonators are capacitively coupled to $50\,\Omega$ transmission lines that are shown in Fig. 8.1(b) and Fig. 8.2(c), respectively. The microwave wiring in Fig. 8.1 indicates that these transmission lines are used to read-out both resonators by measuring the reflection of a multiplexed probe tone at frequency ν_{p}. In addition, we can apply a drive tone at frequency ν_{d} that couples to both qubits via the resonators.

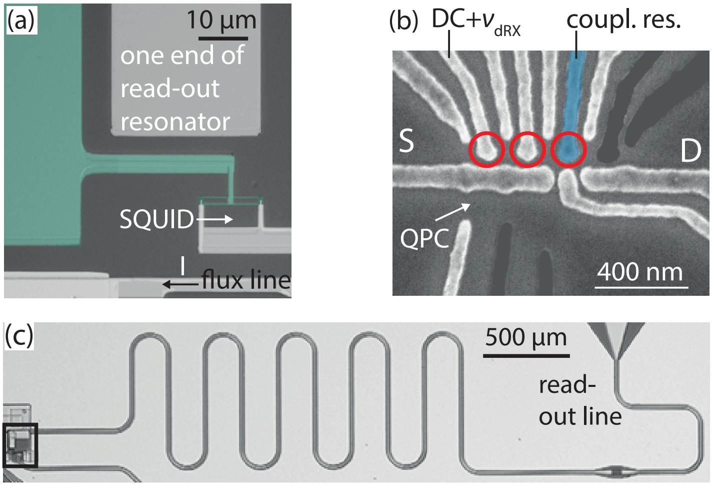

Figure 8.2 Sample details. (a) False-colored optical image of the transmon SQUID and parts of the transmon capacitor (green). The flux line with current I is marked. (b) Scanning electron micrograph of the TQD (red circles) and QPC region of the sample. Unused gate lines are grayed out. The gate line extending to the SQUID array resonator is highlighted in blue. (c) Optical micrograph of the $50\,\Omega$ resonator and its microwave read-out line. The location of the sample region shown in Fig. 8.1(b) is outlined with a black rectangle.

---

[1] Note that $Z_{\mathrm{cr}} \propto 1/\nu_{\mathrm{cr}}$.

The probe tone power is kept sufficiently low for the estimated average number of photons in both resonators to be less than one.

At a distance of a few hundred micrometers from the transmon, we form a TQD in a GaAs/AlGaAs heterostructure by local depletion with Al top gate electrodes shown in Fig. 8.2(b). One of the electrodes extends to the coupling resonator to enable electric dipole interaction between photons and TQD states. Another electrode allows us to apply RF signals at frequency ν_{dRX}. We use a QPC charge detector to help tune the TQD to the three-electron regime. Note that a DC voltage cannot be applied to the gate that extends to the resonator, since our SQUID array resonator design does not include a bias line. In order to still tune the quantum dot that is below the resonator gate [right quantum dot in Fig. 8.2(b)] to the few-electron regime, the gate design had to be adapted compared to the design used for the experiments in chapter 7 [see Fig. 7.1(c)], where DC bias via the NbTiN resonator was possible. As shown in Fig. 8.2(b), we use an additional gate line that is opposite to the resonator gate as a plunger gate.

We configure a RX qubit in the TQD (see section 3.2) using the method explained in section 7.2. For the experiments in chapter 7, the RX qubit was defined by states with $\mathrm{S} = 1/2$, $\mathrm{S}_z = 1/2$ that were split energetically from an equivalent set of states with $\mathrm{S} = 1/2$, $\mathrm{S}_z = -1/2$ by more than the thermal energy in the presence of an external magnetic field of 200 mT. For the measurements in this chapter, both sets of states are thermally occupied since the maximum external magnetic field given by Φ_{cr} is of the order of 1 mT. This however does not influence the resonator-qubit interaction, which is identical for a RX qubit defined in the $\mathrm{S}_z = 1/2$ or the $\mathrm{S}_z = -1/2$ spin subspace. We show in section 8.4 that also the RX coherence as determined by the resonator is not affected.

8.1.2 Sample fabrication

Here we provide an overview of the sample fabrication, which is described in more detail in Appendix C.2. The sample fabrication starts by defining the mesa structure, the ohmic contacts as well as the macroscopic gate lines using the recipes that were described in subsection 6.1.3. As a next step, we pattern the 50 Ω resonator as well as the macroscopic sample ground structures with photolithography and the evaporation of a Ti(3 nm)/Al(200 nm) layer. Subsequently we evaporate Ti(3 nm)/Al(27 nm) on an EBL defined structure in order to fabricate the TQD fine gates. Note that in contrast to subsection 6.1.3 we use Al for the fine gates since this is suspected to reduce the charge noise compared to Au fine gates (Stockklauser, 2017). Next, the SQUID array resonator and the transmon are defined with EBL and shadow evaporation as described in section 4.3.2. We use another EBL step to ensure good electrical connection between the EBL- and photolithography-defined Al structures, where we open the resist in large areas surrounding the overlap regions. An exemplary area is outlined with a dotted line in Fig. 8.1(b). Finally, we evaporate a layer of Ti(3 nm)/Al(200 nm) within theses areas.

8.2 Basic characterization

In this section we present spectroscopic measurements that serve as a basic characterization of the qubit and resonator frequencies as well as of their dependence on experimental control parameters such as magnetic flux and gate voltages.

8.2.1 Flux dependent RF spectrum

In Fig. 8.3 we determine the spectroscopic positions of the coupling resonator, the read-out resonator and the transmon by measuring $|S_{11}|$ as a function of probe frequency ν_p and global flux Φ_cr. This flux is produced by a coil mounted next to the sample and therefore affects the resonance frequencies of the SQUID array (coupling) resonator as well as of the transmon. The response due to the transmon is visible in Fig. 8.3 at around the maximum transmon frequency of $\nu_\mathrm{T} \approx 5.4\,\mathrm{GHz}$. The transmon has a faster periodicity in Φ_cr than the coupling resonator, as the area of the resonator SQUID loops is smaller compared to the area of the transmon SQUID [see Fig. 8.1(b)]. We observe about one periodicity of the coupling resonator in Fig. 8.3 with the maximum frequency at $\nu_\mathrm{cr} \approx 6.8\,\mathrm{GHz}$. The $50\,\Omega$ (read-out) resonator is resonant at $\nu_\mathrm{rr} \approx 5.6\,\mathrm{GHz}$. It is indirectly influenced by Φ_cr via the dispersively coupled transmon.

8.2.2 Transmon

In Fig. 8.4 we characterize the transmon with the two-tone spectroscopy method that was introduced in subsection 5.2.1. The probe tone is on resonance with the read-out resonator ($\nu_\mathrm{p} = \nu_\mathrm{rr}$) and the drive tone at frequency ν_d is swept to probe the transmon resonance. We detect a spectroscopic response of the transmon in Fig. 8.4 as a peak in $|\mathrm{A} - \mathrm{A}_0|$, which is centered at $\nu_\mathrm{d} = \nu_\mathrm{T}(\Phi_\mathrm{T})$. Here, A ($\mathrm{A}_0$) is the complex amplitude of the reflected microwave signal in the presence (absence) of the drive

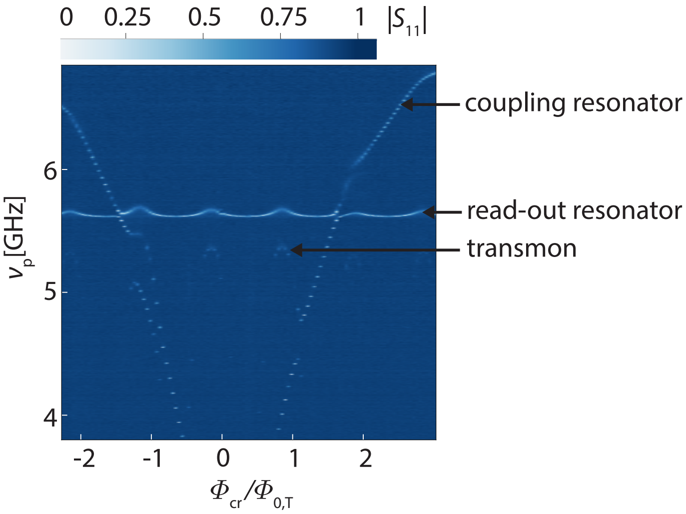

Figure 8.3 Flux dependent microwave response. Spectrum of reflected amplitude $|S_{11}|$ as a function of probe frequency ν_p and flux Φ_{cr}, which is normalized by the transmon flux periodicity $\Phi_{0,T}$. The RX qubit is detuned energetically. Exemplary positions of coupling resonator, read-out resonator and transmon are indicated with arrows.

tone[2]. We fit a Jaynes-Cummings Hamiltonian of the form presented in subsection 5.2.1 to the spectroscopic positions of the read-out resonator (not shown in Fig. 8.4) and the transmon. For the latter we include the position of the first (see Fig. 8.4)

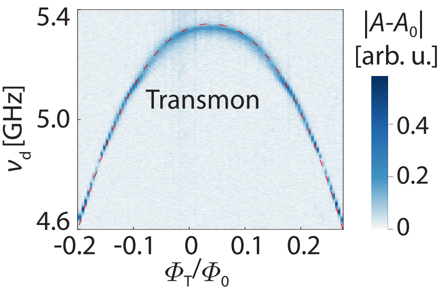

Figure 8.4 Transmon Φ_T-dispersion. Two-tone spectroscopy of the transmon with the RX qubit energetically far detuned. We plot the complex amplitude change $|A-A_0|$ (see main text) as a function of drive frequency ν_d and Φ_T/Φ_0. The dashed line indicates ν_T as obtained from theory (see text).

---

[2] Note that $|A|$ and $|S_{11}|$ are distinct, since the latter is normalized by the reflected signal in the absence of the resonator and therefore it is a unitless quantity.

as well as the second excited state (not shown in Fig. 8.4), which is probed by two photon transitions (Schuster et al., 2005, Schreier et al., 2008, Fink, 2010). Note that the coupling resonator is not considered for the fit since it is far detuned in frequency. We extract the coupling strength $g_{\mathrm{rr}}^{(0)}/2\pi \approx 141\,\mathrm{MHz}$ (at $\Phi_\mathrm{T} = 0$) of transmon and read-out resonator as well as the maximum Josephson energy $\mathrm{E}_\mathrm{J}^{(\mathrm{SQ})} = 18.09\,\mathrm{GHz}$ and the charging energy $\mathrm{E}_\mathrm{C}^{(\mathrm{T})} = 0.22\,\mathrm{GHz}$ of the transmon. Note that the parameters for all theory fits in this chapter can be found in Appendix B.3.

8.2.3 RX qubit

We also utilize two-tone spectroscopy to characterize the RX qubit. We apply a resonant probe tone to the coupling resonator ($\nu_\mathrm{p} = \nu_\mathrm{cr}$), a drive tone at ν_dRX to a TQD gate electrode and sweep the RX qubit energies with ε and Δ. The resulting resonator reflection $|\mathrm{S}_{11}|$ is shown in Fig. 8.5(a) for two different drive frequencies, which are well below ν_cr. In the figure we observe spectroscopic evidence of the RX qubit as local minima $\{\varepsilon_\mathrm{res}, \Delta_\mathrm{res}\}$ in $|\mathrm{S}_{11}|$ whenever drive tone and RX qubit are on resonance ($\nu_\mathrm{dRX} = \nu_\mathrm{RX}$). We fit $\nu_\mathrm{RX}(\varepsilon_\mathrm{res}, \Delta_\mathrm{res})$ calculated from the RX qubit Hamiltonian to these spectroscopic positions in order to extract t_L, t_R as well as the lever arms α_ε and α_Δ[3]. The fit result is shown as a red dashed line in Fig. 8.5(a). Thereby the quality of the fit is improved by performing a simultaneous fit to two datasets with different ν_dRX [see left and right panels in Fig. 8.5(a)].

We use a single-tone simulation to calculate the theoretical response due to a single drive tone in Fig. 8.5(b). Simulating two-tone spectroscopy is numerically challenging, since the Hamiltonian of the system will be explicitly time-dependent and there is no more steady state. Instead of tackling this problem using time-dependent simulations we note that for small amplitudes, in the linear response regime, the signal obtained from two-tone spectroscopy will be proportional to the single frequency response that we obtain from the quantum master equation that was presented in subsection 5.3.1. For every simulation of a two-tone measurement in this chapter we introduce this proportionality constant as an additional free parameter to match experimental two-tone spectroscopy data and simulation. Consequently, the experimental response due to the drive tone in Fig. 8.5(a), i.e. the local minima $\{\varepsilon_r, \Delta_\mathrm{res}\}$ discussed above, is well reproduced by the theoretical result shown in Fig. 8.5(b).

Four similar RX qubit tunnel coupling configurations are used for the experiments presented in this chapter. They are determined using the method explained above and

---

[3] Details of this analysis method are explained in section 7.2.

listed in Table 8.1. Different configurations were necessary in order to realize a certain qubit energy at a desired working point $\{\varepsilon, \Delta\}$. Second, when readjusting the tunnel couplings after the occurrence of a random charge rearrangement in the host material (electrostatic jump), the identical tunnel coupling configuration that was present before the charge rearrangement could not be achieved.

Except for the measurements in Fig. 8.5(a), we configure the RX qubit at the energy minimum in ε (single sweet spot), which is determined with two-tone spectroscopy, in

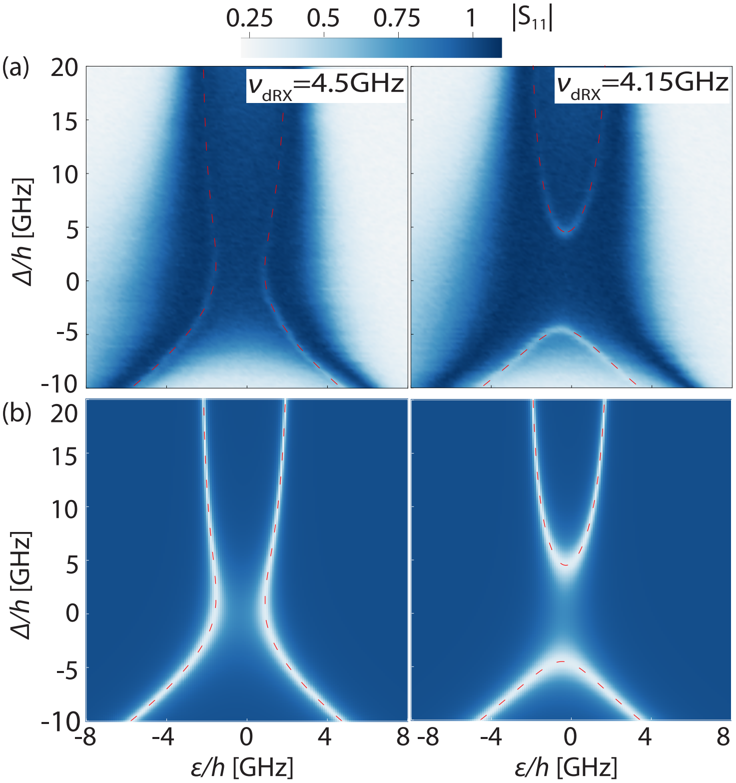

Figure 8.5 RX qubit two-tone spectroscopy. (a) Amplitude $|S_{11}|$ of the reflected microwave probe tone at $\nu_\mathrm{p} \approx \nu_\mathrm{cr} = 4.84\,\mathrm{GHz}$ as a function of RX qubit detuning Δ and asymmetry ε for $\nu_\mathrm{dRX} = 4.5\,\mathrm{GHz}$ and $\nu_\mathrm{dRX} = 4.15\,\mathrm{GHz}$ in the left and right panels, respectively. The dashed line shows the bare RX qubit energy contour for $\nu_\mathrm{RX} = \nu_\mathrm{dRX} = 4.5\,\mathrm{GHz}$ in the left and $\nu_\mathrm{RX} = \nu_\mathrm{dRX} = 4.15\,\mathrm{GHz}$ in the right panel for the couplings $t_\mathrm{L}/h = 8.52\,\mathrm{GHz}$ and $t_\mathrm{R}/h = 8.18\,\mathrm{GHz}$ as extracted from a fit to the spectroscopic response (see text). (b) Single drive tone simulations of (a). The dashed lines in (a) and (b) are identical.

RX qubit configuration	t_L/h [GHz]	t_R/h [GHz]
1	9.91	8.26
2	9.22	8.73
3	8.52	8.18
4	8.80	8.77

Table 8.1 RX qubit tunnel coupling configurations used in this chapter.

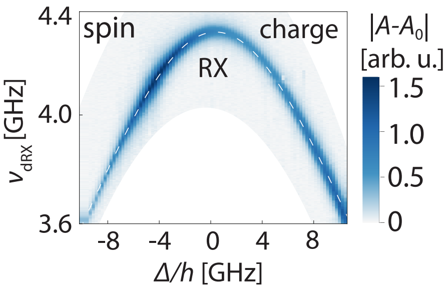

Figure 8.6 RX qubit Δ-dispersion. (b) Two-tone spectroscopy of the RX qubit (tunnel coupling configuration 3), with the transmon energetically far detuned for $\nu_p \approx \nu_{cr} = 4.84\,\text{GHz}$ as a function of Δ and ν_{dRX}. The dashed line shows the theoretically expected qubit frequency (see text).

order to protect it from charge noise (that couples to ε) to first order. The two-tone spectroscopy response of the RX qubit at this sweet spot as a function of Δ is indicated in Fig. 8.6. This measurement maps the RX qubit Δ—dispersion, which agrees well with the theoretical result obtained from the eigenenergies of a Jaynes-Cummings model. The model takes the spectroscopic positions of the coupling resonator (not shown in Fig. 8.6) and the RX qubit into account. Remember from section 3.2, that the RX qubit has a dominant spin or charge character for $\Delta < 0$ or $\Delta > 0$, respectively. This is indicated in Fig. 8.6.

8.3 Resonant interaction

First, we investigate the resonant interaction between the coupling resonator and the RX qubit. To start with, both qubits are detuned energetically from the coupling resonator. Then, we sweep Δ to cross a resonance between the RX qubit and the resonator, while keeping the transmon far detuned. We observe a well resolved avoided crossing in the $|S_{11}|$ reflectance spectrum shown in Fig. 8.7(a) and extract a spin qubit-photon coupling strength of $g_{\mathrm{RX}}/2\pi = 52\,\mathrm{MHz}$ from a fit of a quantum master equation simulation (see subsection 5.3.1) to the vacuum Rabi mode splitting [black in Fig. 8.7(c)]. The spin qubit and the coupling resonator photons are strongly coupled since $g_{\mathrm{RX}} > \kappa_{\mathrm{cr}}, \gamma_{2,\mathrm{RX}}$, with the RX qubit decoherence rate $\gamma_{2,\mathrm{RX}}/2\pi = 11\,\mathrm{MHz}$ and the bare coupling resonator linewidth $\kappa_{\mathrm{cr}}/2\pi = 4.6\,\mathrm{MHz}$. The decoherence rate is determined independently with power dependent two-tone spectroscopy: we dispersively detune the coupling resonator with Φ_{cr} from the RX qubit and extrapolate the width of the peak observed in the two-one spectroscopy response (c.f. Fig. 8.6) to zero drive power (see section 7.5).

Note that the extracted spin-photon coupling strength corresponds to a charge coupling strength $g^{(0)}_{\mathrm{c,RX}} = 186\,\mathrm{MHz}$, which is a factor of ≈ 2.6 larger compared to the experiments presented in chapter 7 (see section 7.4). In the following we discuss possible reasons for this enhancement. First, the characteristic impedance of the SQUID array resonator is larger compared to the NbTiN resonator. We estimate $Z_{\mathrm{cr}} \approx 2.2\,\mathrm{k\Omega}$ on resonance ($\nu_{\mathrm{cr}} \approx 4.2\,\mathrm{GHz}$) in Fig. 8.7(a), which enhances $g^{(0)}_{\mathrm{c,RX}} \propto \sqrt{Z_{\mathrm{cr}}}$ by a factor of ≈ 1.3 compared to the experiments in chapter 7. Second, the TQD is positioned at

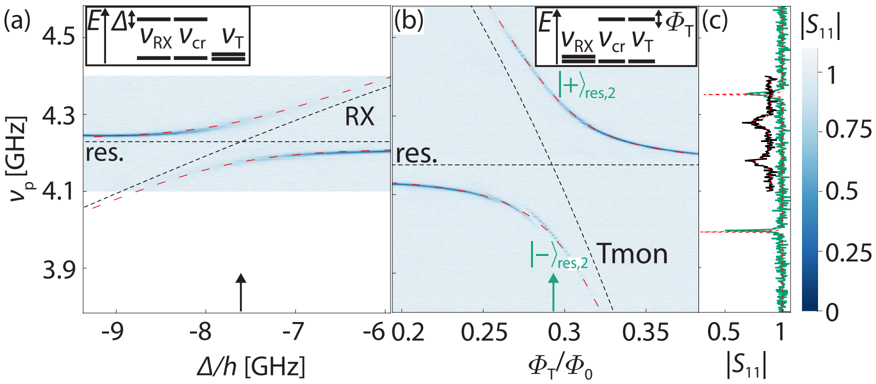

Figure 8.7 Resonant qubit-coupling resonator interaction. The schematics at the top of the graphs indicate the energy levels of the RX qubit (ν_{RX}), coupling resonator (ν_{cr}) and transmon (ν_{T}). Theory curves in the absence (presence) of coupling are shown as dashed black (red) lines. (a) Reflected amplitude $|S_{11}|$ as a function of RX detuning Δ and probe frequency ν_{p} for RX qubit tunnel coupling configuration 2. (b) Reflected amplitude $|S_{11}|$ as a function of relative transmon flux Φ_{T}/Φ_0 and ν_{p}. The states $|\pm\rangle_{\mathrm{res,2}}$ are discussed in the text. (c) Cuts from panel (a) at $\Delta/h \approx -7.6\,\mathrm{GHz}$ (black) and from panel (b) at $\Phi_{\mathrm{T}}/\Phi_0 \approx 0.3$ (green) as marked with arrows in the respective panels. The black trace is offset in $|S_{11}|$ by 0.1. Theory fits are shown as red dashed lines.

the end of the SQUID array resonator and therefore at the maximum of the voltage fluctuations, while there is a spatial offset from this maximum for the experiments in chapter 7 [see Fig. 7.1(b)]. Third, the design of the TQD fine gates was modified for the sample used in this chapter in order to enlarge the overlap of the resonator gate with the underlying quantum dot compared to the device presented in chapter 7. The increased capacitance between the gate and the dot enhances the resonator lever arm. Finally, the dependence of the lever arm on the position of the TQD with respect to the fine gates also possibly contributes to the coupling strength enhancement. Note that notable differences in the qubit-photon coupling strength were also observed by modifying the gate design of DQD charge qubit devices in Ref. Stockklauser, 2017.

Next, we characterize the interaction between the transmon and the coupling resonator. We tune the transmon through the resonator resonance by sweeping Φ_T. For this measurement the RX qubit is far detuned in energy. We resolve the hybridized states of the transmon and the resonator photons in the measured $|\mathrm{S}_{11}|$ spectrum in Fig. 8.7(b). They are separated in energy by the vacuum Rabi mode splitting $2g_\mathrm{T}/2\pi = 360\,\mathrm{MHz}$ illustrated in Fig. 8.7(c) in green. We perform power dependent two-tone spectroscopy to extract the transmon linewidth by probing the read-out resonator. We obtain $\gamma_{2,\mathrm{T}}/2\pi = 0.7\,\mathrm{MHz}$, which we estimate to be limited by Purcell decay (see subsection 5.4.3). Consequently, the strong coupling limit $g_\mathrm{T} > \kappa_\mathrm{cr}, \gamma_{2,\mathrm{T}}$ is also realized for transmon and coupling resonator.

We now demonstrate that the two qubits interact coherently via resonant interaction with the coupling resonator. For this purpose, we first tune the transmon and the coupling resonator into resonance, where the coupled system forms the superposition states $|\pm\rangle_{\mathrm{res},2} = (|1_\mathrm{cr}, 0_\mathrm{T}\rangle \pm |0_\mathrm{cr}, 1_\mathrm{T}\rangle)/\sqrt{2}$ (see subsection 5.2.1) of a single excitation in either the resonator or the qubit. Then, we sweep Δ to tune the RX qubit through a resonance with both the lower energy state $|-\rangle_{\mathrm{res},2}$ and the higher energy state $|+\rangle_{\mathrm{res},2}$. In the $|\mathrm{S}_{11}|$ spectrum in Fig. 8.8(a), avoided crossings are visible at both resonance points. This indicates the coherent interaction of the three quantum systems, which form the states $|-,\pm\rangle \approx \frac{1}{2}(|1_\mathrm{cr}, 0_\mathrm{T}, 0_\mathrm{RX}\rangle - |0_\mathrm{cr}, 1_\mathrm{T}, 0_\mathrm{RX}\rangle) \pm \frac{1}{\sqrt{2}}|0_\mathrm{cr} 0_\mathrm{T} 1_\mathrm{RX}\rangle$ and $|+,\pm\rangle \approx \frac{1}{2}(|1_\mathrm{cr}, 0_\mathrm{T}, 0_\mathrm{RX}\rangle + |0_\mathrm{cr}, 1_\mathrm{T}, 0_\mathrm{RX}\rangle) \pm \frac{1}{\sqrt{2}}|0_\mathrm{cr} 0_\mathrm{T} 1_\mathrm{RX}\rangle$. These states are symmetric or antisymmetric superpositions of the RX qubit state with the transmon-resonator $|\pm\rangle_{\mathrm{res},2}$ states. Note that the bare qubit energies are on resonance ($\nu_\mathrm{RX} = \nu_\mathrm{T}$) at $\Delta/h \approx -7.7\,\mathrm{GHz}$ between the two avoided crossing points observed in Fig. 8.8(a). There, the states are approximately given by $|0\rangle_{\mathrm{res},3}$ and $|\pm\rangle_{\mathrm{res},3}$ that were derived in subsection 5.2.2. The splitting $2g_\mp$ between $|-,\pm\rangle$ and $|+,\pm\rangle$ is extracted from the $|\mathrm{S}_{11}|$ reflection measurements in Fig. 8.8(c). We obtain $2g_+/2\pi = 84\,\mathrm{MHz}$ at

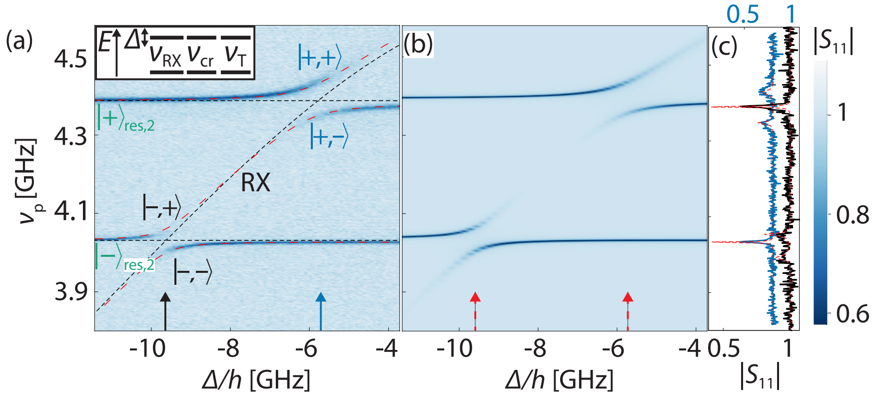

Figure 8.8 Resonant transmon-RX qubit interaction. (a) $|S_{11}|$ as a function of Δ and ν_p for RX qubit tunnel coupling configuration 2. The measurement is performed while transmon and coupling resonator are tuned on resonance, where they form the states $|\pm\rangle_{\text{res},2}$ [see green arrow in Fig. 8.7(b)]. The states $|-,\pm\rangle$ and $|+,\pm\rangle$ are explained in the text. (b) Result of a master equation simulation for parameters as in (a). The values for $|S_{11}|$ are scaled to the experimental data range in (a). (c) $|S_{11}(\nu_p)|$ at $\Delta/h \approx -9.8\,\text{GHz}$ and $\Delta/h \approx -5.6\,\text{GHz}$ as marked with the corresponding colored arrows in panels (a) and (b). The blue trace is offset in $|S_{11}|$ by 0.2.

$\Delta/h \approx -5.6\,\text{GHz}$ and $2g_-/2\pi = 63\,\text{MHz}$ at $\Delta/h \approx -9.8\,\text{GHz}$ from the fits in Fig. 8.8(c). The smaller g_- compared to g_+ is due the decrease of the RX qubit dipole moment with more negative Δ. The experimental observation in Fig. 8.8(a) is well reproduced by a quantum master equation simulation (see subsection 5.3.1) shown in Fig. 8.8(b).

8.4 RX optimal working point

While $\gamma_{2,\text{T}}$ is limited by Purcell decay and therefore does not depend on Φ_T, $\gamma_{2,\text{RX}}$ changes with Δ (see section 7.5). We use power dependent two-tone spectroscopy via the coupling resonator to measure $\gamma_{2,\text{RX}}$ as a function of Δ. The result is shown in Fig. 8.9(a). We observe an increase of $\gamma_{2,\text{RX}}$ as the charge character of the qubit is increased with Δ. This is consistent with Fig. 7.7(a), where however a smaller range in Δ was measured. Compared to Fig. 7.7(a), the data in Fig. 8.5(a) also covers the range $|\Delta| \gg t_{\text{L,R}}$.

In this paragraph we discuss the observation in Fig. 8.9(a) for $\Delta \ll 0$. The data suggests a lower limit of $\gamma_{2,\text{RX}}/2\pi \approx 6.5\,\text{MHz}$ for $\Delta \ll 0$ similar to the measurements in section 7.5 that were performed in an external magnetic field of 200 mT. Hence, our experiment indicates that the RX qubit can be operated near zero magnetic field without reducing its optimal coherence. We use the same noise model as in section 7.5 to fit to the measured decoherence rate. Theory and experiment in Fig. 8.9(a) match for a width $\sigma_{\mathrm{HF}} = 3.48 \pm 0.06\,\mathrm{mT}$ of the hyperfine field fluctuations, which agrees within the error range with $\sigma_{\mathrm{HF}} = 3.51 \pm 0.28\,\mathrm{mT}$ as obtained in section 7.5 and is in agreement with other work on spin in GaAs (Petta et al., 2005, Johnson et al., 2005b, Koppens et al., 2005, 2006, Koppens et al., 2008). We therefore draw the same conclusion as in section 7.5, that $\gamma_{2,\mathrm{RX}}$ is limited by hyperfine interaction. The fact that we obtain the same σ_{HF} for both magnetic field values suggests the validity of our hyperfine noise model presented in subsection 5.4.1.1. Note that this noise model could be checked further by measuring $\gamma_{2,\mathrm{RX}}$ in the regime where $\gamma_{\varphi,\mathrm{RX}}^{\mathrm{HF},\perp}$ exhibits a maximum [around 700 mT in Fig. 5.8(b)].

We now focus on the parameter range $\Delta > 0$ in Fig. 8.9(a). The maximal $\gamma_{2,\mathrm{RX}} \approx 20\,\mathrm{MHz}$ is smaller compared to $\gamma_{2,\mathrm{RX}} \approx 30\,\mathrm{MHz}$ obtained in Fig. 7.7. This difference is reflected in the smaller charge noise parameter $\beta = 62.9$ for the fit of the noise model to the data in Fig. 8.9(a) compared to $\beta = 129.4$ obtained from the fit in Fig. 7.7(a). A

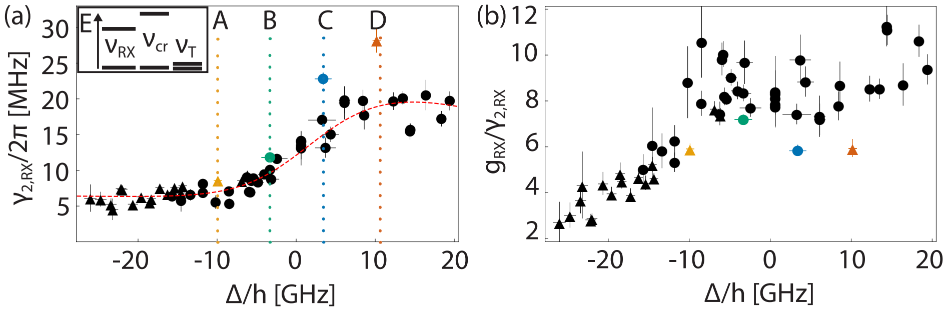

Figure 8.9 RX qubit working points. (a) RX qubit decoherence rate $\gamma_{2,\mathrm{RX}}$ as a function of Δ. The dotted vertical lines specify the four working points used for the measurements in section 8.5. The corresponding colored data points were obtained for a coupling resonator-RX qubit detuning of $\nu_{\mathrm{cr}} - \nu_{\mathrm{RX}} \approx (13.7, 8.0, 5.1, 4.4) g_{\mathrm{RX}}$ for $\Delta/h \approx (-9.9, -3.3, 3.4, 10.2)$ GHz and the RX qubit tunnel coupling configurations 3 (circle) and 4 (triangle). For the black data points, $\nu_{\mathrm{cr}} - \nu_{\mathrm{RX}} \geq 9.7\, g_{\mathrm{RX}}$ with qubit tunnel coupling configuration 1 (circle) and 2 (triangle). The dashed red line is a fit of a theory model (see main text) to the black data points. The error bars indicate the standard error of fits and an estimated uncertainty of the RX qubit energy of 50 MHz. (b) Ratio of g_{RX}, as obtained from theory, and $\gamma_{2,\mathrm{RX}}$ as shown in (a). The color and shape code of the data points is the same as in (a).

possible explanation for the reduced charge noise for the experiments in this chapter is the usage of Al fine gates for the TQD compared to Au gate lines that were employed in chapter 7. This would be in agreement with Ref. Premakumar et al., 2018, where superconducting gates were predicted to reduce evanescent wave Johnson noise. The same argument was used to explain an improved charge qubit coherence for Al instead of Au gates in Ref. Stockklauser, 2017.

The colored data points in Fig. 8.9(a) were measured for a smaller RX qubit-coupling resonator detuning compared to the black data points (numbers are given in Fig. 8.9 caption). The smaller detuning is used for the virtual interaction measurements presented in section 8.5. We observe an increase of $\gamma_{2,\mathrm{RX}}$ for small qubit-resonator detuning compared to large detuning. This increase is about one order of magnitude larger than our estimated difference of Purcell decay and measurement induced dephasing for those different data sets (see Appendix B.3.1). In contrast, for the transmon that is less sensitive to charge noise, we do not observe this effect. This suggests that the effect is due to charge noise induced by the coupling resonator.

Next, we investigate whether an optimal working point for the RX qubit exists, i.e. a Δ-operation point where the ratio $g_{\mathrm{RX}}/\gamma_{2,\mathrm{RX}}$ is maximal. While a distinct optimal point is not discernible for the black data points in Fig. 8.9(b), the averaged value of $g_{\mathrm{RX}}/\gamma_{2,\mathrm{RX}} \approx 9$ in the spin dominated regime for $-6 < \Delta/h < 0\,\mathrm{GHz}$ is about a factor of 1.7 larger than values reported so far for Si spin qubits in a circuit QED device (Samkharadze et al., 2018, Mi et al., 2018). In contrast, for the colored data points we observe an optimal working point at $\Delta/h \approx -3.3\,\mathrm{GHz}$ since $g_{\mathrm{RX}}/\gamma_{2,\mathrm{RX}}$ is reduced at small qubit-resonator detuning in Fig. 8.9(b) compared to the black data points at large detuning due to the influence of the coupling resonator on $\gamma_{2,\mathrm{RX}}$ discussed above.

8.5 Virtual-photon-mediated interaction

In this section we investigate RX qubit-transmon interaction mediated by virtual photons in the coupling resonator at the RX qubit working points marked in color in Fig. 8.9(a). The two qubits are resonant while the coupling resonator is energetically detuned, such that the photon excitation is not dominant in the superposed two-qubit eigenstates. This coupling scheme, illustrated in Fig. 8.10, is typically used for superconducting qubits to realize two-qubit operations (DiCarlo et al., 2009).

We measure the virtual coupling at the optimal working point ($\Delta/h \approx -3.3\,\mathrm{GHz}$), at $\Delta/h \approx -9.9\,\mathrm{GHz}$ and at $\Delta/h \approx 10.2\,\mathrm{GHz}$, where $\gamma_{2,\mathrm{RX}}$ in Fig. 8.9(a) saturates, as well as in the intermediate regime at $\Delta/h \approx 3.4\,\mathrm{GHz}$. While the RX qubit is tuned

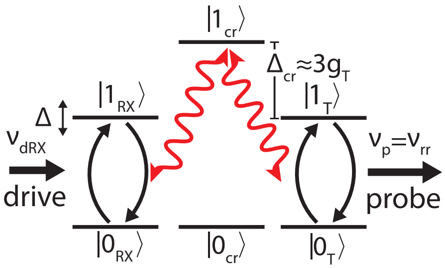

Figure 8.10 Virtual interaction measurement scheme. (a) Bare qubit transitions (black arrows) are coupled by virtual photon excitations (red arrows) in the detuned coupling resonator ($|(0/1)_{cr}\rangle$ are the two lowest photon number states). The RX qubit is driven at frequency ν_{dRX}, the transmon is probed via the read-out resonator at frequency ν_{rr}.

through a resonance with the transmon by changing Δ, they are both detuned by $\Delta_{cr} \equiv \nu_{cr} - \nu_T \approx 3g_T$ from the coupling resonator. To realize this detuning for every working point, we adjust the qubit and resonator energies with Φ_T, $t_{L,R}$ and Φ_{cr}.

As illustrated in Fig. 8.10, we drive the RX qubit via a gate line at frequency ν_{dRX} and investigate its coupling to the transmon by probing the dispersively coupled read-out resonator at its resonance frequency ($\nu_p = \nu_{rr} \approx 5.6\,\mathrm{GHz}$). This measurement is shown in Fig. 8.11(a) for the working point at $\Delta/h \approx -9.9\,\mathrm{GHz}$. For large transmon-spin qubit detuning ($\Delta/h \ll -10\,\mathrm{GHz}$), the spectroscopic signal of the transmon is barely visible as the drive mainly excites the bare RX qubit. The signal increases with Δ as the RX qubit approaches resonance with the transmon, such that driving the RX qubit also excites the transmon due to their increasing mutual hybridization. On resonance, we resolve the two hybridized spin qubit-transmon states $|\pm\rangle_{disp,3} \approx (|0_{RX}, 1_T\rangle \pm |1_{RX}, 0_T\rangle)/\sqrt{2}$ (see subsection 5.2.2) by about a linewidth. These states are separated in energy by the virtual-photon-mediated exchange splitting $2J \approx 2g_{RX}g_T/\Delta_{cr}$. The exchange splitting is enhanced at the other working points in Figs. 8.11(b)-(d), for which the RX qubit control parameter Δ and consequently g_{RX} is larger. The result of a master equation simulation shown in Fig. 8.11(b) agrees well with the experimental observation.

The influence of the RX qubit decoherence rate $\gamma_{2,RX}$ on the virtual interaction measurement is quantified in Fig. 8.12, where we show averaged measurements of the two-tone spectroscopy signal from Figs. 8.12(a)-(d) at Δ as indicated by arrows in the corresponding panels. We also show fits of a master equation model in Fig. 8.12. The exchange splitting is best resolved at the optimal working point, corresponding to the solid green curve in Fig. 8.12, where we obtain $2J/2\pi \approx 32\,\mathrm{MHz}$ from the fit. Note that it turned out that there was significant power broadening present in the experiments. This manifested itself in a reduced size of the observed anti-crossing

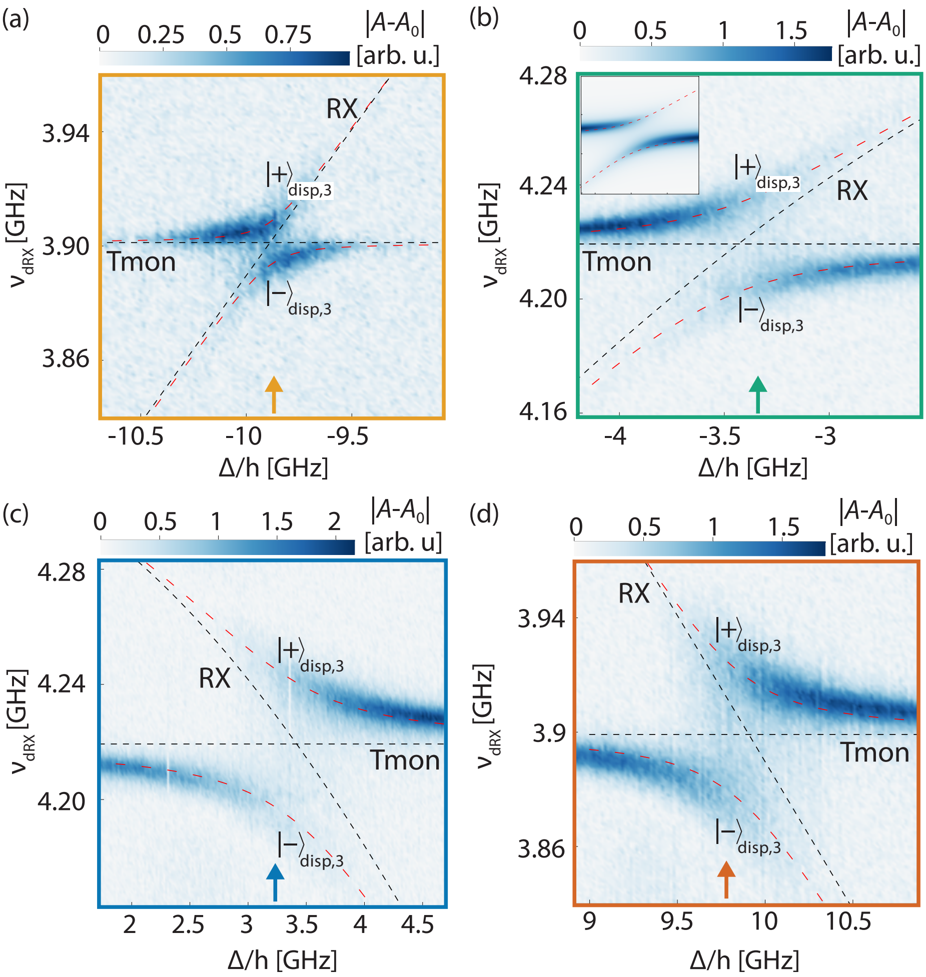

Figure 8.11 Virtual-photon-mediated RX qubit-transmon interaction. (a)-(d) Two-tone spectroscopy at $\nu_\mathrm{p} = \nu_\mathrm{rr} \approx 5.6\,\mathrm{GHz}$ as a function of Δ and drive frequency ν_dRX, realizing the measurement scheme in Fig. 8.10. Dashed black (red) lines indicate transmon and RX qubit energies in the absence (presence) of coupling. The frame color refers to the RX qubit working points as specified in Fig. 8.9(a). The inset in (b) shows the result from a master equation simulation with the same axes as the main graph.

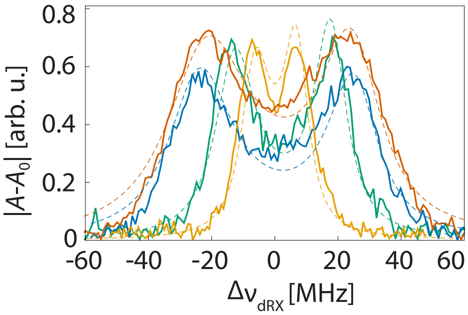

Figure 8.12 Exchange splittings. Two-tone spectroscopy response from Figs. 8.11(a)-(d) at Δ as specified with arrows in the corresponding panels. The cuts are centered around zero by accounting for a frequency offset $\nu_{\mathrm{dRX},0} \equiv \nu_{\mathrm{dRX}} - \Delta\,\nu_{\mathrm{dRX}}$. The dashed lines show the corresponding theory results.

compared to the expected value when applying the parameters obtained in previous fits (c.f. Fig. 8.7). As our fitting procedure, first adjusting Hamiltonian parameters using observed peak positions and then fitting the linewidth, cannot account for this kind of power broadening by itself, we adapted the fits to adjust the observed coupling strength between the RX qubit and the coupling resonator to account for the observed values (see Appendix B.3.2 for fit parameter values). Additionally, when subsequently fitting the linewidths, we had to introduce significant additional broadening to the transmon linewidth $\gamma_{2,\mathrm{T}}$, for simplicity setting it equal to the RX linewidth $\gamma_{2,\mathrm{RX}}$ obtained in Fig. 8.9(a). This combination leads to excellent quantitative agreement of theory and experiment in Fig. 8.12.

In Fig. 8.11, virtual-photon-mediated transmon-RX qubit interaction was realized by driving the RX qubit and tuning its energy with Δ into resonance with the transmon. Alternatively, both qubits can be tuned on resonance by changing the transmon energy with Φ_T. Such a measurement is shown for RX qubit working point B in Fig. 8.13(a). The anti-crossings in Fig. 8.11(b) and Fig. 8.13(a) are very similar, as it is equivalent to sweep Δ or Φ_T to tune both qubits on resonance.

In Fig. 8.13(b) we realize another alternative virtual interaction measurement scheme. There, we apply the drive tone via the resonators and tune both qubits on resonance by sweeping Δ. In contrast to the previous measurements in this section, this drive excites the transmon, which we observe spectroscopically in Fig. 8.13(b) if it is detuned from the RX qubit. The visibility of the spectroscopic signal is reduced by approaching the two-qubit resonance condition with Δ since the coherence of the hybridized transmon-RX qubit system is smaller compared to the bare transmon

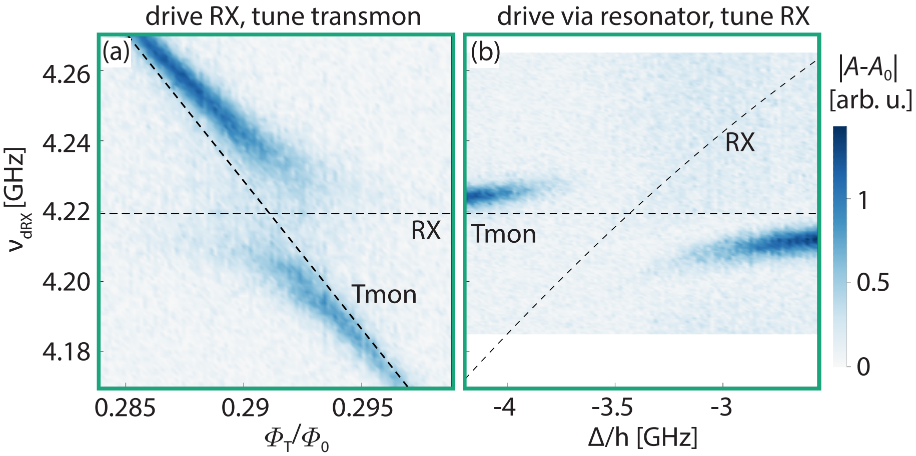

Figure 8.13 Alternative realizations of virtual-photon-mediated RX qubit-transmon interaction. The dashed lines are the bare RX and transmon energies. (a) Two-tone response at $\nu_p = \nu_{rr} = 5.63\,\mathrm{GHz}$ as a function drive frequency ν_{dRX} and normalized transmon flux Φ_T/Φ_0. The measurement parameters are identical to Fig. 8.11. (b) Identical to (a) except for sweeping the RX qubit energy with Δ and applying the drive tone via the resonator.

coherence. This reduced visibility is in contrast to Fig. 8.11(b), where the coherence of the hybrid system is improved compared to the bare RX qubit coherence off resonance. By increasing the drive power for a measurement as in Fig. 8.13(b), we would expect the visibility on resonance to increase however at the cost of adding power broadening to the system.

8.6 Conclusion and outlook

In conclusion, we have implemented a coherent long-distance link between a RX qubit and a transmon. The link either utilizes real or virtual microwave photons for the qubit-qubit interaction. The RX qubit was operated in both spin and charge dominated regimes. We found an optimal working point at which the ratio between its resonator coupling rate and its decoherence rate is maximal and comparable to state-of-the-art values achieved with spin qubits in Si. We also reported that the coupling resonator potentially introduces charge noise that can have significant impact on the RX qubit coherence. The performance of the quantum link in this work is limited by the minimum decoherence rate of the qubit, which is determined by hyperfine interaction in the GaAs host material. Once the spin coherence is enhanced by using hyperfine-free material systems such as graphene (Trauzettel et al., 2007, Eich et al., 2018) or isotopically purified Si (Zwanenburg et al., 2013), the spin could be used as a memory that can be coupled on-demand to the transmon by pulsing the qubit control parameter. As the coherence properties of the RX qubit are retained at zero magnetic field in contrast to other spin qubit implementations, the quantum device architecture used in this work is compatible for realizing a high fidelity transmon–spin-qubit and spin-qubit–spin-qubit (Srinivasa et al., 2016) interface in a future quantum processor.

Chapter 9

Conclusion and outlook

In this thesis, we have studied different solid-state quantum systems as well as their interaction with single photons at a fundamental level using hybrid circuit QED technology. We thereby put the focus on quantum systems that are formed by few-electron spin states in double or triple quantum dots in a GaAs/AlGaAs heterostructure. The basis of these studies was set by an experimental setup that connects microwave and DC electronics at room temperature to the quantum systems that are kept at mK temperatures with the constraints that the microwave signals are at the level of single microwave photons and sub 100 mK electronic temperatures can be achieved. The setup was assembled and in large parts also developed from scratch in this work.

Another important ingredient for our experiments was to further develop the hybrid circuit QED sample architecture introduced in earlier studies (Frey et al., 2012, Petersson et al., 2012) with two goals. The first goal was to achieve compatibility in large magnetic fields, motivated by the ability to investigate spin properties of the quantum systems in a magnetic field. The second goals was to enhance the qubit-photon coupling strength, driven by the intention to reach the strong coupling limit. We realized both goals by designing and fabricating a coplanar-waveguide type superconducting NbTiN microwave resonator. The thin and narrow film of the resonator center conductor makes it resilient to parallel magnetic fields and leads to a high characteristic resonator impedance that in turn enhances the coupling strength. Test resonators were characterized and reasonable quality factors of the order of 10^3 as well as a magnetic field resilience of up to two tesla was demonstrated.

The magnetic field resilience of the resonator was employed in a first experiment (Landig et al., 2019b) to investigate spin states of few electrons in a DQD, which was coupled to the resonator in the weak coupling regime. By probing the resonator transmission, we could distinguish two-electron spin-singlet from spin-triplet states due to the vanishing electric susceptibility of the latter. We used this spin selectivity of the resonator to map the crossover of the two-electron DQD ground state from a spin-singlet to a spin-triplet state in a magnetic field. We also investigated Pauli spin-blockade known from transport experiments at finite source-drain bias, where we discovered an unconventional spin blockade triggered by the absorption of resonator photons. This first experiment demonstrated the usability of a magnetic-field-compatible hybrid circuit QED system to investigate DQD spin physics from a different experimental perspective compared to for example electronic transport related studies. The presented approach can be a key technology in future experiments to investigate spin-related properties in other material systems including 2D materials. It can also be further developed to realize fast spin state read-out (Zheng et al., 2019) or to study spin in larger quantum dot systems such as for example in a 2D array of quantum dots (Mortemousque et al., 2018).

In the second experiment (Landig et al., 2018), we focused on the quantum information aspect of the hybrid circuit QED system. There, we demonstrated strong coupling between single microwave photons in a NbTiN high impedance resonator and a spin qubit that is based on exchange interaction between three electron spins in a TQD. We resolved the vacuum Rabi mode splitting and demonstrated electrostatic tunability of the qubit-photon coupling strength as well as of its coherence time. Similar to the demonstration of strong coupling for superconducting qubits (Wallraff et al., 2004), the realization of coherent spin-photon interaction in this work and in Refs. Mi et al., 2018, Samkharadze et al., 2018 will likely trigger a variety of follow-up hybrid circuit QED experiments involving spin qubits such as long-range qubit-qubit coupling (Srinivasa et al., 2016, Benito et al., 2019) as well as dispersive single-shot spin qubit read-out (D'Anjou et al., 2019). These experiments pursue the goal of realizing a large-scale spin-qubit based quantum processor architecture (Vandersypen et al., 2017). Integrating the RX qubit into such an architecture can be advantageous compared to using other quantum dot based spin-qubit systems, which require an external magnetic field and rely on spin-charge hybridization due to local magnetic stray fields or material intrinsic spin-orbit interaction in order to realize spin-photon coupling. Spin-charge hybridization is inherent for the RX qubit and full electrical control is possible without the necessity of ferromagnetic materials in the vicinity of the qubit.

The coherence performance of the RX qubit is unchanged even at zero magnetic field (Landig et al., 2019a), which makes it compatible with superconducting qubits. We used this advantage in our third experiment to coherently couple a transmon and a RX qubit on-chip over a distance that exceeds the extent of the spin qubit by three orders of magnitude. The coupling was realized with a frequency-tunable high impedance SQUID array resonator (Stockklauser et al., 2017, Scarlino et al., 2019b). We demonstrated resonant as well as virtual photon-mediated interaction of both qubits. In the latter case the RX qubit was among others operated at a working point where its coupling to decoherence ratio is maximal and state of the art for spin qubits in hybrid circuit QED (Mi et al., 2018, Samkharadze et al., 2018). While we found spectroscopic indication for qubit-qubit entanglement in our measurements, time-resolved experiments that capture and control the coherent qubit dynamics will allow to perform state tomography by dispersive read-out (Blais et al., 2004) and ultimately to implement single and two-qubit gate operations (Srinivasa et al., 2016, Benito et al., 2019). A characteristic quantity for such controlled qubit operations is the fidelity of the target state, which is among others limited by the ratio of the total time required for qubit gate operations and read-out over the qubit coherence time. In order to eventually reach the fidelities that are routinely achieved with superconducting qubits (Andersen et al., 2019), the coherence time of the RX qubit needs to be significantly increased from the value of about 20 ns as measured in our second and third experiment by at least three orders of magnitude. For an even further prolonged coherence, the spin qubit could serve as a quantum memory (Xiang et al., 2013).

We concluded from our second and third experiment that the RX qubit coherence time is limited by hyperfine-induced dephasing and can therefore likely be boosted by realizing the qubit in a material platform with minimal hyperfine interaction, such as graphene (Trauzettel et al., 2007) or silicon (Zwanenburg et al., 2013). The residual isotopes with finite nuclear spin can be further reduced in both materials by isotopic purification (Becker et al., 1995, Chen et al., 2012), which allowed to achieve coherence times in the millisecond range for spin qubits in Si quantum dots (Veldhorst et al., 2014). For graphene, where high quality single electron quantum dots were recently realized in Ref. Eich et al., 2018, measurements of the spin coherence are still to be performed. A possible challenge for a graphene- or silicon-based RX qubit could be to reach sufficient electrostatic control in the TQD in order to realize tunnel couplings of the order of 10 GHz simultaneously between the left and middle and the middle and right quantum dots. Further complications might arise due to the valley degree of freedom in silicon based systems (Yang et al., 2013, Russ et al., 2017, Mi et al., 2017c) as well as in graphene.

Instead of eliminating the hyperfine field in the qubit host material, insensitivity of a spin qubit to magnetic field noise to first order can be achieved by encoding the qubit states in the total spin $S = 0$ subspace. Such an exchange based qubit has been proposed with four electrons in a triple (Russ et al., 2018) or quadruple (Sala et al., 2017) quantum dot, where in the latter case the additional quantum dot is required due to the absence of a valley splitting in the qubit material system.

Independent of the exact number of electrons or quantum dots that are required to implement a quantum dot based spin-qubit, the qubit initialization is currently far more complex compared to other solid-state based qubits such as superconducting qubits. It requires tuning of multiple gate voltages, which can vary significantly from qubit to qubit due to fabrication related imprecisions as well due to local differences in the electrostatic solid-state environment. This inhomogeneity can be a major obstacle for scalability. Current approaches to tackle this challenge include to employ industrial CMOS technology for device fabrication (Maurand et al., 2016, Sabbagh et al., 2019) as well as to use automated gate tuning algorithms (Baart et al., 2016, Botzem et al., 2018, Kalantre et al., 2019). If this particular challenge can be overcome, as for any other qubit technologies, there will likely be further unforeseen challenges ahead and hopefully rich physics to discover on the long path towards a large-scale quantum information processor.

Appendix A

Three-electron wave-function representations

The wave-function representation of the three-electron states from Table 3.2 has the form (Ihn, 2018)

$$
\begin{aligned}
\Psi = & \frac{1}{\sqrt{3!}}(|\Psi_\mathrm{L}\Psi_\mathrm{M}\Psi_\mathrm{R}\rangle \otimes |\sigma_1\sigma_2\sigma_3\rangle + |\Psi_\mathrm{M}\Psi_\mathrm{R}\Psi_\mathrm{L}\rangle \otimes |\sigma_2\sigma_3\sigma_1\rangle \\
& + |\Psi_\mathrm{R}\Psi_\mathrm{L}\Psi_\mathrm{M}\rangle \otimes |\sigma_3\sigma_1\sigma_2\rangle - |\Psi_\mathrm{L}\Psi_\mathrm{R}\Psi_\mathrm{M}\rangle \otimes |\sigma_1\sigma_3\sigma_2\rangle \\
& - |\Psi_\mathrm{R}\Psi_\mathrm{M}\Psi_\mathrm{L}\rangle \otimes |\sigma_3\sigma_2\sigma_1\rangle - |\Psi_\mathrm{M}\Psi_\mathrm{L}\Psi_\mathrm{R}\rangle \otimes |\sigma_2\sigma_1\sigma_3\rangle),
\end{aligned}
\tag{A.1}
$$

where for example $|\Psi_\mathrm{M}\Psi_\mathrm{R}\Psi_\mathrm{L}\rangle$ indicates that electron one, two and three occupy the middle, right and left quantum dot orbital states Ψ_M, Ψ_R and Ψ_L, respectively. The exemplary spin part of the wave function $|\sigma_2\sigma_3\sigma_1\rangle$ with $\sigma_i = \{\uparrow, \downarrow\}$ denotes that electrons one, two and three are in the spin state σ_2, σ_3 and σ_1, respectively. While $\mathrm{Q}_{+3/2}$ from Table 3.2 is given by the single Slater determinant from Eq. (A.1) for $\sigma_{1,2,3} =\uparrow$, the wave function representation of other states can be constructed as a linear superposition of Eq. (A.1).

For the asymmetric charge configurations, the wave-function representation of, for example, $\mathrm{D}_{\mathrm{R},1/2}$ from Table 3.3 can be written as (Ihn, 2018)

$$
\begin{aligned}
|\uparrow\downarrow, 0, \uparrow\rangle = & \frac{1}{\sqrt{6}}[(|\Psi_\mathrm{L}\Psi_\mathrm{L}\Psi_\mathrm{R}\rangle - |\Psi_\mathrm{R}\Psi_\mathrm{L}\Psi_\mathrm{L}\rangle) \otimes |\uparrow\downarrow\uparrow\rangle \\
& + (|\Psi_\mathrm{L}\Psi_\mathrm{R}\Psi_\mathrm{L}\rangle - |\Psi_\mathrm{L}\Psi_\mathrm{L}\Psi_\mathrm{R}\rangle) \otimes |\downarrow\uparrow\uparrow\rangle \\
& + (|\Psi_\mathrm{R}\Psi_\mathrm{L}\Psi_\mathrm{L}\rangle - |\Psi_\mathrm{L}\Psi_\mathrm{R}\Psi_\mathrm{L}\rangle) \otimes |\uparrow\uparrow\downarrow\rangle].
\end{aligned}
\tag{A.2}
$$

Appendix B

Appendix for chapter 8

B.1 Additional data

B.1.1 Resonant RX-resonator interaction for multiple Δ

In section 7.6 we determined the RX qubit-photon coupling strength g_{RX} by utilizing the ac Stark shift. In Fig. B.1 we extract g_{RX} from resonant qubit-resonator interaction. There we set Δ to the RX qubit working points presented in section 8.4, adjust ν_{cr} with Φ_{cr} and tune RX qubit and coupling resonator on resonance by sweeping ε. Note

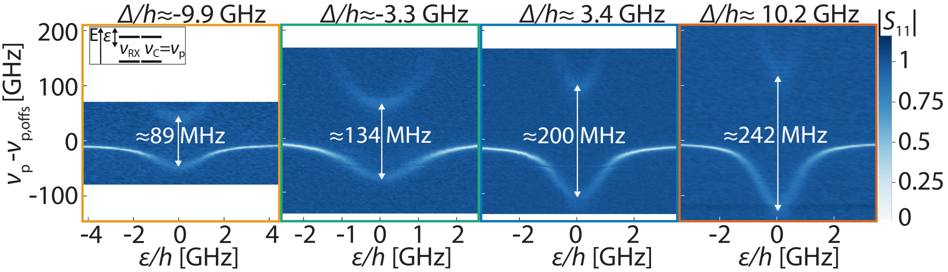

Figure B.1 Resonant RX qubit-resonator interaction. Spectrum of $|S_{11}|$ as a function of coupling resonator probe frequency ν_{p} and RX qubit asymmetry ε for increasing Δ from the left to the right panel. The transmon is detuned energetically for this measurement. The RX qubit tunnel couplings and Δ-positions are identified by the frame colors, which refer to the same colored working points in Fig. 8.9(a). Note that an offset in ε was added such that the energy minimum is at $\varepsilon \approx 0$. The approximate vacuum Rabi mode splitting is indicated. It is centered around $\nu_{\mathrm{p}} - \nu_{\mathrm{p,offs}} = 0$, where $\nu_{\mathrm{p,offs}}$ is a frequency offset that varies for the different panels.

that the transmon is detuned for this measurement. We observe anti-crossings in the $|S_{11}|$ reflectance spectra with increasing separation by increasing Δ from the left to the right panel. As the separation is $\approx 2g_{\mathrm{RX}}$, g_{RX} increases with Δ consistent with the measurement in section 7.6 and the theoretically expected behavior.

B.2 Additional data for virtual-photon-mediated interaction

In Fig. 8.13(b) we presented two-tone spectroscopy data for virtual-photon mediated RX qubit-transmon interaction that was measured at one RX qubit working point by driving the transmon and tuning the RX qubit energy with Δ. We use the same measurement scheme [see Fig. B.2(a)] in Figure B.2(b)-(d) to determine the two-tone response

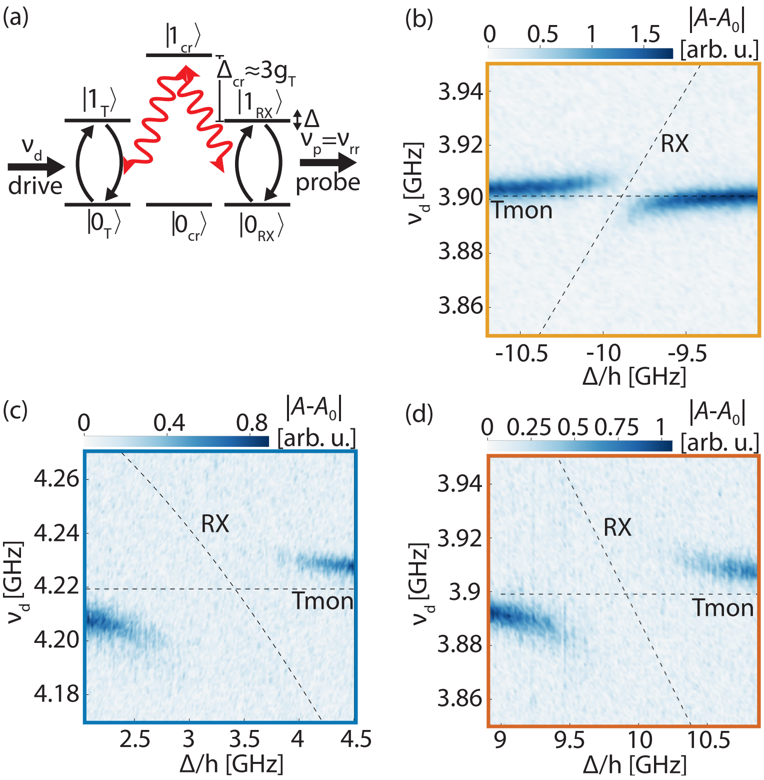

Figure B.2 Additional data on virtual RX-transmon interaction. The frame colors refer to the RX qubit working points in Fig. 8.9. (a) Measurement scheme for (b)-(d) similar to Fig. 8.10. (b)-(d) Two-tone spectroscopy signal at $\nu_{\mathrm{p}} = \nu_{\mathrm{rr}} \simeq 5.6\,\mathrm{GHz}$ as a function of ν_{d} and Δ.

at the remaining three RX qubit working points. As in Fig. 8.13(b), the spectroscopic response of the transmon vanishes once the RX qubit is tuned close in energy due to the larger decoherence rate of the RX qubit compared to the transmon.

B.3 Parameter tables

B.3.1 Experimental parameters for RX qubit decoherence data

In Table B.1 we show relevant experimental parameters of coupling resonator and RX qubit that were present when measuring $\gamma_{2,\mathrm{RX}}$ in Fig. 8.9 for the qubit working points for small and large coupling resonator-qubit detuning. As discussed in section 8.4, we observe a significant increase in $\gamma_{2,\mathrm{RX}}$ at $\Delta > 0$ for small detuning. We extract from Table B.1 that this increase cannot be explained by Purcell decay at rate γ_P or measurement-induced-dephasing at rate γ_MID (see subsection 5.4.3).

B.3.2 Theory fit parameters for experiments in chapter 8

In Tables B.2-B.10 we indicate fixed and free parameters of the theory fits that were used in chapter 8. Fixed fit parameters are marked with a star. They were either directly extracted from the experiment (e.g. resonance frequencies) or from previous fits (e.g. qubit parameters).

Working point Δ/h [GHz]	RX qubit config.	ν_{RX} [GHz]	$\gamma_{2,\mathrm{RX}}/2\pi$ [MHz]	$g_{\mathrm{RX}}/2\pi$ [MHz]	ν_{cr} [GHz]	$\kappa_{\mathrm{cr}}/2\pi$ [MHz]	$\bar{n}$	$\gamma_{\mathrm{P}}/2\pi$ [MHz]	$\gamma_{\mathrm{MID}}/2\pi$ [MHz]
$\simeq -9.9$	4	3901	8.7 ± 0.3	45.2	4519	4.1	0.04	0.02	0.09
$\simeq -9.9$	4	3903	8.3 ± 0.4	48.3	5164	5.0	0.03	0.01	0.11
$\simeq -3.3$	3	4225	11.9 ± 0.3	77.9	4845	5.1	0.01	0.08	0.10
$\simeq -3.3$	3	4228	7.8 ± 0.5	86.1	5895	9.2	0.04	0.02	0.36
$\simeq 3.4$	3	4221	22.9 ± 0.9	121.3	4845	7.0	0.04	0.24	0.55
$\simeq 3.4$	3	4222	14.8 ± 1.5	133.7	5894	6.9	0.02	0.04	0.25
$\simeq 10.2$	4	3871	28.3 ± 1.8	147.6	4541	7.0	0.04	0.30	0.55
$\simeq 10.2$	4	3895	18.9 ± 1.2	167.4	5902	7.9	0.02	0.05	0.29

Table B.1 Experimental parameters for decoherence measurements at RX qubit working points in Fig. 8.9(a) for small and large coupling resonator-qubit detuning. The coupling strength g_{RX} is obtained from theory using $g_{\mathrm{c,RX}}^{(0)}$ as extracted from the Fig. 8.7(a) fit (see Table B.4). The average number $\bar{n}$ of photons in the coupling resonator is estimated from ac Stark shift measurements.

ω_{rr} [GHz]	$g_{\mathrm{rr}}^{(0)}/2\pi$ [MHz]	$\mathrm{E}_{\mathrm{J}}^{(\mathrm{SQ})}$ [GHz]	$\mathrm{E}_{\mathrm{C}}^{(\mathrm{T})}$ [GHz]
5.594 ± 0.002	141 ± 3	18.085 ± 0.282	0.221 ± 0.004

Table B.2 Fit parameters for theory curve in Fig. 8.4.

RX config*	3
$g_{\mathrm{c,RX}}^{(0)}/2\pi$ [MHz]*	186

Table B.3 Fit parameters for theory curve in Fig. 8.6.

RX config.*	2
$\kappa_{\mathrm{cr,int}}/2\pi$ [MHz]*	1.8
$\kappa_{\mathrm{cr,ext}}/2\pi$ [MHz]*	2.8
ν_{cr} [GHz]	4.229 ± 0.001
$g_{\mathrm{c,RX}}^{(0)}/2\pi$ [MHz]	186 ± 2
$\gamma_{2,\mathrm{RX}}/2\pi$ [MHz]	15 ± 1

Table B.4 Fit parameters for theory curve in Fig. 8.7(a) and fit to black curve in Fig. 8.7(c).

$\mathrm{E}_{\mathrm{C}}^{(\mathrm{T})}$ [GHz]*	0.221
$\mathrm{E}_{\mathrm{J}}^{(\mathrm{SQ})}$ [GHz]*	18.085
$\gamma_{2,\mathrm{T}}/2\pi$ [MHz]*	1.0
$\kappa_{\mathrm{cr,int}}/2\pi$ [MHz]*	2.0
$\kappa_{\mathrm{cr,ext}}/2\pi$ [MHz]*	2.6
ν_{cr} [GHz]	4.175 ± 0.0003
$g_{\mathrm{T}}^{(0)}/2\pi$ [MHz]	205 ± 0.3

Table B.5 Fit parameters for theory curve in Fig. 8.7(b) and fit to green curve in Fig. 8.7(c).

RX config.*	2
$\kappa_{\mathrm{cr,int}}/2\pi\,[\mathrm{MHz}]^*$	1.8
$\kappa_{\mathrm{cr,ext}}/2\pi\,[\mathrm{MHz}]^*$	2.8
$\mathrm{E}_{\mathrm{J}}^{(\mathrm{SQ})}\,[\mathrm{GHz}]^*$	18.085
$\mathrm{E}_{\mathrm{C}}^{(\mathrm{T})}\,[\mathrm{GHz}]^*$	0.221
$\gamma_{2,\mathrm{RX}}/2\pi\,[\mathrm{MHz}]^*$	Fig. 8.9(a) fit
$\gamma_{2,\mathrm{T}}/2\pi\,[\mathrm{MHz}]^*$	1.0
$\nu_{\mathrm{cr}}\,[\mathrm{GHz}]$	4.209 ± 0.0002
$g_{\mathrm{c,RX}}^{(0)}/2\pi\,[\mathrm{MHz}]$	180 ± 2.0
$g_{\mathrm{T}}^{(0)}/2\pi\,[\mathrm{MHz}]$	203 ± 0.2
ν_{T}	ν_{cr}
$2g_{-}/2\pi\,[\mathrm{MHz}]\ @\Delta/h = -9.77\,\mathrm{GHz}$	63 ± 1
$2g_{+}/2\pi\,[\mathrm{MHz}]\ @\Delta/h = -5.65\,\mathrm{GHz}$	84 ± 1

Table B.6 Fit parameters for theory curves in Figs. 8.8(a)-(c).

RX config.*	2
$\sigma_{\mathrm{HF}}\,[\mathrm{mT}]$	3.48 ± 0.06
β	62.9 ± 0.84

Table B.7 Fit parameters for theory curve in Fig. 8.9(a).

$\mathrm{E}_{\mathrm{J}}^{(\mathrm{SQ})}\,[\mathrm{GHz}]^*$	18.085
$\mathrm{E}_{\mathrm{C}}^{(\mathrm{T})}\,[\mathrm{GHz}]^*$	0.221

Table B.8 Shared parameters for theory curves in Figs. 8.11 and 8.12.

	c)	b)	remarks
RX config.*	3	3	
$\kappa_{\mathrm{cr,ext}}/2\pi^*\,[\mathrm{MHz}]$	2.7	2.5	
$\kappa_{\mathrm{cr,int}}/2\pi^*\,[\mathrm{MHz}]$	5.4	4.4	
$\nu_{\mathrm{cr}}\,[\mathrm{GHz}]$	4.764 ± 0.002	4.768 ± 0.001	
$\nu_{\mathrm{T}}\,[\mathrm{GHz}]$	4.292 ± 0.002	4.292 ± 0.002	
$g_{\mathrm{c,RX}}^{(0)}/2\pi\,[\mathrm{MHz}]$	113 ± 1	115 ± 1	
$g_{\mathrm{T}}^{(0)}/2\pi\,[\mathrm{MHz}]$	219 ± 2	219 ± 2	
$\gamma_{2,\mathrm{RX}}/2\pi\,[\mathrm{MHz}]$	15.2	9.7	from Fig. 8.9(a) fit
$\gamma_{2,\mathrm{T}}/2\pi\,[\mathrm{MHz}]$	15.2	9.7	power broadened
$2\mathrm{J}/2\pi\,[\mathrm{MHz}]$	51.4	31.9	virtual splitting

Table B.9 Parameters for theory curves in Figs. 8.11(b), (c) and associated linecuts in Fig. 8.12.

	d)	a)	remarks
RX config.*	4	4	
$\kappa_{\mathrm{cr,ext}}/2\pi^*$ [MHz]	3	3	
$\kappa_{\mathrm{cr,int}}/2\pi^*$ [MHz]	4	4	
ν_{cr} [GHz]	4.495 ± 0.004	4.481 ± 0.001	
ν_{T} [GHz]	3.958 ± 0.002	3.961 ± 0.002	
$g_{\mathrm{c,RX}}^{(0)}/2\pi$ [MHz]	96 ± 2	101 ± 3	
$g_{\mathrm{T}}^{(0)}/2\pi$ [MHz]	213 ± 2	212 ± 2	
$\gamma_{2,\mathrm{RX}}/2\pi$ [MHz]	18.9	7.2	from Fig. 8.9(a) fit
$\gamma_{2,\mathrm{T}}/2\pi$ [MHz]	18.9	7.2	power broadened
$2J/2\pi$ [MHz]	49.2	14.9	virtual splitting

Table B.10 Parameters for theory curves in Figs. 8.11(a), (d) and associated linecuts in Fig. 8.12.

Appendix C

Fabrication recipes

In this chapter we present the recipes for the fabrication of the samples used in chapters 6-8. We thereby provide a detailed list for the fabrication steps of the recipes that are different compared to earlier work in Ref. Stockklauser, 2017.

C.1 Samples in chapters 6-7

The samples used for the experiments in chapter 6 (sample name “s1701131”, wafer name “D160513A”) and chapter 7 (sample names “s1705261”, “s1706111”, wafer name “D160513A”) were fabricated as indicated below.

1. **Cleaving and cleaning**
    - Cleave $1 \times 1\,\mathrm{cm}^2$ from heterostructure wafer.
    - Clean 1 min in acetone, 1 min in Isopropanol (IPA), blow dry.
2. **Global Au markers**
    - Spin AR-P 617.06 at 2000/2/60 (rpm/ramp [s]/total [s]).
    - Bake at 180°C for 300 s.
    - Spin AR-P 672.03 at 6000/6/60.
    - Bake at 180°C for 300 s.
    - EBL at Binnig and Rohrer Nanotechnology Center (BRNC) with 100 keV system.
    - Develop in Methyl isobutyl ketone (MIBK):IPA (1:2) for 90 s, then rinse in IPA for 50 s.

- Electron beam evaporation of Ti(3 nm)/Au(200 nm) at rate 0.1/0.5 nm/s.

3. **Mesa fabrication, ohmic contacts, gate lines**

   - Identical to recipes “Mesa fabrication”, “Ohmic contacts” and “Gate lines” in Ref. Stockklauser, 2017 Appendix B.
   - Remark: “Low vacuum contact” was used with MA6 instead of “vacuum contact” since the latter was found to easily break the chip if there is resist residues at the chip edges after edge bead removal.

4. **NbTiN sputtering**

   - Photolithography according to Appendix B.1.1 in Ref. Stockklauser, 2017.
   - Use PVD magnetron sputter system with $Nb_{0.8}Ti_{0.2}$ target and process parameters $P = 100\,W$, $Ar{:}N_2 = 20 : 5\,sccm$, $p = 1\,mTorr$.
     Remark: Start process with closed target shutter at $p = 5\,mTorr$ for 2 min. Subsequently reduce to $p = 2\,mTorr$ and open target shutter, then reduce to $p = 1\,mTorr$. Ensure stable plasma for 1 min before opening substrate shutter.
   - Sputter on marked glass slide to calibrate deposition rate ($\approx 2.9\,nm/min$). Determine film thickness with Dektak profilometer or atomic force microscope.
   - Sputter 15 nm NbTiN on sample ($\approx 5 : 30\,min$).
   - Liftoff in N-Methyl-2-Pyrrolidone (NMP) at 80°C for 2 h. Use pipette to blow the solvent on the chip. Check whether liftoff is complete (in acetone) under microscope. Possible solutions for incomplete liftoff:
     - Sonication (power level 2 in 40 kHz bath) in acetone for 10 min with cleanroom tissue between sample and beaker to dampen sample-beaker collisions.
     - Keep in NMP (at room temperature) for 24 h, redo sonication.
   - Rinse in acetone, IPA, blow dry.

5. **EBL to define mask for NbTiN etching**

   - Spin CSAR 62 (AR-P 6200.09) at 1600/2/60.
   - Bake at 150°C for 60 s.
   - EBL with BRNC 100 keV system.

- Develop in AR-600-546 for 1 min, then rinse in IPA for 1 min.

6. **Resonator RIE**
   - Standard O_2 cleaning routine of RIE 76 chamber for 20 min.
   - Etch sample with process parameters $\mathrm{P} = 30\,\mathrm{W}$, $\mathrm{SF}_6(12.5\,\mathrm{sccm})$, $p = 33\,\mathrm{mTorr}$ for 7 min.
     Remark: start gas flow 30 s before the process to ensure correct gas pressure during etching.
   - Strip resist in NMP at 80°C for 1 h.
7. **Fine gates, DC bias line**
   - See “Fine gate structure” in Stockklauser, 2017 Appendix B.2.
8. **PCB preparation**
   - Solder SMD components:
     Kemet C0603X103J3GACTU (10 nF) for bias-tee,
     Panasonic ERA-3AED103V (10 kΩ) for bias-tee and filter,
     Kemet C0603X153J3GACTU (15 nF) for filter (line from room temperature),
     Panasonic ERA-3AED103V (50 Ω) for filter (line from sample).
   - Solder SMP connector Rosenberger 19S141-40ML5-NM.
   - Solder DC socket (Preci-Dip 852-10-050-10-001101) and shorten the socket pins at the backside of the PCB to $\leq 2\,\mathrm{mm}$ with pliar. Make sure that conducting wire for ESD protection (Laird 8300-0025-44) can still be attached.
   - Clean 1 min in IPA, blow dry.
9. **Sample cleaving and cleaning**
   - Clean 1 min in acetone, 1 min in IPA, blow dry.
   - Spin protection layer PMMA 950K in Anisole pure at 6000/6/45.
   - Rotate sample (fixed on spinner table) by hand to remove PMMA with cotton swab at sample edges.
   - Bake at 120°C for 300 s.
   - Cleave sample to a size of $2.25 \times 8.3\,\mathrm{mm}^2$. Start with long sample edges, cut at least 3 times and blow N_2 before and after every cleaving step.

- Remove PMMA in Dimethyl Sulfoxide (DMSO) at 80°C for 20 min.

10. **Gluing and bonding**
    - Clean sample 1 min in acetone, 1 min in IPA, blow dry.
    - Glue sample to PCB with PMMA 950K in Anisole pure for 300 s at 180°C .
    - Fix conducting wire for ESD protection at back of the DC socket.
    - Al bonder (general settings: loop 50, pull 34, tail 30). Bond from PCB to NbTiN if possible. Typical bonder settings:
      PCB: 180 W/200 ms/low
      Au: 160 W/200 ms/low
      NbTiN: 220 W/45 ms/low

C.2 Sample in chapter 8

The sample used for the experiment in chapter 6 (sample name “s1808201”, wafer name “D160729A”) was fabricated as follows:

1. **Cleaving**
    - Follow 1. from Appendix section C.1.
2. **Mesa fabrication - SQUID array resonator**
    - Follow fabrication steps “Mesa fabrication” to “SQUID array” from Ref. Stockklauser, 2017 Appendix B.2.
      Remark: evaporate Al instead of Au for fine gates: Ti(3 nm)/Al(27 nm).
3. **Bandage EBL** (ensure good electrical connection of photolithography and EBL defined Al layers (see discussion in subsection 8.1.2) with additional EBL defined Al layer).
    - Follow EBL recipe in Appendix B.1.2 of Ref. Stockklauser, 2017.
    - Electron beam evaporation of Ti(3 nm)/Al(200 nm) at rate 0.1/0.5 nm/s.
    - Liftoff in DMSO at 80°C for 20 min.
4. **PCB, gluing and bonding**
    - Follow 8.-10. from Appendix C.1. Bond parameters for Al: 240 W/30 ms/low.

C.3 NbTiN resonators in chapter 4

Below we list the fabrication recipe for the NbTiN resonators that were used in the characterization measurements from section 4.3.1.

1. **Cleaving**
   - Cleave $1 \times 1\,\mathrm{cm}^2$ from bare GaAs wafer.
   - Clean 1 min in acetone, 1 min in IPA, blow dry.
2. **Resonator**
   - Follow 4.-6. according to Appendix C.1.
3. **PCB, gluing and bonding**
   - Prepare desired PCB.
   - Follow 9. and 10. from Appendix C.1. Note that ESD protection is not necessary.

Appendix D

Parts list for experimental setup

Here we list components of the experimental setup from chapter 2 that are commercially available. Note that the list may not be complete and some components may no longer be available. We indicate with “(ch. X)” if different components were used for the experiments in chapters 6-8.

1. Cryogenic setup

Component	Part number	Distributor/Manufacturer
Attenuators	2082-6243-20,2082-6242-10, 2082-6240-03	East Coast Microwave
Circulator (with B-field shield)	RADC-4-8-Cryo-0.02-4K-S23-1WR-MS-b	Raditek
Copper RF line	UT-085-TP	Rosenberger Micro-Coax
Copper RF line connector	9401-1583-010	East Coast Microwave
Dilution refrigerator	DR200	Oxford Instruments
HEMT	CITCRYO04-12A (ch. 6-7) LNF-LNC4_8C (ch. 8)	Caltech Low Noise Factory
Isolator (with B-field shield)	CWJ1015KS	Pamtech
NbTi RF line	NbTiNbTi085A	Keycom
NbTi RF line connector	1050611-1	AMP
RF lines room temperature feed through	34_SMA-50-0-3/111_NE	Huber+Suhner
Stainless steel line connector	200-36-20-850, 200-37-20-850	C.W. Swift & Associates, Inc.
Stainless steel RF line	UT-085-SS-SS	Rosenberger Micro-Coax

2. Room temperature setup

Component	Part number	Distributor/Manufacturer
Amplifier $0.1-500$ MHz	ZFL-500LN+	Mini-Circuits
Attenuator x dB	BW-SxW2+	Mini-Circuits
DC block	Inmet 8039	Richardson RFPD
DC block inner conductor	BLK-89-S+	Mini-Circuits
High frequency lock-in	UHFLI with options UHF-DIG, UHF-RUB	Zurich Instruments
LN amplifier	AFS3-00101200-42-LN-HS (ch. 6,7) AFS3-00101200-18-10P-4-HS (ch. 8)	Miteq
LPF DC-48 MHz	SLP-50+	Mini-Circuits
Mixer	ZMX-8GH	Mini-Circuits
Multimeter	34401	Agilent
RF generators	2× SMB100A, SMF100A, SMR40	Rhode&Schwarz
SMA female-female	SF-SF50+	Mini-Circuits
SMA male-male	231-502SF	Southwest Microwave
SMA right angle male-female	SFR-SM50+	Mini-Circuits
Splitter	ZX10-2-98+	Mini-Circuits
ULN amplifier	AFS3-04000800-08-10P-4-HS	Miteq

Bibliography

Acín, A., I. Bloch, H. Buhrman, T. Calarco, C. Eichler, J. Eisert, D. Esteve, N. Gisin, S. J. Glaser, F. Jelezko, S. Kuhr, M. Lewenstein, M. F. Riedel, P. O. Schmidt, R. Thew, A. Wallraff, I. Walmsley, and F. K. Wilhelm (2018), “The quantum technologies roadmap: A European community view”, *New Journal of Physics* **20**, 080201.

Altimiras, C., O. Parlavecchio, P. Joyez, D. Vion, P. Roche, D. Esteve, and F. Portier (2013), “Tunable microwave impedance matching to a high impedance source using a Josephson metamaterial”, *Applied Physics Letters* **103**, 212601.

Andersen, C. K., A. Remm, S. Balasiu, S. Krinner, J. Heinsoo, J.-C. Besse, M. Gabureac, A. Wallraff, and C. Eichler (2019), “Entanglement stabilization using ancilla-based parity detection and real-time feedback in superconducting circuits”, *npj Quantum Information* **5**, 69.

Annunziata, A. J., D. F. Santavicca, L. Frunzio, G. Catelani, M. J. Rooks, A. Frydman, and D. E. Prober (2010), “Tunable superconducting nanoinductors”, *Nanotechnology* **21**, 445202.

Awschalom, D. D., L. C. Bassett, A. S. Dzurak, E. L. Hu, and J. R. Petta (2013), “Quantum Spintronics: Engineering and Manipulating Atom-Like Spins in Semiconductors”, *Science* **339**, 1174–1179.

Baart, T. A., P. T. Eendebak, C. Reichl, W. Wegscheider, and L. M. K. Vandersypen (2016), “Computer-automated tuning of semiconductor double quantum dots into the single-electron regime”, *Applied Physics Letters* **108**, 213104.

Baart, T. A., T. Fujita, C. Reichl, W. Wegscheider, and L. M. K. Vandersypen (2017), “Coherent spin-exchange via a quantum mediator”, *Nature Nanotechnology* **12**, 26–30.

Baer, S. and K. Ensslin (2015), *Transport Spectroscopy of Confined Fractional Quantum Hall Systems*, Cham: Springer.

Barends, R., J. Kelly, A. Megrant, A. Veitia, D. Sank, E. Jeffrey, T. C. White, J. Mutus, A. G. Fowler, B. Campbell, Y. Chen, Z. Chen, B. Chiaro, A. Dunsworth, C. Neill,

P. O'Malley, P. Roushan, A. Vainsencher, J. Wenner, A. N. Korotkov, A. N. Cleland, and J. M. Martinis (2014), "Superconducting quantum circuits at the surface code threshold for fault tolerance", *Nature* **508**, 500–503.

Barthel, C., M. Kjærgaard, J. Medford, M. Stopa, C. M. Marcus, M. P. Hanson, and A. C. Gossard (2010), "Fast sensing of double-dot charge arrangement and spin state with a radio-frequency sensor quantum dot", *Physical Review B* **81**, 161308.

Basset, J., D.-D. Jarausch, A. Stockklauser, T. Frey, C. Reichl, W. Wegscheider, T. M. Ihn, K. Ensslin, and A. Wallraff (2013), "Single-electron double quantum dot dipole-coupled to a single photonic mode", *Physical Review B* **88**, 125312.

Beaudoin, F, D Lachance-Quirion, W. A. Coish, and M Pioro-Ladrière (2016), "Quantum simulation with interacting photons Coupling a single electron spin to a microwave resonator : controlling transverse and longitudinal couplings", *Nanotechnology* **27**, 464003.

Becker, P., H. Bettin, P. De Bievre, C. Holm, U. Kutgens, F. Spieweck, J. Stumpel, S. Valkiers, and W. Zulehner (1995), "The silicon-28 path to the Avogadro constant-first experiments and outlook", *IEEE Transactions on Instrumentation and Measurement* **44**, 522–525.

Benito, M., J. R. Petta, and G. Burkard (2019), "Optimized cavity-mediated dispersive two-qubit gates between spin qubits", *Physical Review B* **100**, 081412.

Benito, M., X Mi, J. M. Taylor, J. R. Petta, and G. Burkard (2017), "Input-output theory for spin-photon coupling in Si double quantum dots", *Physical Review B* **96**, 235434.

Betz, A. C., R. Wacquez, M. Vinet, X. Jehl, A. L. Saraiva, M. Sanquer, A. J. Ferguson, and M. F. Gonzalez-Zalba (2015), "Dispersively Detected Pauli Spin-Blockade in a Silicon Nanowire Field-Effect Transistor", *Nano Letters* **15**, 4622–4627.

Bianchetti, R. (2010), "Control and readout of a superconducting artificial atom", Ph.D. thesis, ETH Zurich.

Blais, A., R.-S. Huang, A. Wallraff, S. M. Girvin, and R. J. Schoelkopf (2004), "Cavity quantum electrodynamics for superconducting electrical circuits: An architecture for quantum computation", *Physical Review A* **69**, 062320.

Blais, A., J. Gambetta, A. Wallraff, D. I. Schuster, S. M. Girvin, M. H. Devoret, and R. J. Schoelkopf (2007), "Quantum-information processing with circuit quantum electrodynamics", *Physical Review A* **75**, 032329.

Bluhm, H., S. Foletti, I. Neder, M. Rudner, D. Mahalu, V. Umansky, and A. Yacoby (2011), "Dephasing time of GaAs electron-spin qubits coupled to a nuclear bath exceeding 200 μs", *Nature Physics* **7**, 109–113.

Botzem, T., M. D. Shulman, S. Foletti, S. P. Harvey, O. E. Dial, P. Bethke, P. Cerfontaine, R. P. G. McNeil, D. Mahalu, V. Umansky, A. Ludwig, A. Wieck, D. Schuh, D. Bougeard, A. Yacoby, and H. Bluhm (2018), “Tuning Methods for Semiconductor Spin Qubits”, *Physical Review Applied* **10**, 054026.

Bräm, B. (2018), “Imaging Charge Transport through Nanostructures on High-Mobility Electron Gases”, Ph.D. thesis, ETH Zurich.

Bravyi, S., D. P. DiVincenzo, and D. Loss (2011), “Schrieffer-Wolff transformation for quantum many-body systems”, *Annals of Physics* **326**, 2793–2826.

Bruhat, L. E, T. Cubaynes, J. J. Viennot, M. C. Dartiailh, M. M. Desjardins, A. Cottet, and T. Kontos (2018), “Circuit QED with a quantum-dot charge qubit dressed by Cooper pairs”, *Physical Review B* **98**, 155313.

Buizert, C., F. H. L. Koppens, M. Pioro-Ladrière, H.-P. Tranitz, I. T. Vink, S. Tarucha, W. Wegscheider, and L. M. K. Vandersypen (2008), “InSitu Reduction of Charge Noise in GaAs/$\mathrm{Al}_x\mathrm{Ga}_{1-x}\mathrm{As}$”, *Physical Review Letters* **101**, 226603.

Burkard, G. (2001), “Quantum Computation and Communication using Electron Spins in Quantum Dots and Wires”, Ph.D. thesis, University of Basel.

Burkard, G., D. Loss, and D. P. DiVincenzo (1999), “Coupled quantum dots as quantum gates”, *Physical Review B* **59**, 2070–2078.

Burkard, G. and A. Imamoglu (2006), “Ultra-long-distance interaction between spin qubits”, *Physical Review B* **74**, 041307.

Burkard, G. and J. R. Petta (2016), “Dispersive readout of valley splittings in cavity-coupled silicon quantum dots”, *Physical Review B* **94**, 195305.

Burkard, G., M. J. Gullans, X. Mi, and J. R. Petta (2019), “Superconductor-semiconductor hybrid cavity quantum electrodynamics”, *arXiv:* 1905.01155.

Burnett, J., J. Sagar, O. W. Kennedy, P. A. Warburton, and J. C. Fenton (2017), “Low-Loss Superconducting Nanowire Circuits Using a Neon Focused Ion Beam”, *Physical Review Applied* **8**, 014039.

Businger, M. (2015), “Further developments on the Conversion Box”, Semester thesis, ETH Zurich.

Callen, H. B. and T. A. Welton (1951), “Irreversibility and generalized noise”, *Physical Review* **83**, 34–40.

Castellanos-Beltran, M. A. (2002), “Development of a Josephson Parametric Amplifier for the Preparation and Detection of Nonclassical States of Microwave Fields”, Ph.D. thesis, University of Colorado.

Chen, F., A. J. Sirois, R. W. Simmonds, and A. J. Rimberg (2011), “Introduction of a dc bias into a high- Q superconducting microwave cavity”, *Applied Physics Letters* **98**, 132509.

Chen, S., Q. Wu, C. Mishra, J. Kang, H. Zhang, K. Cho, W. Cai, A. A. Balandin, and R. S. Ruoff (2012), “Thermal conductivity of isotopically modified graphene”, *Nature Materials* **11**, 203–207.

Childress, L., A. S. Sørensen, and M. D. Lukin (2004), “Mesoscopic cavity quantum electrodynamics with quantum dots”, *Physical Review A* **69**, 042302.

Clarke, J. and F. K. Wilhelm (2008), “Superconducting quantum bits”, *Nature* **453**, 1031–1042.

Clerk, A. A., M. H. Devoret, S. M. Girvin, F. Marquardt, and R. J. Schoelkopf (2010), “Introduction to quantum noise, measurement, and amplification”, *Reviews of Modern Physics* **82**, 1155–1208.

Coish, W. A. and J. Baugh (2009), “Nuclear spins in nanostructures”, *Phys. Status Solidi B* **246**, 2203–2215.

Collett, M. J. and C. W. Gardiner (1984), “Squeezing of intracavity and traveling-wave light fields produced in parametric amplification”, *Physical Review A* **30**, 1386–1391.

Combes, J., J. Kerckhoff, and M. Sarovar (2017), “The SLH framework for modeling quantum input-output networks”, *Advances in Physics: X* **2**, 784–888.

Cottet, A. and T. Kontos (2010), “Spin Quantum Bit with Ferromagnetic Contacts for Circuit QED”, *Physical Review Letters* **105**, 160502.

Coumou, P. C. J. J., M. R. Zuiddam, E. F. C. Driessen, P. J. De Visser, J. J. A. Baselmans, and T. M. Klapwijk (2013), “Microwave properties of superconducting atomic-layer deposited TiN films”, *IEEE Transactions on Applied Superconductivity* **23**, 7500404.

D’Anjou, B. and G. Burkard (2019), “Optimal Dispersive Readout of a Spin Qubit with a Microwave Cavity”, *arXiv:* 1905.09702.

Danon, J. (2013), “Spin-flip phonon-mediated charge relaxation in double quantum dots”, *Physical Review B* **88**, 075306.

Day, P. K., H. G. LeDuc, B. A. Mazin, A. Vayonakis, and J. Zmuidzinas (2003), “A broadband superconducting detector suitable for use in large arrays”, *Nature* **425**, 817–821.

Delbecq, M. R., V. Schmitt, F. D. Parmentier, N. Roch, J. J. Viennot, G. Fève, B. Huard, C. Mora, A. Cottet, and T. Kontos (2011), “Coupling a Quantum Dot, Fermionic Leads, and a Microwave Cavity on a Chip”, *Physical Review Letters* **107**, 256804.

Deng, G.-W., D. Wei, J. R. Johansson, M.-L. Zhang, S.-X. Li, H.-O. Li, G. Cao, M. Xiao, T. Tu, G.-C. Guo, H.-W. Jiang, F. Nori, and G.-P. Guo (2015), “Charge Number Dependence of the Dephasing Rates of a Graphene Double Quantum Dot in a Circuit QED Architecture”, *Physical Review Letters* **115**, 126804.

Devoret, M. H. and J. M. Martinis (2005), *Implementing Qubits with Superconducting Integrated Circuits*, Boston: Springer.

Dial, O. E., M. D. Shulman, S. P. Harvey, H. Bluhm, V. Umansky, and A. Yacoby (2013), “Charge Noise Spectroscopy Using Coherent Exchange Oscillations in a Singlet-Triplet Qubit”, *Physical Review Letters* **110**, 146804.

DiCarlo, L., J. M. Chow, J. M. Gambetta, L. S. Bishop, B. R. Johnson, D. I. Schuster, J. Majer, A. Blais, L. Frunzio, S. M. Girvin, and R. J. Schoelkopf (2009), “Demonstration of two-qubit algorithms with a superconducting quantum processor”, *Nature* **460**, 240–244.

DiVincenzo, D. P., D. Bacon, J. Kempe, G. Burkard, and K. B. Whaley (2000), “Universal quantum computation with the exchange interaction”, *Nature* **408**, 339–342.

DiVincenzo, D. P. (2000), “The Physical Implementation of Quantum Computation”, *Fortschritte der Physik* **48**, 771–783.

Dupré, O., A. Benoît, M. Calvo, A. Catalano, J. Goupy, C. Hoarau, T. Klein, K. L. Calvez, B. Sacépé, A. Monfardini, and F. Levy-Bertrand (2017), “Tunable sub-gap radiation detection with superconducting resonators”, *Superconductor Science and Technology* **30**, 045007.

Eich, M., R. Pisoni, H. Overweg, A. Kurzmann, Y. Lee, P. Rickhaus, T. Ihn, K. Ensslin, F. Herman, M. Sigrist, K. Watanabe, and T. Taniguchi (2018), “Spin and Valley States in Gate-Defined Bilayer Graphene Quantum Dots”, *Physical Review X* **8**, 031023.

Eichler, C., Y. Salathe, J. Mlynek, S. Schmidt, and A. Wallraff (2014), “Quantum-Limited Amplification and Entanglement in Coupled Nonlinear Resonators”, *Physical Review Letters* **113**, 110502.

Elzerman, J. M., R. Hanson, J. S. Greidanus, L. H. Willems van Beveren, S. De Franceschi, L. M. K. Vandersypen, S. Tarucha, and L. P. Kouwenhoven (2003), “Few-electron quantum dot circuit with integrated charge read out”, *Physical Review B* **67**, 161308.

Fei, J., J.-T. Hung, T. S. Koh, Y.-P. Shim, S. N. Coppersmith, X. Hu, and M. Friesen (2015), “Characterizing gate operations near the sweet spot of an exchange-only qubit”, *Physical Review B* **91**, 205434.

Feynman, R., R. B. Leighton, and Sands (1989), *The Feynman lectures on physics*, Boston: Addison-Wesley.

Field, M., C. G. Smith, M. Pepper, D. A. Ritchie, J. E. F. Frost, G. A. C. Jones, and D. G. Hasko (1993), “Measurements of Coulomb blockade with a noninvasive voltage probe”, *Physical Review Letters* **70**, 1311–1314.

Fink, J. (2010), "Quantum nonlinearities in strong coupling circuit QED", Ph.D. thesis, ETH Zurich.

Foletti, S., H. Bluhm, D. Mahalu, V. Umansky, and A. Yacoby (2009), "Universal quantum control of two-electron spin quantum bits using dynamic nuclear polarization", *Nature Physics* **5**, 903–908.

Frey, T (2013), "Interaction between quantum dots and superconducting microwave resonators", Ph.D. thesis, ETH Zurich.

Frey, T., P. J. Leek, M. Beck, A. Blais, T. Ihn, K. Ensslin, and A. Wallraff (2012), "Dipole Coupling of a Double Quantum Dot to a Microwave Resonator", *Physical Review Letters* **108**, 046807.

Gambetta, J., A. Blais, D. I. Schuster, A. Wallraff, L. Frunzio, J. Majer, M. H. Devoret, S. M. Girvin, and R. J. Schoelkopf (2006), "Qubit-photon interactions in a cavity: Measurement-induced dephasing and number splitting", *Physical Review A* **74**, 042318.

Gao, J., M. Daal, A. Vayonakis, S. Kumar, J. Zmuidzinas, B. Sadoulet, B. A. Mazin, P. K. Day, and H. G. Leduc (2008), "Experimental evidence for a surface distribution of two-level systems in superconducting lithographed microwave resonators", *Applied Physics Letters* **92**, 152505.

Gasser, U., S. Gustavsson, B. Küng, K. Ensslin, T. Ihn, D. C. Driscoll, and A. C. Gossard (2009), "Statistical electron excitation in a double quantum dot induced by two independent quantum point contacts", *Physical Review B* **79**, 035303.

Gaudreau, L., A. Kam, G. Granger, S. A. Studenikin, P. Zawadzki, and A. S. Sachrajda (2009), "A tunable few electron triple quantum dot", *Applied Physics Letters* **95**, 193101.

Gaudreau, L., G. Granger, A. Kam, G. C. Aers, S. A. Studenikin, P. Zawadzki, M. Pioro-Ladrière, Z. R. Wasilewski, and A. S. Sachrajda (2012), "Coherent control of three-spin states in a triple quantum dot", *Nature Physics* **8**, 54–58.

Girvin, S. M. (2014), *Circuit QED: superconducting qubits coupled to microwave photons*, New York: Oxford University Press.

Göppl, M. (2009), "Realization and Characterization of Circuit Quantum Electrodynamics Systems Engineering Quantum Electronic Chips", Ph.D. thesis, ETH Zurich.

Göppl, M., A. Fragner, M. Baur, R. Bianchetti, S. Filipp, J. M. Fink, P. J. Leek, G. Puebla, L. Steffen, and A. Wallraff (2008), "Coplanar waveguide resonators for circuit quantum electrodynamics", *Journal of Applied Physics* **104**, 113904.

Granger, G., L. Gaudreau, A. Kam, M. Pioro-Ladrière, S. A. Studenikin, Z. R. Wasilewski, P. Zawadzki, and A. S. Sachrajda (2010), “Three-dimensional transport diagram of a triple quantum dot”, *Physical Review B* **82**, 075304.

Gross, M. (2006), “Applied Superconductivity”, Lecture notes, TU Munich.

Hanson, R., L. P. Kouwenhoven, J. R. Petta, S. Tarucha, and L. M. Vandersypen (2007), “Spins in few-electron quantum dots”, *Reviews of Modern Physics* **79**, 1217–1265.

Hanson, R. and D. D. Awschalom (2008), “Coherent manipulation of single spins in semiconductors”, *Nature* **453**, 1043–1049.

Hayashi, T., T. Fujisawa, H. D. Cheong, Y. H. Jeong, and Y. Hirayama (2003), “Coherent Manipulation of Electronic States in a Double Quantum Dot”, *Physical Review Letters* **91**, 226804.

Hitachi, K., T. Ota, and K. Muraki (2013), “Intrinsic and extrinsic origins of low-frequency noise in GaAs/AlGaAs Schottky-gated nanostructures”, *Applied Physics Letters* **102**, 192104.

Houck, A. A., D. I. Schuster, J. M. Gambetta, J. A. Schreier, B. R. Johnson, J. M. Chow, L. Frunzio, J. Majer, M. H. Devoret, S. M. Girvin, and R. J. Schoelkopf (2007), “Generating single microwave photons in a circuit”, *Nature* **449**, 328–331.

House, M. G., T. Kobayashi, B. Weber, S. J. Hile, T. F. Watson, J. van der Heijden, S. Rogge, and M. Y. Simmons (2015), “Radio frequency measurements of tunnel couplings and singlet–triplet spin states in Si:P quantum dots”, *Nature Communications* **6**, 8848.

Hu, X., Y.-x. Liu, and F. Nori (2012), “Strong coupling of a spin qubit to a superconducting stripline cavity”, *Physical Review B* **86**, 035314.

Hung, J.-T., J. Fei, M. Friesen, and X. Hu (2014), “Decoherence of an exchange qubit by hyperfine interaction”, *Physical Review B* **90**, 045308.

Ihn, T. (2018), “Three-electron quantum dot”, private communication, ETH Zurich.

Ihn, T. (2010), *Semiconductor Nanostructures: Quantum states and electronic transport*, New York: Oxford University Press.

Jin, P.-Q., M. Marthaler, A. Shnirman, and G. Schön (2012), “Strong Coupling of Spin Qubits to a Transmission Line Resonator”, *Physical Review Letters* **108**, 190506.

Johnson, A. C., J. R. Petta, C. M. Marcus, M. P. Hanson, and A. C. Gossard (2005a), “Singlet-triplet spin blockade and charge sensing in a few-electron double quantum dot”, *Physical Review B* **72**, 165308.

Johnson, A. C., J. R. Petta, J. M. Taylor, A. Yacoby, M. D. Lukin, C. M. Marcus, M. P. Hanson, and A. C. Gossard (2005b), “Triplet-singlet spin relaxation via nuclei in a double quantum dot”, *Nature* **435**, 925–928.

Kalantre, S. S., J. P. Zwolak, S. Ragole, X. Wu, N. M. Zimmerman, M. D. Stewart, and J. M. Taylor (2019), "Machine learning techniques for state recognition and auto-tuning in quantum dots", *npj Quantum Information* **5**, 6.

Kastner, M. A. (1992), "The single-electron transistor", *Reviews of Modern Physics* **64**, 849–858.

Kawakami, E, P Scarlino, D. R. Ward, F. R. Braakman, D. E. Savage, M. G. Lagally, M. Friesen, S. N. Coppersmith, M. a. Eriksson, and L. M. K. Vandersypen (2014), "Electrical control of a long-lived spin qubit in a Si/SiGe quantum dot.", *Nature nanotechnology* **9**, 666–70.

Kish, L. B., G. A. Niklasson, and C. G. Granqvist (2016), "Zero-point term and quantum effects in the Johnson noise of resistors: A critical appraisal", *Journal of Statistical Mechanics: Theory and Experiment* **2016**, 054006.

Koch, J., T. M. Yu, J. Gambetta, A. A. Houck, D. I. Schuster, J. Majer, A. Blais, M. H. Devoret, S. M. Girvin, and R. J. Schoelkopf (2007), "Charge-insensitive qubit design derived from the Cooper pair box", *Physical Review A* **76**, 042319.

Koch, R. H., D. J. Van Harlingen, and J. Clarke (1981), "Observation of Zero-Point Fluctuations in a Resistively Shunted Josephson Tunnel Junction", *Physical Review Letters* **47**, 1216–1219.

Koppens, F. H. L., K. C. Nowack, and L. M. K. Vandersypen (2008), "Spin Echo of a Single Electron Spin in a Quantum Dot", *Physical Review Letters* **100**, 236802.

Koppens, F. H., J. A. Folk, J. M. Elzerman, R. Hanson, L. H. Willems Van Beveren, I. T. Vink, H. P. Tranitz, W. Wegscheider, L. P. Kouwenhoven, and L. M. Vandersypen (2005), "Control and Detection of Singlet-Triplet Mixing in a Random Nuclear Field", *Science* **309**, 1346–1350.

Koppens, F. H., C. Buizert, K. J. Tielrooij, I. T. Vink, K. C. Nowack, T. Meunier, L. P. Kouwenhoven, and L. M. Vandersypen (2006), "Driven coherent oscillations of a single electron spin in a quantum dot", *Nature* **442**, 766–771.

Koski, J. V. (2019), "Leverarm for a DQD charge qubit", private communication, ETH Zurich.

Koski, J. V., A. J. Landig, A. Pályi, P. Scarlino, C. Reichl, W. Wegscheider, G. Burkard, A. Wallraff, K. Ensslin, and T. Ihn (2018), "Floquet Spectroscopy of a Strongly Driven Quantum Dot Charge Qubit with a Microwave Resonator", *Physical Review Letters* **121**, 043603.

Kouwenhoven, L. P., C. M. Marcus, P. L. McEuen, S. Tarucha, R. M. Westervelt, and N. S. Wingreen (1997), *Electron Transport in Quantum Dots*, Kluwer, pp. 105–214.

Krinner, S., S. Storz, P. Kurpiers, P. Magnard, J. Heinsoo, R. Keller, J. Lütolf, C. Eichler, and A. Wallraff (2019), "Engineering cryogenic setups for 100-qubit scale superconducting circuit systems", *EPJ Quantum Technology* **6**, 2.

Kroll, J. G., F. Borsoi, K. L. van der Enden, W. Uilhoorn, D. de Jong, M Quintero-Pérez, D. J. van Woerkom, A. Bruno, S. R. Plissard, D. Car, E. P. A. M. Bakkers, M. C. Cassidy, and L. P. Kouwenhoven (2018), "Magnetic field resilient superconducting coplanar waveguide resonators for hybrid cQED experiments", *arXiv:* 1809.03932.

Kuit, K. H., J. R. Kirtley, W. van der Veur, C. G. Molenaar, F. J. G. Roesthuis, A. G. P. Troeman, J. R. Clem, H. Hilgenkamp, H. Rogalla, and J. Flokstra (2008), "Vortex trapping and expulsion in thin-film $YBa_2Cu_3O_7$", *Physical Review B* **77**, 134504.

Laird, E. A., C. Barthel, E. I. Rashba, C. M. Marcus, M. P. Hanson, and A. C. Gossard (2007), "Hyperfine-Mediated Gate-Driven Electron Spin Resonance", *Physical Review Letters* **99**, 246601.

Laird, E. A., J. M. Taylor, D. P. DiVincenzo, C. M. Marcus, M. P. Hanson, and A. C. Gossard (2010), "Coherent spin manipulation in an exchange-only qubit", *Physical Review B* **82**, 075403.

Laloy, A. P. (2010), "Superconducting qubit in a resonator:test of the Leggett-Garg inequality and single-shot readout", Ph.D. thesis, CEA Saclay.

Landig, A. J., J. V. Koski, P. Scarlino, U. C. Mendes, A. Blais, C. Reichl, W. Wegscheider, A. Wallraff, K. Ensslin, and T. Ihn (2018), "Coherent spin–photon coupling using a resonant exchange qubit", *Nature* **560**, 179–184.

Landig, A. J., J. V. Koski, P. Scarlino, C. Müller, J. C. Abadillo-Uriel, B Kratochwil, C. Reichl, W. Wegscheider, S. N. Coppersmith, M. Friesen, A Wallraff, T Ihn, and K Ensslin (2019a), "Coherent long-distance spin-qubit-transmon coupling", *arXiv:* 1903.04022.

Landig, A. J., J. V. Koski, P. Scarlino, C. Reichl, W. Wegscheider, A. Wallraff, K. Ensslin, and T. Ihn (2019b), "Microwave-Cavity-Detected Spin Blockade in a Few-Electron Double Quantum Dot", *Physical Review Letters* **122**, 213601.

Langsjoen, L. S., A. Poudel, M. G. Vavilov, and R. Joynt (2012), "Qubit relaxation from evanescent-wave Johnson noise", *Physical Review A* **86**, 010301.

Loss, D. and D. P. DiVincenzo (1998), "Quantum computation with quantum dots", *Physical Review A* **57**, 120–126.

Luthi, F., T. Stavenga, O. W. Enzing, A. Bruno, C. Dickel, N. K. Langford, M. A. Rol, T. S. Jespersen, J. Nygård, P. Krogstrup, and L. DiCarlo (2018), "Evolution of Nanowire Transmon Qubits and Their Coherence in a Magnetic Field", *Physical Review Letters* **120**, 100502.

Mabuchi, H. and A. C. Doherty (2002), “Cavity Quantum Electrodynamics: Coherence in Context”, *Science* **298**, 1372–1377.

Macklin, C., K. O’Brien, D. Hover, M. E. Schwartz, V. Bolkhovsky, X. Zhang, W. D. Oliver, and I. Siddiqi (2015), “A near-quantum-limited Josephson traveling-wave parametric amplifier”, *Science* **350**, 307–310.

Majer, J., J. M. Chow, J. M. Gambetta, J. Koch, B. R. Johnson, J. A. Schreier, L. Frunzio, D. I. Schuster, A. A. Houck, A. Wallraff, A. Blais, M. H. Devoret, S. M. Girvin, and R. J. Schoelkopf (2007), “Coupling superconducting qubits via a cavity bus”, *Nature* **449**, 443–447.

Malinowski, F. K., F. Martins, P. D. Nissen, S. Fallahi, G. C. Gardner, M. J. Manfra, C. M. Marcus, and F. Kuemmeth (2017), “Symmetric operation of the resonant exchange qubit”, *Physical Review B* **96**, 045443.

Manfra, M. J. (2014), “Molecular Beam Epitaxy of Ultra-High-Quality AlGaAs/GaAs Heterostructures: Enabling Physics in Low-Dimensional Electronic Systems”, *Annual Review of Condensed Matter Physics* **5**, 347–373.

Masluk, N. A., I. M. Pop, A. Kamal, Z. K. Minev, and M. H. Devoret (2012), “Microwave Characterization of Josephson Junction Arrays: Implementing a Low Loss Superinductance”, *Physical Review Letters* **109**, 137002.

Maurand, R, X Jehl, D Kotekar-Patil, A Corna, H Bohuslavskyi, R Laviéville, L Hutin, S Barraud, M Vinet, M Sanquer, and S De Franceschi (2016), “A CMOS silicon spin qubit”, *Nature Communications* **7**, 13575.

Mc Mahill, D. (2009), Coplanar Waveguide Analysis/Synthesis Calculator, URL: http://wcalc.sourceforge.net/cgi-bin/coplanar.cgi (visited on 06/2019).

Medford, J., J. Beil, J. M. Taylor, E. I. Rashba, H. Lu, A. C. Gossard, and C. M. Marcus (2013a), “Quantum-Dot-Based Resonant Exchange Qubit”, *Physical Review Letters* **111**, 050501.

Medford, J., J. Beil, J. M. Taylor, S. D. Bartlett, A. C. Doherty, E. I. Rashba, D. P. DiVincenzo, H. Lu, A. C. Gossard, and C. M. Marcus (2013b), “Self-consistent measurement and state tomography of an exchange-only spin qubit”, *Nature Nanotechnology* **8**, 654–659.

Mehl, S. and D. P. DiVincenzo (2013), “Noise analysis of qubits implemented in triple quantum dot systems in a Davies master equation approach”, *Physical Review B* **87**, 195309.

Merkulov, I. A., A. L. Efros, and M. Rosen (2002), “Electron spin relaxation by nuclei in semiconductor quantum dots”, *Physical Review B* **65**, 205309.

Meservey, R. and P. M. Tedrow (1969), “Measurements of the kinetic inductance of superconducting linear structures”, *Journal of Applied Physics* **40**, 2028–2034.

Mi, X. (2018), “Circuit Quantum Electrodynamics with Silicon Charge and Spin Qubits”, Ph.D. thesis, Princeton University.

Mi, X., J. V. Cady, D. M. Zajac, J. Stehlik, L. F. Edge, and J. R. Petta (2017a), “Circuit quantum electrodynamics architecture for gate-defined quantum dots in silicon”, *Applied Physics Letters* **110**, 043502.

Mi, X., C. G. Péterfalvi, G. Burkard, and J. R. Petta (2017b), “High-Resolution Valley Spectroscopy of Si Quantum Dots”, *Physical Review Letters* **119**, 176803.

Mi, X., J. V. Cady, D. M. Zajac, P. W. Deelman, and J. R. Petta (2017c), “Strong coupling of a single electron in silicon to a microwave photon”, *Science* **355**, 156–158.

Mi, X., M. Benito, S. Putz, D. M. Zajac, J. M. Taylor, G. Burkard, and J. R. Petta (2018), “A coherent spin–photon interface in silicon”, *Nature* **555**, 599–603.

Mills, A. R., D. M. Zajac, M. J. Gullans, F. J. Schupp, T. M. Hazard, and J. R. Petta (2019), “Shuttling a single charge across a one-dimensional array of silicon quantum dots”, *Nature Communications* **10**, 1063.

Moore, G. E. (1965), “Cramming more components onto integrated circuits”, *Electronics* **38**.

Mortemousque, P.-A., E. Chanrion, B. Jadot, H. Flentje, A. Ludwig, A. D. Wieck, M. Urdampilleta, C. Bauerle, and T. Meunier (2018), “Coherent control of individual electron spins in a two dimensional array of quantum dots”, *arXiv:* 1808.06180.

Müller, C., J. Combes, A. R. Hamann, A. Fedorov, and T. M. Stace (2017a), “Nonreciprocal atomic scattering: A saturable, quantum Yagi-Uda antenna”, *Physical Review A* **96**, 053817.

Müller, C., J. H. Cole, and J. Lisenfeld (2017b), “Towards understanding two-level-systems in amorphous solids - Insights from quantum circuits”, *arXiv:* 1705.01108.

Nakamura, Y., Y. A. Pashkin, and J. S. Tsai (1999), “Coherent control of macroscopic quantum states in a single-Cooper-pair box”, *Nature* **398**, 786–788.

Nicolí, G., M. S. Ferguson, C. Rössler, A. Wolfertz, G. Blatter, T. Ihn, K. Ensslin, C. Reichl, W. Wegscheider, and O. Zilberberg (2018), “Cavity-Mediated Coherent Coupling between Distant Quantum Dots”, *Physical Review Letters* **120**, 236801.

Niepce, D., J. Burnett, and J. Bylander (2019), “High Kinetic Inductance Nb N Nanowire Superinductors”, *Physical Review Applied* **11**, 044014.

Nowack, K. C., F. H. L. Koppens, Y. V. Nazarov, and L. M. K. Vandersypen (2007), “Coherent Control of a Single Electron Spin with Electric Fields”, *Science* **318**, 1430–1433.

Nyquist, H. (1928), “Thermal agitation of electric charge in conductors”, *Physical Review* **32**, 110–113.

O’Connell, A. D., M. Ansmann, R. C. Bialczak, M. Hofheinz, N. Katz, E. Lucero, C. McKenney, M. Neeley, H. Wang, E. M. Weig, A. N. Cleland, and J. M. Martinis (2008), “Microwave dielectric loss at single photon energies and millikelvin temperatures”, *Applied Physics Letters* **92**, 112903.

Ono, K., D. G. Austing, Y. Tokura, and S. Tarucha (2002), “Current Rectification by Pauli Exclusion in a Weakly Coupled Double Quantum Dot system”, *Science* **297**, 1313–1317.

Paladino, E., Y. Galperin, G. Falci, and B. L. Altshuler (2014), “1/ f noise: Implications for solid-state quantum information”, *Reviews of Modern Physics* **86**, 361–418.

Pauli, W. (1940), “The connection between spin and statistics”, *Physical Review* **58**, 716–722.

Petersson, K. D., L. W. McFaul, M. D. Schroer, M. Jung, J. M. Taylor, A. A. Houck, and J. R. Petta (2012), “Circuit quantum electrodynamics with a spin qubit”, *Nature* **490**, 380–383.

Petta, J. R., A. C. Johnson, J. M. Taylor, E. A. Laird, A. Yacoby, M. D. Lukin, C. M. Marcus, M. P. Hanson, and A. C. Gossard (2005), “Coherent Manipulation of Coupled Electron Spins in Semiconductor Quantum Dots”, *Science* **309**, 2180–2184.

Pioro-Ladrière, M., T. Obata, Y. Tokura, Y. S. Shin, T. Kubo, K. Yoshida, T. Taniyama, and S. Tarucha (2008), “Electrically driven single-electron spin resonance in a slanting Zeeman field”, *Nature Physics* **4**, 776–779.

Pobell, F. (2007), *Matter and methods at low temperatures*, Berlin, Heidelberg: Springer.

Poudel, A., L. S. Langsjoen, M. G. Vavilov, and R. Joynt (2013), “Relaxation in quantum dots due to evanescent-wave Johnson noise”, *Physical Review B* **87**, 045301.

Pozar, D. M. (2005), *Microwave Engineering*, Hoboken: John Wiley and Sons Inc.

Premakumar, V. N., M. G. Vavilov, and R. Joynt (2018), “Evanescent-wave Johnson noise in small devices”, *Quantum Science and Technology* **3**, 015001.

Purcell, E. M., H. C. Torrey, and R. V. Pound (1946), “Resonance Absorption by Nuclear Magnetic Moments in a Solid”, *Physical Review* **69**, 37–38.

Raimond, J. M., M. Brune, and S. Haroche (2001), “Colloquium: Manipulating quantum entanglement with atoms and photons in a cavity”, *Reviews of Modern Physics* **73**, 565–582.

Reichl, C. (2014), “MBE growth of ultrahigh-mobility 2DEGs in GaAs/AlGaAs”, Ph.D. thesis, ETH Zurich.

Rotzinger, H., S. T. Skacel, M. Pfirrmann, J. N. Voss, J. Münzberg, S. Probst, P. Bushev, M. P. Weides, A. V. Ustinov, and J. E. Mooij (2017), "Aluminium-oxide wires for superconducting high kinetic inductance circuits", *Superconductor Science and Technology* **30**, 025002.

Roushan, P., C. Neill, A. Megrant, Y. Chen, R. Babbush, R. Barends, B. Campbell, Z. Chen, B. Chiaro, A. Dunsworth, A. Fowler, E. Jeffrey, J. Kelly, E. Lucero, J. Mutus, P. J. O'Malley, M. Neeley, C. Quintana, D. Sank, A. Vainsencher, J. Wenner, T. White, E. Kapit, H. Neven, and J. Martinis (2017), "Chiral ground-state currents of interacting photons in a synthetic magnetic field", *Nature Physics* **13**, 146–151.

Russ, M. and G. Burkard (2015a), "Asymmetric resonant exchange qubit under the influence of electrical noise", *Physical Review B* **91**, 235411.

— (2015b), "Long distance coupling of resonant exchange qubits", *Physical Review B* **92**, 205412.

— (2017), "Three-electron spin qubits", *Journal of Physics Condensed Matter* **29**, 393001.

Russ, M., J. R. Petta, and G. Burkard (2018), "Quadrupolar Exchange-Only Spin Qubit", *Physical Review Letters* **121**, 177701.

Sabbagh, D., N. Thomas, J. Torres, R. Pillarisetty, P. Amin, H. C. George, K. Singh, A. Budrevich, M. Robinson, D. Merrill, L. Ross, J. Roberts, L. Lampert, L. Massa, S. Amitonov, J. Boter, G. Droulers, H. G. J. Eenink, M. van Hezel, D. Donelson, M. Veldhorst, L. M. K. Vandersypen, J. S. Clarke, and G. Scappucci (2019), "Quantum transport properties of industrial ^{28}Si^{28}SiO$_2$", *Physical Review Applied* **12**, 014013.

Sala, A. and J. Danon (2017), "Exchange-only singlet-only spin qubit", *Physical Review B* **95**, 241303.

Samkharadze, N., A. Kumar, M. J. Manfra, L. N. Pfeiffer, K. W. West, and G. A. Csáthy (2011), "Integrated electronic transport and thermometry at milliKelvin temperatures and in strong magnetic fields", *Review of Scientific Instruments* **82**, 053902.

Samkharadze, N., A. Bruno, P. Scarlino, G. Zheng, D. P. DiVincenzo, L. DiCarlo, and L. M. K. Vandersypen (2016), "High-Kinetic-Inductance Superconducting Nanowire Resonators for Circuit QED in a Magnetic Field", *Physical Review Applied* **5**, 044004.

Samkharadze, N., G. Zheng, N. Kalhor, D. Brousse, A. Sammak, U. C. Mendes, A. Blais, G. Scappucci, and L. M. K. Vandersypen (2018), "Strong spin-photon coupling in silicon", *Science* **359**, 1123–1127.

Sarma, S. D., M. Freedman, and C. Nayak (2015), "Majorana zero modes and topological quantum computation", *npj Quantum Information* **1**, 15001.

Scarlino, P., D. J. van Woerkom, A. Stockklauser, J. V. Koski, M. C. Collodo, S. Gasparinetti, C. Reichl, W. Wegscheider, T. Ihn, K. Ensslin, and A. Wallraff (2019a), "All-

Microwave Control and Dispersive Readout of Gate-Defined Quantum Dot Qubits in Circuit Quantum Electrodynamics”, *Physical Review Letters* **122**, 206802.

Scarlino, P., D. J. van Woerkom, U. C. Mendes, J. V. Koski, A. J. Landig, C. K. Andersen, S. Gasparinetti, C. Reichl, W. Wegscheider, K. Ensslin, T. Ihn, A. Blais, and A. Wallraff (2019b), “Coherent microwave-photon-mediated coupling between a semiconductor and a superconducting qubit”, *Nature Communications* **10**, 3011.

Schoelkopf, R. J. and S. M. Girvin (2008), “Wiring up quantum systems”, *Nature* **451**, 664–669.

Schreier, J. A., A. A. Houck, J. Koch, D. I. Schuster, B. R. Johnson, J. M. Chow, J. M. Gambetta, J. Majer, L. Frunzio, M. H. Devoret, S. M. Girvin, and R. J. Schoelkopf (2008), “Suppressing charge noise decoherence in superconducting charge qubits”, *Physical Review B* **77**, 180502.

Schröer, D., A. D. Greentree, L. Gaudreau, K. Eberl, L. C. L. Hollenberg, J. P. Kotthaus, and S. Ludwig (2007), “Electrostatically defined serial triple quantum dot charged with few electrons”, *Physical Review B* **76**, 075306.

Schroer, M. D., M. Jung, K. D. Petersson, and J. R. Petta (2012), “Radio Frequency Charge Parity Meter”, *Physical Review Letters* **109**, 166804.

Schuster, D. I. (2007), “Circuit Quantum Electrodynamics”, Ph.D. thesis, Yale University.

Schuster, D. I., A Wallraff, A Blais, L Frunzio, R.-S. Huang, J Majer, S. M. Girvin, and R. J. Schoelkopf (2005), “ac Stark Shift and Dephasing of a Superconducting Qubit Strongly Coupled to a Cavity Field”, *Physical Review Letters* **94**, 123602.

Scott-Thomas, J. H. F., S. B. Field, M. A. Kastner, H. I. Smith, and D. A. Antoniadis (1989), “Conductance Oscillations Periodic in the Density of a One-Dimensional Electron Gas”, *Physical Review Letters* **62**, 583–586.

Semenov, A. D., K. Il’In, M. Siegel, A. Smirnov, S. Pavlov, H. Richter, and H. W. Hübers (2006), “Evidence of non-bolometric mixing in the bandwidth of a hot-electron bolometer”, *Superconductor Science and Technology* **19**, 1051–1056.

Sete, E. A., J. M. Gambetta, and A. N. Korotkov (2014), “Purcell effect with microwave drive: Suppression of qubit relaxation rate”, *Physical Review B* **89**, 104516.

Shnirman, A., G. Schön, and Z. Hermon (1997), “Quantum Manipulations of Small Josephson Junctions”, *Physical Review Letters* **79**, 2371–2374.

Shnirman, A., Y. Makhlin, and G. Schön (2002), “Noise and Decoherence in Quantum Two-Level Systems”, *Physica Scripta* **T102**, 147.

Shulman, M. D., O. E. Dial, S. P. Harvey, H. Bluhm, V. Umansky, and A. Yacoby (2012), “Demonstration of Entanglement of Electrostatically Coupled Singlet-Triplet Qubits”, *Science* **336**, 202–205.

Sigrist, M. (2016), "Superconductivity", Lecture notes, ETH Zürich.

Sillanpää, M. A., J. I. Park, and R. W. Simmonds (2007), "Coherent quantum state storage and transfer between two phase qubits via a resonant cavity", *Nature* **449**, 438–442.

Slichter, C. P. (1990), *Principles of Magnetic Resonance*, Berlin, Heidelberg: Springer.

Song, C., T. W. Heitmann, M. P. DeFeo, K. Yu, R. McDermott, M. Neeley, J. M. Martinis, and B. L. T. Plourde (2009), "Microwave response of vortices in superconducting thin films of Re and Al", *Physical Review B* **79**, 174512.

Srinivasa, V., J. M. Taylor, and C. Tahan (2016), "Entangling distant resonant exchange qubits via circuit quantum electrodynamics", *Physical Review B* **94**, 205421.

Stepanenko, D., M. Rudner, B. I. Halperin, and D. Loss (2012), "Singlet-triplet splitting in double quantum dots due to spin-orbit and hyperfine interactions", *Physical Review B* **85**, 075416.

Stockklauser, A. (2017), "Strong Coupling Circuit QED with Semiconductor Quantum Dots", Ph.D. thesis, ETH Zurich.

Stockklauser, A., V. F. Maisi, J. Basset, K. Cujia, C. Reichl, W. Wegscheider, T. Ihn, A. Wallraff, and K. Ensslin (2015), "Microwave Emission from Hybridized States in a Semiconductor Charge Qubit", *Physical Review Letters* **115**, 046802.

Stockklauser, A., P. Scarlino, J. V. Koski, S. Gasparinetti, C. K. Andersen, C. Reichl, W. Wegscheider, T. Ihn, K. Ensslin, and A. Wallraff (2017), "Strong Coupling Cavity QED with Gate-Defined Double Quantum Dots Enabled by a High Impedance Resonator", *Physical Review X* **7**, 011030.

Takakura, T., M. Pioro-Ladrière, T. Obata, Y. S. Shin, R. Brunner, K. Yoshida, T. Taniyama, and S. Tarucha (2010), "Triple quantum dot device designed for three spin qubits", *Applied Physics Letters* **97**, 212104.

Tarucha, S., D. G. Austing, T. Honda, R. J. van der Hage, and L. P. Kouwenhoven (1996), "Shell Filling and Spin Effects in a Few Electron Quantum Dot", *Physical Review Letters* **77**, 3613–3616.

Tavis, M. and F. W. Cummings (1968), "Exact solution for an N-molecule-radiation-field Hamiltonian", *Physical Review* **170**, 379–384.

Taylor, J. M., V. Srinivasa, and J. Medford (2013), "Electrically Protected Resonant Exchange Qubits in Triple Quantum Dots", *Physical Review Letters* **111**, 050502.

Taylor, R. P., P. T. Coleridge, M. Davies, Y. Feng, J. P. McCaffrey, and P. A. Marshall (1994), "Physical and electrical investigation of ohmic contacts to AlGaAs/GaAs heterostructures", *Journal of Applied Physics* **76**, 7966–7972.

The BIG Bell Test Collaboration (2018), “Challenging local realism with human choices”, *Nature* **557**, 212–216.

Thompson, R. J., G. Rempe, and H. J. Kimble (1992), “Observation of normal-mode splitting for an atom in an optical cavity”, *Physical Review Letters* **68**, 1132–1135.

Tinkham, M. (1996), *Introduction to Superconductivity*, New York: McGraw-Hill.

Toida, H., T. Nakajima, and S. Komiyama (2013), “Vacuum Rabi Splitting in a Semiconductor Circuit QED System”, *Physical Review Letters* **110**, 066802.

Tokura, Y., W. G. van der Wiel, T. Obata, and S. Tarucha (2006), “Coherent Single Electron Spin Control in a Slanting Zeeman Field”, *Physical Review Letters* **96**, 047202.

Trauzettel, B., D. V. Bulaev, D. Loss, and G. Burkard (2007), “Spin qubits in graphene quantum dots”, *Nature Physics* **3**, 192–196.

Trif, M., V. N. Golovach, and D. Loss (2008), “Spin dynamics in InAs nanowire quantum dots coupled to a transmission line”, *Physical Review B* **77**, 045434.

Van Woerkom, D. J., A. Proutski, R. J. Van Gulik, T. Kriváchy, D. Car, S. R. Plissard, E. P. Bakkers, L. P. Kouwenhoven, and A. Geresdi (2017), “Josephson radiation and shot noise of a semiconductor nanowire junction”, *Physical Review B* **96**, 094508.

Vandersypen, L. M. K., H. Bluhm, J. S. Clarke, A. S. Dzurak, R. Ishihara, A. Morello, D. J. Reilly, L. R. Schreiber, and M. Veldhorst (2017), “Interfacing spin qubits in quantum dots and donors—hot, dense, and coherent”, *npj Quantum Information* **3**, 34.

Veldhorst, M., J. C. Hwang, C. H. Yang, A. W. Leenstra, B. De Ronde, J. P. Dehollain, J. T. Muhonen, F. E. Hudson, K. M. Itoh, A. Morello, and A. S. Dzurak (2014), “An addressable quantum dot qubit with fault-tolerant control-fidelity”, *Nature Nanotechnology* **9**, 981–985.

Veldhorst, M, C. H. Yang, J. C. C. Hwang, W Huang, J. P. Dehollain, J. T. Muhonen, S Simmons, A Laucht, F. E. Hudson, K. M. Itoh, A Morello, and A. S. Dzurak (2015), “A two-qubit logic gate in silicon”, *Nature* **526**, 410–414.

Viennot, J. J., M. R. Delbecq, M. C. Dartiailh, A. Cottet, and T. Kontos (2014), “Out-of-equilibrium charge dynamics in a hybrid circuit quantum electrodynamics architecture”, *Physical Review B* **89**, 165404.

Viennot, J. J., M. C. Dartiailh, A. Cottet, and T. Kontos (2015), “Coherent coupling of a single spin to microwave cavity photons”, *Science* **349**, 408–411.

Volokitin, A. I. and B. N. Persson (2007), “Near-field radiative heat transfer and noncontact friction”, *Reviews of Modern Physics* **79**, 1291–1329.

Wallraff, A., D. I. Schuster, A. Blais, L. Frunzio, R. S. Huang, J. Majer, S. Kumar, S. M. Girvin, and R. J. Schoelkopf (2004), "Strong coupling of a single photon to a superconducting qubit using circuit quantum electrodynamics", *Nature* **431**, 162–167.

Wallraff, A., D. I. Schuster, A. Blais, L. Frunzio, J. Majer, M. H. Devoret, S. M. Girvin, and R. J. Schoelkopf (2005), "Approaching Unit Visibility for Control of a Superconducting Qubit with Dispersive Readout", *Physical Review Letters* **95**, 060501.

Walls, D. F. and G. J. Milburn (2008), *Quantum Optics*, Berlin, Heidelberg: Springer.

Walter, T., P. Kurpiers, S. Gasparinetti, P. Magnard, A. Potočnik, Y. Salathé, M. Pechal, M. Mondal, M. Oppliger, C. Eichler, and A. Wallraff (2017), "Rapid High-Fidelity Single-Shot Dispersive Readout of Superconducting Qubits", *Physical Review Applied* **7**, 054020.

Wang, C., C. Axline, Y. Y. Gao, T. Brecht, Y. Chu, L. Frunzio, M. H. Devoret, and R. J. Schoelkopf (2015), "Surface participation and dielectric loss in superconducting qubits", *Applied Physics Letters* **107**, 162601.

Watson, T. F., S. G. Philips, E. Kawakami, D. R. Ward, P. Scarlino, M. Veldhorst, D. E. Savage, M. G. Lagally, M. Friesen, S. N. Coppersmith, M. A. Eriksson, and L. M. Vandersypen (2018), "A programmable two-qubit quantum processor in silicon", *Nature* **555**, 633–637.

Wees, B. J. van, L. P. Kouwenhoven, C. J. P. M. Harmans, J. G. Williamson, C. E. Timmering, M. E. I. Broekaart, C. T. Foxon, and J. J. Harris (1989), "Observation of zero-dimensional states in a one-dimensional electron interferometer", *Physical Review Letters* **62**, 2523–2526.

Wennberg, A. K., S. N. Ytterboe, C. M. Gould, H. M. Bozler, J. Klem, and H. Morkoç (1986), "Electron heating in a multiple-quantum-well structure below 1 K", *Physical Review B* **34**, 4409–4411.

Wiel, W. G. van der, S. De Franceschi, J. M. Elzerman, T. Fujisawa, S. Tarucha, and L. P. Kouwenhoven (2002), "Electron transport through double quantum dots", *Reviews of Modern Physics* **75**, 1–22.

Woerkom, D. J. van, P. Scarlino, J. H. Ungerer, C. Müller, J. V. Koski, A. J. Landig, C. Reichl, W. Wegscheider, T. Ihn, K. Ensslin, and A. Wallraff (2018), "Microwave Photon-Mediated Interactions between Semiconductor Qubits", *Physical Review X* **8**, 041018.

Wolff, I. (2006), *Coplanar Microwave Integrated Circuits*, Hoboken: John Wiley and Sons Inc.

Wu, X., D. R. Ward, J. R. Prance, D. Kim, J. K. Gamble, R. T. Mohr, Z. Shi, D. E. Savage, M. G. Lagally, M. Friesen, S. N. Coppersmith, and M. A. Eriksson (2014), "Two-axis control of a singlet-triplet qubit with an integrated micromagnet", *Proceedings of the National Academy of Sciences* **111**, 11938–11942.

Xiang, Z. L., S. Ashhab, J. Q. You, and F. Nori (2013), "Hybrid quantum circuits: Superconducting circuits interacting with other quantum systems", *Reviews of Modern Physics* **85**, 623–653.

Yang, C. H., A. Rossi, R. Ruskov, N. S. Lai, F. A. Mohiyaddin, S. Lee, C. Tahan, G. Klimeck, A. Morello, and A. S. Dzurak (2013), "Spin-valley lifetimes in a silicon quantum dot with tunable valley splitting", *Nature Communications* **4**, 2069.

Yoneda, J., K. Takeda, T. Otsuka, T. Nakajima, M. R. Delbecq, G. Allison, T. Honda, T. Kodera, S. Oda, Y. Hoshi, N. Usami, K. M. Itoh, and S. Tarucha (2018), "A quantum-dot spin qubit with coherence limited by charge noise and fidelity higher than 99.9%", *Nature Nanotechnology* **13**, 102–106.

Zajac, D. M., A. J. Sigillito, M. Russ, F. Borjans, J. M. Taylor, G. Burkard, and J. R. Petta (2018), "Resonantly driven CNOT gate for electron spins", *Science* **359**, 439–442.

Zhang, W., K. Kalashnikov, W. S. Lu, P. Kamenov, T. Dinapoli, and M. E. Gershenson (2019), "Microresonators Fabricated from High-Kinetic-Inductance Aluminum Films", *Physical Review Applied* **11**, 011003.

Zheng, G., N. Samkharadze, M. L. Noordam, N. Kalhor, D. Brousse, A. Sammak, G. Scappucci, and L. M. K. Vandersypen (2019), "Rapid gate-based spin read-out in silicon using an on-chip resonator", *Nature Nanotechnology* **14**, 742–746.

Zorin, A. B. (1995), "The thermocoax cable as the microwave frequency filter for single electron circuits", *Review of Scientific Instruments* **66**, 4296–4300.

Zwanenburg, F. A., A. S. Dzurak, A. Morello, M. Y. Simmons, L. C. Hollenberg, G. Klimeck, S. Rogge, S. N. Coppersmith, and M. A. Eriksson (2013), "Silicon quantum electronics", *Reviews of Modern Physics* **85**, 961–1019.

List of publications

1. A. J. Landig, J. V. Koski, P. Scarlino, U.C. Mendes, A. Blais, C. Reichl, W. Wegscheider, A. Wallraff, K. Ensslin and T. Ihn (2018), “Coherent spin-photon coupling using a resonant exchange qubit”, Nature **560**, 179-184.
2. A. J. Landig, J. V. Koski, P. Scarlino, C. Reichl, W. Wegscheider, A. Wallraff, K. Ensslin and T. Ihn (2019), “Cavity-Detected Spin Blockade in a Few-Electron Double Quantum Dot”, PRL **122**, 213601.
3. A. J. Landig, J. V. Koski, P. Scarlino, C. Müller, J. C. Abadillo-Uriel, B. Kratochwil, C. Reichl, W. Wegscheider, S. N. Coppersmith, Mark Friesen, A. Wallraff, T. Ihn and K. Ensslin (2019), “Coherent long-distance spin-qubit–transmon coupling”, arXiv: 1903.04022.
4. J. V. Koski, A. J. Landig, A. Pályi, P. Scarlino, C. Reichl, W. Wegscheider, G. Burkard, A. Wallraff, K. Ensslin and T. Ihn (2018), “Floquet spectroscopy of a strongly driven quantum dot charge qubit with a microwave resonator”, PRL **121**, 043603.
5. J. V. Koski, A. J. Landig, M. Russ, J. C. Abadillo-Uriel, P. Scarlino, B. Kratochwil, C. Reichl, W. Wegscheider, G. Burkard, Mark Friesen, S. N. Coppersmith, A. Wallraff, K. Ensslin and T. Ihn (2019), “Strong photon coupling to the quadrupole moment of an electron in solid state”, arXiv: 1905.00846.
6. D. J. van Woerkom, P. Scarlino, J. H. Ungerer, C. Müller, J. V. Koski, A. J. Landig, C. Reichl, W. Wegscheider, T. Ihn, K. Ensslin and A. Wallraff (2018), “Microwave Photon-Mediated Interactions between Semiconductor Qubits”, PRX **8**, 041018.
7. P. Scarlino, D. J. van Woerkom, U. C. Mendes, J. V. Koski, A. J. Landig, C. K. Andersen, S. Gasparinetti, C. Reichl, W. Wegscheider, K. Ensslin, T. Ihn, A. Blais and A. Wallraff (2019), “Coherent microwave photon mediated coupling between a semiconductor and a superconductor qubit”, Nature Communications **10**, 3011.

Acknowledgements

I would first of all like to thank Klaus Ensslin for giving me the opportunity and putting his trust in me to set up a new experiment in his lab. I felt very well supported by his balance between guiding our research plans while leaving me freedom to pursue my own ideas. I am also very grateful for the support from Thomas Ihn especially for sharing his intuitive understanding of physical concepts and digging deep into our results to help understanding many details. This thesis has immensely profited from the close collaboration between the group of Klaus Ensslin and Thomas Ihn and the group of Andreas Wallraff. Many thanks to Andreas for his valuable input and for sharing the knowledge of his group about microwave technology. I would also like to thank Guido Burkard for helpful discussions during my work and for examining my thesis.

I very much enjoyed working closely together with Jonne Koski and Pasquale Scarlino and I am grateful for their continuous support and dedication to our projects. Many thanks to Jonne for sharing his experimental intuition and profound theoretical knowledge at any time. Many thanks also to Pasquale for his inspiring ideas and his indispensable fab support. I am thankful to Benedikt Kratochwil for this selfless support in the lab. I wish him many exciting results with our setup. I also thank Anna Stockklauser, Ville Maisi and David van Woerkom for their contributions. Special thanks to Anna for introducing me to the clean room and for sharing her thesis template.

I am thankful to Peter Märki for contributing his immense technical and electrical engineering skills to our experimental setup. I will always remember how he fixed a leak in our dilution circuit at one of the most difficult locations as if it would be his daily business. I would also like to thank him for his help in many other occasions and for keeping up a good atmosphere in our group at any time. Thanks also to Andreas Stuker and his team for their excellent work in the workshop and thanks to Erwin Studer and Beat Bräm for their technical support.

I felt a supportive atmosphere from many members of Andreas Wallraff's group that were not directly involved in the collaboration. When designing and assembling

the microwave setup, I could count on the support from Philipp Kurpiers and Theodore Walter, for which I am very grateful. Thanks a lot also to Michele Collodo for always being open to share his knowledge in many helpful discussions. I would also like to acknowledge discussions with Christian Andersen and the fab support from Mihai Gabureac, Anton Potočnik and Mintu Mondal.

I would like to thank QSIT for funding my work, our collaborators Christian Reichl and Werner Wegscheider for providing the heterostructure and José Carlos Abadillo-Uriel, Alexandre Blais, Susan Coppersmith, Mark Friesen, Udson Cabral Mendes and Clemens Müller for their theory support.

Thanks to my family and friends for their endless support and thank you Raliza and Aurelia for making my life also outside the world of physics so enjoyable!